Ultrafast induced structural dynamics probed by time-resolved photoelectron spectroscopy

Manuel de Anda Villa

THÈSE DE DOCTORAT
DE SORBONNE UNIVERSITÉ

Spécialité : Physique

École doctorale n°564: Physique en Île-de-France

réalisée

à l'Institut des Nanosciences de Paris

sous la direction de Dominique Vernhet

présentée par

Manuel DE ANDA VILLA

pour obtenir le grade de :

DOCTEUR DE SORBONNE UNIVERSITÉ

Sujet de la thèse :

Dynamique structurelle induite par laser ultrabref sondée par spectroscopie des photoélectrons résolue en temps

soutenue le 17 décembre 2019

devant le jury composé de :

M.	Aurélien CRUT	Rapporteur
M.	Michael MEYER	Rapporteur
M.	Martin GARCIA	Examinateur
M^{me}	Claire LAUHLE	Examinatrice
M.	Richard TAIEB	Examinateur
M^{me}	Dominique VERNHET	Directrice de thèse
M^{me}	Anna LEVY	Co-encadrante

A mis padres y mi a hermana.

Acknowledgements

In these pages, it is reflected all my gratitude for so many people that I've met during the last three years and that have supported me one way or another. Evidently, words can only begin to describe how I feel and I plead the limitations of the written word for everything that I left unsaid.

First of all, I would like thank to the directors of the Institut des Nanosciences de Paris (INSP), Christophe Testelin and Massimiliano Marangolo. The INSP is a very nourishing place to work in, thanks to all its members, including all faculty, engineers, staff, and student members.

I want to express the greatest gratitude to the members of the ASUR team. When I arrived three years ago, I was not only arriving to a new project, but also to a new country, culture, and a new life. They warmly welcomed me from day one and made me feel much supported in a friendly environment that was determinant for my wellbeing and my fulfilment.

I am thankful to my very patient and understanding Ph.D. advisors: Anna Lévy and Dominique Vernhet, who guided me with kindness and enthusiasm throughout the project. I also want to acknowledge Martino Trassinelli, Emily Lamour, and Christophe Prigent for always being there for fruitful discussions and for their knowledgeable advice. I am also very thankful with Stephane Macé, who devoted himself to our experiment design and development; his contributions were essential for the success of our experiments. Likewise I want to thank Sebastien Steydli and Daniel Schury. Moreover, I want to thank former members of the ASUR team: Sophie Cervera and Ajit Gupta.

I am very grateful to all the members of the CELIA laboratory in Bordeaux, who were very welcoming, and who contributed deeply in the success of the project. I want to especially recognize Jérôme Gaudin and Nikita Fedorov, for all those long days and nights that we spent in the lab. I also acknowledge Patrick Martin for being a great host and getting involved with our project. Furthermore, I want to thank Dominique Descamps, who always kept the laser running smoothly and was available for friendly discussions. Valérie Blanchet, Yann Mairesse, Fabien Dorchies also helped us with their expertise. Thanks also to Minna Patanen and the people from the PLEIADES beamline at the synchrotron SOLEIL for sharing their expertise in synchrotron-based experiments.

I want to thank as well Robert Grisenti and Ryszard Sobierajski, with whom I also shared many long days during experiments and many amazing dinners in Bordeaux.

Big thank you to Hervé Jouin, with whom I enjoyed very much discussing physics in Spanish and was also a great host in Bordeaux. He was extremely kind and warm to me.

I also want to thank Caterina Riconda and Samuel Marini from the LULI laboratory. Both were very optimistic with the project and contributed by performing simulations. They were very patient with me and always available when I needed their advice.

I want to thank the jury: Aurelien Crut, Michael Meyer, Martin Garcia, Claire Lauhle and Richard Taieb. They read my manuscript with enthusiasm and their comments and discussion we had was very enriching. Finally I want to acknowledge the great effort that they made coming to Paris in the middle of the strikes.

I am very thankful to Xavier Fresquet, Charlotte Mansour and Chantal Stehle, from the LABEX Plas@Par. They created an amazing environment that deeply enriched my professional experience. Their motivation was truly inspiring to me.

This project was also successful thanks to the support from CONACYT, the people, and the government of Mexico. I'm grateful for the confidence and the effort made for financing my graduate studies, from the beginning of my Master's degree to the completion of my PhD. I acknowledge also the committee abroad of CONACYT scholars: Carlos Pellicer Camara and all their wonderful members: ¡La unión hace la fuerza! Estoy en deuda con ustedes.

During these three years I encountered amazing people working at Sorbonne Université that were also part of this life experience and to whom I am also grateful: Jaqui Ortega, Ericka Hervé, Naiara Muro, Carla Alves, Marifer Salas, Gerardo Perfors and many others.

I want to thank as well Cedric Brudermann and Jennifer Chaumont-Sturtevant and all my colleagues from the Languages Department. I also express my gratitude to Guadalupe Arellano, Uriel Esparza and Angus Dunnet, from the INSP. And the friends that I made at CELIA: Pedro Gonzalez de Alaiza and Giedre Achipovaite, and all the people from Bordeaux.

I want to thank my family who always supported me and believed in me. Armèle for all her support. My friends in Mexico (notably La Banda), France and other countries. I refrain myself from listing you in fear of forgetting anyone.

I want to especially thank Julia, whose support and kindness were essential during the last part of my PhD.

Finally, I should also acknowledge Pedro Infante, Jorge Negrete, Chava Flores, Agustin Lara and Guty Cardenas, for all those long hours that sang for me while I was doing research and writing my manuscript.

I repeated these verses in my head countless times. Mantra or else, today they have a clear meaning:

Un sauce de cristal, un chopo de agua,
un alto surtidor que el viento arquea,
un árbol bien plantado mas danzante,
un caminar de río que se curva,
avanza, retrocede, da un rodeo
y llega siempre.
–
Octavio Paz

Contents

Introduction

The development of intense femtosecond lasers, after the invention of the chirped pulse amplification technique (CPA) in 1985 [1], has given access to high excitation regimes of matter that were not available before. This has allowed the scientific community to explore the atomic lattice dynamics happening at femtosecond and picosecond timescales on materials under strong excitation. Moreover, a huge range of applications have been developed using ultrafast lasers, such as welding [2] and micromachining [3] to biomedical applications such as cell surgery [4] or photothermal therapies for illness treatment [5, 6]. Thus, studying the ultrafast laser-matter interaction becomes pertinent from a practical and a theoretical point of view.

When matter is irradiated with high intensity and femtosecond-to-picosecond laser pulses, a thermal non-equilibrium between hot electrons and cold ions is established in the material for a certain time (on the order of 10 ps). This situation modifies the properties of matter governing the response to the excitation. For example, solid-liquid phase-transitions can happen at temperatures lower than the standard melting temperature of certain semiconductors (called non-thermal fusion [7]). Or, on the contrary, the melting temperature can be risen due to the high excitation of electrons in some metals (called bond hardening [8]). The modelling of these processes is complex and there is still debate regarding the description of the material properties [9]. Input is needed from experimental studies to complete the understanding of such processes. For example, having information on dynamics of the electronic structure of the material could give access to the evolution of the atomic structural changes happening upon laser irradiation.

To study the dynamics of matter under ultrafast excitation, many time-resolved techniques have been used. Some examples are, x-ray absorption spectroscopy [10], x-ray and electron diffraction [11] or even optical interferometry [12] and ellipsometry [13]. All of these experiments study the evolution of material properties related to the lattice dynamics such as atomic ordering, electron temperature, the electronic structure of the material or the dielectric constant.

This thesis presents another approach, which is complementary to the previously mentioned ones: time-resolved photoelectron spectroscopy (Tr-PES). This technique consists in the detection of the photoelectron spectrum triggered by an XUV probe beam after sample excitation by an infrared pump laser pulse. The photoelectron spectrum is a picture of the electronic structure of the material. It also carries important information about the lattice structure. Associating the temporal evolution of the photoelectron spectrum with lattice dynamics can give important insight about the behavior of the material under excitation. Especifically, information about the electronic density of occupied states,

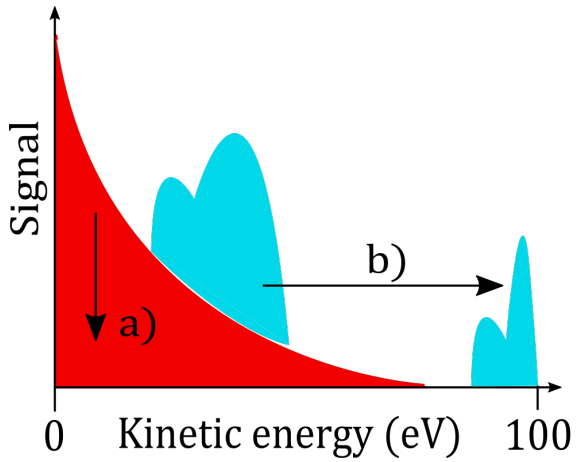

Fig. .1 *Scheme of the probe photoelectron spectrum (blue) and the pump photoelectron background (red). To avoid probe spectrum distortions two things need to be done. a) The pump background must be reduced, and b) the probe spectrum must be shifted to higher kinetic energies.*

lattice temperature and structure could become accessible.

We study metals with Tr-PES aiming to trigger dynamics as close as possible to their melting threshold. It is expected that their photoelectron spectrum is dependent on the lattice structure of the sample [14], making it possible to witness phase transitions with this technique.

Time-resolved photoelectron spectroscopy presents a big challenge. When irradiating metallic samples with ultrafast pump pulses, non-linear effects such as multiphoton ionization can take place and generate photoelectrons with tens of eV in kinetic energy (called "pump electrons"). The problem posed by the pump electrons is depicted in Figure .1. If they are emitted in a sufficient amount, they can form an important background that can conceal the probe-generated photoelectron spectrum (called "probe electrons"). Additionally, the electric field created by the pump electrons is capable of perturbing the probe spectrum. This perturbation, called space-charge effect [15], leads, in the worst case scenario, to a spectral deformation entailing an important loss of the carried information, and, in the best one, to a degradation of the spectral and temporal resolutions.

To solve these problems one can, on one hand, reduce the pump photoelectron background (Fig. .1 a)). On the other hand, one can make sure that the probe photoelectron spectrum is located at high kinetic energies to avoid the overlap with the pump background (Fig. .1 b)). But in any case, it is important to understand the mutual interaction between pump and probe electrons to disentangle heating-induced modifications of the spectrum from a possible space-charge effect.

Within the framework of this thesis, a dedicated experimental setup for time-resolved photoelectron spectroscopy was built and characterized. It consists in a pump/probe experiment with a probe arm based on a high-order harmonic generation beamline that produces extreme-ultraviolet (XUV) photon pulses with femtosecond duration. The XUV

photon energy is ~ 100 eV, which is sufficient to generate the probe photoelectron spectrum away from the pump background. Also, our pump/probe setup allows to reach the pump laser energies close to the threshold for triggering solid/liquid phase transitions. The material dynamics can be investigated in the vicinities of the melting threshold with enough resolution to detect laser heating-induced changes in the photoelectron spectrum.

The space-charge effect is present in numerous photoelectron spectroscopy experiments. For instance, there are light sources so brilliant that the number of photoelectrons issued from the XUV or x-ray probe is enough to generate space-charge distortions (as in free-electron lasers) [16].

In time-resolved photoelectron spectroscopy, the pump-induced space-charge effect has been observed by many different research groups working on numerous experiments, such as, time-and-angle-resolved PES [17, 18] or time-and-spin-resolved PES [19]. Given the importance of the pump-induced space-charge effect, this thesis presents an in-depth study and modelling of this process. We performed experimental measurements of this phenomenon with our setup. And, using different theoretical models we aimed to understand every aspect of the space-charge effect: the pump multiphoton photoemission process, the possibility of laser-electron interactions and the Coulomb interactions between pump and probe electrons travelling in vacuum before being detected.

Thanks to the experimental development and the space-charge study carried out beforehand, we were able to perform a proof-of-principle experiment for measurements of the dynamics on a metallic sample irradiated by an ultrafast laser. The experimental conditions were tuned to reduce the space-charge effect. Notably, we used a Cu sample with a reduced surface roughness (few nm) and a s-polarized pump laser with the adequate pulse duration and fluence. Moreover, Cu was chosen because it presents a large photoionization cross section at 100 eV compared to other metals, leading to experiments with sufficient signal-to-noise ratio. Finally, previous studies have predicted the expected spectral modifications in Cu [14].

The measurements were carefully analyzed and compared to numerical simulations to disentangle the spectral shape modifications issued from the space-charge effect from those induced by the pump-induced sample heating. Finally we proposed a strategy to pave the way towards an interpretation of the results consisting in the comparison, first, with the quantum-calculated electronic structure of the sample, and secondly, with thermodynamic simulations of the sample's response to the laser excitation.

The manuscript is organized as follows:

Chapter 1 details the scientific context that encircles this thesis. It includes the theoretical models and experimental state of the art to study matter under extreme conditions. The approach chosen for this thesis, which is time-resolved photoelectron spectroscopy is proposed.

Chapter 2 introduces the experimental development and the measured performances of our probe XUV beamline based on high order harmonics. Finally, the pump/probe setup is presented.

Chapter 3 deals with our in-depth study of the space-charge effect. It meticulously examines the different aspects of this phenomenon using experimental measurements and numerical calculations. Finally, experimental considerations are addressed, leading to the final chapter of this thesis.

Chapter 4 presents time-resolved photoelectron spectroscopy measurements on a well characterized Cu sample irradiated by ultrafast infrared laser pulses. The photoelectron spectrum modifications associated to lattice dynamics and its disentanglement from the space-charge induced ones are discussed along with a strategy for interpreting the results.

This manuscript will end with a conclusion and future perspectives.

Chapter I

Matter under extreme conditions

Some of the most used models and simulations describing laser-matter interactions in the picosecond and femtosecond time scale, still need improvement and insight. Input from experimental studies is highly important in order to compare the observed dynamics and physical properties to their predicting models.

In this chapter, I will present the topic of matter under ultrafast laser excitation. Along this chapter, the different models for studying this phenomenon will be addressed and the experimental techniques currently used will be detailed. Finally, our proposed experimental strategy in the context of ultrafast melting will be presented.

I.1 Ultrafast lattice dynamics and solid-liquid phase transitions

Ultrafast heating of materials give rise to phenomena and modification of material properties that are not accessible when exciting in longer timescales. The dynamics happening at the femtosecond and picosecond timescales need a precise framework and the constant input from experiments and models. This section will present the basic ultrafast heating process and the tools for describing it: the two-temperature model (TTM), hydrodynamic simulations, classical molecular dynamics and quantum molecular dynamics.

I.1.1 Phenomenological description

a) Energy absorption, heating and equilibration

Heating of materials with femtosecond laser pulses can give rise to a non-equilibrium state where the electronic and ionic temperature, T_e and T_i respectively, can differ by a few orders of magnitude. For example, T_e=10000 K and T_i= 300 K are observed in Cu using a 30 fs laser pulse at a fluence F = 10000 J/m^2 [20]. This specific out-of-equilibrium state can drastically modify the heating and cooling dynamics of matter. Thus, tracking the process of heating, electron-ion thermal equilibration and relaxation of the materials becomes fundamental to obtain insight on material properties such as electron and ion heat capacity, electron conductivity or electron-phonon coupling [9].

As depicted in Figure I.1 a), the energy upon ultrashort laser pulse irradiation of a material is deposited within the so-called skin depth δ_e, which is a parameter determining

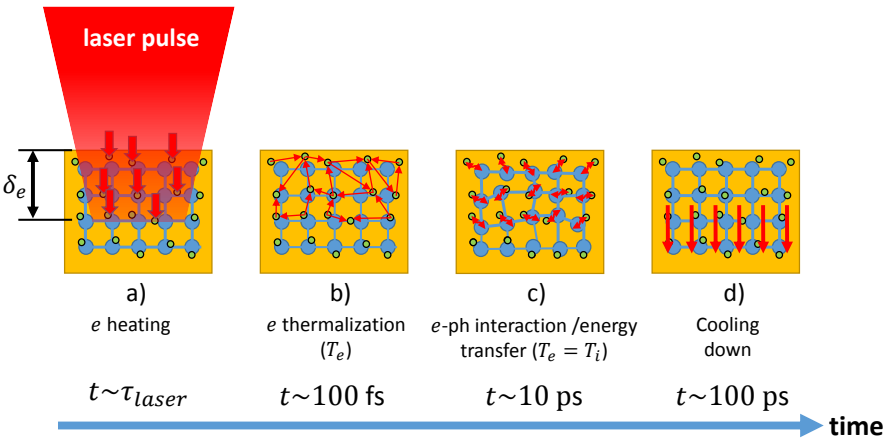

Fig. I.1 *Stages of the laser-matter interaction process: a)laser absorption by electrons within the skin depth δ_e b) electron thermalization by electron-electron collissions, c) energy transfer to the lattice via electron-phonon interactions and d) energy dissipation and cooling of the sample.*

the penetration depth of the oscillating laser electric field. The laser energy is firstly absorbed by the electron population. If the laser pulse impinging on the material is short enough (< few ps) it can lead to a significant rise of the electronic temperature (typically a few thousands of Kelvin) while the atomic lattice remains at its initial temperature.

At the end of the laser pulse, the energy is inhomogeneously distributed among the electrons. Then, processes happening at different timescales start to develop. By means of electron-electron collisions and energy transfer, electrons reach a Fermi-Dirac distribution characterized by a temperature T_e (Figure I.1 b)). This happens within a hundred femtoseconds and before this distribution is reached, the concept of temperature cannot be used [21].

The electronic population at T_e interacts with the atomic lattice at a temperature T_i via vibrational excitations known as phonons (Figure I.1 c)). The main relaxation channel of electron excitation is the electron-phonon interaction that supplies energy to the lattice. This electron-phonon interaction leads to thermal equilibrium between the electron and the phonon distributions ($T_e = T_i$). This happens typically within ten picoseconds [13].

Once the thermal equilibrium between electrons and phonons is reached, both T_e and T_i will evolve together as energy gets dissipated through radiative or non-radiative channels into the sample surroundings (bulk, substrate or environment; see Figure I.1 d)).

b) Thermal and non-thermal phase transitions

If sufficient energy is deposited by the laser pulse in the system, a phase transition can take place. Depending on the chemical nature and geometry of the target (bulk, thin layer or other) and the characteristics of the laser pulse, different processes may occur.

Thermal fusion. The ionic temperature increases due to the energy transfer from the electronic to the ionic population via electron-phonon collisions. If the melting temperature of the material is reached, a phase transition from solid to liquid can happen.

This process happens within a few ps after excitation. This process has been observed in Al [22] and other metals under low excitation levels, for example on Au (F = 400 J/m^2) [23] or Cu (F $\leq$ 200 J/m^2) [24].

Non-thermal fusion. It can take place for example, in semiconductors. A high level of electronic excitation can weaken the lattice interatomic bonds, thus disordering the lattice while it remains vibrationally cold. It has been reported that removing around 10% of the valence electrons from the bonding orbitals can weaken the lattice [7]. Another proposed origin of non-thermal melting for low bandgap semiconductors (such as $Ge_2Sb_2Te_5$ with a bandgap of 0.5 eV) is the indirect carrier multiplication produced by electron-electron scattering at high excitation energies [25]. This destabilization of the lattice can result in a phase transition happening in much shorter times ($\leq$ 500 fs) than the required one for electron-phonon temperature equilibration (few ps), and at a temperature that is much lower than the melting temperature (T_m) [26]. For example, a non-thermal melting of $Ge_2Sb_2Te_5$ has been assessed at temperatures of T $<$ 720 K whereas T_m = 900 K [25]; for InSb the melting has been estimated to happen at T between 400-550 K, which is below T_m=798 K [27, 28]. Other materials have been found to present non-thermal phase transitions such as GaAs [26], Si [29], Sb [30] and VO_2 [31].

Bond hardening. For some metals, an inverse situation to the non-thermal fusion mechanism can take place. Under strong electronic excitation, the screening of the attractive internuclear potential is reduced, and the phonon dispersion present an increase in the amplitude [8]. This means that the phonon modes become harder to excite. This "phonon hardening" yields a decrease in the ionic heat capacity. As a result, the Debye and melting temperatures (T_m) increase and the lattice stabilizes. The T_m increase is observed experimentally. Also, the thermal melting becomes delayed [32, 33]. This usually happens in metals whose density of occupied states (DOS) changes significantly at high T_e, such as Au. For example, for Au, the melting temperature have been predicted to increase from 1337 K to 3604 K (for T_e=70000 K) [8] and the predicted melting time has been observed to increase from 1 ps to $\sim$7 ps for a thin Au film [34]. On the contrary, in metals like Al whose DOS don't change significantly with increasing T_e, this effect is not expected [8].

As it can be noted, these phase transitions are dependent on the relationship between the electronic and ionic structures. This evidences the importance of studying the evolution of different physical observables such as electronic density of states or the ordering of the atomic lattice, which we aimed to study in this thesis.

Finally, the possibility and the type of phase transition will depend on the dynamics upon excitation that is governed by the material properties, the target geometry (thickness, substrate, etc.) and the energy deposited in the system.

In order to model the ultrafast heating of materials and phase transitions, a theoretical framework is presented in the next section.

I.1.2 Theory: modelling and limitations

a) Energy absorption

The energy of the incoming infrared laser pulse is mainly absorbed by free electrons in the material. In a classical picture, the electrons are oscillating with the laser electric field, and in order for them to absorb the energy, a change in momentum parallel to the oscillation must occur. This happens mainly via a collision with a third partner such as an ion. A similar scenario is observed from the quantum picture: a third collision partner is needed to ensure energy and momentum conservation in order for an electron to absorb a photon.

Mathematically, the electron-ion collision leading to energy absorption and the electron-phonon interaction can be separated. This guides us to see that the collisions with fixed ions only change the momentum of the electron whereas collisions with ion vibrations (i.e. phonons) change the energy of the electrons [21].

Once the energy is absorbed, within the duration of the laser pulse, the electronic population is driven out of equilibrium, meaning that they cannot be described by a Fermi-Dirac distribution characterized by a temperature. Thermal equilibrium of the electronic population can be reached after a few 100 fs or even up to the picosecond regime [21]. Special attention must be taken when modelling the electron-phonon interaction for times shorter than the electron thermal equilibration. But in our case of interest, the electron thermalization time will not be investigated as the timescales studied are longer than these characteristic times.

b) The two-temperature model

A model commonly used to study the electron-phonon interaction upon laser irradiation is the so-called Two-Temperature Model (TTM), first proposed by Kaganov et al. in 1957 [35] and then formulated as used nowadays by Anisimov et al. in 1974 [36]. It describes the temporal and spatial evolution of the lattice and electron temperatures T_e and T_i (see Fig. I.2) by means of a pair of coupled non-linear differential equations:

$$C_e(T_e)\frac{\partial T_e}{\partial t} = \nabla[K_e(T_e,T_i)\nabla T_e] - G(T_e)(T_e - T_i) + S(\vec{r},t) \tag{I.1}$$

$$C_i(T_i)\frac{\partial T_i}{\partial t} = \nabla[K_i(T_i)\nabla T_i] + G(T_e)(T_e - T_i) \tag{I.2}$$

where $C_{e,i}$ is the electron and ion heat capacity, $K_{e,i}$ the thermal conductivity of the electron and lattice distributions, $G(T_e)$ is the electron-phonon coupling, and S is the source term that accounts for the energy being deposited in the target. In our case, the S term is associated to the laser pulse. In metals, the lattice heat conductivity is usually not taken into account due to its negligible contribution compared to the electron heat conductivity.

This fairly simple model has been extended to include different phenomena such as the description of grain scattering, energy transfer by ballistic electrons or the transient non-thermal electron dynamics happening after energy absorption (for these extended TT models see refs. in [9]). Furthermore, it has also been shown that electron-phonon energy transfer can lead at early times to non-thermal phonon distributions, and corrections to

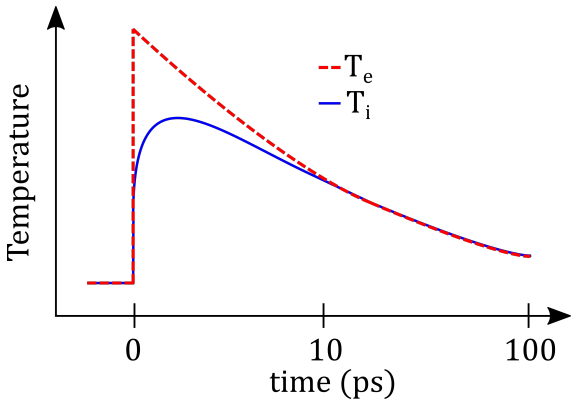

Fig. I.2 *Two-temperature model output showing the temporal evolution of the T_e and T_i.*

the TTM have been proposed in this direction by including different phonon populations [37].

The parameters used in the TTM ($C_{e,i}$, $K_{e,i}$ and G) are also subject of analysis and debate. For some ranges of T_e usually restricted to low temperatures (few 1000 K), the thermophysical properties can be calculated following some approximations, as it will be seen in the following paragraphs. However in the case of high T_e (usually above 5000 K), the properties of the material can be affected by the high electron excitation of lower band electrons. Lin et al. [9] have calculated the temperature dependent electron heat capacity and electron-phonon coupling by connecting the electronic density of states (DOS) of the material and these temperature dependencies. In order to perform these calculations, sufficient knowledge of the DOS is needed.

For many situations, approximating the material DOS to the free electron gas DOS can yield values for the thermophysical properties that are accurate enough. This is true especially when calculating the properties of Al, whose DOS deviates only slightly from the free electron gas model. But when calculating the thermophysical properties of other materials under strong T_e-T_i non-equilibrium, it becomes necessary to use more accurate descriptions. Lin et al. have compared the use of the free electron gas and the specific DOS calculated using the Vienna ab initio simulation package (VASP) for different metals and have found significant deviations from the free electron gas model and other common approximations such as the Sommerfeld expansion used for calculating the electron heat capacity.

Furthermore, if the electronic excitation is strong enough to modify the DOS, these changes need to be taken into account for calculating the correct value of the thermophysical properties [38, 8].

In the following, a description of the aforementioned quantities is given using the most adequate models.

Ion heat capacity, C_i

This parameter can be defined as the energy necessary to increase T_i by a given quantity. It is one of the parameters that govern the equilibration temperature between T_e and T_i:

$$C_i(T_i) = \frac{\partial E_i}{\partial T_i}, \tag{I.3}$$

where E_i is the internal energy of the ion population.

Usually, this quantity is only dependent on the T_i and not on the electronic excitation and thus can be calculated from equations of state $f(p, T, \rho) = 0$ where p and ρ are pressure and density respectively [39]. Another approximation can be obtained from the Dulong-Petit law that states a contribution of $3k_B$ per ion, where k_B is the Boltzmann constant. For Cu we find $C_i = 3.5\times\ 10^6$ J/m^{3}K [14].

Electron Heat Capacity, C_e

This parameter is defined as the energy necessary to increase T_e by a given quantity. It has an influence on the maximal T_e as well as on the equilibration temperature.

Following the Sommerfeld expansion at low T_e (for Cu $T_e < 3000$ K) one finds an electron heat capacity linearly dependent on the electronic temperature:

$$C_e(T_e) = \frac{\partial E_e}{\partial T_e} = \gamma T_e, \tag{I.4}$$

where E_e is the internal energy of the electron population, $\gamma = \pi^2 k_B^2 g(\varepsilon_F)/3$ is the electronic heat capacity constant and $g(\varepsilon_F)$ is the DOS evaluated at the Fermi energy. For example, in the case of Cu calculations yield $\gamma = 96.8$ Jm^{-3}K^{-2} [9].

For higher temperatures, this approximation is no longer valid and it is necessary to take into account the full spectrum of the DOS:

$$C_e(T_e) = \frac{\partial E_e}{\partial T_e} = \int_{-\infty}^{+\infty} \frac{\partial f(\varepsilon, \mu, T_e)}{\partial T_e} g(\varepsilon)\varepsilon d\varepsilon, \tag{I.5}$$

where the Fermi-Dirac distribution is $f(\varepsilon, \mu, T_e) = \{\exp[(\varepsilon - \mu)/k_B T_e] + 1\}^{-1}$.

This representation needs the evaluation of the chemical potential $\mu(T_e)$. This is done in [9] using the fact that the total number of electrons (N_e) is:

$$N_e = \int_{-\infty}^{+\infty} f(\varepsilon, \mu, T_e) g(\varepsilon) d\varepsilon, \tag{I.6}$$

and then, solving for $\mu(T_e)$. Another approximation for calculating $\mu(T_e)$ has been given in [40] where the T_e and the electronic density n_e are needed.

A comparison between C_e obtained with the DOS and the $C_e(T_e) = \gamma T_e$ is presented in Figure I.3 (adapted from [9]). Two values of γ are used: one obtained theoretically (γ_{theo}) and other experimentally (γ_{exp}). At very low T_e, both $C_e(T_e) = \gamma T_e$ agree with the one calculated using the DOS. At higher temperatures the C_e is underestimated by the linear approximations.

This evidences the necessity of including the DOS in the C_e calculation at high temperatures. Moreover, it becomes important to have an adequate knowledge on the density of occupied states that can undergo modifications at high T_e.

Electron-phonon coupling, G

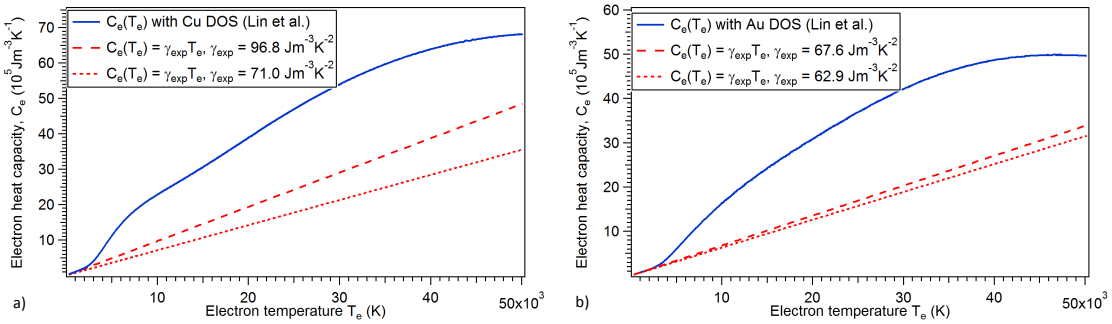

Fig. I.3 *Electron heat capacity C_e obtained using the Sommerfeld expansion and yielding $C_e(T_e) = \gamma T_e$ and obtained using the DOS for a) Cu and b) Au from [9].*

This quantity is defined as the rate of energy transfer between the electron and ion populations. It will mainly determine the equilibration time for $T_e = T_i$.

The electron-phonon coupling can be expressed in terms of the electron relaxation times at temperature T_e:

$$G = \frac{\pi^2}{6} \frac{m_e C_s^2 n_e}{\tau(T_e) T_e}, \tag{I.7}$$

where C_s is the speed of sound, n_e the density of electrons and $\tau(T_e)$ is the electron-phonon scattering time evaluated assuming $T_e = T_i$ [9]. When the condition $T_e = T_i$ is fulfilled, then $\tau(T_e) \sim 1/T_e$ and the value of equation (I.7) becomes a constant.

Following the treatment by Lin et al. [9], when the electronic temperature becomes so important that the scattering must also include electrons away from the Fermi surface, then the electron-phonon coupling can be calculated as:

$$G(T_e) = \frac{\pi \hbar k_B \lambda \langle \omega^2 \rangle}{g(\varepsilon_F)} \int_{-\infty}^{+\infty} g^2(\varepsilon)(-\frac{\partial f}{\partial \varepsilon}) \, d\varepsilon, \tag{I.8}$$

where λ is the electron-phonon mass enhancement parameter and $\langle \omega^2 \rangle$ is the second moment of the phonon spectrum.

Figure I.4 presents the comparison between the electron-phonon coupling factor G calculated using the total DOS of materials [9] and an experimental evaluation at low T_e [41]. In the case of Cu, the experimental measurement of G does not agree with the DOS-calculated G, not even at low T_e, where it is overestimated. At higher temperatures, the experimental measurements for both Cu and Au underestimate the value of G.

The experimental value discrepancy with the electron-phonon coupling using the DOS evidences that to properly describe the electron-phonon interaction at high T_e, a constant approximation does not suffice. It becomes relevant, again, to have information regarding the electronic structure of the material.

Electron heat conductivity K_e

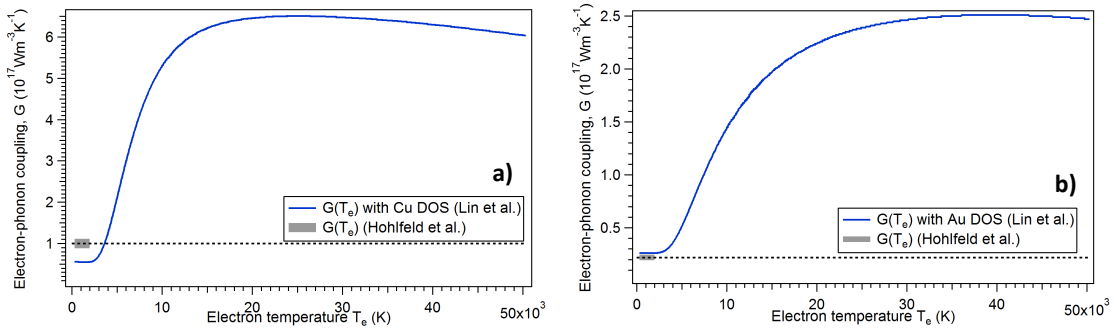

Fig. I.4 *Electron-phonon coupling G of a) Cu and b) Au, calculated using the DOS by Lin et al. [9] and determined experimentally by Hohlfeld et al. [41]. The thick gray line determine the range of T_e values of the experimental measurement.*

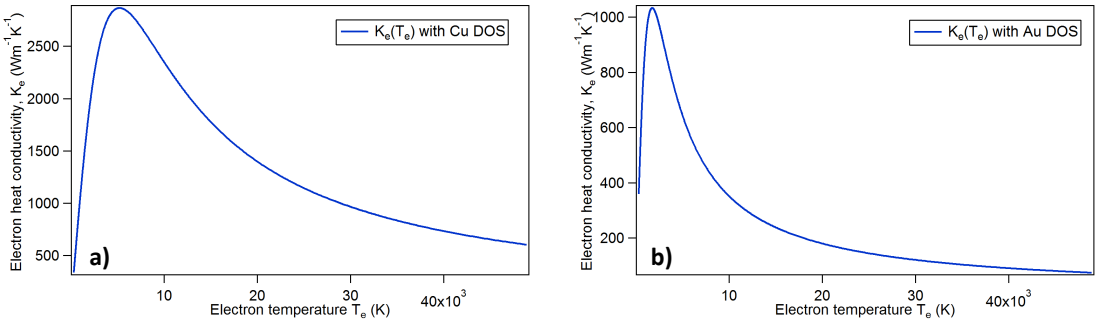

Fig. I.5 *Electron thermal conductivity K_e for a) Cu and b) Au as a function of electron temperature T_e following the model from [9].*

This quantity governs the diffusion of heat inside the material. Its contribution becomes important when the energy deposition in the material is inhomogeneous, for instance when irradiating metallic samples thicker than the skin depth δ_e with infrared lasers. In the case of Cu, $\delta_e \sim 3.4$ nm for a laser pulse at λ=800 nm. This means that, beyond this thickness, the material will be significantly colder right after excitation and the temperature gradient will establish a heat flow.

For a situation where there is a negligible temperature gradient, which is the case of a very thin material, for example a free-standing nanolayer [42], this term can be neglected as no effective energy transport can take place.

The electron heat conductivity can be calculated from the Drude model relationship

$$K_e(T_e, T_i) = v_F^2 C_e(T_e)\tau_e(T_e, T_i)/3, \tag{I.9}$$

where v_F is the Fermi velocity and $\tau_e(T_e, T_i)$ is the total scattering time of electrons [43, 13]. From this equation, it is evident that the electron heat conductivity can undergo modifications from electronic excitation as it is related to the electron heat capacity C_e, and through modifications of $\tau_e(T_e, T_i)$.

Lin et al. [9] present a model where the contribution from electron-electron scattering rate is $1/\tau_{e-e} = AT_e^2$ and from electron-phonon scattering rate is $1/\tau_{e-ph} = BT_i$. Thence, $1/\tau_e = 1/\tau_{e-e} + 1/\tau_{e-ph} = AT_e^2 + BT_i$. For Cu, these coefficients are estimated to be $A = 2.66 \times 10^6 s^{-1}K^{-2}$ and $B = 2.41 \times 10^{11} s^{-1}K^{-1}$ [44], whereas for Au $A = 1.2 \times 10^7 s^{-1}K^{-2}$ and $B = 1.23 \times 10^{11} s^{-1}K^{-1}$ [23] yielding a K_e that is dependent on T_e, as depicted on Figure I.5.

Other models for K_e have been proposed (and are not discussed here), for example, by Anisimov in 1997 [45] and the model by Winter et al. in 2017 [13] where the main difference is the treatment of τ_{e-e}.

The TTM is a very useful tool for describing the evolution of the energy deposition and the temperatures of the electronic and ionic systems. Additional models including the hydrodynamic evolution of the materials (that follow the changes in density, for example), and others describing the microscopic aspects of the ultrafast laser excitation, are presented in the following sections.

c) Hydrodynamic simulations

Another description of excited matter comes from the hydrodynamic perspective [46]. The laser energy deposition, electron thermalization and electron-phonon equilibration (T_e=T_i) happen usually in times faster than the expansion of the material. Thus, a simple expansion model can be used to describe the expansion of the material. The equations of fluid dynamics describe the expanding sample:

$$\frac{\partial \rho}{\partial t} + \frac{\partial}{\partial x}(\rho u) = 0 \tag{I.10}$$

$$\frac{\partial u}{\partial t} + u\frac{\partial u}{\partial x} = -\frac{1}{\rho}\frac{\partial p}{\partial x}, \tag{I.11}$$

where ρ is the density, p the pressure, x and u are the position and velocity of expansion respectively.

There are also hybrid models that combine the description of the TTM with the hydrodynamic perspective and the energy deposition. In the present thesis, the hybrid code ESTHER [47] will be presented in chapter IV. In this fashion, the predictions of the TTM can be linked to the hydrodynamic evolution of the material, yielding, for instance, phase transitions. As will be seen in section I.2, there are experimental techniques that assess directly the expansion of the materials, thus a code including these kind of predictions allows for a direct model-experiment comparison.

In this thesis, the comparison between our experiments and the predictions of ESTHER is indirect, but, as it will be presented in chapter IV, a precise link between our measured observable and the hydrodynamic quantities can be established.

The hydrodynamic simulations are macroscopic descriptions of the evolution of the excited material. In the following, a microscopic approach is presented.

d) Molecular dynamic simulations

Molecular dynamic simulations can help the understanding of ultrafast laser heating of materials by calculating the motion of N simulated particles. The simulations solve the classical newtonian equations of motion for each individual ion in the lattice:

$$m_j \frac{d^2\mathbf{r}_j(t)}{dt^2} = \mathbf{F}_i(t) \tag{I.12}$$

$$\mathbf{F}_i(t) = \frac{\partial V(\mathbf{r}^N)}{\partial \mathbf{r}_j}, \tag{I.13}$$

where m_j is the mass of the j ion, $\mathbf{r}_j$ its position and V the potential acting on it [46].

Usually, an interaction potential and the number of particles need to be chosen wisely to represent the system in the most realistic manner [46].

Molecular dynamics have an advantage over hydrodynamic calculations: they include naturally the possibility of phase transitions (such as solid-solid or solid-liquid) or nucleation kinetics without any supplementary assumptions.

The thermodynamic quantities of the system such as density, temperature, or pressure are averaged over a fraction of the total particles in the simulation [46]. For N particles inside a volume V_N, the density is $n = N/V_N$. The local temperature T_N is determined from the equipartition theorem:

$$\frac{3}{2} n k_B T_N = \Sigma_{j=1}^{N} \frac{N}{2} |\mathbf{v}_j^T|^2, \tag{I.14}$$

where $\mathbf{v}_j^T = d\mathbf{r}_j/dt - \mathbf{v}^c$ is the thermal velocity of particle j with respect to the center of mass velocity $\mathbf{v}^c$ of the total particle cell.

Finally, the pressure can also be calculated through the virial theorem for an ideal gas:

$$p_N = n k_B T_N + \frac{n}{6} \Sigma_{j=1}^{N} \mathbf{F}_j \cdot \mathbf{r}_{j,N}, \tag{I.15}$$

with $\mathbf{F}_j$ the force acting on particle j and $\mathbf{r}_{j,N}$ the distance from the center of the cell.

Molecular dynamics only deal with the ionic population. For a more accurate description including both electron and ion populations a quantum model called quantum molecular dyamics should be used.

e) Quantum molecular dynamic simulations

Quantum molecular dynamics (QMD) are simulations modelling both the ionic and electronic populations of a system of particles. The goal of these simulations is to obtain the ionic and electronic structure of the system. For this purpose, the system will evolve from an initial condition until stability is reached for a desired configuration given by (ρ, T_e,

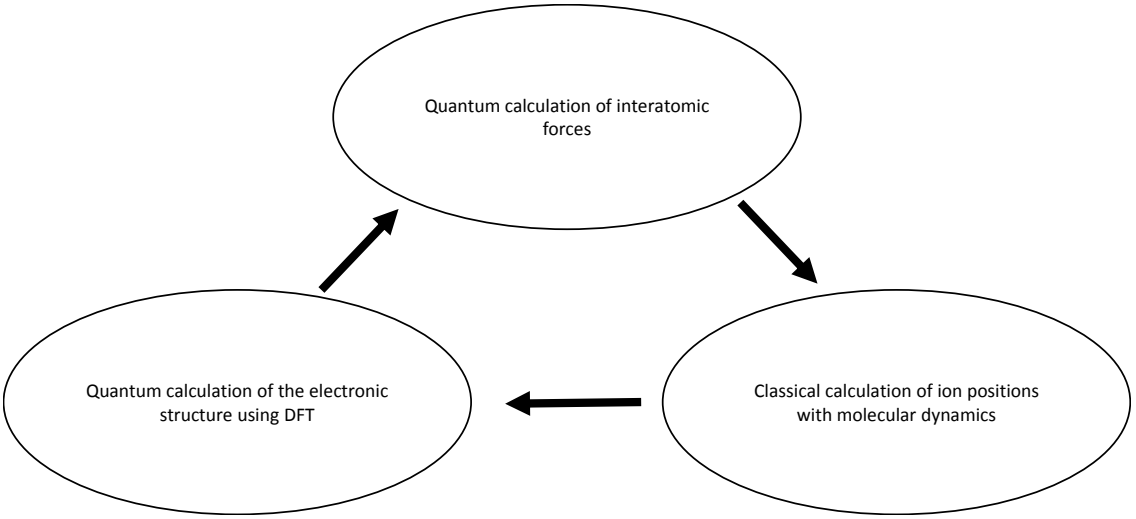

Fig. I.6 *Diagram for each time step in quantum molecular dynamic calculations.*

T_i). For example, this configuration might correspond to a calculation by the TTM at a precise instant of time.

The motion of the ions are treated classically using molecular dynamics while the electrons are treated quantum-mecanically using, for example the Density Functional Theory (DFT) [48]. This separation between ions and electrons is justified by the fact that the electronic time scale is much shorter than the ionic one due to their mass difference (like the Born-Oppenheimer separation for molecular studies). Within this approximation, the Hamiltonian operator can be separated into electronic and nuclear terms while the cross-terms are neglected.

For the electronic population, the Schrödinger equation reads

$$\left[\frac{-\hbar^2}{2m}\Sigma_i^N \nabla_i^2 + V_{ext}(\mathbf{r}) + V_{e-e}(\mathbf{r})\right]\Phi = E\Phi, \tag{I.16}$$

where the $V_{ext}(\mathbf{r})$ refers to the external potential from the ion lattice and the $V_{e-e}(\mathbf{r})$ to the electron-electron interaction potential. This last term can become quite complex and to solve it, DFT becomes useful.

Within the DFT approach, electrons are treated as a system of independent particles ($V_{e-e}(\mathbf{r}) = 0$) under the influence of an effective potential V_{eff}. In order to find the effective potential, approximations have been proposed (such as local density approximation or the generalized gradient approximation) that involve numerical calculations [48].

The DFT is a model for $T_e = 0$. In our case of interest, which is the one of laser excited materials, $T_e \gg 0$. To describe this situation, an extension to other values of T_e was proposed by Mermin [49]. The used system is a grand canonical ensemble in thermodynamical equilibrium where the occupation states are determined by the Fermi-Dirac distribution $f(\epsilon, \mu, T_e)$.

As mentioned before, when exciting materials with ultrafast lasers, $T_i \neq T_e$ before equilibrium is reached. Within QMD, the classically treated ions are placed in contact with a thermostat at temperature T_i to fix their temperature, which is independent from

the defined T_e.

The iterative strategy of QMD is depicted in Figure I.6. The forces acting on the ions, which have both ionic and electronic contributions, are calculated quantum mechanically. The ion movement is calculated classically. Once the atomic configuration is obtained, it is used to calculate the electronic structure, which in turn will generate new forces acting on the ions. Every time step, the electronic and ionic potentials, the new position of the ions and the new electronic structure are computed until equilibrium is reached. The equilibrium is defined with respect to the pressure. After a certain number of time steps, the pressure will fluctuate around well defined central value.

The fact that QMD calculations can model a system with $T_i \neq T_e$, makes it a very useful tool for the subject of ultrafast laser excited materials. In order to choose the different values of T_i and T_e, the predictions of the TTM presented before can be used. In this fashion, the QMD calculations for precise values of T_i and T_e would correspond to the predictions at different times after excitation. In chapter IV, I will present a comparison between the electronic structure calculated using QMD and our experimental measurements.

After describing the theoretical modelling of ultrafast heating of materials, we will focus in the following on the different experimental techniques.

I.2 Experimental state of the art

Theory and models need constant comparison and input from experiments as there is still controversy on the correct representation of the different thermo-physical properties that mediate the time evolution of the irradiated targets.

This section aims to present the main experimental techniques used in the context of ultrafast laser excitation, the information that they provide and the interpretation through comparison with theoretical models.

The dynamics of materials irradiated by ultrashort laser pulses are usually studied experimentally by using setups in the pump/probe configuration that allow to obtain time-resolved measurements with the required femtosecond-to-picosecond time resolution (see Figure I.1). In all experiments that will be presented, an ultrafast infrared pump pulse excites the target and triggers the ultrafast dynamics inside the material. Then, a probe beam (optical, x-ray or electron pulse) arrives and interrogates the same region of excited material. Figure I.7 presents the different techniques according to the detected signal and Table I.1 presents a comparison of the different methods, which will be detailed in the following.

There are two ways to retrieve the dynamics of the measured observable with sufficiently accurate resolution: (1) using a femtosecond to picosecond-duration probe pulse and changing its arrival time to the sample in a multi-shot experiment or, (2) using a several picosecond probe pulse and a fast detector such as a streak camera, that can extract the time dependence of the measured signal in a single-shot experiment. Along the following subsections either one or the other technique will be mentioned.

Experiment	XAS	ED and XRD	Optical techniques	PES
Quantity measured	photon absorption	diffraction pattern	optical intensity and phase changes	photoelectron spectrum
Information	– T_e – interatomic distance – atomic structure	– lattice structure – atomic plane displacements	– T_e – surface expansion	– T_i – lattice structure – occupied DOS
Characteristics	– bulk diagnostic	– transmission or reflection – XRD: 100's nm depth – ED: few nm depth	– surface sensitive ($\sim$ 0.5 nm)	– surface sensitive ($\sim$ 0.5 nm)
Source	– fs and broadband or adjustable hν – 10's of ps pulse + fast detector	fs to ps pulses with keV to MeV energies	fs to ps optical pulses	fs XUV or x-ray pulses
Sample	nm-thick layers	– 100's nm thick for reflection – 10's nm thick for transmission	– surface with optical quality – no restriction on thickness	no restriction on thickness

Table I.1: Comparative of the different experimental techniques. XAS: x-ray absorption spectroscopy. ED: electron diffraction. XRD: x-ray diffraction. PES: photoelectron spectroscopy.

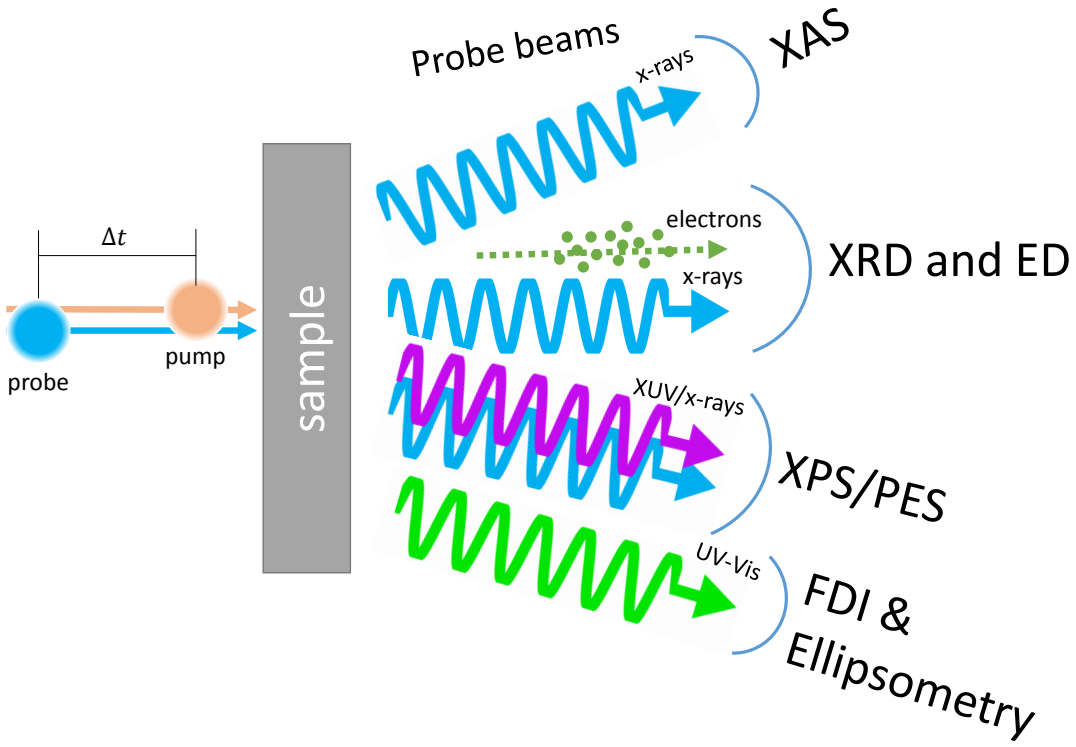

Fig. I.7 *Pump/probe experimental techniques and their different probe beams. Δt corresponds to the delay between pump and probe pulse arrivals. XAS: x-ray absorption spectroscopy, XRD: x-ray diffraction, ED: electron diffraction, XPS: x-ray photoelectron spectroscopy, PES: photoelectron spectroscopy, FDI: frequency-domain interferometry.*

I.2.1 Time-resolved x-ray absorption spectroscopy

The atomic and electronic structure of matter is investigated by means of their absorption spectrum in the x-ray domain. Rich and element-specific information is contained in the different regions of the absorption spectrum as it is explained below.

This technique is based on the photoabsorption process: when a photon with sufficient energy is absorbed, an electron can be excited and promoted to an unoccupied state.

The probability of a transition from an initial state ϕ_{ini} to a final state ϕ_{fin} is given by Fermi's golden rule:

$$w = \frac{2\pi}{\hbar}|\langle\phi_{fin}|\delta H|\phi_{ini}\rangle|^2\rho_f(E_{ini}), \tag{I.17}$$

where δH is the perturbation caused by the photon, and $\rho_f(E_{ini}) = 1 - f(E_{ini}, \mu, T_e)$ (with $f(E_{ini}, \mu, T_e)$ being the Fermi-Dirac distribution) corresponds to the density of unoccupied final electronic states at the initial energy E_{ini} [10]. The wavefunction $|\phi_{fin}\rangle$ corresponds to the superposition of the freed photoelectron and the diffusion (scattering) over neighboring atoms. Thus, the atomic distance and the lattice structure will influence the final states and the absorption spectrum [48].

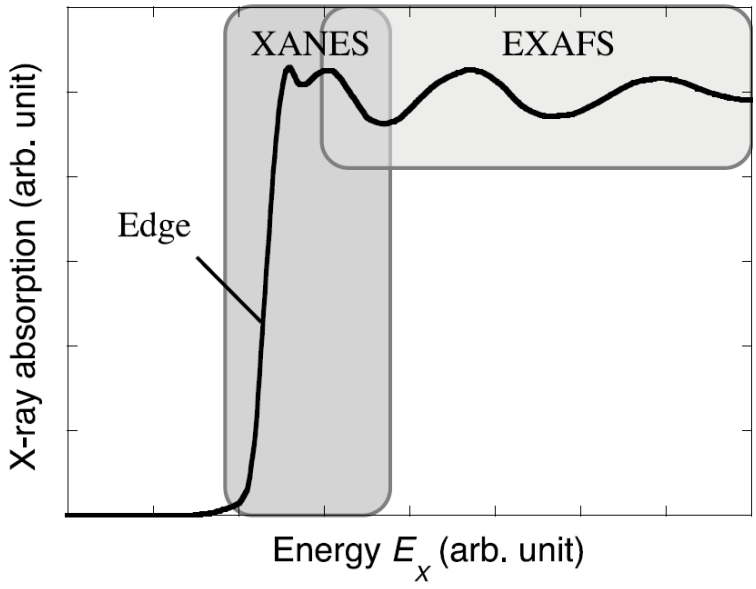

Fig. I.8 *X-ray absorption spectrum with its three main regions: the edge, XANES and EXAFS regions (adapted from [10]).*

The conduction electrons in a material follow the Fermi-Dirac distribution. At 0 K temperature the electrons fill all the states up to the Fermi energy and leave unoccupied states above this level. As the temperature increases, states below the Fermi energy become unoccupied and states above become occupied. For an electron to be freed into the conduction band upon absorption of an upcoming photon it is necessary that the final state is unoccupied. In this sense, x-ray absorption (XAS) probes the density of unoccupied states.

Fig. I.8 presents a typical example of an XAS spectrum showing the three regions of interest near an absorption edge: the rising edge, the x-ray absorption near edge spectrum (XANES) and the extended x-ray absorption fine structure (EXAFS).

The absorption edges in the XAS spectrum arise from the different thresholds corresponding to a transition from a bound state to a free state. The steepness of these edges gives direct information about the electronic temperature T_e of the material.

The second region, XANES [39], evaluates the spectrum with photons close to the absorption edge, generating photoelectrons with low kinetic energy. The photoelectron wave function is modified from scattering with many of the neighbouring ions (multiple diffusion) and finally modifying the absorption spectrum. These multiple diffusions appear as non-periodic modulations with an important amplitude in the spectrum. The analysis of the XANES spectrum is complex and it requires a precise comparison with a calculated XANES spectrum. The spectrum calculations can be performed, for example with quantum molecular dynamics (QMD) [20].

In contrast, the third region, EXAFS, focuses on the study of the absorption spectrum a few tens of eV after the edge, corresponding to photoelectrons with an important kinetic energy that only scatter once over the closest neighboring ions (simple diffusion), giving rise to periodical modulations that are low in amplitude due to inelastic scattering.

The interatomic distance can be obtained by a Fourier analysis of the spectrum even for matter not structured in the long-distance range.

In order to perform XAS measurements, the probe beam needs to be either broadband (several tenths of eV) or adjustable in energy. So, these experiments can be performed at synchrotron facilities or using laser-based sources such as betatron sources, which by the acceleration of electrons in a laser-generated plasma can produce x-rays [50].

In summary, the information obtained from the XAS is the local structure of the material, the interatomic distance and the unnoccupied DOS (from both XANES and EXAFS), and the electronic distribution (from the absorption edge). In the context of ultrafast heating of materials, XAS can give insight into the electron and ion dynamics by following the evolution of the spectrum.

Recently, ultrafast heated Cu foils have been studied by XAS using 70 ps pulses from synchrotron radiation and a streak camera yielding 2 ps time resolution [14]. Another XAS study in Cu foils make use of betatron radiation using 9 fs x-ray pulses and a CCD camera [20]. Both studies show the modification of the x-ray spectrum and obtain direct information about the electron temperature and the unoccupied density of states that corresponds well to the TTM predictions using the electron-phonon coupling G calculated by Lin. et al [9].

I.2.2 Time-resolved optical measurements

The ultrafast laser heating can also modify the optical properties of materials. Therefore, the analysis of an optical probe pulse reflected on the sample can provide interesting direct or indirect information about the electron and ion dynamics.

The principle of these techniques relies on the measurement of the optical modifications of the probe beam, such as phase, amplitude and polarization. Frequency Domain Interferometry (FDI) and time-resolved ellipsometry are examples of these techniques.

FDI uses two optical probe pulses that are reflected upon the surface of the target [51]. The first probe pulse arrives before the pump pulse and the second one after. The probe pulses interfere before being detected, therefore producing an interference pattern for both P and S polarization which can be detected separately.

Time-resolved ellipsometry analyzes changes in the polarization state from the reflected light at different angles.

The goal of these optical techniques is to reconstruct the dielectric function, that depends upon the state of the sample (solid, liquid, plasma), the electronic density n_e and the T_e and T_i [13].

The optical techniques need ultrafast optical pulses to attain the desired temporal resolution. At the same time, the surface quality of the sample must be sufficiently good to allow a proper reflection of the probe beams.

The information obtained with these techniques is mainly related to the electronic population of the sample. The reflectivity of metals depends directly on the conduction band electrons through its complex dielectric constant. Also, with the FDI technique it is possible to obtain, through the measured optical phase changes, direct information about the sample surface, whether if its expanding or losing its sharpness (in the case of an expanding plasma generated at the surface) [12].

Numerical simulations such as a TTM including the hydrodynamic evolution of the target and its optical response, can then be used to obtain the characteristic curves of the measured optical parameters and compare with experimental data. In this way, the structural changes, such as lattice structure, are obtained indirectly.

Recently, the FDI technique has been demonstrated for the ultrafast surface expansion of aluminum targets with nm accuracy while maintaining its sharpness [12].

In the case of ellipsometry, copper targets heated close to the ablation threshold have been studied. The results were able to reproduce the evolution of the complex dielectric function using the TTM coupled with a thermomechanical model. Thus, showing the different stages of heating and cooling of the material [13].

I.2.3 Time-resolved x-ray and electron diffraction

The properties of the material can also be explored by means of measuring the diffraction of the probe beam upon interaction with the sample. The two possibilites for the composition of the probe are either x-rays or electron bunches with sufficient energy, as it is detailed below.

The principle of this techique relies in Bragg diffraction law, that states that atoms in matter can diffract electrons and x-rays producing constructive interference patterns according to the relation

$$2d \sin\theta = n\lambda, \tag{I.18}$$

where d is the interplanar spacing, θ the incidence angle, n an integer number, and λ the x-ray or electron wavelength. By rearranging Bragg equation it is possible to obtain $\Delta d/d = -\Delta\theta/\tan\theta$. Using a small angle approximation one finds that $\Delta d/d = -\Delta\theta/\theta$, connecting the changes in the interatomic planes and the diffraction angles [11].

The techniques using diffraction can work either in reflection or transmission configuration. For example, to perform x-ray diffraction in reflectivity mode, the sample can be thick (hundreds of nm) and the photon energy needs to be on the order of keV. At these energies the x-rays penetrate deep into the sample, thus probing a much thicker region than the skin depth where the pump laser pulse was absorbed. On the contrary, in order to perform transmission electron diffraction, the sample needs to be thin (few tens of nm).

Another requirement for diffraction experiments is an ultrafast x-ray pulse or electron bunch that can be either in the fs or few ps range, depending on the desired resolution. X-rays with these characteristics can be generated for example by laser-plasma interaction systems [11]. Electron bunches can be generated by DC photocatodes yielding keV electrons [11], radio-frequency photocathodes yielding MeV electrons [52], or by laser-plasma acceleration [53].

The information provided by diffraction experiments is related to the lattice order and thus can reaveal changes due to displacements or phase changes such as solid-solid or solid-liquid transitions.

Both x-ray and electron diffraction techniques can be complementary of each other as their penetration length can be different: keV electron beams penetrate in the order of few nm which is comparable to the skin depth of the pump pulse. Thence, they

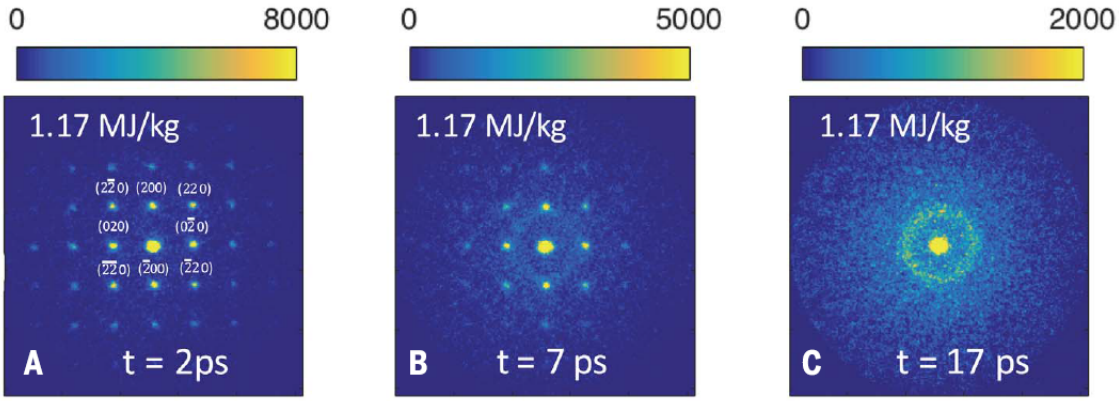

Fig. I.9 *Ultrafast electron diffraction from [42] in gold nanofilms. The diffraction peaks from crystalline structure disappear and rings from liquid state appear at times as fast as 7ps.*

exclusively probe the irradiated region. In contrast, x-rays can penetrate much deeper into the sample (tenths of nm) probing both the irradiated and non-irradiated regions of the sample, thus providing information about the heat distribution in the sample. It is also important to mention that electron pulses can be disturbed by electromagnetic fields that might be present in metallic or semiconducting targets. These perturbations can make the pattern interpretation more difficult. But in the case of studying warm dense matter or plasmas, using charged particles to interrogate the state of the target allows to retrieve the evolution of the plasma electro-magnetic fields, obtaining valuable information on its dynamics [54].

A recent work studies the lattice deformations using both time-resolved x-ray and electron diffraction experiments in the keV energy range. They observe oscillatory displacements of the atomic planes before reaching a stable displacement while excited. The oscillations are observed for 20-40 ps with electron diffraction whereas they last up to 150 ps using x-rays. These differences originate from the different probing depths of both techniques: electrons probe only a few nm into the sample while the probing depth of x-rays extends to tenths of nm. As the probing regions deepens, the x-rays observe the energy transfer to initially cold regions of the sample, which takes longer times [11].

Another study has reported the ultrafast melting in gold foils using electron diffraction at MeV energies [42]. In Fig. I.9 A, it is possible to observe the distinctive diffraction patterns of a crystalline state. They start to disappear as early as 7 ps (Fig. I.9 B), when sufficient energy is transferred into the lattice from the hot electrons and ring diffraction patterns indicating a liquid state appear. These rings become dominant at later times (Fig. I.9 C).

The techniques mentioned provide insight in the ultrafast excitation regime. They measure the material properties either directly (for example the T_e from the XAS absorption edge, or the interatomic distance with x-ray and electron diffraction) or indirectly, through model comparison (for example FDI and ellipsometry relating the dielectric function to the hydrodynamic state). They are all complementary in the sense that they

provide different information about the processes of interest. Among them, we can also count photoelectron spectroscopy (PES), which is the technique used in the present work and is presented next.

I.3 Time-resolved photoelectron spectroscopy

We have selected photoelectron spectroscopy (PES) as our experimental technique. It consists in the detection of photoelectrons using what is called an electron energy analyzer that is capable of detecting electrons as a function of their kinetic energies forming a spectrum. The generated photoelectron spectrum carries important information about the material. As it will be discussed in this section, PES probes the electronic states through the photoelectron spectrum that are sensitive to the conditions of the lattice such as temperature and ordering. In this way, PES retrieves indirect information about the structure of the atomic lattice.

Historically, P. Lenard was the first to correctly describe, in 1902 the light-induced emission of electrons from metals including the so-called work function that couldn't be described by the classical wave theory of light [55]. In 1905, Einstein proposed the quantum perspective of photoemission stating clearly that the photoemitted electrons contain information about the material [56]. In 1914, a team led by Rutherford realized that the kinetic energy of the photoelectron is equal to the difference between the photon energy and the binding energy of the electrons [57].

The utility of x-ray PES (XPS) in chemical analysis was recognized in the 20-30's when line shifts caused by the chemical bonding were observed [58]. In the 50's the first XPS apparatus with high resolution was built allowing to record photoelectron spectra where the definition of the lines was limited by their natural linewidth [59]. This motivated the development of the technique and more robust equipments were built to the point that nowadays XPS is a routine technique in many fields of research such as chemistry, surface analysis and material science.

The PES technique in a time-resolved configuration (Tr-PES) is suitable for studying ultrafast phenomena. Tr-PES has become more common thanks to the development of femtosecond table-top lasers with pulse energies in the mJ range, meeting the conditions needed for the ultraviolet (UV) and extreme-ultraviolet (XUV) light generation [60, 61, 62] (using up-conversion or High-Order Harmonic Generation, for example). This makes the table-top, laser-based Tr-PES setups quite convenient, suitable and more available than Tr-PES experiments at large-scale facilities such as synchrotrons and x-ray free electron lasers (XFELs).

As all other mentioned techniques, Tr-PES setups are also ideal for studying the ultrafast laser-matter interaction because the picosecond and femtosecond required resolution can be achieved. These reasons lead us to choose the Tr-PES technique based on a high-order harmonic generation beamline, as it will be detailed in chapter II.

This technique is versatile as it can also be coupled with different detectors for angle resolved PES [63], spin-resolved PES suitable for magnetic materials [64] and finally, this technique can be used with semiconducting and metallic targets.

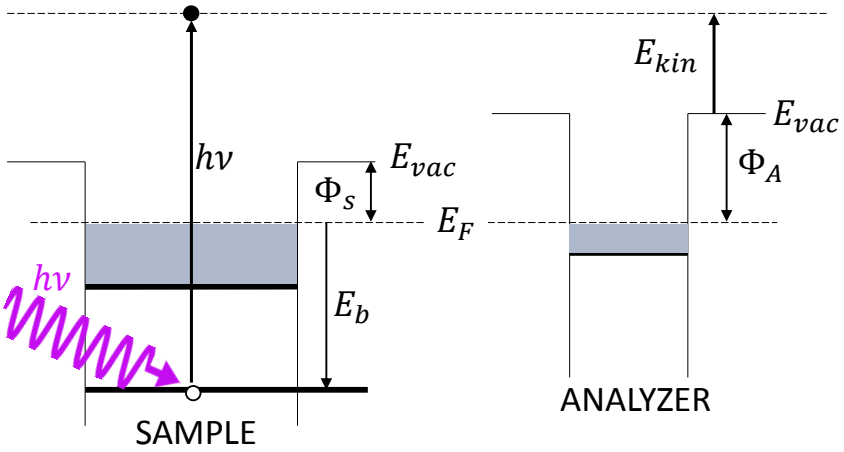

Fig. I.10 *Diagram showing the energy relations in photoemission experiment. Adapted from [57].*

I.3.1 Principle

PES is based on the photoelectric effect, which can be thought as a three step process:

1. When photons with energy equal or greater than the bound energy of an electronic state impinge on a surface, they can interact with the material electrons promoting them to free states. The free electrons are called photoelectrons.

2. These electrons move through the solid being subject to elastic and inelastic scattering processes (the latter contributing to the signal background).

3. If their energy allows them to overcome the work function, they will be freed into vacuum. These photoelectrons can be detected using a dedicated setup.

In the case of an electric contact between the electron energy analyzer (detector) and the sample, their Fermi levels become aligned (E_F), as depicted in Figure I.10. The kinetic energy of a photoelectron is $E_{kin} = h\nu - E_b - \Phi_S$, where E_b is the electron binding energy, and Φ_S is the work function of the sample (difference between the Fermi level E_F and the vacuum level E_{vac}). Thus, the kinetic energy of the phoelectron as detected by the electron analyzer (whose work function is Φ_A) is $E_{kin} = h\nu - E_b - \Phi_S - (\Phi_A - \Phi_S) = h\nu - E_b - \Phi_A$. Finally, the binding energy is

$$E_b = h\nu - E_{kin} - \Phi_A. \tag{I.19}$$

The work function of the target cancels out in equation I.19 and only the constant work function of the analyzer relates the kinetic energy to binding energy. This equation is valid only for conducting targets in electric contact with the detector, allowing for the Fermi level of the detector and target to be aligned.

The PES spectrum is usually recorded by scanning the energy of the emitted electrons, so it is given by intensity (counts per second) as a function of the kinetic (or binding)

energy (in eV). This PES spectrum is structurated and two general components are observed. (1) Different peaks, corresponding to different electronic levels and transitions. And (2), a non-uniform background originated from photoelectrons that have scattered inelastically inside the material, called secondary photoelectrons.

The following section will detail the interpretation of the PES spectrum.

I.3.2 Interpretation

The PES spectrum needs to be carefully analyzed to obtain qualitative and quantitative information about the sample. The peaks in the spectrum can have different origins like core levels, valence band levels, Auger electronic transitions, satellites and energy loss peaks from different mechanisms such as plasmon structures. They can be analyzed regarding their positions and shapes. These specific structures contain rich information about the sample as they can change their characteristics (binding energy, peak width, shape) depending on the bonding or chemical state of the atoms.

The peaks arising from electron transitions from core levels and the valence band present a single structure for levels corresponding to the s total angular momentum level, and doublet structure for the p, d and f levels. The valence band (VB) spectrum is a convoluted picture of the density of occupied states (DOS) depending on the band structure of the solid. The specific information obtained from the VB will be described in the following subsections.

The intensity $I(E_f)$ of the peaks is related to the photoemission probability, that is proportional to Fermi's golden rule (see subsection I.2.1):

$$I(E_f) \propto \frac{2\pi}{\hbar}|\langle\phi_{fin}|\delta H|\phi_{ini}\rangle|^2\rho_f(E_{ini}). \tag{I.20}$$

The initial states ϕ_{ini} correspond to the occupied density of states, whereas the ϕ_{fin} correspond to the unoccupied density of states. In this sense, the photoelectron spectrum is the measurement of the projection of the initial states over the final states. In order to have a spectrum reflecting only the structures of the occupied DOS, it is necessary that the final states ϕ_{fin} are structureless. This can be ensured by selecting a photon energy where the final states become available from all initial states. In the case of the VB in metals such as Cu (our material of interest), this can be ensured with photon energies of $h\nu \geq 50$ eV [65, 66].

The background present in the photoelectron spectrum is smooth. It is originated from electrons originally coming from a fundamental peak or band structure that are scattered inelastically. The PES background intensity increases towards the low kinetic energy side of the spectrum. The PES spectrum interpretation relies on a precise subtraction of this background, for which some methods and implemented algorithms have been proposed [67, 68, 69].

The following sections will present important details about the PES technique that need to be taken into account for allowing to perform succesful experiments.

I.3.3 Characteristics

a) Probing depth

The probing depth is an important parameter to consider when performing pump/probe experiments. Ideally, in the case of PES, the probe pulse will only interrogate regions of the sample that are subject to excitation by the pump pulse. Failing to do this can result in the retrieving of a spectrum that is a sum of spectra originated from both excited and not excited sample regions.

The PES probing depth can be related to two concepts. (1) The attenuation length (L_{att}) of the x-rays inside the material, defined as the length for the x-ray intensity to decay in a factor of 1/e. (2) The inelastic mean free path (L_{IMFP}) defined as the distance travelled by an electron between successive inelastic collisions. The electrons having undergone one or more inelastic collisions form the PES background.

As seen in Fig. I.11, for energies ranging the 100-1000 eV, the attenuation length of the x-rays for Cu is between 20 nm and 500 nm, whereas the L_{IMFP} for electrons in the same energy range is 0.5 nm and 1.6 nm. This means that the probing depth depends only on the electron escape distance and that the PES measurements are extremely surface sensitive for this energy range: they interrogate the very first atomic layers of the targets.

The data for x-ray attenuation length was calculated by Henke et al. [70] and is available through the Lawrence Berkeley National Laboratory's website CXRO [71]. The data for inelastic mean free path is obtained from [72] and available through the National Institute of Standards and Technology IMFP database [73].

b) Photoionization cross section

In the context of PES, the photoionization cross section (σ_{ph}) refers to the probability of an electron being emitted from its bound state. This quantity is material, electronic level and energy dependent. Figure I.12 presents the cross sections for Au 5d and Cu 3d levels, corresponding to the valence band. The values for all elements and their principal electronic levels and photon energies have been calculated in the dipole approximation [74] and are available online through the Elettra VUO website [75].

The knowledge of this quantity is of great importance for many spectroscopic experiments on gases, solids and liquids. In our specific case, this quantity is a parameter that allows to compare the expected signal level in our measurements and an important factor for designing the experimental tool (by selecting a photon energy $h\nu$ for example) and choosing the targets to be measured. Also, sometimes a compromise between σ_{ph} and the L_{IMFP} needs to be found depending on the experimental needs such as probing depth and signal-to-noise ratio.

I.3.4 Photoelectron spectroscopy in the context of lattice heating

a) State of the art

Both core-level and valence band PES spectra are sources of valuable information regarding the material chemical composition, oxidation state and even crystalline structure. The study of core-level peaks in steady-state PES for quantitative analysis is very well

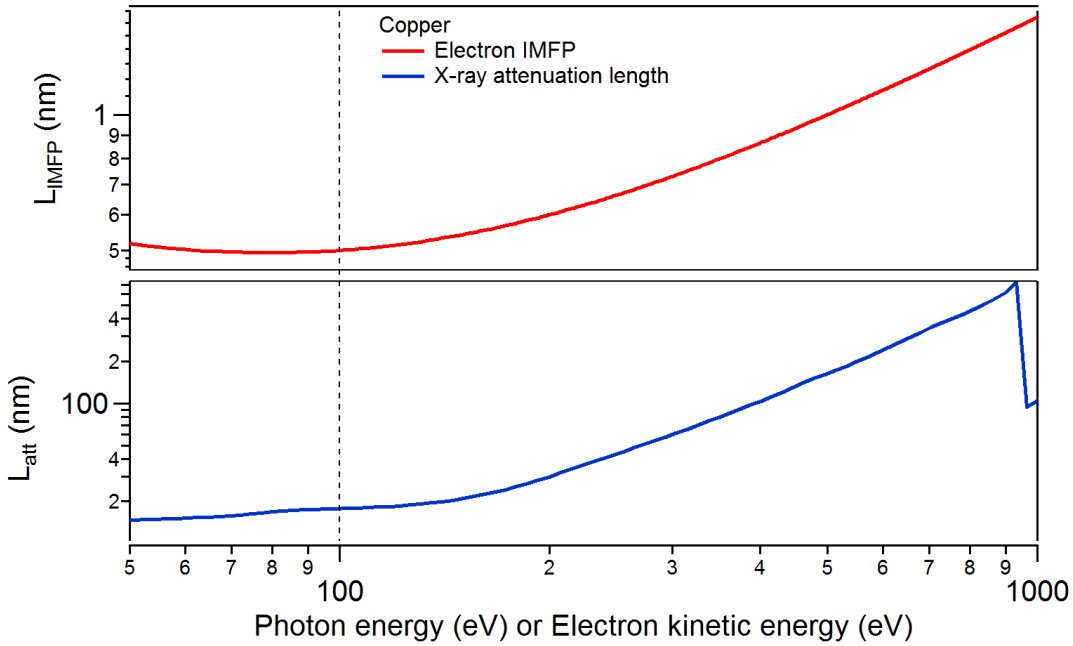

Fig. I.11 *Top: Inelastic mean free path(L_{IMFP}) of electrons in Cu obtained from [73]. Bottom: attenuation length (L_{att}) of photons in Cu [71]. The dashed vertical line is a guide to the eye for photon/electron energy at 100 eV where L_{IMFP} = 0.5 nm and L_{att} =17 nm.*

established and developed [57], whereas the valence band (VB) spectrum is much more complex and is still not routinely used as a standard practice.

Core-level and VB-level can both be studied by Tr-PES in order to obtain insight about the evolution of T_e and T_i. Core-level peaks can broaden upon heating of the lattice, giving an indirect measurement of the T_i [63]. On the other hand, the Fermi edge can be fitted to an exponential function distribution to deduce the T_e [76]. The works from Refs. [63, 76] performed these type of measurements on superconducting and topological insulators optically pumped at very low fluences (1-10 J/m^2). In order to perform these kind of measurements a very fine spectral resolution is needed ($<$ 200 meV) which is not the case of our experimental setup due to the spectral width of our photon source ($\sim$ 1 eV). And, as it will be discussed later, performing Tr-PES with high pump energies (enough to induce a phase transition in metals, as in our case), imposes some constraints that entail a loss of resolution due to multiphoton emission of electrons that disturb the photoelectron spectrum [77].

In our case of interest, which is the ultrafast heating of metals, we will focus on the study of the VB changes. It is expected that after heating of the sample, the VB changes can be unveiled using the Tr-PES technique. This is the goal of this work.

The study of the VB spectrum evolution upon heating of the sample is justified if it is sensitive to the temperature and structural changes. We justify this approach based on different published works that measure statically the VB at different temperatures, assess the modification of the DOS performing theoretical calculations and study the VB in a

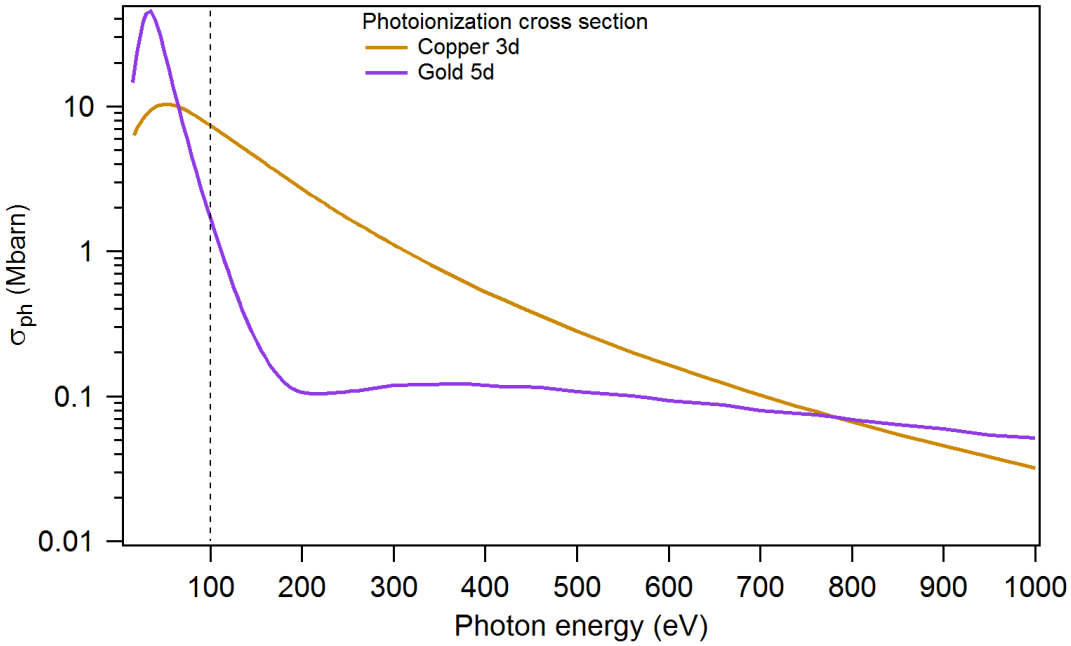

Fig. I.12 *Photoionization cross sections for Cu 3d and Au 5d levels (corresponding to the VB) at different photon energies. The vertical dashed line is a guide for 100 eV where the cross section values are 7.4 Mbarn and 1.7 Mbarn for Cu and Au respectively.*

time resolved manner.

XPS steady state measurements show that the crystalline state and the liquid state yield different VB spectra. Fig. I.13 shows the example of measurements performed in Cu and Ni in solid state at room temperature, and in liquid state, at 100 K above their melting temperatures using an Al Kα 1486.6 eV x-ray source [78]. It is seen that, in both cases, specific spectral features are formed in the DOS structure when going from solid to liquid state. The Cu sample is especially modified at $E_{bin} \sim 4.5$ eV.

Theoretical studies have also validated the modification of the T_i-dependent DOS. In Fig. I.14 a) the case of Au at different temperatures show a smoothing of the structured DOS when increasing the temperature, calculated with the tight-binding method (TBMD) [79] whereas Fig. I.14 b) presents the solid and liquid DOS of Cu calculated with density functional theory (DFT) [14]. The lowering of the shoulder around $E\text{-}E_f = -5$ eV (when going from solid to liquid) in the Cu calculated DOS seems to correspond to the $E_{bin} \sim 4.5$ eV in Fig. I.13 presented in [78].

The contribution of the T_e to the DOS modification has been assessed theoretically and only plays an important role for an elevated range of temperatures that are unlikely to be reached in the present work. Figure I.15 show the dependence of the DOS at three different T_e while keeping the $T_i = 0$ K [38]. Even at $T_e = 10000$ K the difference in Cu is a 0.3 eV shift and for Au it is even smaller. On the contrary, at T_e=50000 K it is

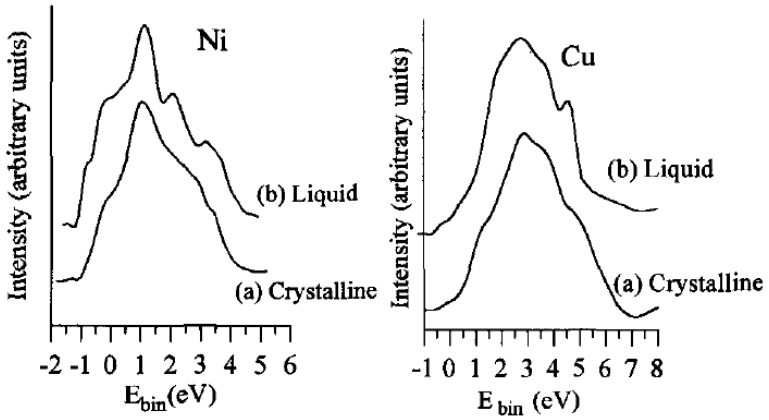

Fig. I.13 *VB spectra of Ni and Cu at solid state (room temperature) and liquid state (1850 K and 1700 K, respectively) using ħν=1486 eV (from [78]).*

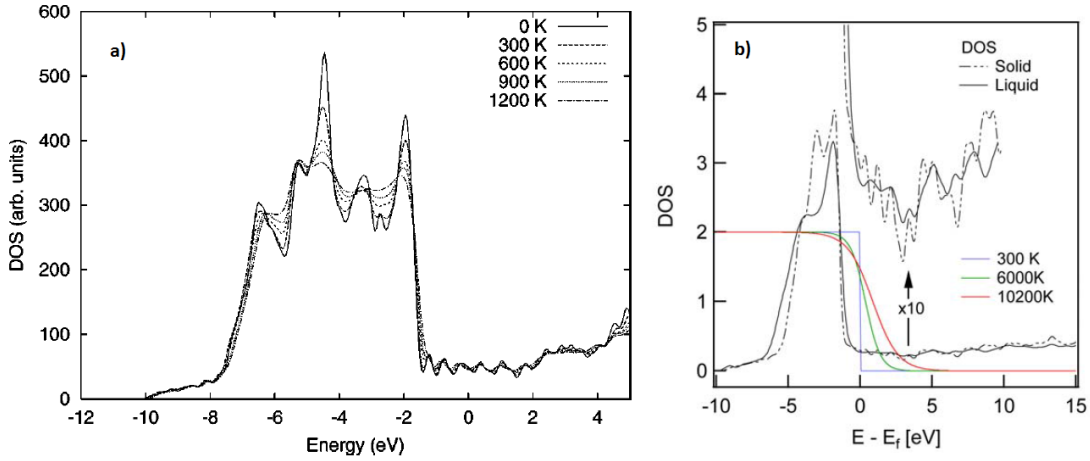

Fig. I.14 *DOS calculations of a) Au at different lattice temperatures using the TBMD [79] and b) Cu in solid and liquid states, also showing the Fermi distribution at different T_e using DFT [14].*

possible to observe a shrinking and displacement of the DOS, but as already mentioned, this temperature will not be reached for the range of studied laser energies.

Time-resolved measurements of the VB spectrum in the microsecond regime of Pd targets undergoing solid-liquid phase transitions were reported in [80]. These experiments kept the targets at a stable temperature of T = 780 K before triggering the phase transition with a 2.1 μs pulse at 595 nm. Fig. I.16 presents the PES spectra recorded at different time windows Wi using a photon energy hν = 21.2 eV.

The measurements at different time windows show notorious differences in the VB through the process of laser induced phase transition with a maximum difference when the liquid state is attained (W3). Evidently in these experiments, given the time duration of

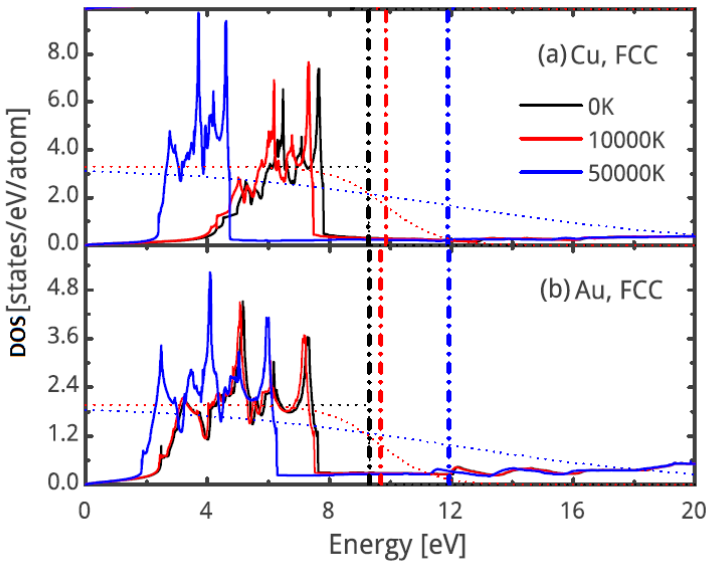

Fig. I.15 *Calculated DOS at different T_e temperatures while keeping T_i=0 K (solid lines). Fermi-Dirac distributions (dotted lines) and electronic chemical potential (dashed vertical lines) for a)Cu and b)Au from [38].*

the laser pulses, the heating and phase transition happen in thermal equilibrium between the electronic and ionic population.

In the picosecond regime, the first Tr-PES experiment used to study the ultrafast heating of metals, was attempted in 2005. Time-resolved VB photoelectron measurements of an ultrafast heated Cu 50 nm-thick foils were reported by Nelson et al. [81]. They used a single-shot time-of-flight spectrometer to record the spectrum at a pump/probe delay of $\sim$ 5 ps. Modifications of the spectrum were reported using fluences on the order of $\sim$7200 J/m^2.

All these experiments (steady-state and time-resolved) set the precedent for photoelectron studies in the ultrafast regime with electron-ion temperature out-of-equilibrium conditions.

Based on what has been learned through the previous studies presented in this chapter, including their limitations, we have built a dedicated experimental setup consisting of an ultrafast XUV beamline and we have adressed the specific challenges.

b) Experimental scheme

The experimental setup used for measuring the PES spectrum at different times after ultrafast laser excitation is presented in Fig. I.17. It has been designed in a pump/probe configuration, as mentioned earlier, where a femtosecond laser pulse triggers the lattice dynamics and a probe interrogates the target at different times after the initial excitation. In chapter II I will do a detailed presentation of our experimental development.

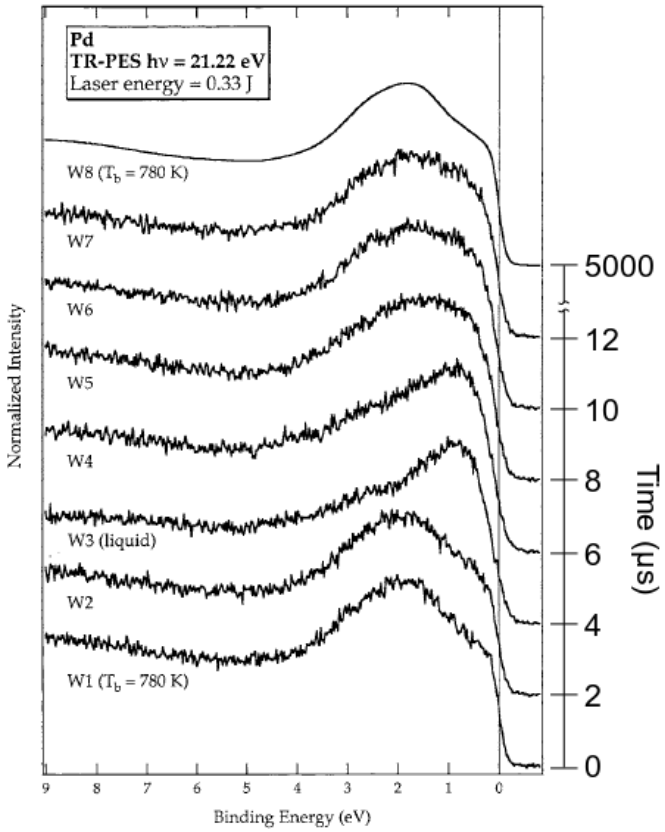

Fig. I.16 *Tr-PES measurements on a Pd thick sample at different time windows after excitation. The starting time for each window is shown on the right: W1-W7 cover 14 μs and correspond to the integrated signal over 2 μs each. W8 is set to start 5 ms after the laser pulse and correspond to the integrated signal over 2 ms. [80].*

An infrared femtosecond laser pulse is generated by the main laser source (arriving from the left in Fig. I.17) and is divided in two branches to form the pump and the probe arms of the experiment. The pump beam is steered through an extendable delay line to control the time of arrival of the laser pulse relative to the probe pulse. Finally, the pump pulse is directed to a lens in order to be focused on the target surface.

The probe beam is generated by focusing the IR beam onto a gas cell in order to generate High Order Harmonics (HHG) of the fundamental laser beam [82, 83]. These harmonics can reach energies up to 100 eV and have enough energy to extract the valence band electrons from the target surface. A filter removes the remaining infrared light and a reflective monochromator selects the energy that will be used to probe the target. Finally, the probe beam is focused onto the target surface on the same area that has been irradiated by the pump beam. An electron energy analyzer is used to record the photoelectrons forming a spectrum.

Finally with this setup, the evolution of the VB spectrum can be recorded with femtosecond resolution. But these kind of setups present important challenges that need to

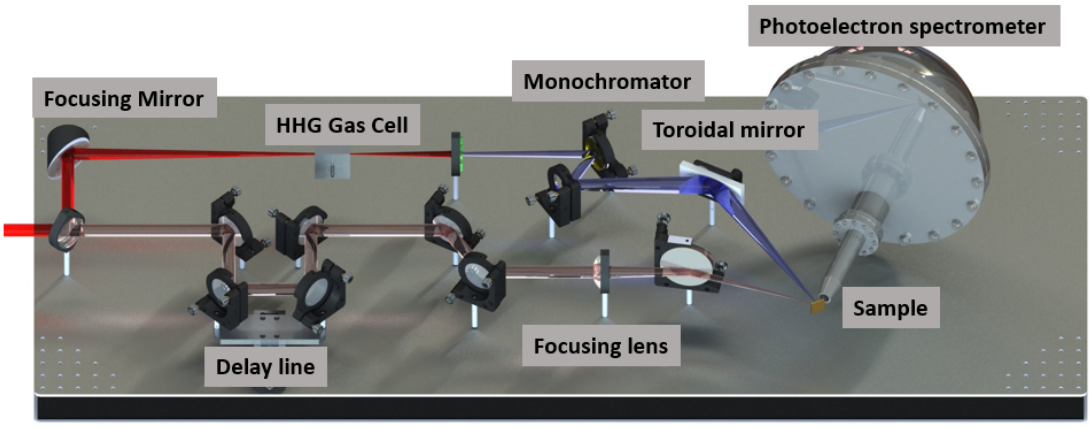

Fig. I.17 *Schematic depiction of the Tr-PES experiment (described in the text).*

be adressed. Next section will introduce them.

c) Challenges

The Tr-PES experiment has some delicate aspects that need to be addressed in order to have a good performance and a sufficient signal-to-noise ratio. As mentioned before, when a sample is excited with a sufficiently intense pump laser pulse, non-linear effects such as multiphoton ionization can take place. The multiphoton photoemission from the pump generates an important background of photoelectrons [84, 85]. This "pump photoelectron background" poses a double challenge. First, it can superimpose on the photoelectron spectrum generated by the probe beam. Secondly, if the pump electrons are sufficiently numerous, they can generate an electric field capable of disturbing the probe photoelectron spectrum yielding a loss of information [86, 87]. This phenomenon is called "space-charge effect".

The first challenge, which is the superposition of the pump photoelectron background with the probe photoelectron spectrum can be adressed by spectrally shifting the latter to higher kinetic energies. For this purpose, we have built an XUV beamline based on HHG capable of delivering photons with energies up to 100 eV. This energy is sufficient to generate the probe photoelectron spectrum away from the low energy pump photoelectron background. The development and the measured performances of our beamline will be presented in chapter II.

The second challenge is related to the space-charge effect. It constrains the pump pulse duration and excitation fluence that can be used. It has a direct impact on the availability of the excitation regimes and even on the temporal and spectral resolution of the experiment. Given the importance of the space-charge effect, we decided to study it in depth with aims to understand it, control it and, if possible, to supress it from our measurements. Chapter III in this thesis will present our findings.

After addressing those two challenges, we were able to perform pump/probe Tr-PES experiments on a Cu sample were the space-charge effect was controlled. The measured changes in the photoelectron spectrum were directly attributed to laser-induced excitation

of the sample. These results will be presented in chapter IV.

.

Chapter II

Experimental method

This chapter presents the experimental scheme and implementation that was designed and built to study lattice structural modifications of metals induced by femtosecond laser pulses. The first part will concern the main laser source facility. Following, I will present the XUV beamline that was developed to form the probe arm of the time-resolved photoelectron spectroscopy (Tr-PES) experiment and its measured performance. Then, the pump fluence control and pump/probe beams spatial overlapping and synchronization will be discussed. Finally, the interaction chamber will be presented along with the technical requirements for photoelectron spectroscopy, and the sample preparation and characterization protocols that were followed during the experiments.

II.1 Infrared femtosecond laser source: the Aurore facility

The experimental study presented in this manuscript uses a laser source with very specific characteristics as high pulse energy ($\sim$ 15 mJ), high repetition rate (1 kHz), ultrashort pulse duration (25 fs), high energy stability, a sufficient temporal contrast (10^7). The laser Aurore facility, at the Centre Lasers Intenses et Applications (CELIA) laboratory (Bordeaux, France) that provides laser pulses with such characteristics, was used as light source for the Tr-PES experimental setup.

The Aurore laser (see Fig II.1) is composed by an oscillator and two amplification stages (Regen and Multipass Amplifier) based on the Chirped Pulse Amplification (CPA)

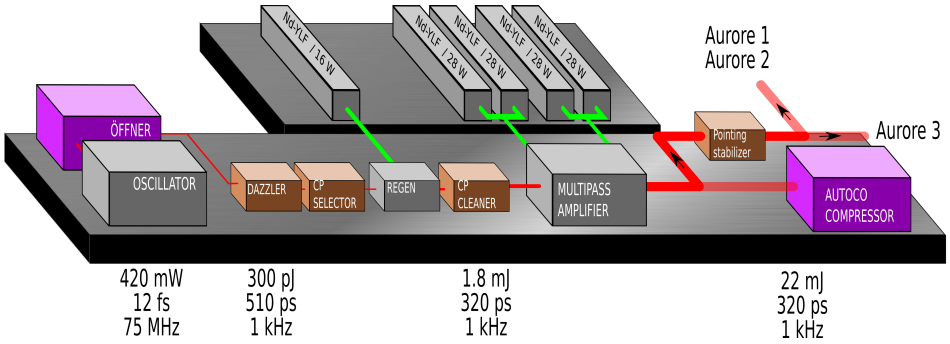

Fig. II.1 *Main components of the Aurore laser system.*

technique [1]. First, the modelocked oscillator (model Fusion Pro, fabricated by Femtolasers GmbH) generates 420 mW, 12 fs laser pulses at a repetition rate of 75 MHz with a central wavelength of $\lambda = 800$ nm. The pulses are then stretched with an Offner-type stretcher to 510 ps, and shaped and phase-corrected with an acousto-optic filter (Dazzler, fabricated by Fastlite). Next, a Pockels-cell pulse picker (Cp selector) reduces the repetition rate to 1 kHz before the pulses are sent to the first amplification stage consisting in regenerative amplifier (Regen) pumped by a Nd:YLF laser increasing the pulse energy to 1.8 mJ/pulse.

A Pockels-cell pulse cleaner (Cp cleaner) removes spurious reflections and the beam is sent to the second amplification stage: a multi-pass amplifier (Multipass amplifier) consisting of a Ti:Sapphire crystal kept at -170 °C with a helium cryostat and pumped with four Nd:YLF lasers (1 kHz, 28 W, 532 nm, model Jade2, fabricated by Thales). The laser output energy is 22 mJ with a flat-top shaped spectrum of 52 nm full width at half maximum (FWHM) centered at 800 nm, 320 ps long. A mirror leak is temporally compressed and monitored to fine tune the Dazzler and obtain a Fourier-limited pulse shape.

The final uncompressed output of the Aurore laser is distributed between six beamlines dedicated to different experiments and research fields, including where the Tr-PES experiment is performed, called Aurore 3 [88]. When arriving, the beam has already travelled ∼10 m, so the pointing stability is handled actively.

The Aurore 3 experimental room has two pulse compressors for the experiment, allowing to control the pulse duration independently for both pump and probe arms of the setup. The minimum duration of the laser pulses after compression is 25 fs. Moreover, each arm of the setup is also independent in terms of energy control thanks to two separate half-wave plate/polarizing beamsplitting cube systems. Section II.2 is dedicated to the probe beam whereas section II.3 is dedicated to the pump one.

II.2 XUV source: a 100 eV beamline based on high order harmonic generation

The probe arm is constituted by a beamline based on High Order Harmonic Generation (HHG) in Ne gas. First, a brief description of the theoretical fundamentals of HHG will be presented. Then, the main components of the XUV beamline will be described along with its characterization and performance.

II.2.1 Theoretical principles of high order harmonic generation

a) Microscopic aspects of the HHG

From a microscopic point of view and considering a single atom, the HHG process can be understood by a three-step quantum-classical model originally proposed by Corkum [89] and Krause et al. [90].

Considering the core electron of an atom under the potential of the nucleus $V_0 = -1/r$, when an electric field (E) polarized along the x axis is applied, the potential becomes $V(x) = V_0(x) - Ex$ and the potential barrier can be lowered on one side of the potential

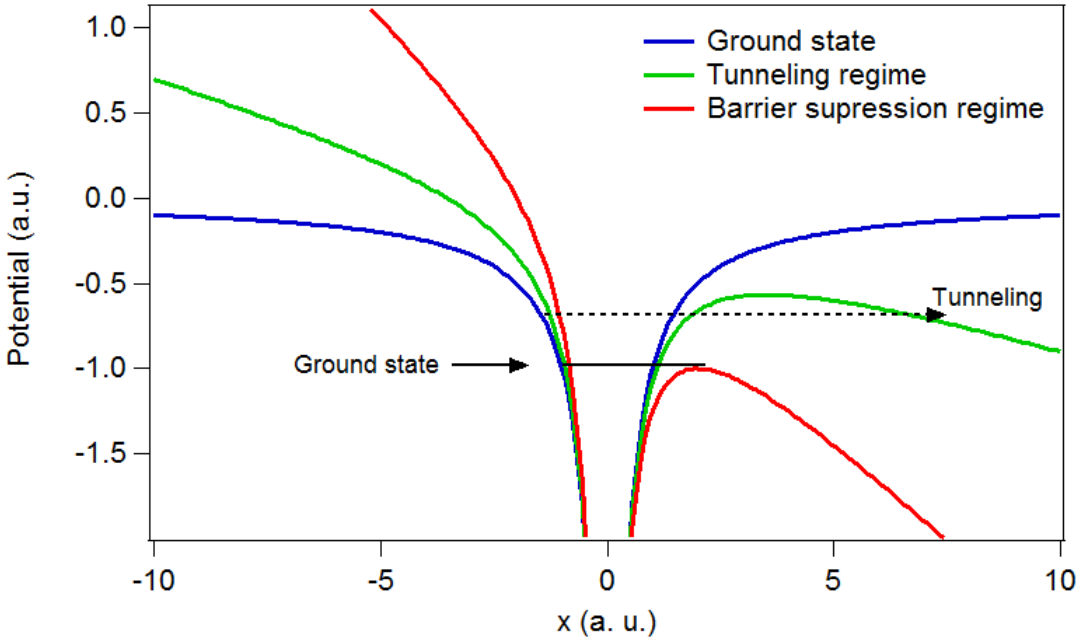

Fig. II.2 *Atomic potential under the influence of a linearly polarized electric field.*

well (see Fig. II.2). Depending on the intensity of the laser field (and keeping the wavelength constant), three regimes can be distinguished:

- Multiphoton ionization (blue): when the laser intensity is moderate, it is only possible for an electron to be freed if enough photons are absorbed, overcoming the binding energy to the nucleus.
- Tunnel effect ionization (green): if the laser intensity (I) is strong enough, the potential barrier can be lowered enough for an electron to tunnel through. This is the ideal regime for HHG. In the case of Ne this happens with I $\sim 1.8 \times 10^{14}$ W/cm^2.
- Barrier suppression regime (red): a sufficiently intense laser field can completely suppress the nucleus coulomb potential and the ionization probability becomes 1. This regime is not propitious of an optimized HHG process, as neutral atoms are needed. In Ne it happens when $I > 8.20 \times 10^{14}$ W/cm^2

The intensity required to suppress the energy barrier (I_{BSI}) can be calculated [91] from the following expression:

$$I_{BSI}(W/cm^2) = 4 \times 10^9 I_p^4(eV), \tag{II.1}$$

where I_p is the ionization potential, which in the case of Neon is $I_p = 21.56$ eV, leading to a $I_{BSI} = 8.20 \times 10^{14}$ W/cm^2.
By keeping the laser intensity below this value, the lowering of the potential barrier occurs

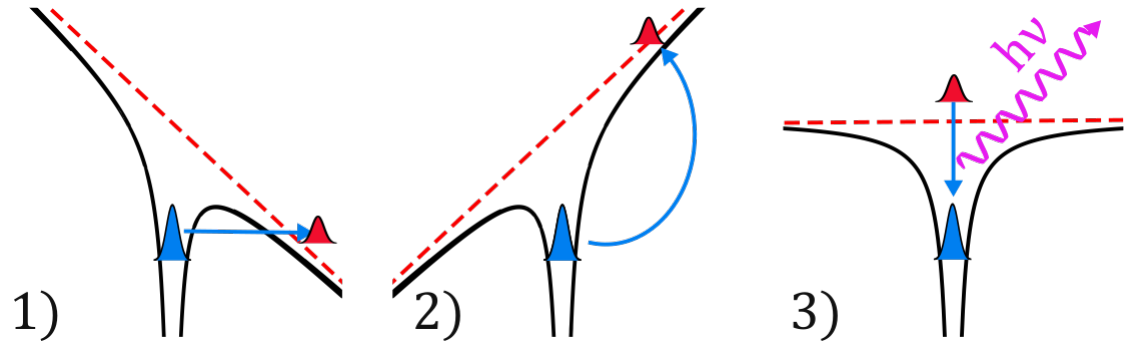

Fig. II.3 *Three-step model: 1) Tunneling over the lowered atomic potential. 2) Acceleration under the laser electric field. 3) Recombination and photon emission, (adapted from [93]).*

twice per optical cycle, as the laser field has two extrema because of its sinusoidal form: $E(t) = E_0 \cos(\omega_0 t)$. Therefore, the tunneling happens at this same rate.

In addition, tunneling ionization can occur if the electron has enough time to go through the lowered potential barrier. The Keldish adiabatic parameter (γ) compares the electron escape time (τ_t) to the laser optical period (T_0):

$$\frac{\tau_t}{T_0} \propto \sqrt{I_p/2U_p} = \gamma, \tag{II.2}$$

where U_p is the ponderomotive potential of the laser field [92]:

$$\begin{aligned} U_p(eV) &= \frac{e^2 I}{2m_e \epsilon_0 \omega^2} \\ &= 9.33 \times 10^{-5} I(10^{15} W/cm^2) \times \lambda^2(nm^2), \end{aligned} \tag{II.3}$$

e and m_e are the electron charge and mass respectively, ϵ_0 the vacuum permittivity, and ω and λ the laser frequency and wavelength, respectively.

According to these expressions, the Keldish parameter depends on the nature of the gas atoms and on the laser characteristics. When $\gamma \gg 1$, the ionization regime is multi-photonic; $\gamma \ll 1$ corresponds to the barrier suppression regime. Finally, $\gamma \simeq 1$ corresponds to the ionization regime, propitious for HHG generation. For a value of $\gamma = 1$ in Ne, the laser intensity is I = $1.8{\times}10^{14}$ W/cm^2.

The three step-model is presented in the Figure II.3. First, tunnel ionization happens when the potential barrier is sufficiently lowered. Then, the freed electron is accelerated by the electric field. As the laser field changes sign, there is the probability that the electron describes a trajectory where it comes back to its original position, and thus, recombining with its parent atom and emitting a photon.

The energy of the emitted photon, $h\nu$, corresponds to the ionization potential energy, I_p, plus the kinetic energy, E_c, gained during the trajectory under the laser field influence: $h\nu = I_p + E_C$. It can reach the XUV domaine as described below.

A purely classical treatment can be followed to gain insight in some important aspects of the HHG process.

The force experienced by the freed electron is due to the laser electric field:

$$F(t) = eE(t) = eE_0 \cos(\omega t) \tag{II.4}$$

Assuming that the electron is freed at the origin (neglecting the barrier thickness) and that the kinetic energy after tunneling is zero, $x(t_i) = 0$ and $\dot{x}(t_i) = 0$, the velocity and position are described by the following equations:

$$\dot{x} = -\frac{eE_0}{m_e\omega}[\sin(\omega t) - \sin(\omega t_i)] \tag{II.5}$$

$$x = -\frac{eE_0}{m_e\omega^2}[\cos(\omega t_i) - \cos(\omega t) + (\omega t_i - \omega t)sin(\omega t_i)] \tag{II.6}$$

It is therefore possible to calculate for which ionization times (t_i) the recombination can occur: twice for each laser oscillation. Moreover, it is possible to show that the emitted harmonics alternate phase each half cycle and then, solutions for the harmonic field are only non-zero for odd multiples of ω. This is why, as seen in Fig. II.4, the emitted harmonic spectrum only contains odd-order harmonics of the fundamental laser frequency [94].

It is also possible to compute the kinetic energy that an electron can obtain from the laser electric field:

$$E_C = \frac{1}{2}m_e\dot{x}^2 = \frac{e^2E_0^2}{2m_e\omega^2}[\sin(\omega t) - \sin(\omega t_i)]^2 \tag{II.7}$$

$$= 2U_p[\sin(\omega t) - \sin(\omega t_i)]^2 \tag{II.8}$$

For certain values of t_i the electron reaches its maximum kinetic energy given by $E_C = 3.17U_p$, leading to a HHG spectrum characterized by a cutoff energy of $h\nu_{cutoff} = I_p + 3.17U_p$ (see Fig. II.4).

According to the above considerations, to obtain a 100 eV HHG XUV source, Neon gas can be chosen as generating medium because of the possibility of reaching this cutoff energy. Indeed to reach this energy, the ponderomotive potential needs to be $U_p \sim$ (100.75 eV - I_p)/3.17 = 24.98 eV. It corresponds to a required laser intensity of $I = 4.18 \times 10^{14}$ W/cm^2 (compare to $I_{BSI} = 8.20 \times 10^{14}$ W/cm^2).

The presented model is a purely classical treatment of the electron excursion under the influence of the laser electric field. In its simplicity it allows to understand the emission times, the origin of the only odd components of the harmonic emission and predicts accurately the cutoff energies. In order to calculate other characteristics of the harmonic field such as phase and polarization, a more complex approach is needed: the quantum model developed by Lewenstein [95] – which also validates the assumptions made in the classical model. For the present case, the purpose of explaining the main features of the HHG process is fulfilled with the classical model and therefore, Lewenstein's model will not be presented.

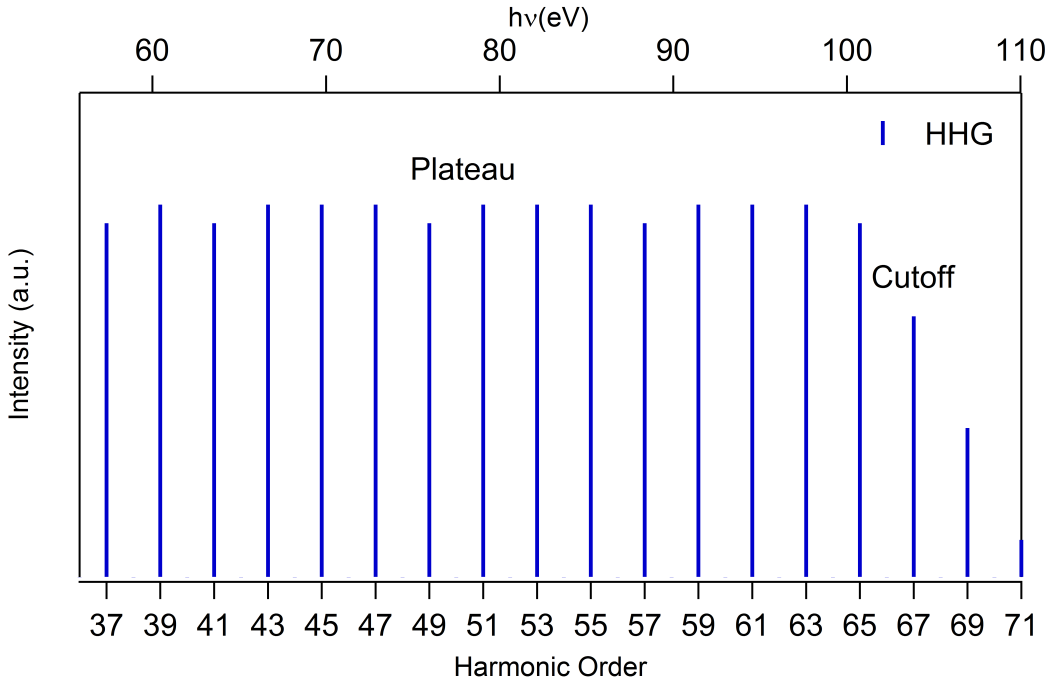

Fig. II.4 *Schematic of the HHG spectrum produced in Ne showing a generation plateau and an abrupt cutoff.*

b) Macroscopic aspects of the HHG

The HHG radiation is the coherent superposition of emission from multiple atoms present in the gas generation cell. One can define the coherence length (l_{coh}) as the distance between two atoms emitting with opposite phase l_{coh}. In order to maximize the XUV generation efficiency, i.e. to avoid the destructive interference of emitted radiation, it is necessary that the medium length l_{med} is smaller than l_{coh}. The coherence length depends on the gas pressure, the focusing conditions and the laser intensity [92].

In addition, if the generating medium is too dense, the XUV absorption can also play an important role and must be taken into consideration to maximize the output beamline brilliance. The absorption length, l_{abs}, is defined as the distance needed for the signal intensity to decay by a factor of $1/e$: $l_{abs} = -l_{med} \log T$, where T is the transmission of the medium (depending on the number of atoms). For example, in Ne $l_{abs} = 1$ mm, (for a pressure of 100 mbar). Thus, in order to optimize the HHG output a compromise between the number of emitting atoms must be found: enough to produce a sufficiently high number of harmonic photons but not so many that XUV absorption becomes an important source of loss.

In practice, the output XUV photon flux is optimized with respect to the number of atoms (depending on the pressure, and l_{med}) and the focusing conditions (meaning that l_{coh} and l_{abs} are also varied). The practical procedure for optimization will be described in section II.2.2 a).

II.2.2 XUV beamline design and characterization

Our XUV beamline, depicted in Fig. II.5, needs ∼6 mJ laser pulses in order to operate. The pulses are delivered by the Aurore laser facility into the experimental setup. They arrive with p-polarization. The beam is divided by a beam splitter (BS). The probe beam goes through an energy regulator (HWP and PC) and directed towards a grating compressor (C1, working in p-polarization). A half-wave plate (HWP) rotates the polarization to s needed for the operation of the beamline (detailed in section b)). Then, the beam is steered inside the XUV vacuum line through a dispersion-less window. The HHG beamline can be divided into three main parts : (1) generation, (2) selection and focusing and (3) characterization. Each of these stages will be presented followed by the beamline performance.

In Figure II.6, a photo of the installation is presented highlighting the already mentioned beamline stages.

a) HH generation stage

The laser beamsize is regulated with a diaphragm (D1 in Fig.II.5) right after compression, and then steered into the vacuum setup. It arrives in the HH Generation stage where it is directed towards a spherical mirror (SM) of 1 m focal length that focuses the beam in the gas cell (GC). This focal length ensures a mild focusing (compared to shorter focal distances) and a larger Rayleigh waist, reducing the phase mismatch from propagation.

The gas cell was designed at the INSP and built to be installed in the beamline. As shown in Fig. II.7 , the specificity of this gas cell is that the gas chamber length can be varied while under vacuum from 1 mm to 20 mm in order to optimize the signal output. Moreover, the gas pressure can be precisely controlled with a manometer and is remotely stabilized. In other words, the number of gas atoms of the generating medium are precisely optimized. The gas cell is completely adjustable under vacuum with respect to the laser axis since it is mounted on:

- a (x, y) micrometric manual stages
- a z pico-motorized stage
- a rotation and tilt angle stages with micrometric screws

The two walls of the cell aligned with the laser axis, were disposable and made of a 200 μm thick brass layer. They were pierced before being installed on the gas cell.

The optimal gas cell operation pressure was found to be ∼200 mbar. To evacuate the gas from the gas vacuum cell chamber (GC on Fig. II.5) a multi-process dry pump (Actatel ADP 602 LM) with pumping speed of 9300 l/min is used. The typical chamber pressure on which the gas cell is enclosed is 10^{-2} mbar. The exit of the chamber is done through a 5 mm hole which is connected to a differential pumping stage (DP on Fig. II.5) pumped by a turbo-molecular pump (250 l/min) to further decrease the pressure, reaching 10^{-5} mbar. In this way, the pressure can be further reduced down the beamline allowing to reach the necessary UHV conditions in the interaction chamber ($\sim 10^{-9}$ mbar).

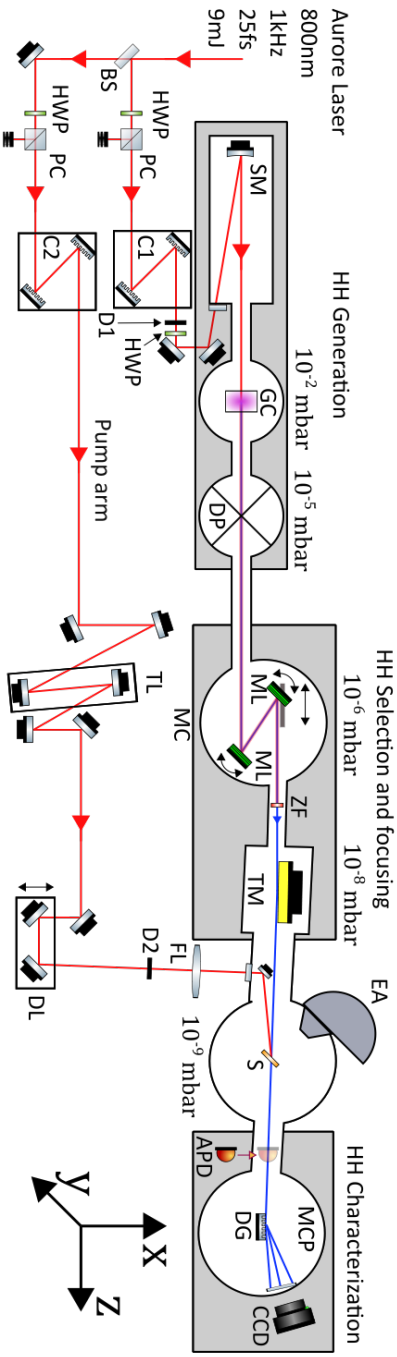

Fig. II.5 *Tr-PES beamline setup. BS: beamsplitter, HWP: half-wave plate, PC: polarizing cube, C1(2): probe (pump) compressor, D1(2): diaphragms, SM: spherical mirror, TL: telescope system, DL: delay line, FL: focusing lens, GC: gas cell, DP: differential pumping, ZF: Zirconium filter, ML: multilayer mirrors, MC: monochromator, TM: Toroidal mirror, EA: electron energy analyzer, S: sample, APD: avalanche photodiode, DG: diffraction grating, MCP: microchannel plate, CCD camera.*

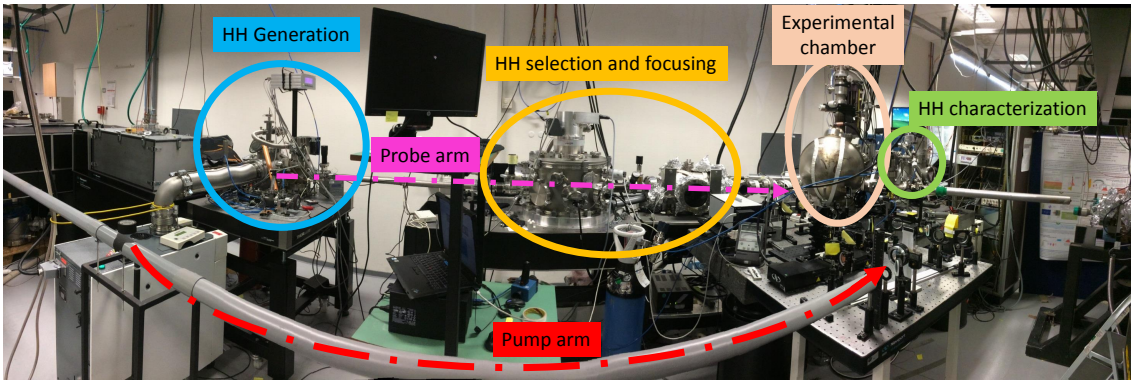

Fig. II.6 *Tr-PES beamline panoramic photograph.*

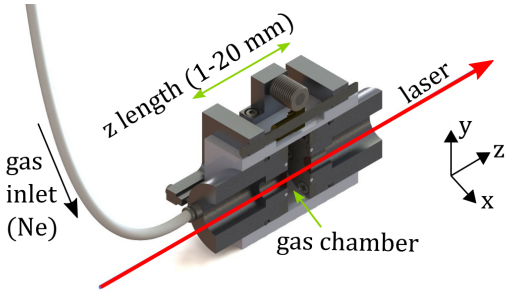

Fig. II.7 *Longitudinal cut of the HHG gas cell design for the XUV beamline.*

Thanks to this mechanical setup, the HHG signal output can be precisely optimized by monitoring the XUV intensity. It is performed by adjusting succesively the following parameters:

1. The diaphragm before focusing: modification of the laser intensity, focal spot size, phase profile and Rayleigh length

2. The position of the gas cell in the laser axis: modification of the distance with respect to the focal point

3. The distance between the diffraction gratings inside the compressor: variation of the velocity group dispersion of the fundamental laser pulse

4. The medium length (cell size)

5. The gas pressure

The parameters 1. and 2. modify the conditions of laser focusing and the generating gas volume, aiming to stay in the tunneling regime. Parameter 3. aims to ensure the largest cutoff by having an optimal pulse compression. The parameters 4. and 5. modify the number of atoms in the medium, aiming to find the desired compromise between generation, absorption (related to l_{abs}) and phase matching (related to l_{coh}).

b) HH selection and focusing

After the HHG are emitted from the generating cell, they propagate through the beamline into the monochromator (HH Selection and Focusing in Fig.II.5) that allows to select a single harmonic through a pair of multilayer mirrors (ML). The monochromator (MC) works at Brewster conditions. Hence, the XUV beam needs to be s-polarized, which is ensured by rotating the polarization from p to s of the IR beam before the HH generation.

ML mirrors consist in a nanostructured stack based on two or more materials. They are composed by multiple layers in order to maximize the reflectivity. The spacing and thickness of the layers are regulated in such a way that all the reflected components interfere in phase, hence constructively. This condition for constructive interference is given by Bragg's law: $\lambda = 2d \sin\theta$, where λ is the photon wavelength, d the interlayer spacing, and θ the incidence angle of the XUV beam.

The ML were designed and provided by OPTIX FAB company (Germany). They have a maximum reflectivity in the 80-100 eV range with a limited bandwidth in order to select a single harmonic at a time (see Fig. II.8). Since the spectral position of the reflectivity peak of the ML is adjustable by varying the angle of incidence, the ML mirrors were mounted on rotation stages to control the selection of the desired harmonic. In order to maintain the beamline alignment, the output axis is kept constant for all incident angles (i.e. all selected harmonic) thanks to a translation stage mounted on the second ML that compensates the distance for every angle. These motorizations are remotely controlled through a LabVIEW program that adjusts the two MLs angles of incidence and 2^{nd} ML translation position. This system constitutes the monochromator (MC) shown in Fig. II.5.

The residual near-IR radiation is filtered out using a 110 nm thick Zr film (Luxel Corp.) with a transmission of 0.52 ± 0.06 (measured for H55, 85.27 eV), located at the exit of the monochromator. The XUV beam is then focused onto the sample surface in the ultra-high vacuum (UHV) interaction chamber using a 1 m grazing incidence gold-coated toroidal mirror. These monochromatization and focusing parts of the probe branch are installed in independent vacuum chambers where the pressure reaches 10^{-7} mbar and 10^{-8} mbar respectively.

c) HH characterization

The beamline characterization has been performed thanks to the characterization stage (HH Characterization) shown in Fig. II.5, which is located just after the interaction chamber.

The XUV flux impinging on the sample surface has been optimized by a precise adjustment of the above mentioned parameters. It has been measured for a selected photon energy range (from H51 to H61), using a calibrated avalanche photodiode (APD, XUV-100 from OSI Optoelectronics) placed in a retractable mounting located after the sample (APD on Fig. II.5).

A XUV diffraction grating (DG) spectrometer is available in the characterization chamber. It is associated with a detection system consisting of a microchannel plate (MCP), a phosphor screen and a CCD camera. Its working principle is the following. XUV photons arrive at grazing incidence to the grating that is energy dispersive. Each photon will collide at a certain x position on the MCP area and ionize a certain channel.

Then by secondary ionization the signal current will be amplified. The electrons emerging from the MCP are accelerated by a high voltage and collide with the phosphor screen that in turn will emit visible photons upon each impact. Finally, a CCD camera records the emitted light.

Images for each selected harmonic are succesively recorded in order to obtain a calibration curve for the energy axis (corresponding to the x axis). The latter is done with CELIA's home-made image processing software that calculates the distance dispersion conversion on the image. In Fig. II.8 are presented the selected harmonics obtained with the described system, along with the reflectivity of the monochromator ML mirrors.

d) Performance

As mentioned above, the highly non-linear HHG mechanism is sensitive to numerous parameters of the driving laser pulse (duration, spatial and temporal chirp, beam profile, intensity and focusing configuration) and of the gas cell (interaction length, pressure and gas nature). In addition, photoelectron emission is a very low efficiency process that usually forbids single shot acquisition and requires long accumulation time. For those reasons, the HHG generation must be precisely controlled and adjusted in order to ensure an optimal output. It also requires a stable monochromatized photon flux and a focusing diameter smaller that the pump spot (in our case $< 280 \times 205$ μm). Therefore, the beamline optimization has been performed during a dedicated experimental commissioning.

The spectral selection is achieved by the ML monochromator described above. The monochromator reflectivity profile is centered at an adjustable photon energy depending on the incidence angle and yields a maximum measured peak reflectivity ranging from 25% to 33% depending on the selected HHG as seen in Figure II.8.

The spectral bandwidth of the reflectivity peak ranges from 2.25 eV to 2.37 eV at FWHM, which is larger than the natural HHG spectral width reported in Table II.1. Therefore, the monochromator only selects a single HHG with no further monochromatization, ensuring a maximization of the XUV photon flux on the sample surface. The overall spectral resolution of the HHG beamline is thus given by the HHG bandwidth ranging from 0.91 to 1.23 eV FWHM, measured with the spectrometer located at the end of the beamline (Fig. II.5).

The photon flux N_{XUV}, evaluated with the APD photodiode, ranges from 0.21 to 2.59 $\times 10^4$ photons/pulse at 1 kHz repetition rate. The corresponding values for each measured HHG are reported in Table II.1.

This precise optimization of the HH generating process has been made possible mainly thanks to the home-made gas cell design adjustable in length. The maximum XUV flux has been obtained in the range of 3 to 12 mm length with a corresponding gas pressure between 100 to 200 mbar. The beam flux stability has been evaluated to be around 8% during operating hours. It is mainly driven by:

1. the remote pressure stabilizer, which ensures a stable density of XUV emitting gas atoms.

2. the heat-dissipating adjustable diaphragm located before the spherical mirror (D1 in Fig. II.5), that used to avoid air turbulences and thus ensuring a stable focusing.

HHG order	central energy eV	N_{XUV} 10^4 photons	FWHM eV
51	79.00	1.20±0.30	0.91±0.17
53	82.15	2.05±0.30	0.94±0.18
55	85.27	2.59±0.26	1.13±0.22
57	88.40	1.95±0.24	1.20±0.25
59	91.69	0.76±0.22	1.23±0.26
61	94.50	0.21±0.20	1.17±0.26

Table II.1: Measured output photon flux and bandwidth (FWHM) per generated harmonic.

3. pre-drilled cell walls made of 200 μm thick brass foils. The holes are sufficiently large to allow the laser beam to go through without enlarging the hole and losing stability, but small enough to keep a reasonable gas consumption.

A focal spot upper limit value of 85×60 μm^2 was found for the XUV focal spot diameter on the sample plane (at 0° incidence). It has been measured by imaging the residual near-IR beam impinging on sample surface, which has a larger divergence than the XUV beam. Hence the imaged near-IR beam focal spot is larger than the XUV one.

II.3 Pump/Probe experiment

This section will describe the pump considerations necessary for carring out pump/probe experiments: the beam focusing and fluence control, the temporal characterization and finally the pump/probe synchronization and spatial overlap in the interaction chamber.

II.3.1 Pump beamline focusing and fluence calculations

As seen on Figure II.5, after the beam splitter (BS) that forms the pump and probe arms of the experimental setup, the pump beam goes through an energy regulator consisting of a half wave plate (HWP) plus a polarizing cube (PC) and then to its dedicated compressor (C2). It is steered through the room towards a motorized delay line (DL) and then directed onto the sample with a 1 inch, 45° mirror placed under vacuum.

The Tr-PES pump/probe experiment has certain requirements for the pump beam focusing:

1. an homogeneous focal spot, ideally with a top-hat or Gaussian profile to ensure an homogeneous transverse heating of the sample

2. a focal spot that is larger than the probe spot to ensure that the probed region is heated uniformly.

3. a sufficiently high fluence to trigger the desired dynamics in the samples (in the range of 5000-9000 J/m^2)

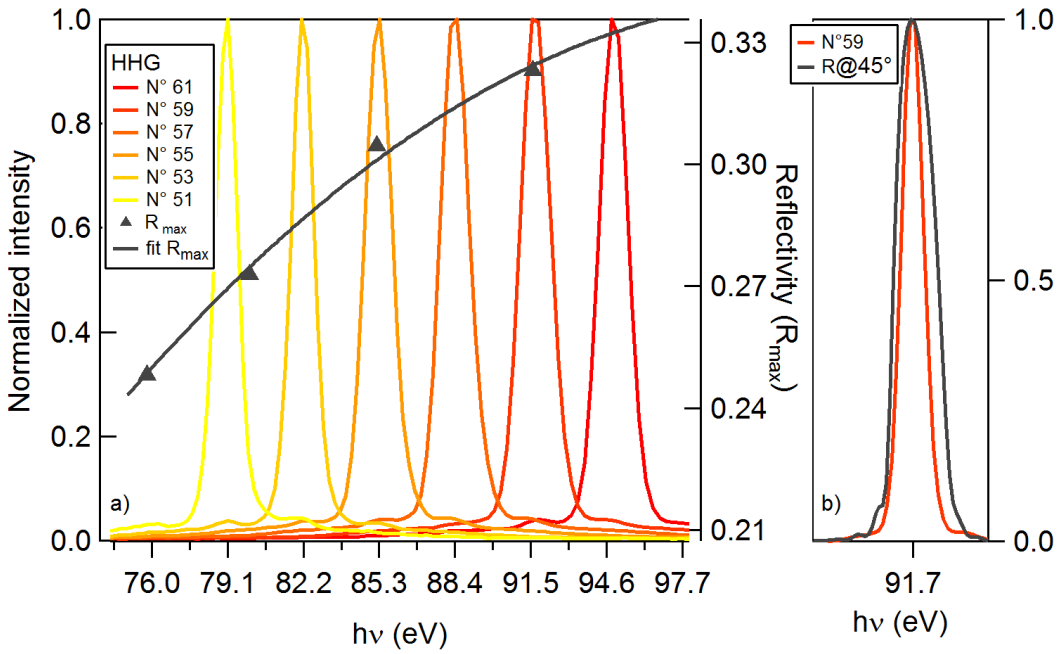

Fig. II.8 *(Left) Measured Normalized HHG obtained after selection along with the maximum reflectivity of the monochromator (provided by the NTTA company) and its corresponding fit. (Right) The spectral reflectivity for the 45° angle showing that its bandwidth is larger than the selected HHG.*

To ensure conditions 1 and 2, the focusing is done with an interchangeable iris (D2) followed by a plano-convex lens (FL) with 2 m focal length placed outside of the vacuum line. The focal spot diameter, d, depends on the numerical aperture (NA) of the system:

$$d = 1.22\lambda/NA = 1.22\lambda \times 2f/nD \tag{II.9}$$

where f is the focal distance, n the refractive index and D the diameter of the collimated pump beam. So, d can be controlled by changing the iris aperture D.

The third condition is assured by concentrating the laser energy in a reduced collimated beam: a telescope system (TL) composed by two spherical mirrors reduce the beam spot diameter by $\times 2.5$. In this fashion, sufficient energy goes through the focusing iris and onto the sample.

The focal spot was monitored using a calibrated imaging system to obtain its intensity profile and dimensions. Thanks to this system, a perfectly 2D Gaussian focal spot was achieved and measured. As the sample is oriented at 45° with respect to the laser axis, the focal spot on the sample is larger in the horizontal plane than in the vertical one, as seen in Fig. II.9. The pulse energy was measured just before the vacuum window using a thermal power sensor. Then, the fluence was calculated assuming that the focal spot followed an Airy disk pattern, where 83.4% of the total energy is in the main disk. Table II.2, presents the found pump focal spot sizes and the maximal attainable fluences.

According to these calculations, we choose an iris diameter of $d = 5$ mm in order to find a compromise between the maximum attainable fluence and the focal spot size, which

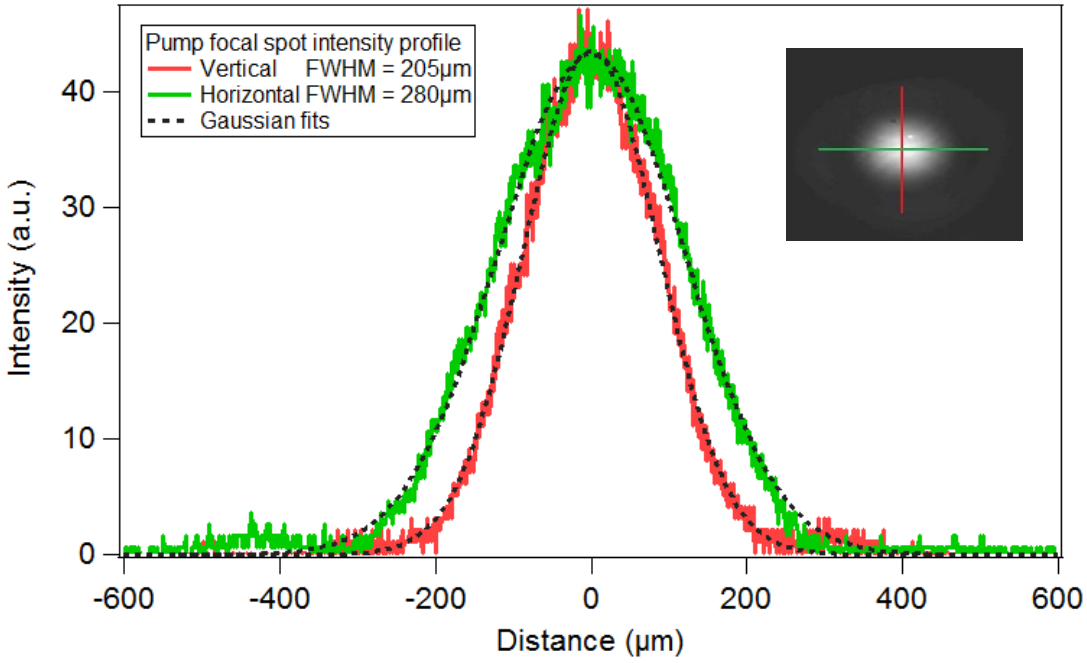

Fig. II.9 *Pump focal spot on the sample plane using an iris of 5 mm. The Gaussian fits and widths (FWHM) correspond to the horizontal and vertical profiles of the picture on the inset.*

needs to be larger than the probe focal spot.

II.3.2 Pump pulse temporal characterization

During the experiments, the pulse duration is monitored to control the laser intensity on the sample. This measurement is done as close as possible to the sample, i.e. after going through the maximum of optical elements (especially after the telescope) and hence, to obtain a good estimation of the pulse duration on the sample plane. The measurement was carried out with a single shot autocorrelator. A minimum pulse duration of 25.0 fs ± 1.7 fs was achieved, meaning that there is negligible dispersion along the beam path.

During the experiments, the pulse duration can be tuned by adjusting the grating compressor. Usually the pulse duration is varied between 25 fs and 5 ps according to the experimental needs.

II.3.3 Pump/Probe synchronization and spatial overlap

Both pump and probe pulses are guided to the interaction chamber where the sample is mounted. The spatial overlap and temporal synchronization are carried out using the fundamental IR beam on both arms:

- Pump: set to minimum energy.
- Probe: set to minimum energy, without the generating gas and the Zr filter removed.

Iris diameter D(mm)	Spot Size FWHM $d_x \times d_y$ (μm^2)	Maximum fluence J/m^2
3	436×328	1830
4	338×244	4600
5	280×205	12300
7	188×158	30000

Table II.2: Measured focal spot size and corresponding maximum fluence for different focusing irises

The spatial overlap is achieved with the sample imaging system and fine tuning of the last optical elements (toroidal mirror and focusing lens).

The synchronization, carried out with both pulses in the same polarization state, so they could interfere, was achieved in two steps:

- A coarse synchronization up to 1 ns (corresponding to 30 cm in optical path difference): with the aid of a fast photodiode, placed close to the image plane of the imaging system, the optical path difference between pump and probe was corrected with a manual delay line (not shown in Fig. II.5)
- A fine synchronization: achieved by looking for pump/probe interference fringes using the imaging system while scanning the motorized picosecond delay line (DL in Fig.II.5). The position of maximum contrast of the fringes was set as zero delay position

The overall temporal resolution corresponding to the maximum contrast of the interference pattern was estimated around $\tau = 1$ ps using an IR pump of 1 ps FWHM and a probe of 25 fs FWHM.

II.4 Interaction chamber for photoelectron spectroscopy

The probe and pump beams are recombined in the interaction chamber where UHV conditions are reached (10^{-9} mbar). As depicted in Figure II.10 , it is equiped with all typical instruments required for sample preparation and photoelectron spectroscopy measurements:

- an Ar ion sputtering gun (EX03, Thermo Fischer Scientific) for sample surface cleaning.
- an electron gun for charge compensation when working with low conductive materials.
- a classic twin anode Al/Mg x-ray source (RS40B1 from Prevac) for sample surface chemical characterization by x-ray photoelectron spectroscopy (XPS).
- an electron energy analyzer (Thermo VGScientific Clam IV) with a 9 channeltrons detection head.

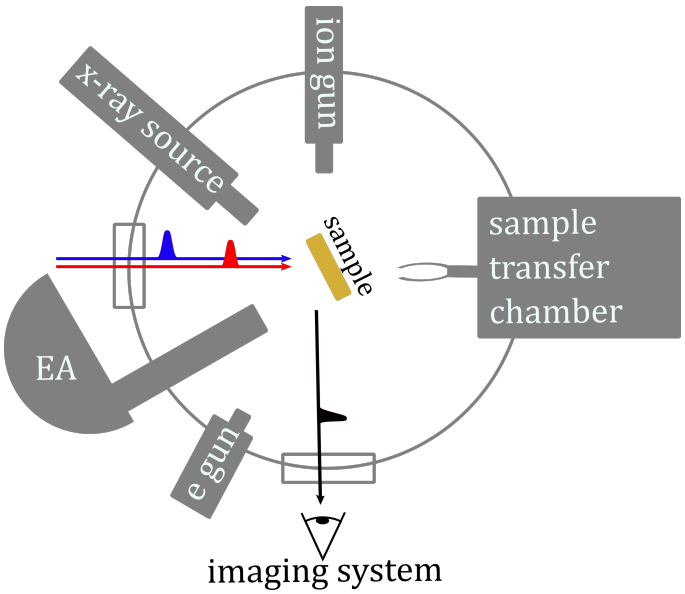

Fig. II.10 *Schematic depiction of the interaction chamber for photoelectron spectroscopy with all the necessary equipment to perform experiments. (EA stands for electron energy analyzer and the sample holder is not shown).*

- An (x, y, z, θ) manual sample holder with sample cooling (-70°C) and annealing (up to 370°C) systems (not shown in the Figure).

This equipment allows to properly perform x-ray photoelectron spectroscopy (XPS) and time-resolved photoelectron spectroscopy (Tr-PES) experiments. In our experimental setup, the electron spectra are recorded at an angle of 0° with respect to the sample normal axis.

Next section details the vacuum requirements of the mentioned equipment and the procedure to reach the needed pressure values.

II.4.1 Vacuum requirements

Most of the mentioned equipment can work under medium to high vacuum ($10^{-3} - 10^{-6}$ mbar), but there are two main reasons for requiring UHV when performing photoelectron spectroscopy for surface analysis [57]:

- to avoid collisions of the photoelectrons when they travel from the sample towards the detector,
- to prevent sample contamination from gas species sticking to its surface and then distorting the photoelectron spectrum, which is sensitive to the chemical environment. Moreover, in the present case of laser sample interaction, sample contamination can also modify the conditions of laser absorption.

The first condition is easily met with pressures on the order of $\sim 10^{-4}$ mbar. At this pressure, gas molecules are $\sim$2 m away from each other.

The second condition depends on the deposition rate of molecules on a surface. For a highly reactive gas with a sticking coefficient of 1 (for example, oxygen on a metallic surface), the monolayer formation time can be approximated as $t_m(s) = 1.27 \times 10^{-6}/p(Torr)$, where p is the pressure [57]. Therefore, the deposition rate decreases proportionally to the pressure.

In order to reach and maintain these vacuum levels it is important firstly, that the beamline connected to the experimental chamber has good levels of vacuum. As mentioned in section II.2, the pressure across the probe beamline drops progressively from 10^{-2} mbar at the generation chamber to 10^{-8} mbar at the focusing chamber.

Secondly, the experimental chamber was baked at $< 100°$ C for more than 48 h to desorb water molecules and the atoms of atmospheric gases and other contaminants from the chamber walls. After the bakeout, the lower degassing rate of the interior surfaces allows to reach much lower pressures (without bakeout it is not possible to attain 10^{-9} mbar within acceptable time scales). The pumping system is composed of a rough pump, a turbomolecular pump and two ionic pumps allowing to reach and maintain these levels of pressure. Finally, the sample transfer chamber, which is $\sim 20\times$ smaller in volume than the interaction chamber, was only opened when pressure was under 10^{-6} mbar for very short periods of time, ensuring that the sample transfer wouldn't contaminate or increase the interaction chamber pressure.

II.4.2 Photoelectron spectrometer

The photoelectron spectrometer has two main components: an electron energy analyzer (EA) and a detection system. The EA installed in the experimental chamber, is a concentric hemispherical analyzer (CHA). It consists of two concentric hemispheres (radii R_1 and R_2) with the outer hemisphere at potentials $-V_1$ and $-V_2$ respectively ($|V_2| > |V_1|$). The mean radius describes an equipotential $R_0 = (R_1 + R_2)/2$ connecting an entrance and an exit slit. Only electrons with the correct energy E (called pass energy) fulfilling the relation

$$e(V_2 - V_1) = e\Delta V = E(R_2/R_1 - R_1/R_2), \tag{II.10}$$

where e is the electron charge, can travel from the entrance slit to the exit slit.

The energy resolution can be approximated, for a point-like source as:

$$\Delta E/E = w_2/(2R_0) + 1/4(\delta\alpha)^2, \tag{II.11}$$

where w_2 is the exit slit width and $\delta\alpha$ the half acceptance angle of the spectrometer.

In order to keep the resolution $\Delta E/E$ constant while recording a spectrum, a retarding lens is used to reduce (or increase) the kinetic energy of the electrons entering the spectrometer, to a fixed value E, called pass energy.

The CLAM IV photoelectron spectrometer resolution has been calibrated by the fabricant using an Mg K-α source and measuring the Ag $3d^{5/2}$ of an Ag sample, yielding the values reported in table II.3:

The CHA is energy dispersive, so an array of detectors can be used to measure different parts of the spectrum over a certain energy range. In this experimental setup the detection

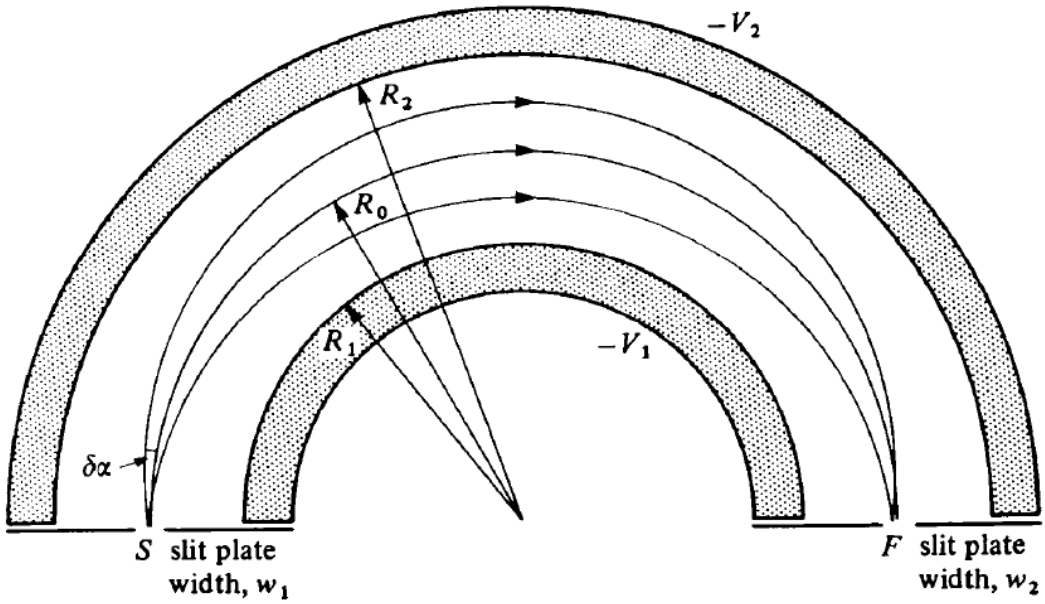

Fig. II.11 *Schema of a concentric hemispherical analyzer (CHA) showing the radii R_1, R_2 and R_0, the entrance and exit slits w_1 and w_2, electric potentials $-V_1$ and $-V_2$ and the half-acceptance angle $\delta\alpha$ (adapted from [96]).*

is done by means of nine channeltrons, reducing the measurement time by a factor of $1/9^{1/2}$ compared to a measurement with a single channeltron.

II.4.3 Sample manipulation, cleaning and XPS characterization

The sample is routinely introduced using the sample transfer chamber connected to the interaction one, mentioned at the end of section II.4.1.

As mentioned before, samples need to be cleaned regularly before performing the PES measurements. For this purpose the sample surface contamination is first characterized by an XPS scan using the Al/Mg K-α x-ray source. Usually oxygen and carbon peaks are present, showing the presence of these surface contaminants. A standard cleaning process is used to remove the oxygen and carbon peaks, consisting of:

- sputtering with inert gas atoms for several minutes ($\sim$ 20 min)
- annealing up to 150 °C for up to 20 minutes

The sputtering is done to remove the contaminants from the surface using argon atoms. As this is an inert gas, its sticking coefficient to surfaces is close to zero and it can easily be extracted by the pumping system. An ion gun produces the argon ions by collision with electrons, and then accelerates them with an electrode to the desired energy (usually ranging between 600-3000 eV). The ion gun spot size can be adjusted to cover the whole sample.

The sample annealing is performed in order to passivate the surface as vacancy defects may be generated by the sputtering cycle. The annealing is achieved using a joule effect

E eV	FWHM eV	Peak/Background count rate Mc/s
2.34	0.788	0.15489
5.85	0.818	0.77696
11.71	0.881	2.545
23.42	1.013	7.353
58.55	1.800	19.710

Table II.3: Photoelectron spectrometer resolutions and signal-to-noise ratios for different pass energies E (measured by the manufacturer).

filament located in the sample holder.

Fig. II.12 presents a typical XPS spectrum before and after applying a cleaning process of a few sputtering-annealing cycles to an Au single crystal sample. As shown, the carbon (C 1s) and oxide (O 1s) peaks are reduced in intensity, while the Au peaks arise. The resiudal C 1s and O 1s peaks remain constant after a few sputtering-annealing cycles. This signal might be coming from the sample holder, given that the x-ray source is not focused and the sample holder is also being irradiated.

II.4.4 Valence band photoelectron spectrum measurements

An example of the measurements that can be performed with our experimental setup is presented here.

Once the beamline has been tuned and stabilized for an optimal HH emission, the sample cleaned and an appropriate vacuum level maintained, PES measurements can be performed.

The sample is placed in position of irradiation, which is at the center of the experimental chamber and at a 45° incidence angle with respect to the probe axis.

The electron spectrometer is set to scan in the desired energy range, in this case around the expected position of the valence band. Also, the pass energy is set sufficiently high to obtain a signal to noise ratio that allows to record the spectra in a reasonable accumulation time but making sure that the resolution is sufficient to depict the spectrum features. Figure II.13, shows typical valence band spectra of Au and Cu recorded with a pass energy of 20 eV. Both samples are single crystals bought from MaTecK GmbH.

Both spectra are the average of multiple scans taking less than 7 minutes of recording (corresponding to $\sim 4.2 \times 10^5$ XUV laser pulses). This is possible thanks to the stability of our beamline. The accumulation time is sufficiently short to allow for complete scans in delay when performing pump/probe experiments.

The Au spectrum clearly shows the 5d spin orbit splitting, the 6s conduction band and the Fermi level. The Cu spectrum shows the known 3d assymetric shoulder in the low kinetic energy side of the spectrum, whereas the 4s band and Fermi level are not well distinguished due to a lack of resolution. This is not an important drawback since modifications upon laser excitation are not expected in that region.

The resolution is directly related to the bandwidth of the probe XUV beam, but also to the possibility of Coulomb repulsion between the probe-generated electrons (called space-charge effect). Since the resolution is constant and sufficient for all the measure-

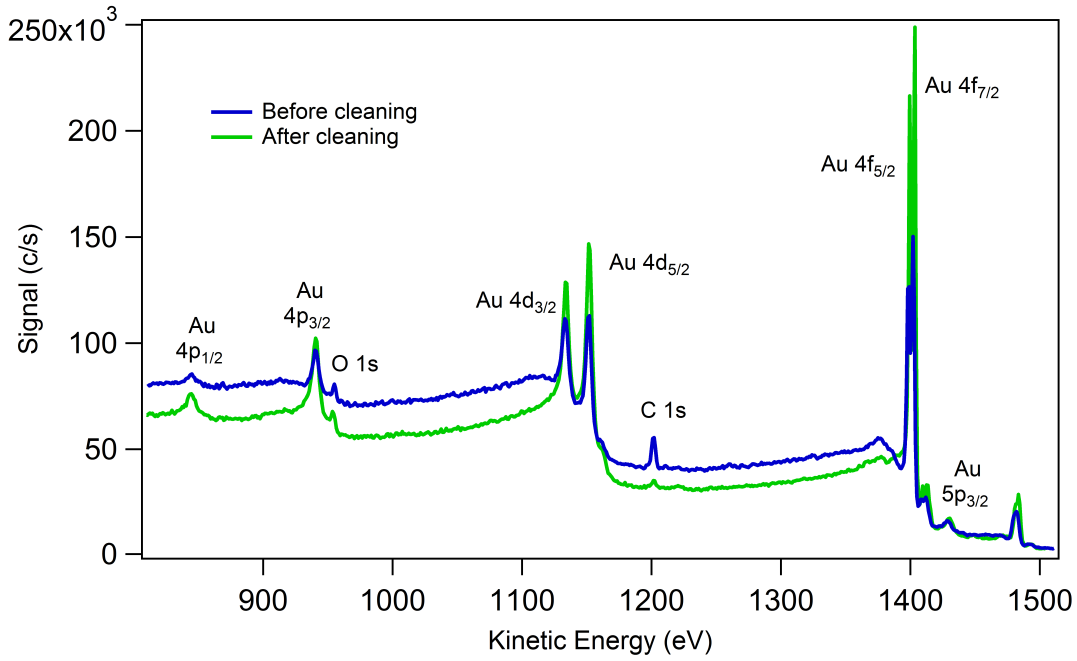

Fig. II.12 *XPS spectrum of a Au single crystal as introduced in the experimental chamber (blue) and after two cycles of sputtering (ion energy = 600 eV) and annealing ($T \simeq 150\ ^{\circ}C$) (green). Both spectra were obtained using Al K-α radiation.*

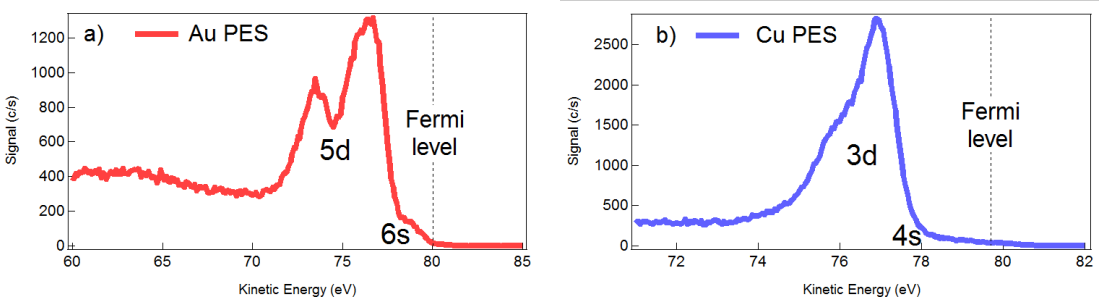

Fig. II.13 *Valence band measurements of a (a)Au single crystal and (b) a Cu single crystal, with a pass energy of 20 eV.*

ments, no further actions were needed to improve it.

The PES measurements presented at the end of this chapter are steady-state, as no pump pulse was present. As it was already mentioned in the introduction and in chapter I, when performing pump/probe measurements, the pump-generated photoelectrons pose a double challenge: they can superimpose to the probe photoelectron spectrum, and they can generate enough space-charge effect to distort it. The first challenge is solved by using our 100 eV beamline to perform Tr-PES experiments. The second challenge is subject to an in-depth study presented in chapter III.

Chapter III

Space-charge effect study

In this chapter, the space-charge effect will be presented. Its importance in pulsed photoemission experiments will be highlighted with a set of experimental measurements. The different aspects of the pump/probe space-charge effect will be discussed along with numerical models describing them. A systematic study of the phenomenon using these models will be presented. The chapter will conclude with a discussion of the calculation findings and with practical considerations for the optimization of the performances of our Tr-PES experiments.

III.1 Introduction and motivation

In photoemission experiments, when moving from continuous to pulsed light sources, the photoelectrons are emitted in packets instead of continuously. In these packets, the electronic density can be so elevated that the photoelectrons can undergo Coulomb interactions, exchanging energy and momentum. Hence, important distortions are produced in the detected energy spectrum in terms of broadening and shifting. This mechanism, which entails a loss of information, is called the space-charge effect.

To maintain the same rate of emitted (or detected) photoelectrons, as the repetition rate of the light source decreases, the photon flux must increase by the same factor. As a result, the density of the photoemitted electron packets increase. For comparison let's consider the following example: A synchrotron can deliver 10^{12} photons/s at a repetition rate of 100-1000 MHz, producing on a sample 10^{11} e/s. Every emitted bunch therefore contains 1000-100 electrons. A HHG source (such as the one used as probe beam in the Aurore facility), with repetition rates of 1-100 kHz would produce for the same sample current, bunches of $10^8 - 10^6$ electrons. The space-charge effect is then much more important for low repetition rate and high-brilliance sources.

Moreover, when performing time-resolved photoelectron spectroscopy (PES), the studied dynamics are usually triggered by ultrafast lasers with intensities sufficiently high to produce photoionization via multiphoton absorption or even, laser acceleration of the photoelectrons. The cloud of generated photoelectrons induced by the pump pulse can also produce space-charge effect distortions in the measured probe photoelectron spectrum. The most delicate aspect of this pump induced space-charge effect is that it depends on the time delay between the pump and probe pulses, i.e. the relative distance between

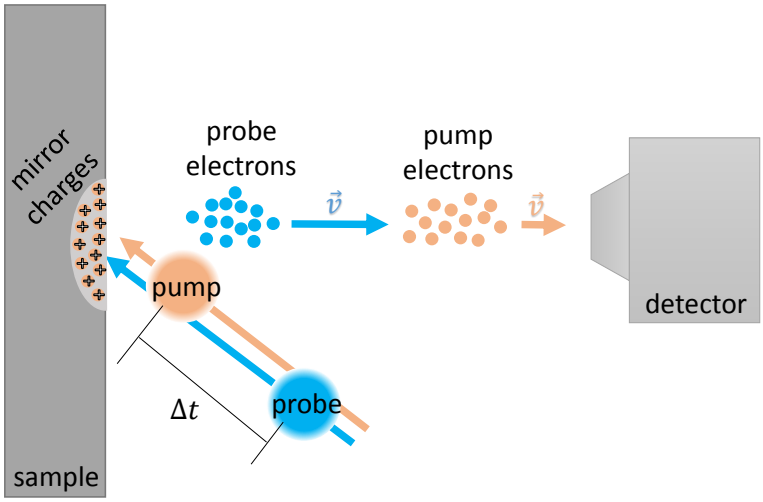

Fig. III.1 *Pump/probe experimental diagram. The pump pulse arrives Δt before the probe pulse. The pump emitted electrons are slower than the probe electrons and they both travel towards the detector. An attractive field is represented as mirror charges.*

probe and pump electrons. Consequently, it becomes quite challenging to disentangle PES changes issued from the pump-triggered dynamics in the sample from the space-charge effect.

The necessity to tackle the space-charge effect is evident in our experiment as in a variety of photoemission experiments. Different groups had addressed this issue from an experimental point of view or had proposed different mathematical models and performed numerical simulations. The space-charge effect has been studied in many different cases: solid-state bulk samples [97, 98, 99] chemisorpted monolayers [15], diluted samples [86]; using different probe photon energies ranging from EUV [97, 86, 100] to hard x-ray [99, 17]; and performing different PES measurements such as valence band PES [18], core level PES [99], time and spin-resolved experiments [19] and time and angle-resolved PES (Tr-ARPES) [17, 18].

The pump/probe space-charge effect dynamics is expected to depend on many parameters: the number of emitted electrons, the electron packet density, the emission angle, the contributions from mirror charges (in the form of an attractive force coming from the electrically grounded sample) and the initial pump and probe photoemitted spectra. Specifically, the initial energy distributions of the pump and probe photoelectrons will define for how long they will travel together towards the detector and how easily they can get out of reach of the mirror charge forces.

Fig.III.1 presents a diagram of the studied pump/probe space-charge dynamics: the pump pulse falls onto the sample surface a time Δt before the probe does. Both pulses generate photoelectrons that interact with each other. Mirror charges are formed at the sample surface and attract the electrons back to the sample.

Most of the aforementioned studies have focused mainly on the probe-only space-

charge effect and less in the pump-probe one. The ones that have addressed this last problem make use of mathematical models and simulations usually not including the pump initial photoelectron spectrum, which is the spectrum just after emission and before any Coulomb interaction (hereon called pump initial spectrum): Al. Obaidi et al. [86] used a "mean field model" where pump and probe electrons are described by averaging the initial and final kinetic energies; L.-P. Oloff et al. [100] developped an analytical model where the electron bunches are modeled as interacting disks of charges with a mean kinetic energy; Dell'angela et al. [15] performed many-body simulations assigning a Gaussian spectrum at an arbitrary central kinetic energy (10 eV) to the pump electrons in order to avoid a loss of particles. In fact, a more complete approach should deal with the specific characteristics of the pump-induced photoemitted spectrum.

Defining the pump initial spectrum is not trivial. Measuring it is usually not possible as the electrons arrive at the detector having already undergone Coulomb interactions and even Coulomb explosion (rapid gain of tens of eV in kinetic energy and expansion of the packet) [101]. The origin of the pump initial spectrum is above threshold ionization (ATI), meaning that the sample is ionized with more than the minimum of required photons for ionization. This phenomenon started to become a common observation (and an important topic of research) as ultrafast amplified lasers with high intensity peak pulses became more available [102, 84, 85]. This multiphoton process has been determined to be dependent on the sample properties such as chemical composition, work function and surface quality (roughness and cleanness) [102]. The dependence on different parameters adds to the complexity of the determination of the pump initial spectrum.

In this work, a more complete approach is proposed to tackle both pump photoelectron dynamics (including the pump initial spectrum and laser-photoelectron acceleration) and its effect on the probe photoelectrons. It has been adapted to our case of interest: solid-state metallic samples irradiated by an infrared ultrafast pump laser and a XUV probe on energy ranges around 100 eV as the ones delivered by our HHG beamline. As it was mentioned at the end of chapter II, the XUV beamline photon output is sufficiently low to disregard the probe-only space-charge effect, meaning that we only account for the effect of pump electrons on the probe ones.

The followed strategy consists in exploring the different contributions from the possible processes happening during the pump/probe experiment:

1. The first process relates to the generation of the pump initial spectrum, calculated by means of a quantum model, called the jellium-Volkov (J-V) approximation that evaluates the probability of the IR pump electrons being ejected by the incident laser electric field [103]. It allows to obtain the pump initial spectrum and its associated emitted electron density.

2. After the pump photoelectrons are emitted, the possibility of the interaction between photoelectrons and the laser electric field is explored. This interaction can supply additional kinetic energy to the pump photoelectrons modifying their spectrum. This effect is assessed using the SMILEI particle-in-cell (PIC) code [104] originally conceived for plasma simulations that can take into account laser pulses irradiating charged particles. This happens during the photoemission process, when the laser field is present.

3. At later times and on a much longer timescale, the contribution from the space-charge effect of electrons travelling from the sample surface towards the detector is assessed. This calculations are performed using the ASTRA PIC code [105] that accounts for the Coulomb interaction between traveling pump and probe electrons up to the detector. The input for ASTRA are the calculated pump initial spectrum from point 1. or the laser-accelerated spectrum from point 2. – along with additional experimental parameters that will be discussed in the following sections.

Nevertheless, it is worth mentioning that other contributions might be present, which are not accounted for in the present study. For instance, one of these unaccounted effects is the space-charge effect produced inside the electron energy analyzer: at the entrance of the detector, an electrostatic lens focuses the beam of electrons into a small slit, effectively increasing the density of electrons and forcing them to interact as the distance between them decreases. As in the space-charge effect happening outside the detector, the larger the density of electrons, the more important the deformation or attained kinetic energies will be.

The purpose of this work is, first to disentangle the effect of the different parameters and shine a light on the most important ones allowing to a control and a reduction of the phenomenon. The strength of this study is that it compares experimental observations and numerical calculations for both pump and probe spectra. Given the complexity of the pump/probe space-charge effect problem, we aim to a qualitative understanding of the phenomenon and, if possible to obtain a reproduction of the magnitude of the attained kinetic energies.

The chapter is divided as follows. First, a set of IR-pump/XUV probe experimental results of the space-charge effect will be presented as the starting point. Then, the three different contributions mentioned above will be presented. Following, the results from each of the three different calculations in our experimental case will be discussed. The ASTRA simulation results encompass a parametric study where the effect of some key parameters will be unveiled. Finally, a discussion on the reduction of the space-charge effect will be presented.

III.2 Experimental Results

In order to study the pump-induced space-charge effect in our detected probe photoelectron spectrum, a set of measurements were carried out on a Copper single crystal with (111) orientation purchased from MaTeck GmbH. The cleaning of the sample was carried out following the same procedure as described in chapter II.

The pump-only and pump/probe spectra at a time delay of +15 ps have been recorded using the experimental parameters summarized in the Table III.1. The pump fluence was varied from 55 J/m^2 to 460 J/m^2 and for each fluence measurements using P and S pump polarization were recorded.

The corresponding measurements are presented in Fig. III.2. The pump-only spectra correspond to the photoelectron distribution upon the pump irradiation. The pump/probe measurements were set to record the valence band of the copper sample (corresponding to the 3d electronic level of Cu), and they are presented background subtracted using an

Parameter	Pump	Probe
τ_{FWHM} (fs)	25	25
x_{FWHM} (μm)	642±22	410±15
y_{FWHM}(μm)	452±16	150±5
Fluence (J/m^2)	55- 460	-
Polarization	P and S	S
Incidence (°)	45	43
Delay (ps)	0	+15

Table III.1: Pump and probe experimental parameters.

appropriate fitting of the data. Two Gaussian functions are used to describe the valence band levels (corresponding to the doublet splitting). The background is assumed to be Shirley and slope type to describe probe secondary photoelectrons, plus an exponentially decaying background associated to the tail of the pump spectrum [106]. The curve labeled as "cold" refers to a probe-only measurement (pump was blocked).

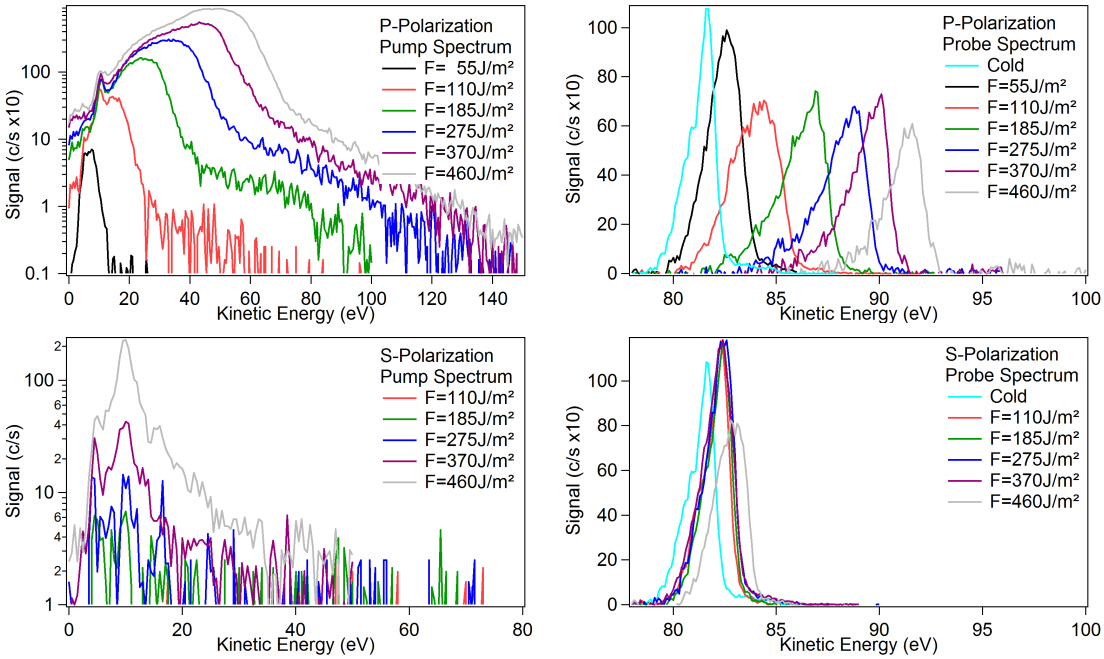

Fig. III.2 *Pump-only and pump/probe photoelectron spectrum measurements on a Cu (111) single crystal with increasing pump laser fluence (F). The pump/probe delay is Δt= +15 ps for all measurements. Upper panel: P-polarized pump, lower panel: S-polarized pump.*

The measurements for both polarization cases show similar trends: as the pump fluence is increased, more pump photoelectrons are emitted and the pump cutoff kinetic energies also increase. This increase in pump photoelectrons and kinetic energies seem to have a direct impact in the measured valence band leading to a greater shift and broadening. It can be noted immediately that the difference between the two polarizations is

drastic: the number of pump emitted electrons, and the attained kinetic energies is much less for the S polarization case, and consequently the effect on the probe spectrum is also much smaller.

It is important to notice that the XUV probe source could fluctuate throughout the measurements, leading mainly to different signal intensities, but inducing only a very small shift ($\sim$ 0.5 eV) and a negligible broadening.

In the following, I will present three models used to study the presented experimental measurements.

III.3 Numerical models for the pump-probe space-charge effect

The three numerical tools presented in this section aim to study the three contributions to the space-charge effect: (1) the pump-induced photoemission is modelled using the jellium-Volkov quantum approximation, (2) the laser-induced acceleration of the pump electrons is assessed with the SMILEI code and, (3) the Coulomb interaction between pump and probe electrons travelling in vacuum towards the detector is modelled with the ASTRA code.

The first two models are used to calculate the pump initial spectrum. Their outputs are used as input for the third model.

III.3.1 Pump initial spectrum calculations: the jellium-Volkov approximation

In order to study the photoelectron emission process by infrared laser pulses leading to the pump initial spectrum, we have used the jellium-Volkov approximation. This is a method approximating the solutions of the time-dependent Schrödinger equation (TDSE). Its validity has been demonstrated by Faraggi et al. in [107], where the calculated photoemission using an ultrashort laser pulse has been compared to results from the numerically solved TDSE. More recently, Jouin et al. [103, 108] published more complex studies, including the surface plasmon-enhanced photoemission process, and compared the calculation results to experimental measurements.

Within this approximation, the medium is represented by the jellium model: valence band electrons are bounded to the surface by a finite step potential. Although the band structure of the solid is neglected by this model, the electronic states are represented by analytical expressions including their corresponding asymptotic conditions.

The parameters used to define a precise system are the work function (Φ_S), which depends on the surface state of the sample (roughness, pollution, etc.) and on its crystallographic orientation, the Fermi energy (E_F), and the skin depth for the irradiation energy. The temperature of the system can also be included when calculating the photoemission probability.

Only the component of the laser electric field that is perpendicular to the sample surface is considered and no photoemission is expected to occur when an s-polarized beam is used. The temporal profile of the laser pulse is modeled in the Jellium-Volkov approximation.

The solution of the TDSE is built using the unperturbed jellium states and the action of the laser field by the inclusion of the phase from the so-called Volkov state, i.e. the

construction of the final states include the perturbation by the laser electric field [107]. For obtaining the transition rates, the initial unperturbed wave functions and the final perturbed wave functions are used as initial and final channels, respectively.

The temporal shape of the laser electric field is given by

$$F(t) = e^{-4\ln 2(\frac{t}{\tau})^2}\cos(\omega_0 t + \phi), \tag{III.1}$$

where τ corresponds to the envelope duration, ω_0 to the angular frequency and ϕ to a phase.

The electronic state wave function, $\Phi(\vec{r},t)$ evolves in time according to the TDSE:

$$i\frac{\partial\Phi(\vec{r},t)}{\partial t} = [H_0 + V_L(z,t)]\Phi(\vec{r},t), \tag{III.2}$$

where $H_0 = -\nabla^2_{\vec{r}/2} + V_s$ corresponds to the unperturbed Hamiltonian, $V_s = -V_c\Theta(-z)$ being the surface potential, with Θ being the Heaviside function and $V_c = E_F + \Phi_S$ where E_F is the Fermi energy and Φ_S, the work function. The potential $V_L = zF(t)$ comes from the laser electric field perpendicular to the surface of the sample.

The eigenfunctions of the unperturbed Hamiltonian H_0 are:

$$\Phi^{\pm}_{\vec{k}}(\vec{r},t) = e^{i\vec{k}\cdot\vec{r}_s}\phi^{\pm}_{k_z}(z)e^{-iE_{\vec{k}}t}, \tag{III.3}$$

where $\vec{r}_s$ is the position component parallel to the surface.

The perturbed final jellium-Volkov state is:

$$\chi_f^{JV-}(\vec{r},t) = \Phi^{-}_{\vec{k}_f}\exp[iD^{-}(k_{fz},z,t)], \tag{III.4}$$

where $D^{-}(k_{fz},z,t)$ is the Volkov phase.

Using these initial and final states, the transition rate induced by the laser field can be obtained as:

$$T_{if}^{JV} = -i\int_{-\infty}^{+\infty} dt\Big\langle \chi_f^{JV-}(t)\Big|V_L(z,t)\Big|\Phi^{+}_{\vec{k}_i}(t)\Big\rangle \tag{III.5}$$

Finally, by integrating over the initial states $\vec{k}_i$ one can obtain a spectrum (ejection probability) as a function of the final energy and for a given angle:

$$D(\theta_e,E_f) = \frac{\partial^2 P}{\partial E_f\partial\Omega_f} = \frac{k'_f k'_{fz}}{k_{fz}}\int d\vec{k}_i f(E,\mu,T)\rho(k_i)|T_{if}^{JV}|^2, \tag{III.6}$$

where the transition happens between $\vec{k}_i$ and the final momentum $\vec{k'_f} = (\vec{k_{fs}}, k'_{fz})$. And with $\rho(k_i)$ being the initial density of occupied states, $f(E,\mu,T)$ the Fermi-Dirac distribution at temperature T, $k'_{fz} = (k^2_{fz} - 2V_c)^{1/2}$ and $v_f = (2E_F)^{1/2}$.

By performing a second integration over $\vec{k}_f$ it is possible to calculate the total emission probability, that corresponds to the ejected electron density [109].

III.3.2 Simulated Matter Irradiated by Light at Extreme Intensities (SMILEI) simulations

The purpose of performing numerical calculations of laser-electron interaction is to explore the possibility of laser acceleration of the pump photoelectrons from the generating laser pulse. These mechanisms could take place if the main laser pump pulse is accompanied by a pre- or postpulse: a prepulse could generate photoelectrons that would be accelerated by the main pulse, whereas a postpulse would accelerate the photoelectrons created by the main pulse.

The Simulated Matter Irradiated by Light at Extreme Intensities (SMILEI) code is a multipurpose tool devoted to simulations for collissionless plasmas developped by a consortium of laboratories of the Plateau de Saclay and has been validated for different applications [104]. The motivation for the development for this code is to study ultra-high intensity laser interaction with matter. SMILEI can include the contributions of laser electric and magnetic fields through boundary conditions that can either inject or absorb external field contributions. SMILEI can be classified within the so-called particle-in-cell codes (PIC). It works in a similar way to other PIC codes such as ASTRA, that is described in the next section.

The general working strategy of a PIC code is depicted in Figure III.3. First, (a) the simulated charged particles and currents are placed within a spatial grid; (b) then, by solving Maxwell's equations, the electric and magnetic fields are calculated on the grid-points; (c) next, the external and internal fields are interpolated to the particle positions; (d) finally, the equations of motion are integrated up to the time step to update the particle positions and momenta. Both SMILEI and ASTRA perform Lorentz transformations when calculating the electromagnetic fields.

SMILEI is initialized with a particle distribution described by particle position and momenta assigned from a Maxwell distribution with temperature T_0. The initial charge and current densities are computed onto a grid that is created to describe the space where the plasma is distributed and the loop is started [104].

SMILEI is a self-consistent code using the Vlasvov-Maxwell model equations, so it naturally takes into account the different collisionless mechanisms for energy transfer from the laser fields to the plasma system [104]:

- **The ponderomotive force**. This mechanism is issued from the magnetic term $v \times B$ component of Lorentz force, exerted on a moving charged particle. The ponderomotive force can be divided into two contributions. The first one is the time-averaged nonlinear force that a particle experiences in an inhomogeneous oscillating electromagnetic field. It tends to expel particles from high laser intensity regions and can be related to the concept of light pressure. Usually this mechanism becomes important for high laser intensities on the order of $\sim 10^{18}$ W/cm^2 [111].

  The second contribution is refered to as $J \times B$ heating. It relates to the oscillating component of the ponderomotive force driving the electrons towards the sample every half-cycle of the laser pulse [112]. It is responsible for electron heating. In this case, absorption can happen with the laser at normal incidence.

- **Resonant Absorption**. This is a mechanism that takes place in a plasma with a density gradient with a laser falling obliquely upon the sample and p-polarization.

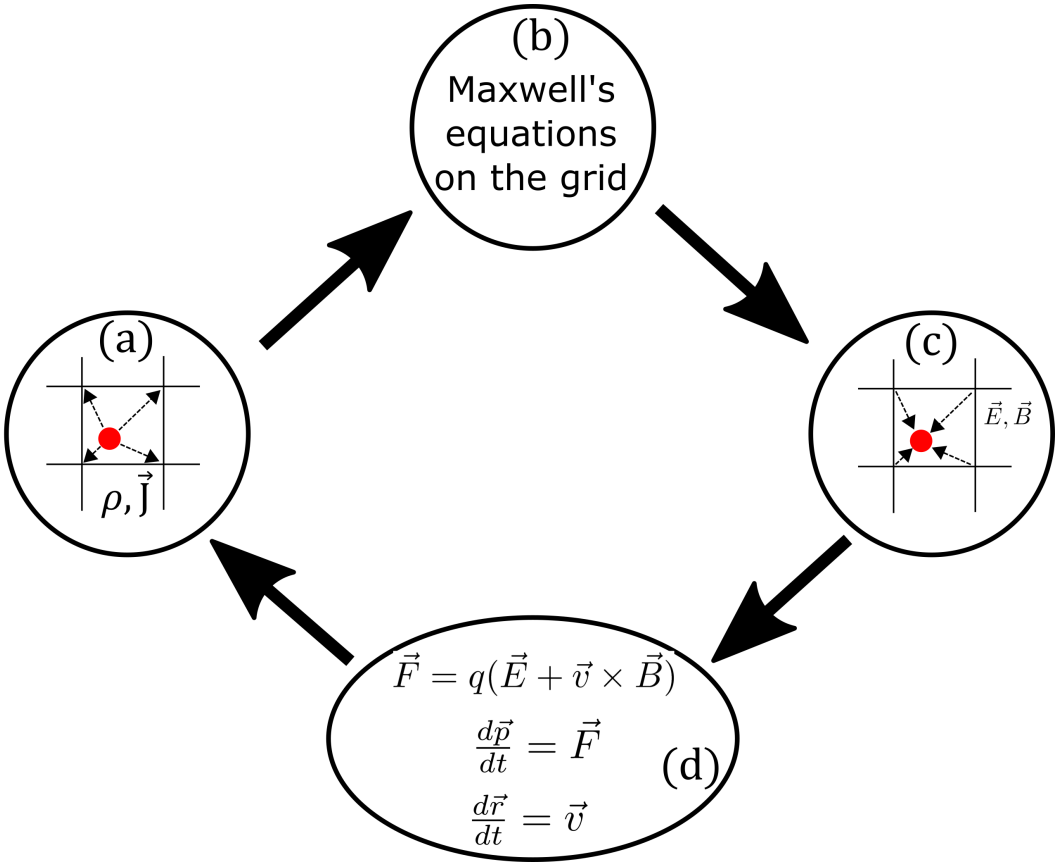

Fig. III.3 *Typical PIC loop: a) The charge and currents are distributed on the gridpoints, b) The Maxwell's equations are solved on the gridpoints, c) The electric and magnetic fields are interpolated to the particle positions, d) The equations of motion are solved. Adapted from [110].*

In this case, the longitudinal component of the electric field can excite a plasma wave [113]. In the critical density region, where the electronic density reaches the critical density n_e, this excitation is resonant, leading to strong absorption. The critical density is defined as $n_e = n_c = \omega^2 m_e / 4\pi e^2$, where ω is the frequency of the laser.

- **Vacuum heating**. In the case of a steep or step-like density gradient in the plasma, resonant absorption is not efficient. Vacuum heating is a mechanism that pulls electrons into the vacuum and then pushes them back into the sample [114]. The electrons re-enter the plasma targed with a velocity close to the quiver velocity. For this mechanism to take place, an oblique incidence of the laser electric field and a p-polarization are needed. This happens over one laser cycle.

The time and distance scales for the laser-induced acceleration of electrons are much smaller compared to the ones necessary for space-charge calculations. For instance, with SMILEI we used simulation boxes of ∼10×60 μm and total simulation times of ∼130 fs, whereas space-charge can evolve up to the nanosecond and hundreds of μm. This means

that even if SMILEI could, in principle, calculate the space-charge effect, it would require much longer calculations and a sufficiently large number of grid cells. This is the reason why SMILEI is only used here for assessing the laser acceleration happening close to the sample. The space-charge effect contributions, explored using ASTRA, are calculated up to the position of the detector.

In other words, the SMILEI output will be used as the pump initial electron spectrum for the ASTRA space-charge simulations.

III.3.3 A Space-Charge Tracking Algorithm (ASTRA) simulations

The initial pump electron spectrum calculated by the jellium-Volkov approximation or SMILEI are used as an input to simulate the space-charge effect expected in pump/probe photoemission experiments. For this purpose, we have selected the ASTRA code, whose name stands for A Space-Charge Tracking Algorithm [105]. This code is designed to calculate the external fields acting on charged particles as they travel through different electromagnetic elements. In the case of the present study, ASTRA will be used to calculate the evolution of the pump and probe electron packets as they travel from the sample to the detector with no additional electromagnetic elements.

ASTRA works following the same strategy described in Figure III.3. The calculations of the electric field at the particle positions are performed using a cubic spline interpolation. The equations of motion are integrated using a Runge Kutta 4^{th} order integrator.

The input for ASTRA is a distribution of particle (in this case electrons) positions (x, y, z) and momenta (p_x, p_y, p_z) in the three coordinates. This initial distribution then evolves every time-step up to a final position defined by the user, corresponding to the detector position, for example.

The initial particle distribution is defined on a spatial grid that can either be cylindrically symmetric 2D or a 3D for non-symmetric problems. We approximate our case as cylindrically symmetric assuming that the pump and probe generated photoelectron packets are distributed according to the optical focal spots in the (x, y) plane following a symmetric 2D Gaussian distribution with diameter $d = 2\sqrt{x_{FWHM} \cdot y_{FWHM}}$. The grid cells are automatically adjusted during the simulation to ensure a homogeneous distribution of the charge density. This treatment is particularly important when an important change is expected in the size of the electron packet while travelling to the final position. In the present case, the particle distribution expands by 2 orders of magnitude in the (x, y) plane up to the detector, whereas in the z direction expands from a few nm up to a few cm. This adaptative mesh makes ASTRA much more suitable to study the space-charge effect than other PIC codes, such as SMILEI that can only follow, although quite precisely, very small volume changes in the distribution.

To simulate the emission from a surface such as in photoemission, the cathode emission mode can be used assigning a departure time t for each particle. Instead of having an (x, y, z) distribution, ASTRA must be initialized with a (x, y, t) distribution. In this case, mirror charges, simulating the effect of a grounded conductor, can be included in the calculation [18]. Mirror charges tend to attract particles back to the emitting surface (cathode). It is assumed that these particles colliding back are reabsorbed and removed from the simulation.

ASTRA requires the charge in each defined electron packet. The electron distributions are initialized according to the jellium-Volkov approximation or SMILEI, which estimate the initial pump distributions. As mentioned before, a charge density is also provided, which has to be converted into a total electron number, N_e for ASTRA.

For this purpose, it is necessary to estimate the volume of the initial distribution at the end of the laser pulse. The charge density is defined by $\rho = e \times N_e/V$ where e is the electron charge and V is the electron cloud volume just after emission. For this calculation, the transverse size (x, y) is assumed equal to the laser focal spot size d. The transverse size Δz, will be estimated by calculating the distance travelled by an electron during presence of the laser pulse.

It should be noted that ASTRA cannot handle the total number of electrons needed for large charge densities, N_p macro-particles representing N_e electrons are used. Each macroparticle will have a total charge $q = e \times (N_e/N_p)$ and a mass $m = m_e \times (N_e/N_p)$. Convergence must be checked as $N_p \to N_e$.

To summarize, our time-resolved photoemission experiment is modeled by initializing two electron packets associated to pump and probe photoelectrons. These (x, y, t) distributions are initialized according to pump and probe pulse parameters respectively: (x, y) dimensions are set equal to the focal spot sizes and their durations to the pulse durations. Pump electrons are set as "active particles": they produce and feel the space-charge electric fields. Probe particles are simulated as "passive particles": they do not contribute to the total electric field but experience the forces produced by pump ones. This effectively neglects any space-charge effect produced by the probe electrons and only simulates the pump-probe space-charge effect.

In the following, I will present the implementation of these three numerical tools to our specific case of study.

III.4 Numerical simulations: results and comparison to experimental measurements

This section will follow the same order as the precedent one: first, in subsection III.4.1, the initial pump spectrum calculations obtained with the Jellium-Volkov approximation will be presented. Subsection III.4.2 will present the laser-electron acceleration calculations.

The last part encompasses a set of space-charge simulations using ASTRA that can be grouped within three main cases regarding the principal contributions to the pump initial spectrum:

- Subsection III.4.3 tests the Jellium-Volkov approximation for the pump initial spectrum in space-charge simulations exploring different parameters
- Subsection III.4.4 assesses the influence of a laser accelerated pump spectrum (output from the SMILEI simulations) in space-charge simulations
- Subsection III.4.5 explores the possibility of an initial pump spectrum derived from the experimentally measured one in space-charge simulations

Finally, an overall summary and discussion will be presented in section III.4.6.

III.4.1 Jellium-Volkov Pump initial emission

Using the experimental parameters from the sample and the laser pulse listed on Table III.2, it has been possible to obtain, by means of the Jellium-Volkov approximation, the pump initial spectrum and its electron density. These calculations have been performed for different laser fluences. As reported in Figure III.4, these pump initial spectra exhibit a similar shape for all fluences: they present different "steps" separated exactly by the energy of one photon (1.55 eV), representing multiphoton processes of different orders. Such shape preservation is highlighted in Figure III.4 b), where all spectra are normalized. Furthermore, as observed experimentally the number of photoemitted electrons increases with the laser fluence.

These spectra will be used as input for the space-charge effect calculations with ASTRA as the initial pump spectrum. Specifically, the shape of all fluences has been assumed to follow the 460 J/m^2 spectrum. This is a reasonable assumption given that the main shape of all spectra corresponding to different fluences are similar, as seen in Figure III.4 b), and the main difference arises from the emitted density.

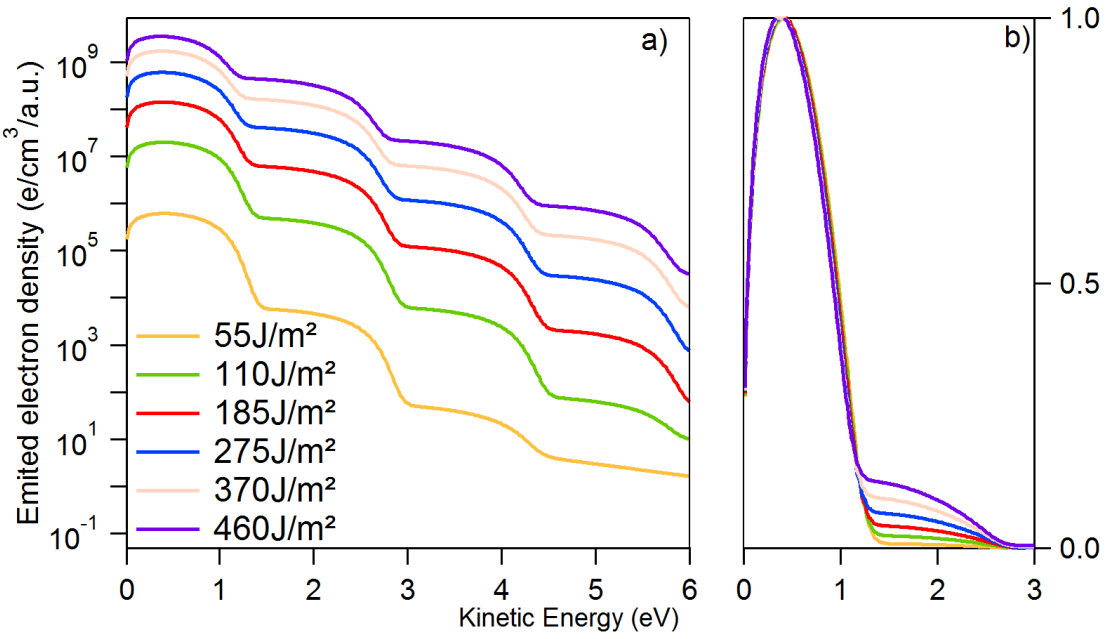

Fig. III.4 *(a) Emitted electron density as a function of the electron kinetic energy calculated with the Jellium-Volkov approximation for a Cu (111) surface. Each curve corresponds to a different laser fluence. (b) Normalized curves.*

In Fig. III.5, the total emitted electron density is reported as a function of the laser fluence. The calculations were performed also for fluences below the smallest experimental one.

An increase of the emitted electron density is observed with the fluence. This agrees qualitatively with the experimental observations from section III.2.

Sample: Cu (111) single crystal		Laser pulse	
Work function	4.94 eV	Angle of incidence	45°
Fermi energy	7 eV	Temporal profile	Gaussian
Skin depth δ_e ($h\nu = 1.55$ eV)	3.38 nm	τ_{FWHM}	25 fs

Table III.2: Experimental parameters used for the Jellium-Volkov calculations.

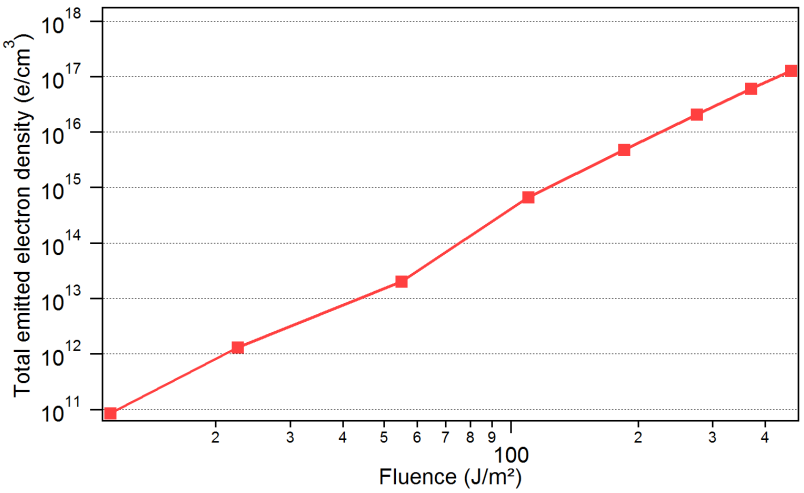

Fig. III.5 *Total emitted electron density upon laser irradiation as a function of laser fluence, calculated with the jellium-Volkov approximation*

III.4.2 SMILEI laser-plasma simulations

The simulations dealing with the laser-electron interactions have been done with SMILEI. The sample has been modeled assuming a plasma with fixed ions and initial electron density $n_e = 50 \times n_c$, with $n_c = 1.71 \times 10^{27}\mathrm{m}^{-3}$ for a laser wavelength of $\lambda = 800$ nm. This n_e corresponds to the density of free electrons in solid copper. The thickness of the sample has been set to 2.4 μm corresponding to 3 times the laser wavelength which is considerably larger than the laser skin depth δ_e.

The laser is on p-polarization state and arrives from the left (-x) at an angle of 45°. It is assumed to be a plane wave with the temporal shape depicted in Figure III.6. This profile is chosen because it allows to simplify the calculations. Even if this pulse duration is larger than the experimental one, we will see that most of the dynamics happen before the end of the pulse.

Three different laser intensities (I) were tested:

1. I $= 2 \times 10^{11}$ W/cm^2 corresponding to the experimental fluence of 55 J/m^2,
2. I $= 2 \times 10^{12}$ W/cm^2 corresponding to 500J/m^2, close to the maximal experimentally explored fluence, and
3. I $= 2 \times 10^{13}$ W/cm^2, to account for a possible intensity enhancement from roughness-induced point-like effects on the sample surface.

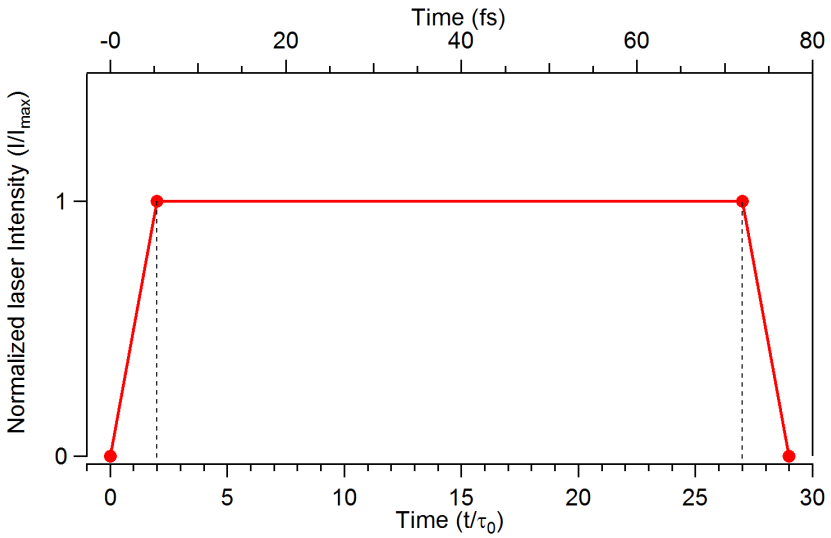

Fig. III.6 *Laser temporal profile used for the SMILEI simulations (see text)*

In order to observe the effect in the electron temperature, the initial T_0 has been set to a specific value for each of the three laser intensity cases: (1) $T_0 = 0.01$ eV for $I = 2 \times 10^{11}$ W/cm^2, (2) $T_0 = 0.1$ eV for $I = 2 \times 10^{12}$ W/cm^2 and (3) $T_0 = 1.0$ eV for $I = 2 \times 10^{13}$ W/cm^2.

A typical result illustrating the laser-induced electron acceleration is reported in Figure III.7 for the case (3). This phase-space representation (p_x, x) evidences an important electron acceleration towards the sample plane (positive p_x and x).

The acceleration of electrons from the sample can be observed in the phase-space plotting of p_x versus x in Figure III.7 for the case (3). The particles are mostly emitted towards the sample plane (positive p_x and x) and a smaller amount is emitted towards the vacuum. Experimentally, only the electrons escaping the sample can contribute to the space charge effect and eventually be detected, so we will restrict the analysis to those electrons.

Selecting these escaping electrons, their spectral evolution of the three different laser intensities is presented in Figure III.8. It evidences that the maximum energy is reached at $t = 24\tau$, which is followed by a decrease in their energy. This is related to the the effect of the positive ions exerting an attractive force on the electrons. This ion force is overestimated because on this PIC code there is no charge compensation as on a grounded conductor. Thus, for the purpose of our analysis, considering the spectra with the highest kinetic energies will suffice as a reasonable approximation.

In summary, SMILEI calculates the laser-electron interaction close to the sample at very short times after irradiation. The next step is to calculate the space-charge effect happening as electrons travel from the sample to the detector. For this purpose, the output from SMILEI is used as pump initial spectrum for ASTRA in section III.4.4.

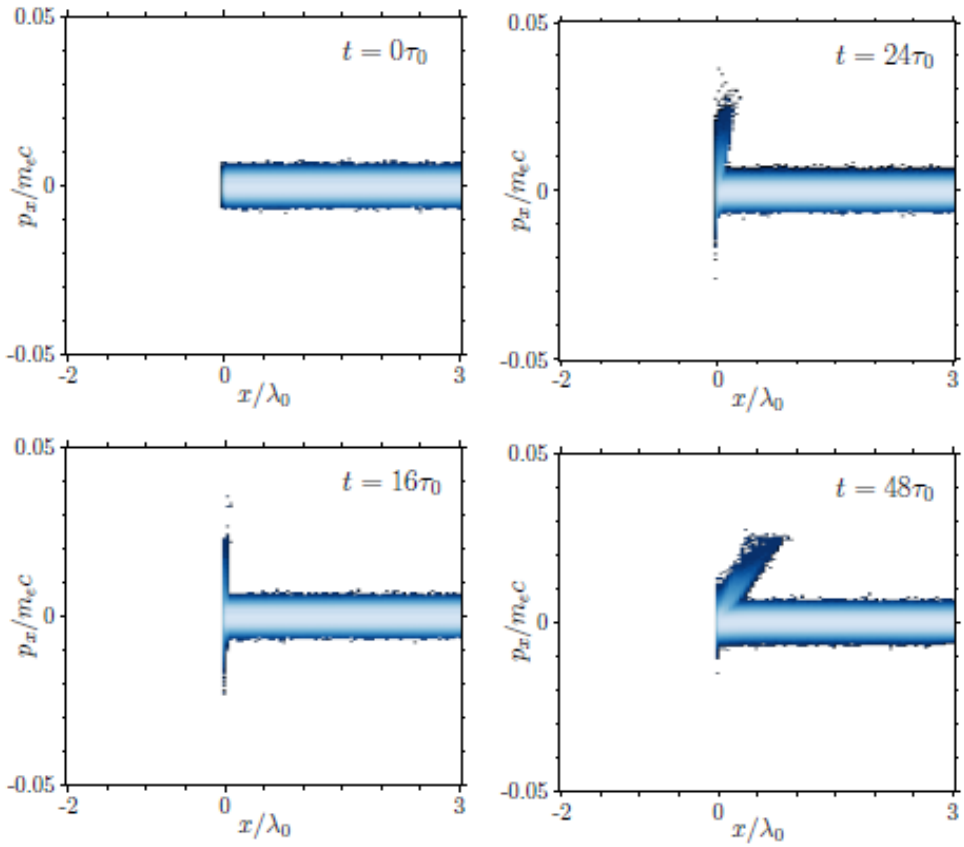

Fig. III.7 *Phase-space (p_x, x) plots at different times after laser irradiation for case (3) $I = 2{\times}10^{13}$ W/cm^2 and $T_0 = 1.0$ eV.*

III.4.3 Pump/probe Jellium-Volkov-ASTRA simulations

The jellium-Volkov calculations of the pump initial spectrum presented in section III.4.1 are now used as input for the space-charge calculations with ASTRA.

ASTRA has been initialized with two electron packets (for pump and probe clouds). I have developed a Matlab code that assigns specific values of position, time of emission and momenta to the particles and construct the initial distribution following the parameters described in Table III.3.

This code first creates the probability density functions for position, time (if using the cathode emission mode), total momentum (from the energy spectrum) and angle of emission and then assigns randomly, to each particle, a value within those probability functions.

In the following, the simulation is allowed to evolve up to an average particle position of $z = 1$ cm. Indeed, in the experiment the detector is positioned 10 cm away from the sample but it has been verified that, in our calculations, most of the Coulomb interactions happen before 1 cm. In consequence, running the simulations for longer distances would

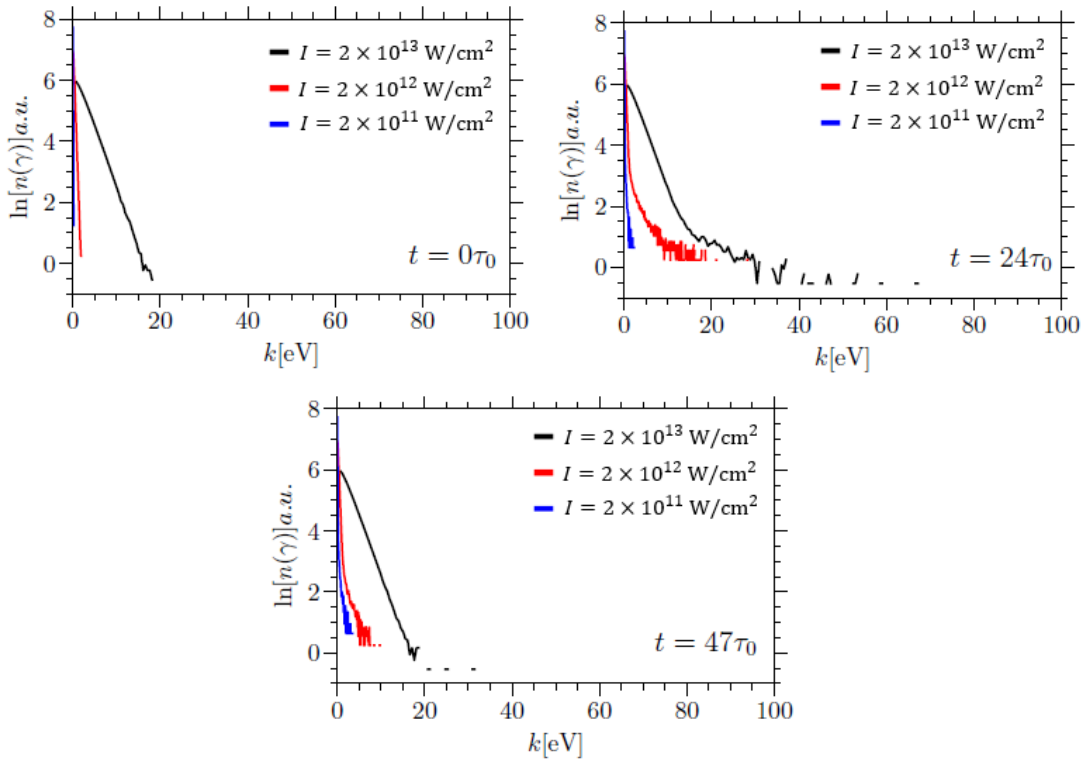

Fig. III.8 *Escaping electron spectra for the three explored intensities at $t = 0\tau$, 24τ and 47τ.*

not change the particle's momentum nor energy and would only increase drastically the calculation time.

The study below explores the influence of the different parameters listed in Table III.3. The first case presented in the next subsection makes use of reasonable assumptions for all these parameters while varying the total number of electrons N_{pump}.

Parameters	Model
(x,y) distribution	From measured focal spot: 2D Gaussian
z distribution/t cathode emission	Calculated distance/Measured laser τ
Energy spectrum	Jellium-Volkov calculation/Experimental measurement
Angle distribution	Assumed: Gaussian at 0° and FWHM=45°

Table III.3: Principal parameters for the ASTRA initial pump and probe distributions.

a) Standard simulation

For this first case, both pump and probe particle distributions have been assumed to follow the IR pump and XUV probe pulse focal spot spatial distributions as they are the

source of the photoemitted electrons.

The pump particle cloud uses a (x, y, z) distribution with a 15 nm Δz Gaussian distribution. Δz = 15 nm is estimated according to the distance traveled by an electron with energy E = 1 eV in 25 fs, which is close to the average kinetic energy (E = 0.7 eV) of the jellium-Volkov initial pump spectrum.

The probe electron cloud uses a (x, y, t) distribution following the probe pulse temporal distribution.

Table III.4 summarizes the corresponding values. The varying parameter is the total number of pump emitted electrons N_{pump} which is equivalent to the electronic emitted density that is expected to strongly depend on the laser fluence. N_{pump} was varied to cover the range of values predicted by the J-V calculations.

Parameter	Pump values	Probe values
(x,y) distribution	FWHM = 540 μm 2D Gaussian	FWHM = 250 μm 2D Gaussian
z or t distribution	Δz = 15 nm Gaussian	FWHM = 25 fs Gaussian
Energy spectrum	Jellium-Volkov calculation for 460J/m^2	Experimental cold measurement
Angle of emission	Gaussian at 0°, FWHM = 45°	Gaussian at 0°, FWHM = 45°

Table III.4: Principal parameter values for the ASTRA initial distributions in standard conditions.

The cases of including and neglecting mirror charges (MC) are explored: for the MC ON case, N_{pump} is varied by 4 orders of magnitude and by a factor of 2 for the MC OFF case. The output of the simulations is presented in Fig. III.9 in solid lines and compared to the experimental measurements in dotted lines.

The MC OFF case, for the two particle numbers explored, yields high pump kinetic energies (cutoffs at 35 eV and 62 eV) compatibles with the experimental results corresponding to 110 J/m^2 in terms of order of magnitude. The calculated spectral shapes do not have the structure observed experimentally.

Even if the calculated pump cutoff energies are compatible with the experiment, the probe calculated shift and broadening exceed considerably the experimental observations.

The MC ON case qualitatively reproduces both the pump cutoff energy and the probe shift and broadening for the very first experimental fluence (55 J/m^2), but not for the subsequent ones.

This case also evidences the important role of mirror charges (MC) in space-charge simulations. The attractive effect towards the sample strongly reduces the pump maximal kinetic energies. Even for the large range of investigated N_{pump} (from 10^6 to 10^{10}), the maximal kinetic energy reached is 17 eV. This is mainly due to the loss of an important number of pump particles that are attracted back to the sample. The effect of the loss of particles is particularly evident for large values of N_{pump} that leads to a slight reduction of the pump cutoff kinetic energies. This is observed for the largest N_{pump} case (N_{pump} = 5.27×10^{10}).

The probe spectra, for the MC ON case, is also sensitive to the mirror charges. The shift and broadening are compatible with the experimental observations but cannot reproduce the shift beyond the experimental curve corresponding to 185 J/m^2: a slight shift

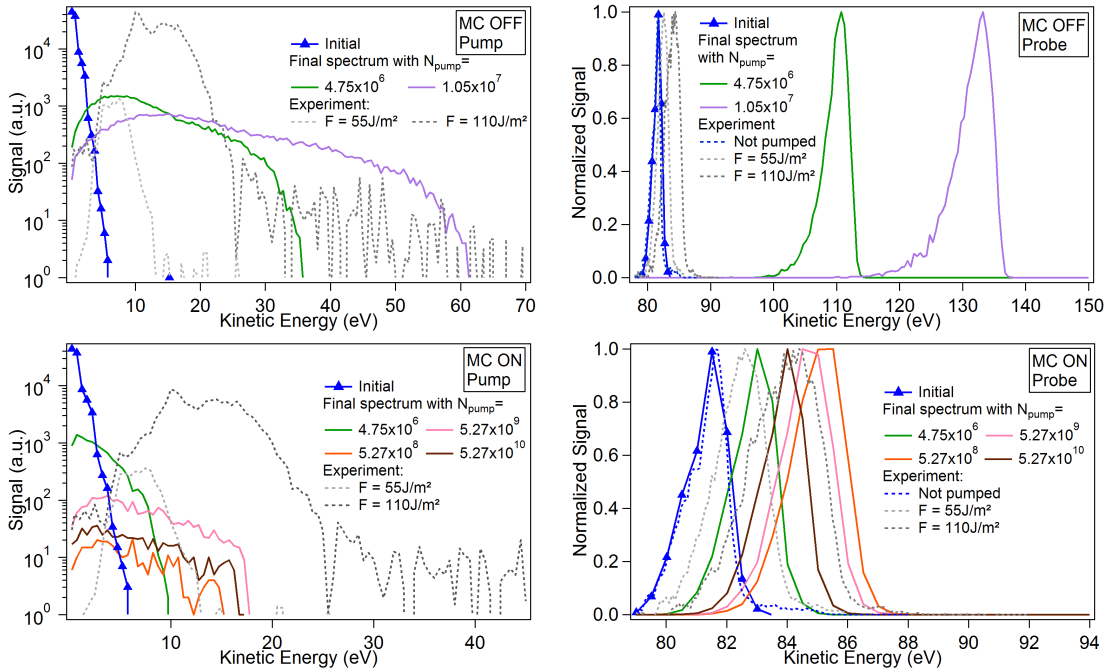

Fig. III.9 *Standard ASTRA simulation pump and probe spectra output for different numbers of pump electrons, N_{pump} compared to measured pump and probe spectra at $F = 55$ J/m^2 and 110 J/m^2. Upper panel: Mirror charges are off. Lower panel: Mirror charges are on.*

reduction is also observed.

In summary, both MC ON and MC OFF calculations yield pump spectra with a smooth shape, not corresponding to the experimetal findings. When observing the cutoff energies, the MC OFF case can reproduce the findings for the first two experimental fluences. However, when looking simultaneously at the pump cutoffs and probe spectral shape and broadening, the simulations do not agree with the experiment.

The MC ON case presents the opposite situation: the pump cutoffs are not reproducing the experimental observations (except for the very first fluence) whereas the probe shift and broadening are close to the measurements.

This lead us to test the validity of the standard case. The influence of different parameters is explored to understand their influence on the outputs and qualitatively reproduce our experimental results. In the following subsections this parametric study is presented.

b) Comparison of the (x, y, z) distribution with an (x, y, t) cathode emission distribution

First of all, the calculations presented as the "standard" case, where N_{pump} was varied, must be validated. Indeed, it should be noted that the jellium-Volkov approximation allows calculating the emitted electron density and not a total number of electrons. As

mentioned before, the number of electrons input was estimated through an electron packet volume approximation. The objective here is to check the validity of this estimation. For that purpose, I compared a pump longitudinal distribution (x, y, z) with a cathode temporal distribution (x, y, t). The probe electrons are always cathode emitted.

The first calculation uses a distribution with a 15 nm Δz Gaussian distribution. Δz = 15 nm is estimated according to the distance traveled by an electron with energy E = 1 eV in 25 fs, which is close to the average kinetic energy (E = 0.7 eV) of the jellium-Volkov initial pump spectrum. The second simulation uses the cathode emission option with a 25 fs Gaussian time distribution and the second one using an (x, y, z). Both simulations use the same $N_{pump} = 9.91\times10^6$ corresponding to a density of 2×10^{15} e/cm^3 (corresponding to the J-V calculated emission for ~ 110 J/m^2)

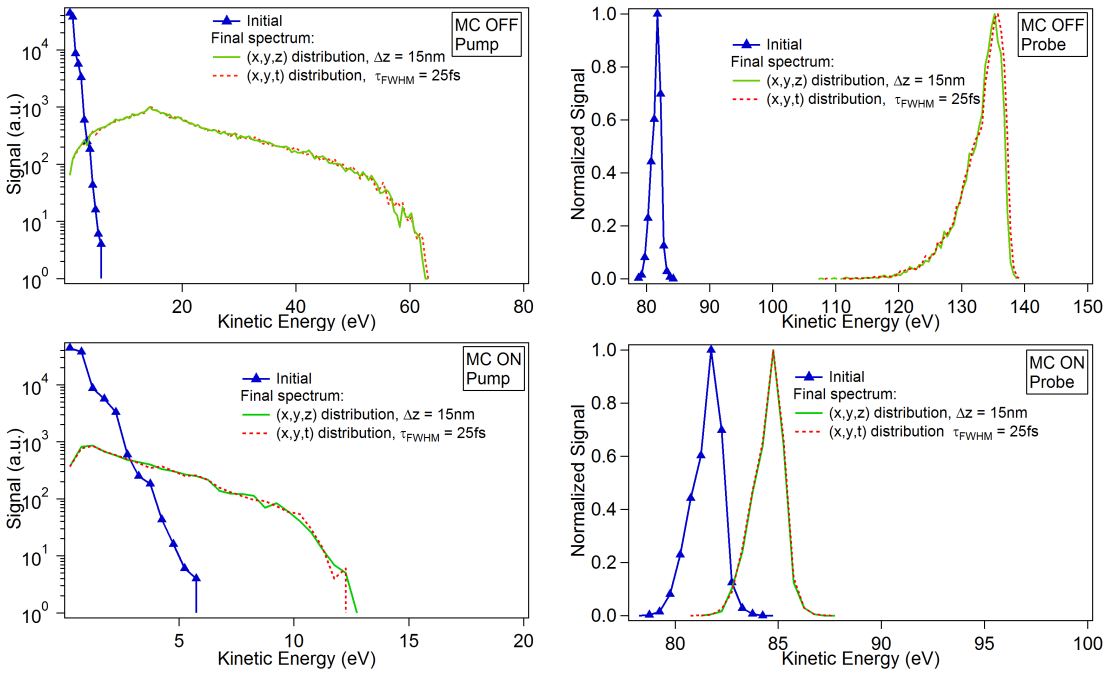

Fig. III.10 *ASTRA simulation pump and probe spectra outputs comparing a pump initial (x, y, z) longitudinal uniform distribution (Δz = 15 nm) with an (x, y, t) Gaussian temporal distribution for a cathode emission (τ_{FWHM}=25 fs). Both simulations use the same initial pump and probe spectra (blue curves) and the same N_{pump} (9.91×10^6). Upper panel: mirror charges are OFF. Lower panel: mirror charges are ON.*

The results of both simulations are reported in Fig. III.10. The MC OFF case yields, for both (x, y, z) and (x, y, t) simulations, basically the same pump and probe spectra. The probe spectrum of the temporal distribution is shifted only by 2 eV on a 50 eV total shift. The MC ON case also shows an almost identical result for the two cases on both pump and probe final spectra.

We can therefore conclude that the comparison between a temporal cathode emission

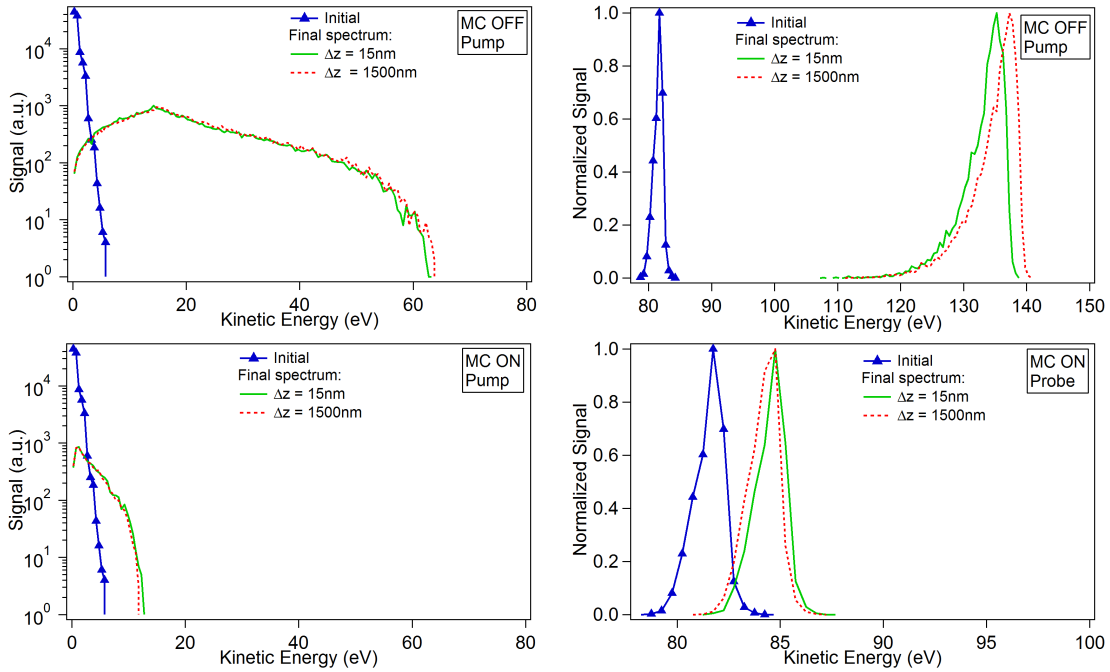

Fig. III.11 *ASTRA simulation pump and probe spectra outputs for different pump longitudinal sizes Δz of an uniform distribution (15 nm and 1500 nm) and constant N_{pump} (9.91×10^6). Upper panel: Mirror charges are off. Lower panel: Mirror charges are on.*

simulation and a longitudinal distribution one with an emitted electronic density is valid.

c) Number of electrons as the key parameter

With the intention of understanding the mechanisms of space-charge effect, it is reasonable to wonder if it is the number of electrons, rather than the electron density playing a role in the results. For this purpose, simulations were carried out using (x, y, z) distributions varying Δz while keeping constant the number of electrons N_{pump}: the electron density effect is explored.

The results are presented in Fig. III.11. Surprisingly, the effect of varying the size of the distributions i.e. the density, even by a factor of 100, is quite small. Both pump and probe spectra yield almost the same result for the two Δz values used.

A qualitative explanation for this result is due to the disk shape of the pump cloud: the transversal size (in the xy plane) is much larger than the longitudinal one ($\Delta z \ll \Delta x, \Delta y$). In this case, the electric field produced by the electron distribution resembles the well-known situation of a charged disk with surface charge density σ: $E_z = \sigma/2\epsilon_0$ in the z direction.

This equivalence while changing the electron density is further confirmed when looking at the electric field of the distributions in Fig. III.12. The z component of the electric field of the 15 nm and 1500 nm distribution simulations are presented at different radial

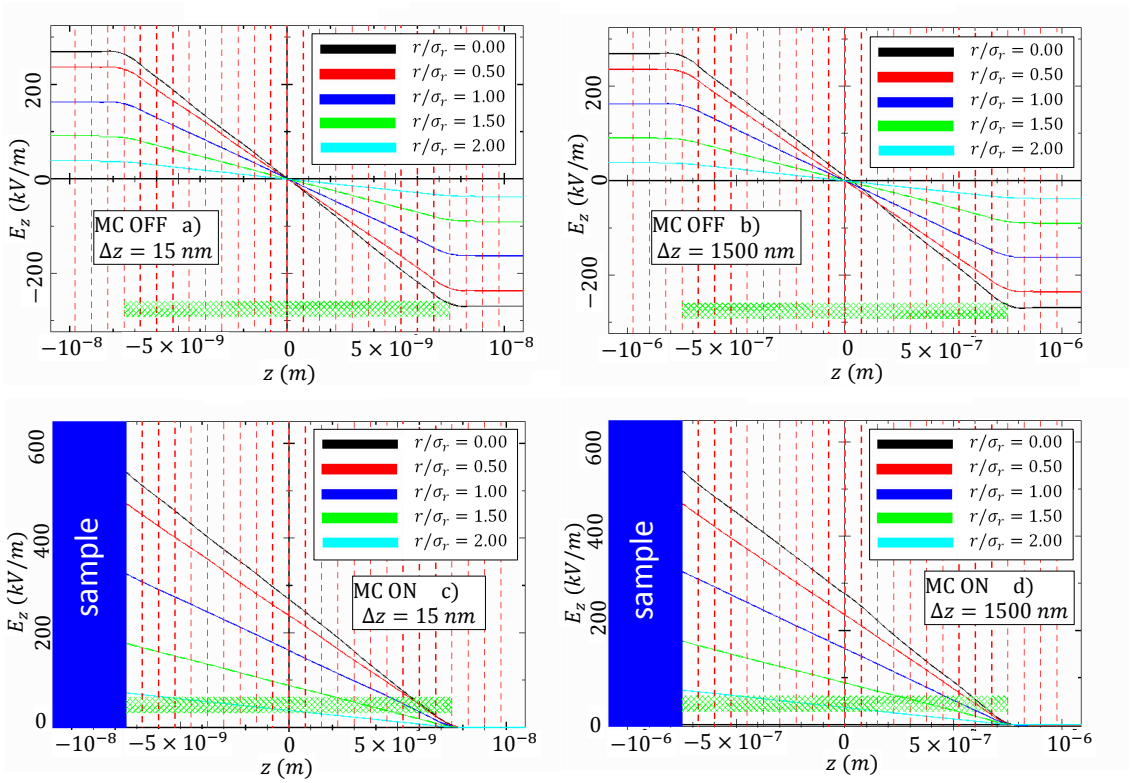

Fig. III.12 *Visualization of the longitudinal component of the distribution electric field lines for two uniform longitudinal distributions with MC OFF a) 15 nm and b) 1500 nm, and MC ON: c) 15 nm and d)1500 nm. The green dashed lines represent the particle distribution position whereas the solid blue slab represent the sample position (only for MC ON).*

positions, showing an almost identical electric field between the two Δz for both MC ON and MC OFF cases. This means that the surface charge distribution σ is the same for both $\Delta z = 15$ nm and 1500 nm. Thus, only σ determines the Coulomb interaction and not the volumetric charge density depending on Δz.

Hence, the space-charge effect is not sensitive to the electron density in our experimental case. Thus, the number of electrons is the key parameter as highlighted in the standard case.

d) Transversal size of the electron bunches

The (x,y) size of the transversal distributions was assumed to be equal to the experimental laser spot size in the standard case. However, a direct measurement of the area of emission is impossible. This assumption is here tested by evaluating the influence of this parameter.

According to the previous discussion, to evaluate the effect of the (x,y) size distribution, the number of electrons should be kept constant. In Figure III.13 this effect is investigated for 540 μm, 350 μm and 270 μm transversal spot sizes.

Reducing the spot size increases effectively the surface charge density σ and in con-

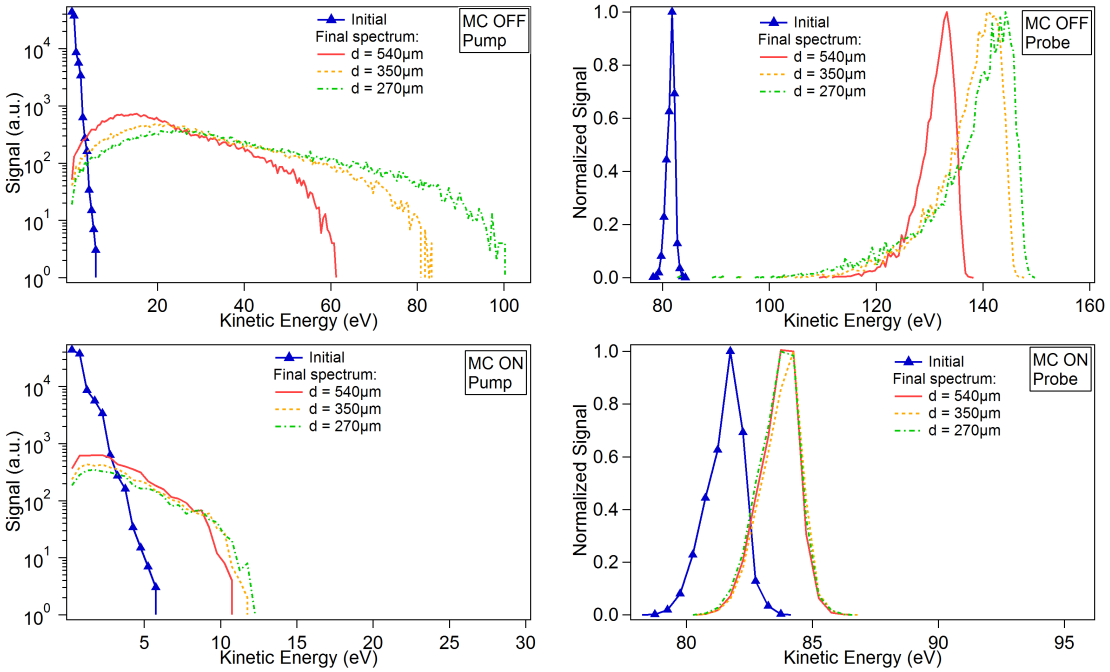

Fig. III.13 *ASTRA simulation pump and probe spectra output for three (x, y) Gaussian particle distributions with d(corresponding to the FWHM): 540 µm, 350 µm, and 270 µm. The size 540 µm corresponds to the measured focal spot usen in the standard simulation. The N_{pump} is kept constant Upper panel: mirror charges are off. Lower panel: mirror charges are on.*

sequence, the z component of the electric field. It is then expected that the space-charge effect is therefore increased with the surface density. Indeed, the MC OFF case shows an increase in the pump cutoff energies as the size decreases. This also correlates to the increase in probe shift and broadening.

On the contrary, including mirror charges (MC ON) balances the increase in the electric field from the disk of charge ($E_z = \sigma/2\epsilon_0$). The mirror field $E_z = -\sigma/2\epsilon_0$ can cancel it for small z distances, yielding three almost identical results for both pump and probe outputs.

One conclusion is that if MC must be excluded, then the choice of the (x,y) spot size is crucial, as the output is very sensitive to it. But, if MC are included, the transversal size is not a key parameter anymore. In any case, even if the assumed (x,y) spot size of the standard case is not correct, this approximation cannot explain the calculation/experiment difference in the standard case, since the same diagreement is observed: both pump and probe results cannot be reproduced at the same time.

e) Angular distribution

As it was mentioned in the presentation of the Jellium-Volkov approximation, it is possible to calculate the photoemission probability as a function of the angle and energy of the photoelectrons. But it is reasonnable to test the influence of the angular distribution influence since no angular measurement was performed during the experiment.

The effect of the angle of emission distribution is explored for different Gaussian widths, all centered at 0° with respect to the sample normal axis and compared to an isotropic emission distribution. Results are reported in Fig. III.14.

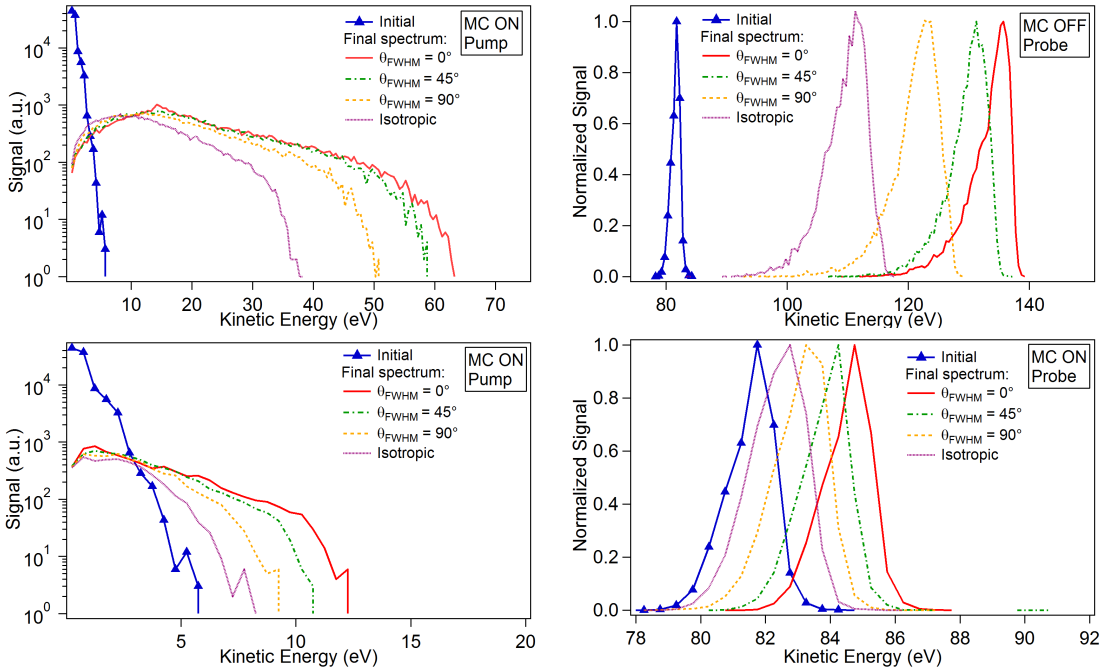

Fig. III.14 *ASTRA simulation pump and probe spectra output for different Gaussian angular distributions with different FWHM and an isotropic distribution. The N_{pump} is kept constant. Upper panel: mirror charges off. Lower panel: mirror charges on.*

The effect of the angle of emission is evident. For both MC OFF and ON cases, a reduced pump electron bunch divergence allows a more efficient energy and momenta transfer reaching higher kinetic energies in both pump and probe. However, this variation cannot explain the calculation/experiment disagreement observed in the standard case.

f) Sorting of particles

Neither from the jellium-Volkov model nor from the experimental measurements, it's possible to know if there is a preferential ordering of the particles. So far in the presented cases, the particles have a randomly assigned position, time, and angle of emission. Here we test two preferential orders:

The first case investigates whether energy and time are correlated. A reasonable assumption would be that the most energetic electrons are emitted when the laser pulse

electric field magnitude is at its maximum (at the center of the pulse).

The second case tests if the energy and transversal position are correlated. Again, it could be expected that the most energetic electrons are emitted at the position where the laser intensity is at its maximum, which corresponds to the center of the laser focal spot.

f).1 Energy and time (or longitudinal)

Using a temporal distribution corresponding to a 25 fs (FWHM) Gaussian function three cases were considered: the most energetic particles leaving at the center of the emission, compared to two extrema situations where the particles are emitted at the beginning or at the end of the laser pulse. In Fig. III.15, the three results are presented along with a case where time and energy are randomly assigned.

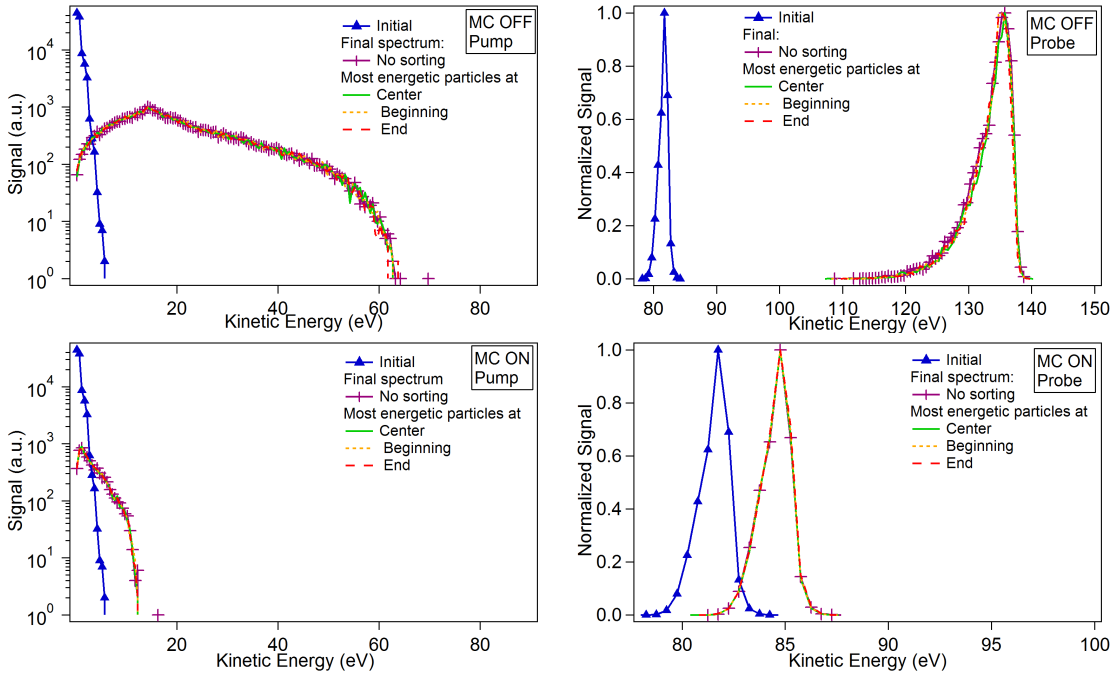

Fig. III.15 *ASTRA simulation pump and probe spectra output for different temporal sorting of particles: most energetic particles leave at the beginning, center or end of the electron bunch. Upper panel: mirror charges are off. Lower panel: mirror charges are on.*

Both simulations MC ON and OFF present no difference between the three considered cases. Such result can be explained by the disk-like shape of the pump electron cloud.

It is possible that the ordering of particles in time and energy don't play a role given that the particles interact mainly as a charged bi-dimensional disk. The initial spectrum reaches up to 6 eV in kinetic energy and the electric field strengths are on the order of kV/m, hence, the kinetic energies of the electrons don't play a significant role.

f).2 Energy and (x, y) transversal position

This particular test evaluates the hypothesis of a preferential ordering of the particles in the laser spot distribution: the most energetic particles probably leave from the center

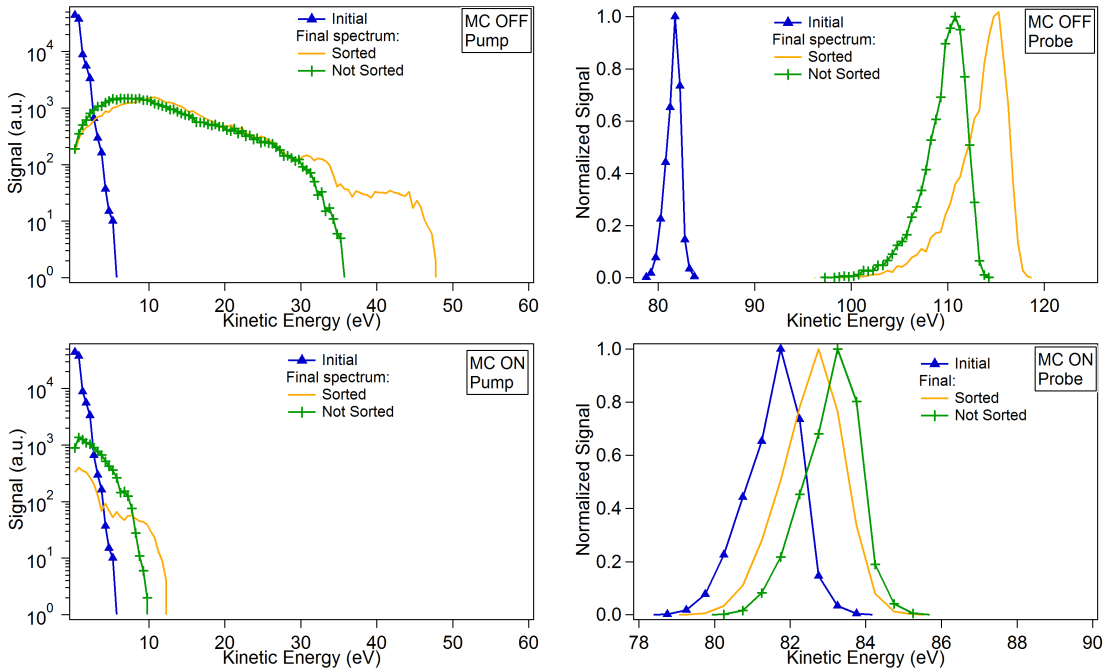

Fig. III.16 *ASTRA simulation pump and probe spectra outputs for sorted and not sorted particles in energy and (x, y) positions. Upper panel: mirror charges are off. Lower panel: mirror charges are on.*

of the spot, where the laser intensity has its maximum.

As seen in the Fig. III.16, for the MC OFF case, an ordering leads to a more structured final shape of the pump spectrum and to a higher cutoff energy, compared to the smooth random spectrum. The probe spectrum presents a larger shift and broadening for the ordered particles. This more structured pump spectrum – compatible with the experimental observations, is thus not associated to a closer agreement with our probe measurements.

On the contrary, the MC ON situation presents, again, a more structured pump spectrum reaching slightly higher kinetic energies and a less shifted probe spectrum than the non-sorted case. This could be a step in the correct direction in terms of shape, as some structures are preserved, nonetheless, the pump kinetic energies are not close to the experimental ones.

These two tests show that sorting the particles do not lead to a better calculation-experiment agreement. And, since no experimental nor theoretical evidence suggest a sorting of any kind, the hypothesis is abandoned.

g) Delay on the mirror charges

From the parameters explored so far, effect of mirror charges is the most important one. Our experimental conditions i.e., photoemission from a metallic surface, suggest that

mirror charges (MC) should be included in the calculations. However, by doing so, the pump photoelectron spectra do not reach neither the observed kinetic cutoff energies, nor the general shape is reproduced. On the other hand, not including them allow for a much more effective Coulomb explosion leading to the experimental pump kinetic energies, but the probe spectrum is shifted and broadened beyond the experimental values. An intermediate situation might be suggested from these observations: applying a delay in starting the MC. In this way, the particle Coulomb interactions can evolve free from the MC attractive electric field for a certain period of time. The delay for turning on the mirror charges was chosen in the order of picoseconds. It is estimated by assuming that the time for establishing the electron distribution at the sample surface is related to the velocity of electrons inside the metal under the influence of the external electric field (from the pump photoelectrons).

The drift velocity inside a metal with an applied electric field E, is $v_d = eE\tau/m_e$, where m_e is the electron mass, e the electron charge and τ the electron scattering time. Using $E = 200 \times 10^3$ V/m (see Fig. III.12), and a skin depth of $\delta_e = 3.4$ nm (see Table III.2), the time for an electron to travel δ_e is $t = \delta_e/v_d \simeq 6$ ps.

Using three different numbers of emitted electrons, the simulations were carried out turning on the mirror charges after a certain time in this order of magnitude. The objective is to compare to the experimental results assuming that the MC ON delay time could vary for each fluence. Fig.III.17 presents three cases with different N_{pump}.

The first case ($N_{pump} = 1.05\times10^7$) allows to describe the probe shift and broadening for low fluences with a modest agreement with the pump cutoff energies. Also, the whole range of probe shifts can be reached. But when describing the measurements at high fluences, the probe broadening is larger than the measurement and the pump spectrum cutoff reaches 25 eV, far away from the 100 eV experimental values.

The second case, having a larger number of electrons ($N_{pump} = 2.64\times10^7$) also reproduces the probe shift but the pump cutoff kinetic energy is not reproduced at the same time.

The last case ($N_{pump} = 5.27\times10^7$) increases the number of electrons. It shows that the probe shift is still easily reproduced but is already too broadened. The pump spectrum does not reach the expected energies.

The first two cases allow to obtain probe spectra that agree with the experimental measurements, specially at low fluences. Nonetheless, matching both pump cutoff and probe modifications are still not reached above 55 J/m^2.

The strategy of delaying the mirror charges is not further pursued.

I have presented the exploration of different parameters in the simulations. So far, certain parameters have been assessed as more important than others. For example, the key parameter is the N_{pump}, and not the density. Nonetheless, except for the first experimental fluence (55 J/m^2), reaching a close agreement between the simulations and the experiment has not been achieved. Evidently, the interaction between pump and probe electrons is quite complex. In the next section I will present a simplified case aimed to gain understanding of the mechanism.

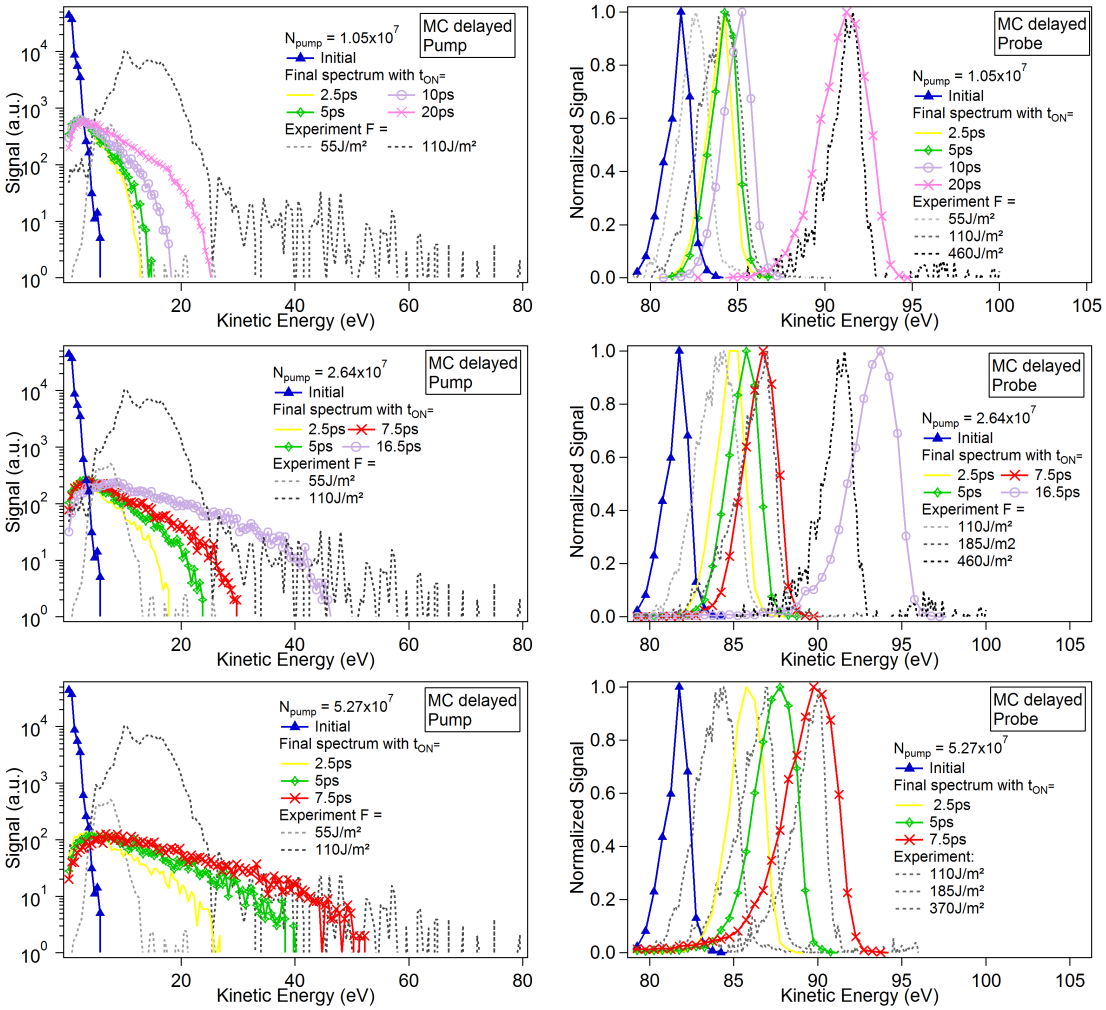

Fig. III.17 *ASTRA simulation pump and probe spectra outputs including a delay for turning on the mirror charges for three different number of electrons: upper panel* $N_{pump} = 1.05\times10^7$, *middle panel* $N_{pump} = 2.64\times10^7$, *lower panel* $N_{pump} = 5.27\times10^7$

h) Analyzing shift and broadening

To correlate the pump and probe interaction a simplified simulation was carried out. The Jellium-Volkov spectrum was used as the initial pump spectrum and mirror charges were turned off. As in all of the presented simulations, the probe electrons leave 15 ps after the pump ones.

The particle positions at different times after the pump emission are presented in Fig. III.18. In Fig. III.19 is presented the evolution of the corresponding pump cutoff energy and probe shift and broadening as a function of time. As before, pump particles are emitted at t = 0 ps whereas probe particles leave the sample at t = 15 ps.

The pump and probe evolution in Fig. III.18 shows the probe bunch (blue) leaving after the pump (red) has already traveled and expanded for 15 ps. The probe electrons

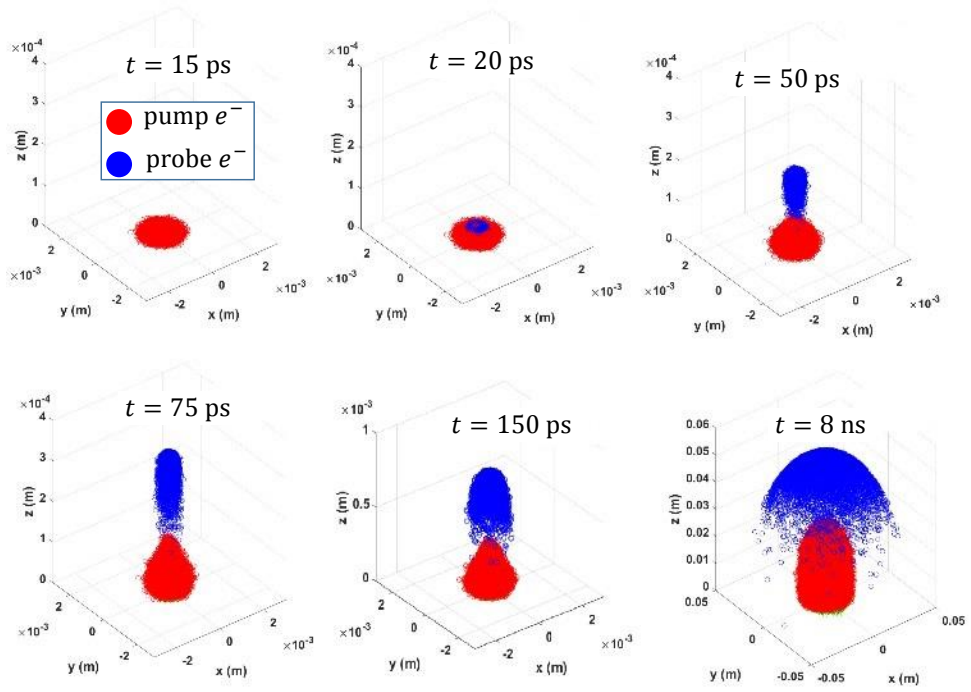

Fig. III.18 *ASTRA simulation pump and probe particle distribution at different times. The input Jellium-Volkov calculated pump spectrum is used. Mirror charges are off*

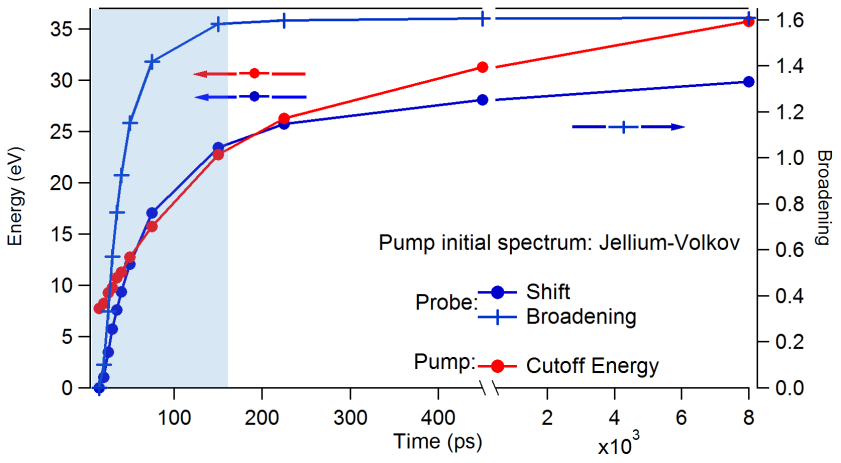

Fig. III.19 *ASTRA simulation outputs: pump cutoff energy and probe shift and broadening as a function of time. The colored area represents the time pump and probe electrons travel together. The Jellium-Volkov calculated pump spectrum is used. Mirror charges are off.*

are, for a brief period of time, behind the pump electrons (between 15 and 20 ps). Since the pump electrons are slower than the probe ones, the latter catch up around t = 20 ps, and, both bunches travel together up to ∼ 150 ps. Finally, the probe bunch leaves the pump behind.

The evolution of the probe spectrum, shown in III.19 is related to the presence of the pump electrons. While both pump and probe travel together (colored blue area) the probe becomes broadened and shifted. After the probe leaves behind the pump and is sufficiently far away (happening ∼150 ps), the increase in shift and broadening stops to remain almost constant for the rest of the simulation.

It is evident that the close presence of pump electrons distorts the probe spectrum. While they travel together they interact. And, the time that both pump and probe electrons remain close to each other depend on their kinetic energies, i.e. their initial spectra. So far, this parameter has not been explored. In the next subsections, (III.4.4 and III.4.5), the effect of using different initial pump spectra, deduced from different considerations will be adressed.

III.4.4 Pump/probe SMILEI-ASTRA simulations

The previous subsection, where the initial pump spectrum calculated with the Jellium-Volkov approximation was used as input for ASTRA, has shown that the parameters explored do not yield significantly different pump and probe spectra.

This section explores the possibility of aditional components in the pump spectrum. Indeed, higher kinetic energies of the pump initial spectrum could lead to larger cutoff energies and sufficient probe shifts and broadenings.

This section explore the use of the pump initial spectrum calculated with the SMILEI code, assuming the possibility of laser acceleration of the photoelectrons.

The calculated SMILEI spectrum with the highest kinetic energies, corresponding to the case where $I = 2 \times 10^{13}$ W/cm^2 and $T_0 = 1.0$ eV at time t = 24 τ_0 (Figure III.8 e)) is here used as reference for a parametric study. The intensity corresponds to a fluence of 5000 J/m^2 which is larger than the experimental fluences. This takes into account a possible laser field enhancement by point-like effects on the surface of the sample.

The mentioned SMILEI spectrum has been fitted with the sum of two exponentially decaying functions accounting for two electronic populations with different temperatures: the first one with high amplitude and decreasing rapidly (low temperature electrons: T_{Low}) and the second one with low amplitude and a slower decay (high temperature electrons: T_{High}). Then, while keeping the ASTRA simulation parameters constant, the initial spectrum described by both populations has been varied. Especifically we varied the slopes (corresponding to T_{Low} and T_{High}) of the two populations, the ratio between the two populations (corresponding to the number of electrons) and the extension of the kinetic energy range of both populations. For this parametric study, the total number of electrons has been kept constant for all the simulations.

The probe broadening reported in this section corresponds to the standard deviation difference between initial and final spectra. The shift is calculated with respect to the high energy edge at half the maximum height of the spectrum.

I aimed here to reproduce the experimental measurements at a fluence of 370 J/m^2, so all the figures in this section show the experimental pump and probe spectrum corresponding to this fluence. It was assumed that if the calculation results were comparable with the experimental findings for this fluence, the rest of the series would also be reproducible.

a) Varying the low temperature (T_{Low})

First, the effect of varying the slope of the T_{Low} population is explored. This corresponds to a variation of its temperature as indicated in Figure III.20 a). Figures III.20 b) and c) show the output probe and pump spectra respectively.

The effect of varying the T_{Low} component of the pump spectrum and its final cutoff energy is very small. The cutoff remains close to 55 eV. It is probably more related to the T_{High} electrons.

The effect on both shift and broadening on the probe electrons is computed and shown in Figure III.20 c). This qualitative representation evidences the T_{Low} slight influence on the probe output: shift and broadening reach a minimum at $T_{Low} = 2.2$ eV before increasing slowly and steadily. Note that in these simulations, the broadening is always greater than the experimental one.

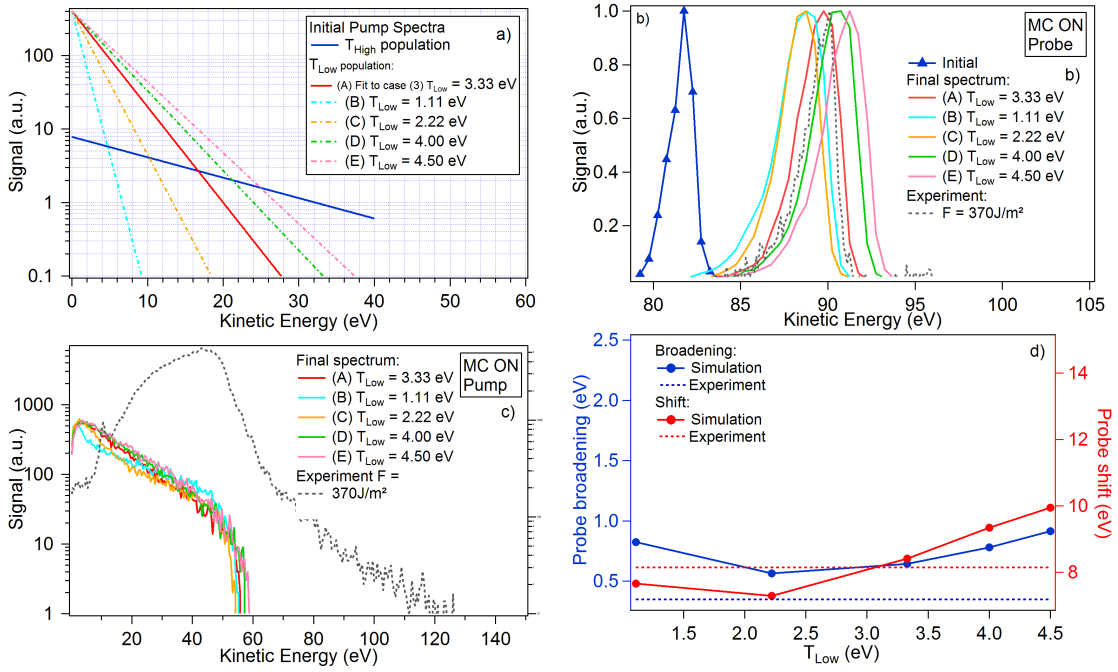

Fig. III.20 *ASTRA simulations using the SMILEI calculated pump spectrum. a) Initial pump spectrum with varying T_{Low}; b) Final probe spectra; c) Final pump spectra; d) computed values from b) for shift and broadening. Mirror charges are on.*

b) Varying the high T temperature (T_{High})

The second parameter varied was the temperature of the T_{High} population. Figure III.21 presents the initial populations and the results of the simulations. The effect on the pump spectral shape and cutoff energies is larger than the effect of T_{Low} but is still far away from the experimental kinetic energies (∼130 eV) as seen in Figure III.21 c). The effect on both shift and broadening of the probe spectra is an increase with the temperature in such a way that matching both quantities with the experimental values is not possible.

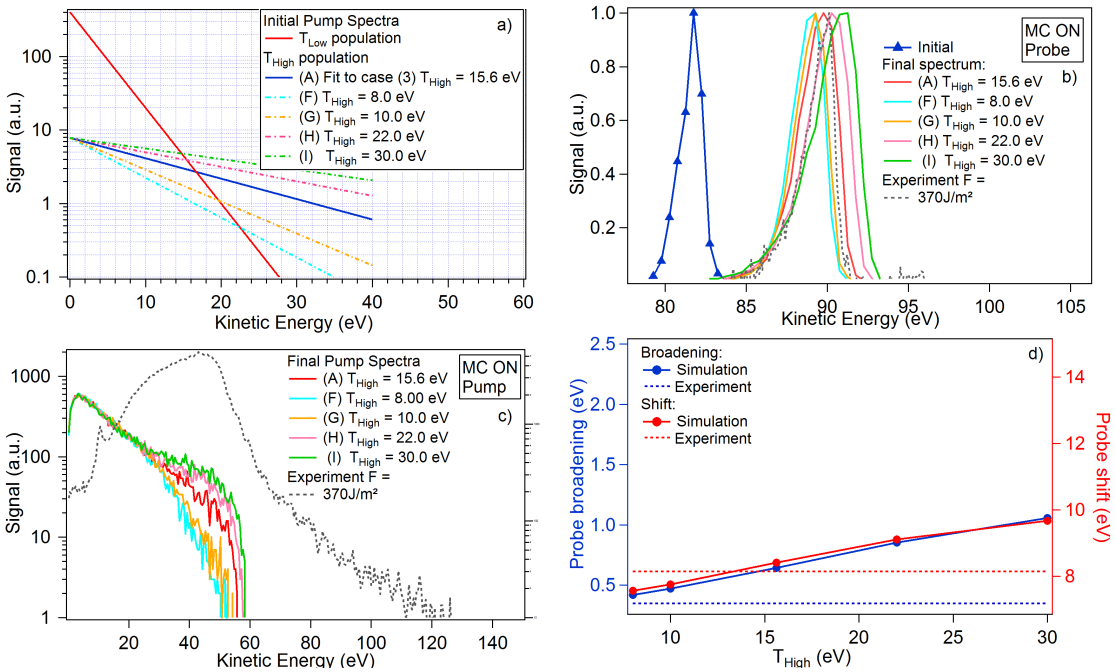

Fig. III.21 *ASTRA simulations using the SMILEI calculated pump spectrum. a) Initial pump spectrum with varying T_{High}; b) Final probe spectra; c) Final pump spectra; d) computed values from b) for shift and broadening. Mirror charges are on.*

c) Varying proportion between T_{High} and T_{Low} populations

The effect of varying the proportion between the number of electrons in the two populations is explored. As expected from the observations in section III.4.3 h) the high kinetic energy electrons travel close and for a long time with the probe ones. In consequence increasing the number of these electrons increases the probe shift and broadening as evidenced in Figure III.22 b)and d). These effects are so large that they tend to go far away from the experimental values.

In addition, it should be mentioned that an increase in the number of T_{High} electrons is unlikely to happen since the initial electronic temperatures in the SMILEI simulation had no effect on the T_{High} electrons.

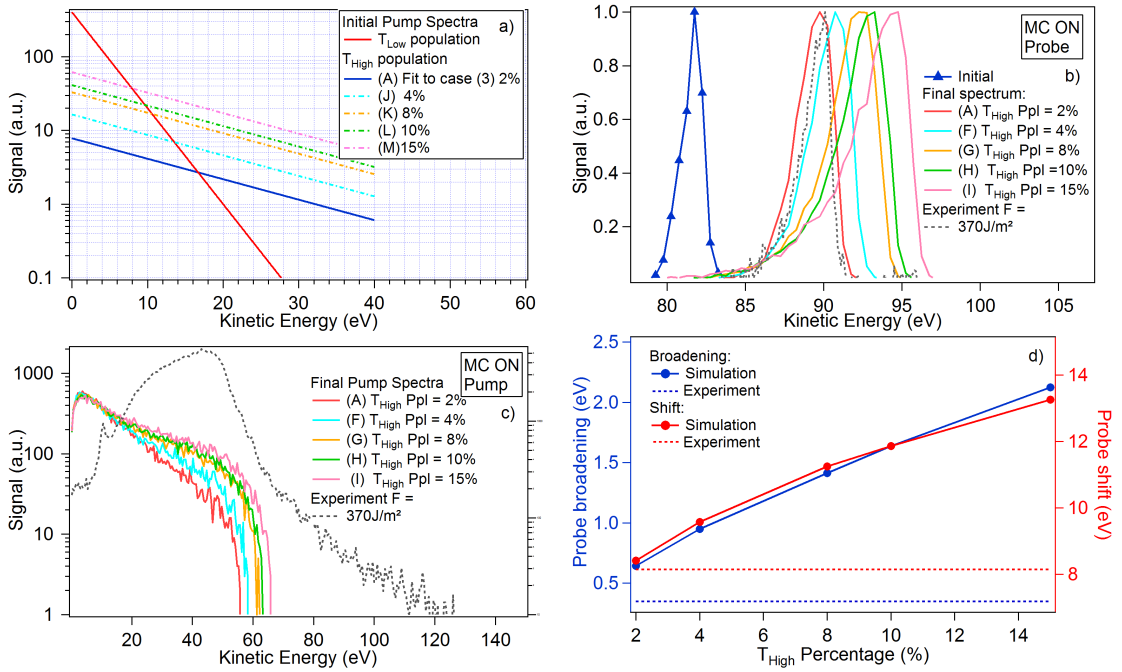

Fig. III.22 *ASTRA simulations using the SMILEI calculated pump spectrum. a) Initial pump spectrum with varying the proportion between the two populations; b) Final probe spectra; c) Final pump spectra; d) computed values from b) for shift and broadening. Mirror charges are on.*

d) Varying the cutoff of the initial pump spectrum

Finally, the cutoff of the initial pump spectrum is varied from 40 eV to 120 eV. We assume an underestimation of the laser-induced acceleration by SMILEI. This could be justified by the fact that SMILEI uses a small number of simulating particles. By including more particles in the simulation following a Maxwellian distribution of energies, the number of particles at higher kinetic energies would also increase.

As seen in Figure III.23 b), c) and d), the main effect of extending the initial cutoff is a pump final cutoff increase whereas the overal shape of both pump and probe final spectra remain unchanged. This can suggest that some electrons can gain high kinetic energies but in such a low number that they do not contribute significantly to the space-charge dynamics. It could explain the experimentally observed cutoffs and the somehow modest probe shifts and broadenings.

As mentioned before, from the previously explored parameters it has not been possible to quantitatively reproduce the experimental pump and probe spectra, especially the pump overall shape and for fluences above 55 J/m^2. Now with the inclusion of a spectrum taking into account the possibility of laser-acceleration of electrons, the pump cutoff and probe spectrum measurements at 370 J/m^2 were reached. This is a lead in the right direction. But the calculated pump spectral shape do not show the structures observed experimentally.

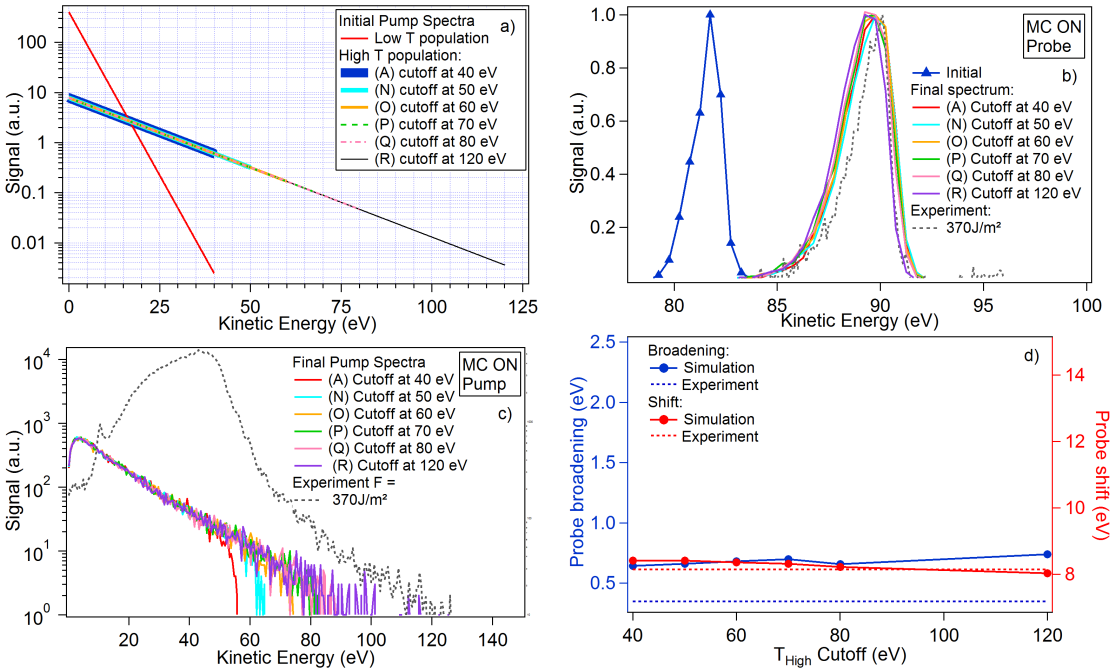

Fig. III.23 *ASTRA simulations using the SMILEI calculated pump spectrum. a) Initial pump spectrum varying the cutoff; b) Final probe spectra; c) Final pump spectra; d) computed values from b) for shift and broadening. Mirror charges are on.*

We have learned that the caluclated pump and probe spectra are especially sensitive to the pump initial spectrum. Next section will continue exploring the space-charge effect varying this parameter.

III.4.5 Pump/probe experimental pump-ASTRA simulations

In this section I will explore the use of different pump initial spectra derived from the experimental measurements, testing two hypothesis:

- The first hypothesis is that pump initial spectrum resembles the measured one at low fluence (55 J/m^2). It is then expected that the spectra measured at higher fluences is the result of the space-charge interaction of this "low fluence" spectrum.
- The second test is an extreme situation opposite to the idea of an initial jellium-Volkov spectrum expanding due to space-charge. It assumes that there is no space-charge among the pump electrons so that the pump initial spectra is equal to the measured spectra for all fluences. Thus, we will try to preserve the overall shape of the pump spectra while observing the changes in the probe spectra.

a) Gaussian fits from the experimental spectrum

For this first test, a Gaussian fit of the 55 J/m^2 pump spectrum is used, assuming that for this fluence the Coulomb explosion is sufficiently weak to partly preserve the spectral

shape and kinetic energies. The Gaussian initial spectrum is reduced in width, expecting that the space-charge effect is at the origin of the broadening. For all the different fluence cases it is assumed that this Gaussian spectrum is qualitatively representative of the initial pump emission.

Three series of simulations were performed using three different central energies E_0 for the Gaussian initial spectrum. The idea behind the variation of E_0 is to test the posibility of varying the influence of the attractive mirror charges. It is expected that, as the electrons are more energetic they will escape more easily the attractive forces. By doing so, higher pump cutoff energies could be reached. For these simulations, mirror charges are always on.

As seen in Fig. III.24, the less energetic initial spectrum (upper panel) leads to smaller final pump cutoff kinetic energies. A saturation effect is observed with respect to the number of electrons in the first two cases: both pump and probe spectra reach a maximum shift and broadening around $N_{pump} = 4.74 \times 10^6$ for the $E_0 = 4.0$ eV case (upper panel), and $N_{pump} = 1.05 \times 10^6$ for the $E_0 = 5.2$ eV case (middle panel). As the initial kinetic energy is increased, the saturation point is reached at higher kinetic energies. For the $E_0 = 6.84$ eV (lower panel) case, the probe spectrum can reach the maximum measured shift. In this case, the 55 J/m^2 pump and probe measurements can be reproduced. For higher N_{pump} the experimental measurements and calculations do not match: the probe is getting too broadened whereas the pump does not reach the measured energies.

Higher central energies E_0 were not tried because, based the jellium-Volkov calculations, electron kinetic energies beyond 6 eV are not expected for the experimental laser fluences. The following subsection will test the hypothesis of higher kinetic energies.

Based on these observations, a qualitative interpretation can be drawn. An increase of the initial kinetic energy of the pump photoelectrons facilitates their escape from the attractive mirror charge field leading to higher cutoff energies and larger probe shifts. This approach is sufficient to describe the measurements at the lowest fluence (55 J/m^2) but fails at higher fluences.

b) Experimental spectrum

It seems that, for fluences beyond 55 J/m^2 it is not possible to obtain the experimental cutoff and shapes of the pump photoelectron spectrum using the Gaussian fit proposed in the precedent section.

With this in mind, new calculations were done using as input the experimentally measured final spectrum. We test an extreme hypothesis, that the pump electrons are measured as emitted from the sample. They would not undergo any distortion due to space-charge effect.

The results corresponding to this assumption are presented in Fig. III.25. For the first three fluences (55, 110 and 185 J/m^2), a relative close agreement for pump and probe is attained: the shape of the initial pump spectrum is somewhat preserved with only a small broadening and a slight increase in the cutoff kinetic energies whereas the probe spectrum shift and broadening are compatible with the experimental observations. This corresponds well to the hypothesis that the final pump spectrum should be equal to the

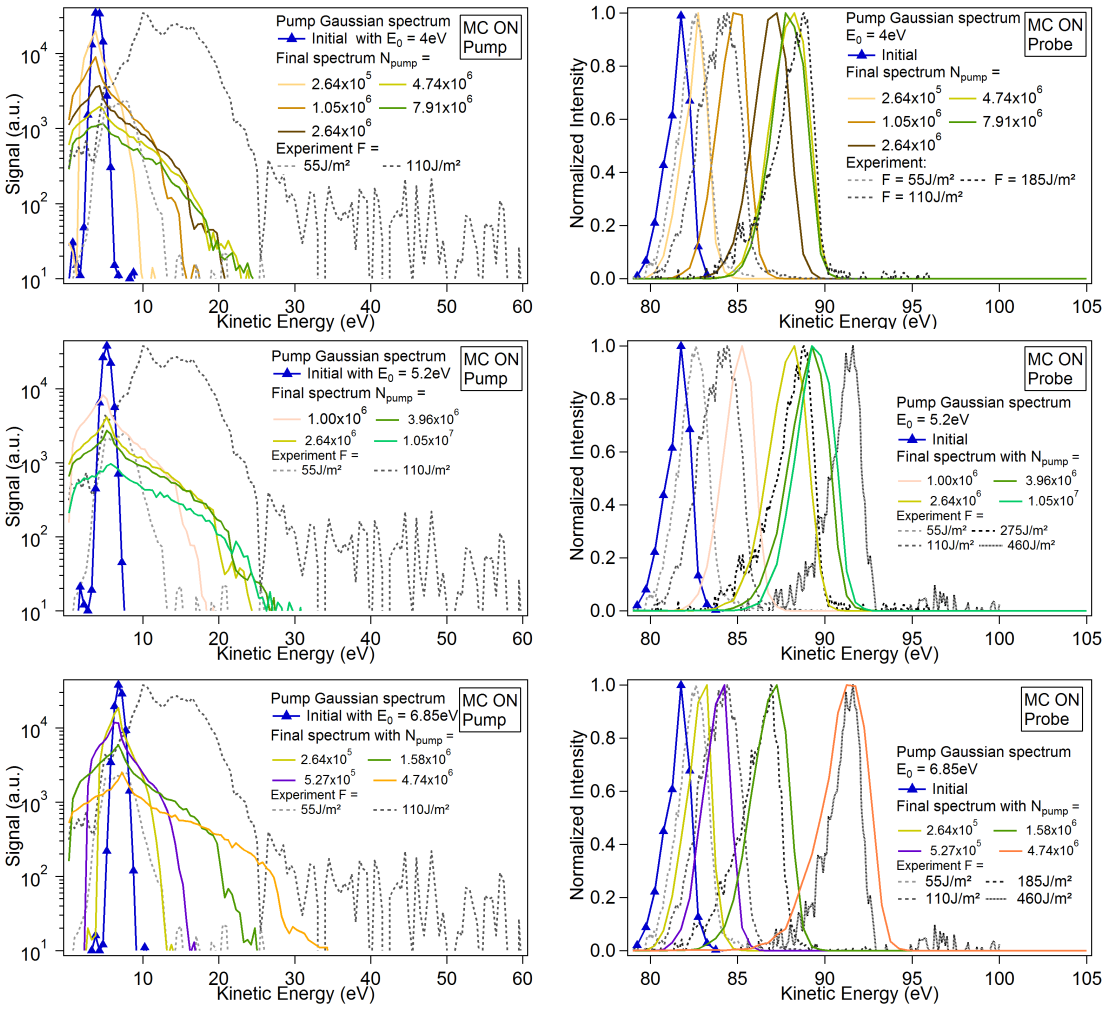

Fig. III.24 . *ASTRA simulation pump and probe spectra output for different initial spectra Gaussian distributions of fixed width 1.78 eV and different central energy: upper panel $E_0 = 4$ eV, middle panel $E_0 = 5.2$ eV, lower panel $E_0 = 6.85$ eV. Mirror charges are on.*

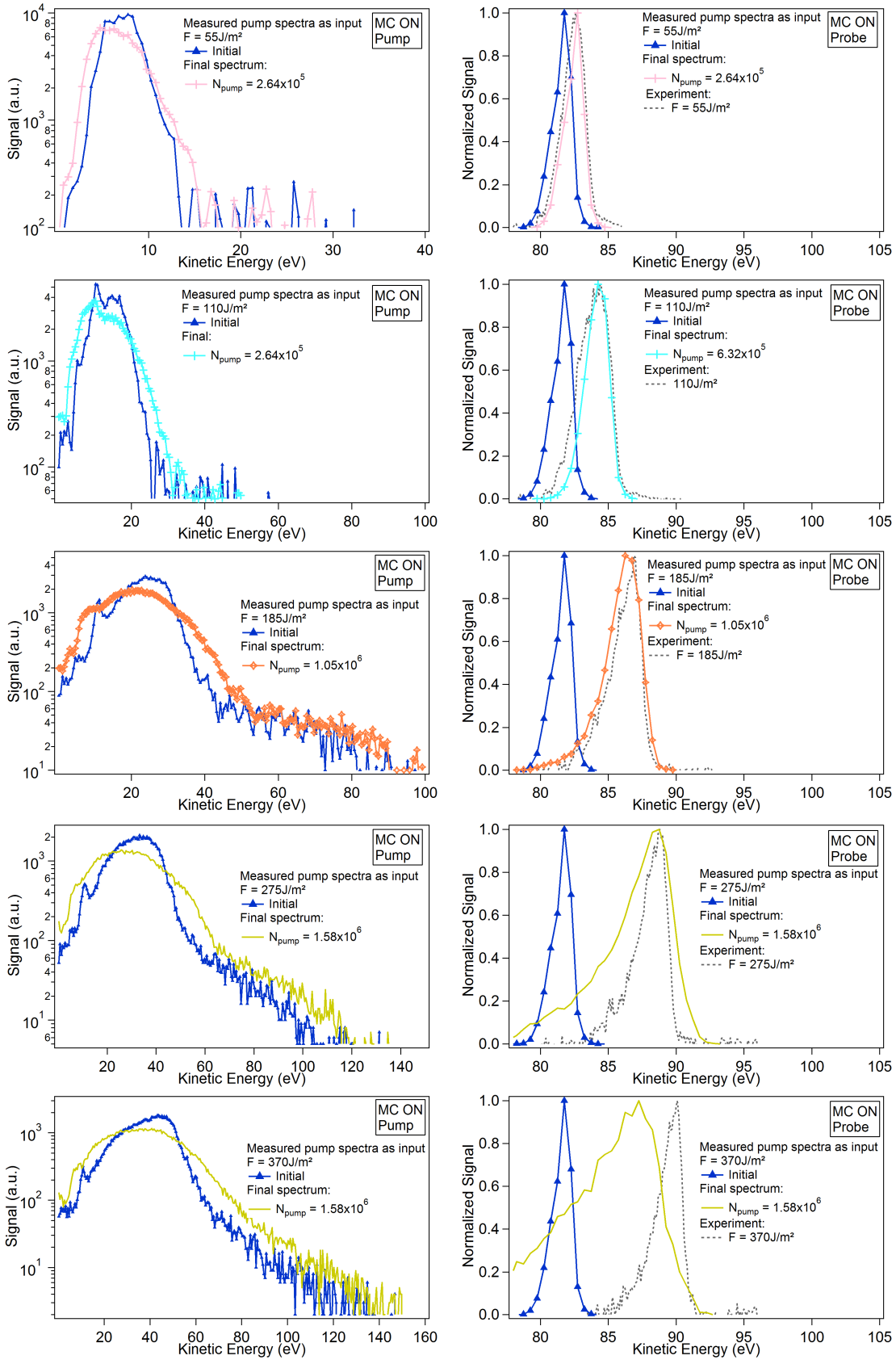

Fig. III.25 *ASTRA simulation pump (right) and probe (left) spectra outputs using the experimentaly measured pump spectrum as pump initial spectrum spectrum. Mirror charges are on.*

initial one. The agreement is no longer true for higher fluences where the probe spectrum broadening is larger than the experimental measurements.

As explained by the findings in section III.4.3 h), the more the initial pump spectrum spans in a larger range of energy, the more time (and distance) both pump and probe bunches will travel together and more shift broadening will appear in the probe spectrum. This is why choosing for the low fluences, a measured spectrum allows to have a good experiment/calculation agreement. These findings reinforce the idea that the initial pump spectrum has different components. On one side, the spectrum calculated by the jellium-Volkov approximation, and on the other side, more energetic contributions from other mechanisms such as laser acceleration.

III.4.6 Summary and discussion of the pump induced space-charge effect study

In order to understand the space-charge effect of pump/probe photoemission experiments, I have analyzed the different contributions to the spectra evolution. Various experimental parameters were taken into account, such as the sample intrinsic constants, the excitation laser parameters that produce above-threshold ionization and the laser acceleration of electrons. These considerations lead to three main space-charge effect cases, corresponding to three different pump initial spectra described by:

1. Above-threshold ionization. Assuming that the pump initial spectrum is described by the jellium-Volkov approximation.
2. Laser-acceleration mechanisms as described by the laser-plasma interaction SMILEI code.
3. Measured pump photoelectron spectrum. Assuming that the measurements were reminiscent of the initial pump spectrum.

Finally, the space-charge effect of electrons travelling from the sample towards the detector was modelled. In the following, the summary and a discussion on our findings are presented.

First it was assessed that the number of electrons is one of the key parameters in our experimental conditions, where the electron bunch transversal (x, y) size is much larger than the longitudinal size z. Neither the volumetric electron density nor the transversal size (for the MC ON case) play a role in the final result.

For case 1. we used the J-V initial pump spectrum and set up a "standard case" where the number of electrons was varied for both MC OFF and ON cases. Calculations and expermiental measurements do not agree. The MC OFF case allowed to obtain pump cutoff energies close to the experimental pump spectra, but not for the probe spectra. On the other hand, the MC ON case allowed to obtain probe final spectra compatible with the experimental findings but not for the pump spectra.

The parametric study, where emission angle, particle sorting were tested, showed weak variations and not in the right direction: increasing the pump final cutoff energies while reproducing the probe shifts and broadenings. The test of MC delay didn't allow to reproduce the experimental findings, especially for high fluences.

The analysis done for the shift and broadening mechanisms following the evolution of both pump and probe spectra in time allowed us to understand the dynamics of the interactions between pump and probe electrons and lead us to propose other shapes of pump spectra.

The case 2. corresponds to an initial pump spectrum generated by the laser acceleration of electrons. We varied some parameters of this spectrum and performed the space-charge simulations aiming to reproduce the experimental measurements for only one of the high fluences (F = 370 J/m^2). The simulations results almost reached the experimental pump cutoff energies while the probe spectrum was also close to the experimental measurement. Nonetheless, the structured shape of the measured pump spectrum was not explained by the laser-accelerated spectrum.

In case 3. it is assumed that the pump initial spectrum followed a shape derived from the experimental measurements. For this, we proposed two forms: a Gaussian form from a low fluence measurement and the final pump experimental spectrum. Both forms yielded results close to the low fluence measurements but not for the high fluences, meaning that other mechanisms were at play when increasing the fluence.

On one hand, using the jellium-Volkov approximation alone do not reproduce the pump cutoff nor the probe shift and broadening. On the other hand, using the laser-accelerated spectrum (calculated with SMILEI) do not reproduce the structured shape of the pump spectrum, but only the pump cutoff, and the probe spectrum lays close to the experimental findings. Hence, we conclude that other factors that are present are not taken into account with our model.

The first thing that could be questioned regarding the pump initial spectrum in case 1. is the extent of the validity of the jellium-Volkov approximation. This approximation leads to calculations underestimating the high energy components on the spectra. A more precise calculation would include solving the time-dependent Schrödinger equation beyond the Jellium-Volkov approximation, for which the pump initial spectrum is expected to be more energetic than the one calculated by jellium-Volkov. A complete calculation following formalisms such as the one proposed by Winger [115] would allow to obtain the pump initial spectrum, the angular distribution, the emitted electron density and the initial positions of those electrons.

Another situation that is not factored in our model is the possibility of space-charge effect happening inside the detector due to the focusing of photoelectrons on the entrance slit by the electrostatic lens. This could explain why the low fluences are easier to be reproduced for both pump and probe. A low electron density means that the space-charge effect inside the detector is less important. At high fluences, having a much larger pump electron density, it is though that a stronger space-charge effect can happen inside the detector, only allowing the probe to be reproduced.

However, we can be sure that at least for the low fluence measurements, the probe modifications due to the presence of the pump photoelectrons happen outside the detector. The difference in the electron kinetic energies allow the probe electrons to leave behind the pump electrons while travelling from the sample towards the detector. For

example, probe electrons with E = 90 eV, reach the detector (placed at ∼10 cm from the sample) in ∼18 ns. At that time, pump electrons with E = ∼15-20 eV are ∼5 cm away. At this distance, the Coulomb interaction between pump and probe electrons is negligible, and it is ensured that probe and pump electrons enter the detector at different times.

It is concluded that there are three main components in our pump/probe photoelectron experiment. The first one, associated to the ejection of electrons as calculated by the jellium-Volkov approximation. The second one corresponding to laser-acceleration mechanisms. And, finally, to the pump/probe space-charge effect.

III.5 Experimental reduction of the pump-probe space-charge effect

This chapter pictures the complexity of modeling the pump-probe space-charge effect. Even if a partial modeling is possible, the best option in order to extract the desired information from Tr-PES is to experimentally reduce the space-charge effect as much as possible. Indeed, a quantitative subtraction of the space-charge effect becomes quite delicate, especially because the pump photoemission is a very complex mechanism that also varies from spot to spot on the sample.

For this purpose, we have experimentally investigated the sensitivity of the space-charge effect on mainly three parameters: sample surface roughness, pump polarization and pump laser intensity. Tuning all three can allow us to find proper conditions for experimental measurements with a diminished pump space-charge effect i.e. the conditions for a minimum pump induced photoemission. Indeed the space-charge effect depends on the number of emitted pump photoelectrons N_{pump}, and N_{pump} depends on the pump absorbed energy by the sample which in turn depends mainly on the intensity of the p-polarized component of the pump laser pulse.

The surface roughness of the sample is a critical parameter since, as previously mentioned, small defects can increase locally the laser field yielding in more photoemission. Thus, controlling carefully this parameter can ensure a reduction of the photoemission. The process of sample fabrication must be done carefully to obtain a sufficiently smooth surface.

Also, as a non-linear mechanism, multiphoton photoemission is greatly dependent on the laser intensity. So, in order to reduce it, one can reduce the laser fluence (either by reducing the laser energy or increasing the laser spot) and/or increase the pulse duration. In this study, we aim to trigger laser-induced phase transitions, so the latter has been preferred because for a given range of pulse duration the phase transition depends mainly on the laser fluence. Finally, as mentioned previously using S polarization will also decrease the pump photoemission.

To conclude this study, I present an example of pump/probe measurements recorded almost free of space-charge. This was possible by taking care of the three mentioned aspects: pump laser polarization and intensity, and sample surface quality. Figure III.26 presents pump/probe measurements as a function of laser fluence. The sample was a smooth Cu (111) single crystal (roughness < 0.01 μm) irradiated with a s-polarized pump

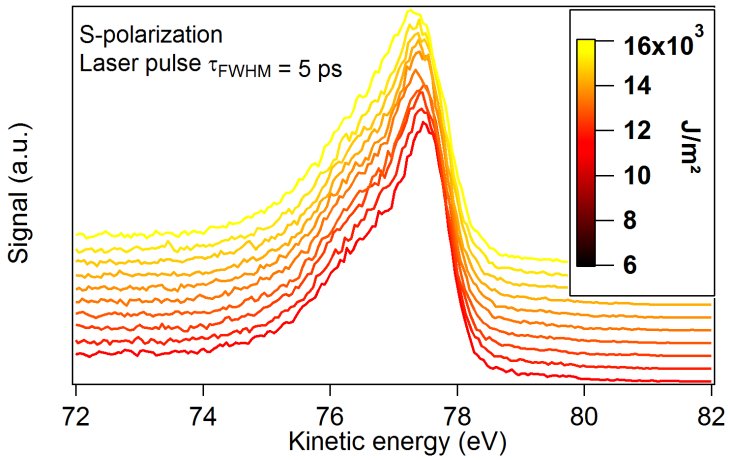

Fig. III.26 *Pump/probe measurements as a function of pump laser fluence (F). An s-polarized and 5 ps laser pulse was used as pump. The delay between pump and probe was set to $\Delta t = 15$ ps. A vertical shift was applied to the spectra for clarity.*

with a pulse duration of $\tau = 5$ ps. The time delay between pump and probe was set to 15 ps.

In chapter IV, we present pump/probe measurements using samples fabricated by molecular beam epitaxy (MBE). This technique allows a monolayer by monolayer fabrication of the sample with a very good surface quality (roughness = 1.4 nm). By improving the surface quality, the pulse duration could be compressed to 1 ps and obtain measurements with a very reduced space-charge effect.

Chapter IV

Ultrafast lattice dynamics studied by photoelectron spectroscopy

This chapter is dedicated to the experimental results obtained using the pump/probe time-resolved photoelectron spectroscopy (Tr-PES) setup, presented in chapter II. It aims to be a proof-of-principle for Tr-PES in metals to study ultrafast lattice dynamics.

An ultrafast infrared laser was used to pump a Cu sample and trigger the lattice dynamics, while an XUV probe interrogated the excited region of the sample. The experiments were performed on the Aurore beamline of the CELIA laboratory (Bordeaux, France). I will first present a detailed description of the samples. Then, the experimental measurements obtained at different laser fluences will be shown. The data treatment will be detailed and the modelling tools to interpret it will be presented. They include simulations to disentangle the space-charge effect from the experimental measurements. Finally, an interpretation of the evolution of the density of occupied states will be proposed, supported by quantum molecular dynamic calculations and hydrodynamic simulations.

IV.1 Sample

IV.1.1 Selection of the samples

In order to investigate the lattice dynamics of matter, it is necessary to wisely select the sample to study: chemical composition, surface quality and geometry (thickness and substrate). These characteristics will determine both the laser-triggered dynamics and the feasibility for measuring those dynamics.

As presented in chapter III, the photoemission generated by the infrared pump is at the origin of the space-charge effect in our experiments. This phenomenon, as already mentioned, entails the loss of information by a distortion of the probe photoelectron spectrum.

Surface quality

The IR-pump photoemission depends greatly on the surface quality of the sample. The main concern regarding the surface is to control the roughness to keep it as small as possible and avoid point-like effects enhancing the laser-induced photoemission.

The Cu single crystal used for the space-charge measurements presented in chapter III

(section III.2), had a minimum roughness of 10 nm as measured by the fabricant. It was grown using the Czochraliski technique [116] that consists in the dipping of a seed crystal on molten material and then pulling it up to crystallize it. The crystal was then polished to reduce the surface roughness. Nonetheless, the single crystal roughness gave rise to an important IR-photoemission and space-charge effect on the probe photoelectron spectrum. The space-charge effect was only reduced when stretching the laser pulse duration to 5 ps (shown at the end of chapter III, section III.5). By reducing the roughness of the sample, the pump laser pulse could be compressed without increasing the pump-photoemission. A shorter pump pulse would allow to access dynamics in the electron-phonon non-equilibrium regime.

We opted for samples fabricated by the Molecular Beam Epitaxy (MBE) technique [117], that consists on the slow deposition (few nm per hour) of sublimated materials onto a substrate, thus finely controlling the ordering and purity of the crystal. The expected roughness is much lower than that of the single crystal.

Chemical composition

The second consideration is related to the material. The photoionization cross section of the electronic levels under study, corresponding to the valence band in our case, must be selected to obtain a sufficiently high signal-to-noise ratio to perform measurements with the required statistics. The statistics are needed to distinguish spectral shape modifications induced by the pump excitation. Table IV.1 compares the photoionization cross section at $h\nu = 100$ eV excitation of a few metallic materials. Au was tried during a first experimental campaign given its interesting properties (such as the possibility of presenting bond-hardening) but abandoned for a material with a larger cross section. Zn or Ni are good candidates, but for this proof-of-principle study whose first objective is to validate the technique, we chose Cu. It has a large cross section and, furthermore, it is a studied material for which there is sufficient information regarding its electronic structure [14, 78], as well as its thermophysical properties [9, 13].

Geometry

Another important aspect to be considered is the geometry of the sample. MBE limits the study to nm thick samples. Free-standing nm layers are not possible to study in our photoemission experiment given the impossibility to refresh the sample after each pump pulse (working at 1 kHz) and a substrate needs to be used. Al_2O_3 was chosen as the substrate material. It has a conductivity of 30 W/m·K, which is much lower than the 400 W/m·K thermal conductivity of Cu. The difference in thermal conductivity increases the energy confinement and decreases the cooling rate inside the Cu layer of the sample. Moreover, by choosing nm-thick samples, the energy confinement becomes more important. By doing so, T_i can reach higher values for longer times than those expected for a thick sample. The expected result is a greater lattice-induced spectral shape modifications on the DOS that are easier to observe, thus, helping us to demonstrate the principle of our technique.

IV.1.2 Sample preparation and characterization

Based on the previous considerations, samples with a Cu thickness of 48 nm were prepared. The samples were deposited on a 1×1 cm^2 Al_2O_3 1 mm-thick substrate coated with a

Material	Valence level	Cross Section (MBarn)
Cu	3d	7
Zn	3d	7
Ni	3d	6
Fe	3d	4
Au	5d	1

Table IV.1: Photoionization cross section of different metals at $h\nu = 100$ eV.

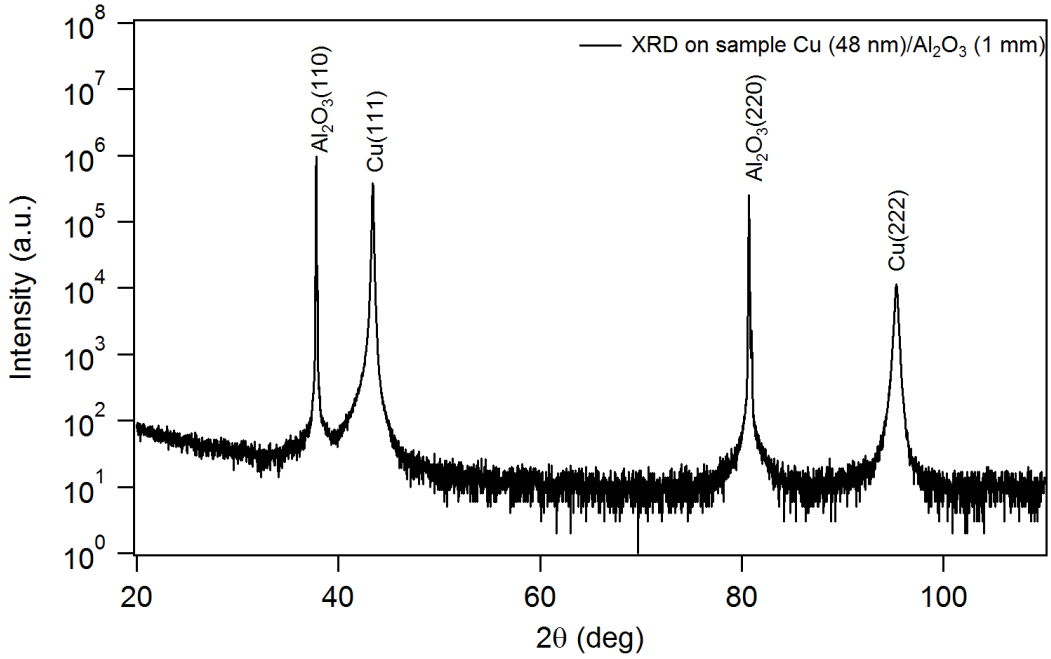

Fig. IV.1 *XRD measurements performed on the Cu (48 nm)/V (2.5 nm)/ Al_2O_3 (1 mm) sample.*

very thin (2.5 nm) vanadium layer to allow a sufficient adherence of the Cu layer onto the substrate. It is not expected that the presence of vanadium would change the dynamics given its reduced thickness and the fact that its thermal conductivity is 35 W/m·K, which is very close to that of Al_2O_3.

The samples were fabricated at the Institute of Physics of the Polish Academy of Sciences (Warsaw, Poland) using MBE. A complete characterization was performed using x-ray diffraction (XRD), x-ray reflectometry (XRR) and atomic-force microscopy (AFM).

The XRD measurements give information regarding the crystallographic surface orientation of the samples. In Figure IV.1 it is possible to identify the peaks corresponding to the substrate and the Cu layer and the second order diffraction. The surface orientation of the Cu layer is (111).

The AFM measurements presented in Figure IV.2 show 2D image of a 10×10 μm^2 region of the sample surface. The height scale is 0-10 nm. The root-mean squared rough-

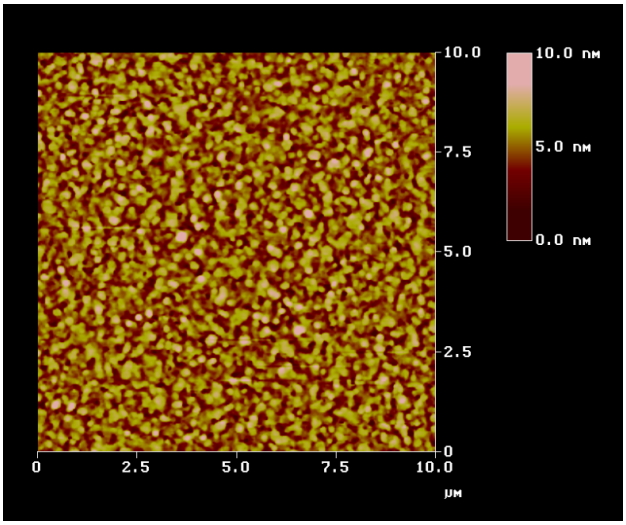

Fig. IV.2 *AFM measurements performed on the Cu (48 nm)/V (2.5 nm)/Al_2O_3 (1 mm) sample on a 10×10 μm^2 region.*

ness, evaluated on this region, is 1.4 nm. This value is smaller compared to the Cu single crystal roughness of 10 nm. Finally, a thickness of 48 nm was found.

The XRR measurements are another source of information about the sample roughness as well as the thickness of the different layers forming it. On top of the Cu layer, an oxidized layer of CuO was formed upon the sample's contact with air. Table IV.2 summarizes these findings. The total thickness (Cu + CuO) is 44.5 nm, which is close to the 48 nm found by AFM. The roughness of the outermost CuO layer, evaluated by XRR, was found to be 1.3 nm, which corresponds to the 1.4 nm roughness found with AFM, because the latter only measures the outermost layer.

Parameter	Thickness (nm)	Roughness (nm)
CuO (oxidized) layer	2.1	1.3
Cu layer	42.4	0.6

Table IV.2: XRR measurements

Once the characterization was completed, the samples were introduced into the experimental chamber using the transfer chamber as described in chapter II. The pressure inside the experimental chamber was 1.4×10^{-9} mbar.

The sample cleaning procedure was adapted to thin samples. Previous tests showed that the Cu thin sample was damaged after our routinary annealing and sputtering 20 minute cycles. For this reason, no annealing was performed on the sample and we only applied 5 minutes of sputtering using Ar ions accelerated to 600 eV. The sample surface chemical composition was monitored before and after sputtering, using XPS with the Al K_α x-ray source as shown in Figure IV.3. The reduced sputtering time sufficed to greatly reduce the presence of oxygen (O 1s) and carbon (C 1s) allowing the Cu peaks (Cu 2p 1/2,

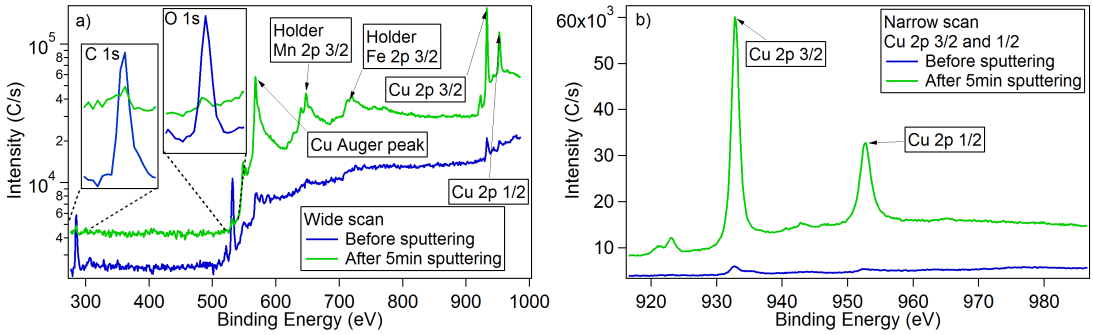

Fig. IV.3 *XPS spectrum of the Cu (48 nm)/V (2.5 nm)/Al_2O_3 (1 mm) sample before and after the cleaning procedure of 5 minutes sputtering was applied: a) wide scan; b) narrower scan.*

3/2 and Auger) and the sample holder peaks (Mn 2p and Fe 2p) to strongly increase their intensity, meaning a removal of the pollution and the oxidized layer. The sputtering can potentially increase the roughness of the sample because of the removal of atoms, but this was not verified as both AFM and XRR were done before performing the experiments.

As already mentioned in chapter II section II.4.3, the residual C 1s and O 1s peaks do not disappear even by increasing the sputtering time. They might come from regions of the sample holder that are also irradiated with the non-focused x-ray source but not properly sputtered. The sample holder is also at the origin of the Mn 2p and Fe 2p peaks.

IV.2 Tr-PES experimental measurements

IV.2.1 Acquisition conditions

The experimental parameters of the optical pulses for the IR-pump/XUV-probe PES measurements are summarized in Table IV.3. The pump focal spot was chosen to be 280×201 μm^2. This allowed us to reach a sufficiently high fluence and to keep, at the same time, a spot size larger than the probe one (found to be 185×124 μm^2). Both pulses are almost collinear, arriving at the sample with a 2° difference.

As mentioned in Chapter III, the pump pulse duration was set to 1 ps in order to have a reduced laser intensity. This, along with the polarization state S and the small sample surface roughness allowed to reduce the pump photoelectron background, and, hence, reduce the space-charge effect.

The acquisition parameters of the electron energy analyzer were chosen to have a compromise between a sufficiently high signal-to-noise ratio and a total measurement time in less than one day of beamtime, as the Aurore laser can only work less than ∼15 hours before thermal instabilities appear. Table IV.4 summarizes these settings.

For a given pump laser fluence, the varied parameter was the time delay between pump and probe. Positive delays correspond to the pump arriving before the probe, whereas negative delays indicate that the probe arrived first.

In order to have sufficient statistics in our measurements, ten scans per time delay were recorded. Performing multiple scans also allowed to monitor fluctuations of the XUV

Parameter	Pump	Probe
Energy (eV)	1.55	88.35 (HH 57)
τ_{FWHM} (fs)	1000	25
x_{FWHM} (μm)	280	185
y_{FWHM}(μm)	201	124
Fluence (J/m^2)	6000-8200	-
Polarization	S	S
Incidence (°)	45	43

Table IV.3: Pump and probe experimental parameters.

Parameter	Value
Pass energy (eV)	20
Energy step (eV)	0.1
Acquisition time (ms)	200
Voltage on analyzer (kV)	2.4
Number of scans	10

Table IV.4: Electron energy analyzer experimental parameters.

probe photon flux.

In the following, four different sets of data corresponding to different pump fluences were recorded: 6000, 7000, 7500 and 8200 J/m^2. Three series of consecutive measurements of the probe-only PES (no pump on) were also recorded in order to asses stability and systematic errors on the measurements.

IV.2.2 Data analysis procedure

As it has been stated in Chapter I, section I.3.4 of this manuscript, it is expected that, upon laser excitation, the PES spectrum, corresponding to the density of occupied states (DOS) undergoes shape modifications on a certain spectral region (from chapter I, see Figs. I.14 and I.13) [14]. The spectral shape modifications could be blurred or entangled with space-charge effect, even if it was reduced to its minimum. Thus, such spectral profile modification must be carefully extracted from our experimental measurements.

Figure IV.4 a) reports, for a given pump fluence (7500 J/m^2), all spectra recorded for a complete set of pump/probe measurements. Each spectrum corresponds to a time delay between pump and probe. They evidence important spectral shifts that are attributed to space-charge effects because for this fluence range, spectral shifts are not expected. The variations in terms of intensity are due to fluctuations of the XUV probe photon flux. In order to compare the different spectra and look for spectral shape modifications, a meticulous and precise procedure was established.

First, all of the iterations for each time delay were averaged (Figure IV.4 a)). No smoothing was applied to the data. Following, each spectrum was individually normalized to the maximum data point (Figure IV.4 b)). Then, to account for the space-charge induced shift, the spectra were shifted to superimpose them at the point at which the

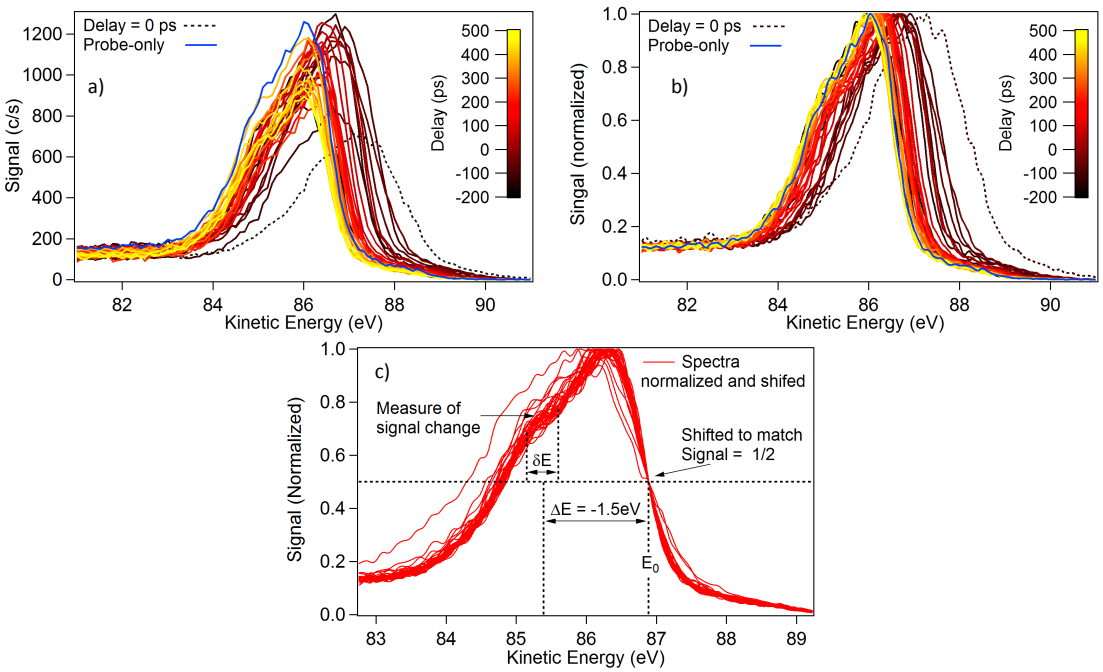

Fig. IV.4 *Data analysis of the spectra: first each spectrum is a) averaged, b) normalized, c) shifted to match I = 0.5 and d) the signal change* $\Delta I = I\text{-}I_{ref}/I_{ref}$ *is extracted at the position* ΔE *by inegrating over* δE.

normalized signal I, has a value of 0.5, designated as E_0 (Figure IV.4 c)). The I = 0.5 was chosen because it was the steepest region in the spectrum, thus allowing a precise alignment of all the spectra. Then, the normalized signal intensities were measured by averaging over a δE around specific spectral positions designated by a distance ΔE from E_0. Averaging over δE is somehow equivalent to applying a smoothing to the raw data.

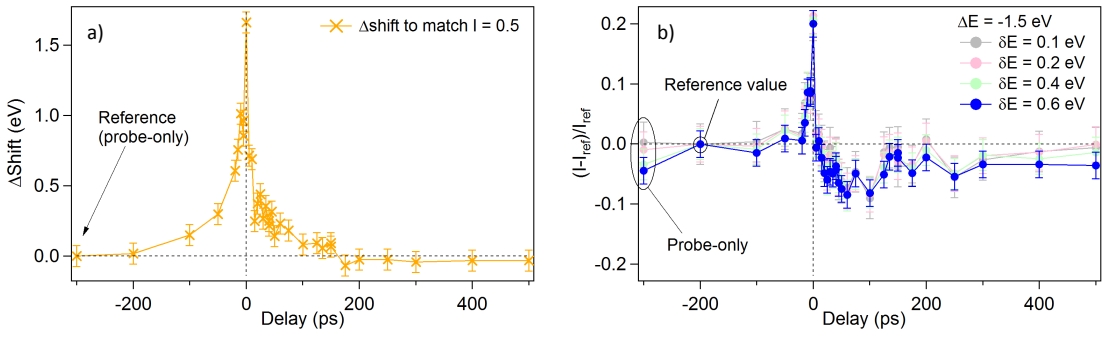

Fig. IV.5 *Results of the data analysis of the spectra: a)applied shift to match I = 0.5, b)the signal change* $\Delta I = I\text{-}I_{ref}/I_{ref}$ *extracted at the position* ΔE *= -1.5 eV by averaging over* δE.

The information extracted from this analysis is presented in Figure Fig. IV.5. It is a quantification of both the shift on the spectra (Fig. IV.5 a)) and the spectral shape modification (Fig. IV.5 b)).

Different values of δE were used ($\delta E = 0.1$, 0.2, 0.4 and 0.6 eV) to look for the spectral shape modifications on the data at different ΔE locations, as can be seen in Figure IV.5 b) for the case $\Delta E = -1.5$ eV. The normalized signal intensities at the ΔE locations were computed as intensity changes (ΔI) relative to the spectrum at a negative delay (either -100 or -200 ps), called I_{ref}. This means that the reported values are $\Delta I = I\text{-}I_{ref}/I_{ref}$. They are the quantification of the spectral shape modification. In other words, δE was varied to find a compromise between the local shape change and the statistical noise of the data, while ΔE was varied to look for the location where the spectral shape changes happened.

Finally, in order to evaluate the uncertainty and calculate the error bars of the $\Delta I = I\text{-}I_{ref}/I_{ref}$ values (as in Fig. IV.5 b)), the same analysis procedure was applied to the probe-only data series. For all the δE and ΔE values, the ΔI of the probe only data was computed and the standard deviation was calculated. The error bars correspond to the latter. Hence, they comprise both systematic errors and fluctuations from the XUV probe photon flux but not the fluctuations of the pump beam. The error was also computed for the applied shift values used to match the spectra at I = 0.5 (E_0 point).

IV.2.3 Measurements of the different pump fluences

The previous analysis procedure was applied to the measurements at all pump fluences (6000, 7000, 7500 and 8200 J/m^2) and the results are presented in this section. First, I will present a comparison of the applied shifts for the four series of measurements and then the $\Delta I = I\text{-}I_{ref}/I_{ref}$ at the different ΔE spectral locations will be compared. In this fashion, the effect of the pump fluence in both the shift and the spectral modifications will be assessed.

Figure IV.6 presents the shifts applied to the four series as a function of the delay between pump and probe. As it can be noted, by increasing the fluence from 6000 to 8200 J/m^2, the shift increases in magnitude. For all of the presented fluences there is a maximum at delay = 0 ps that appears to be considerably larger compared to the neighbouring delays (-5 ps on one side and 2.5ps on the other side). The shift is almost symmetric in shape around 0 ps. It is decaying slightly faster on the positive delay side. It goes back to zero far away from 0 ps (at a delay between 100 and 200 ps on both positive and negative sides). The shift origin is mainly attributed to the space-charge effect because of its presence at negative delays. The pump electrons can interact with the probe electrons even if the probe arrives first. On the contrary, lattice induced spectral shape changes are not expected before the pump arrives.

The spectral shape changes were assessed at different ΔE locations in the spectrum. Figure IV.7 shows the probe-only spectrum and ΔE = -1.0, -1.25, -1.5, and -2.25 eV. In the following, the ΔI spectral shape changes are calculated using an averaging range δE = 0.6 eV.

The ΔI as a function of delay, at the position ΔE = -0.25 eV is presented in Fig. IV.8. For all fluences, the value of ΔI remains close to zero except in the vicinities of

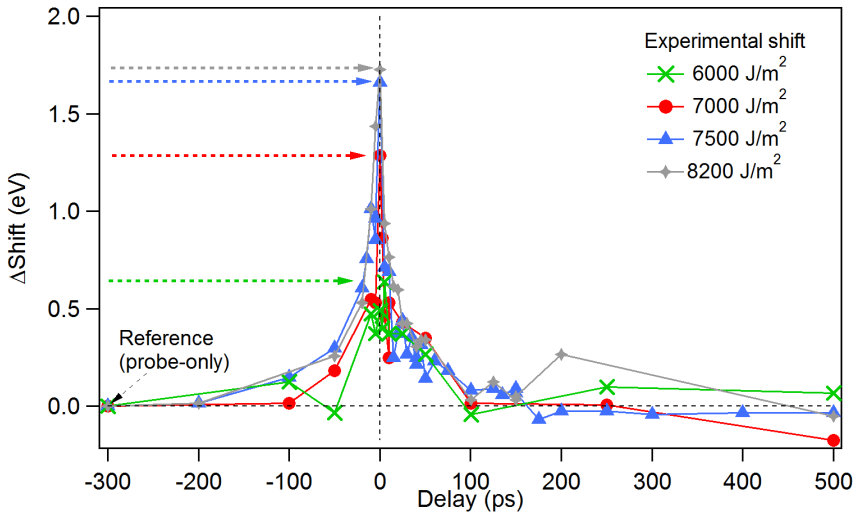

Fig. IV.6 *Experimental shifts of the spectra for the four measured fluences.*

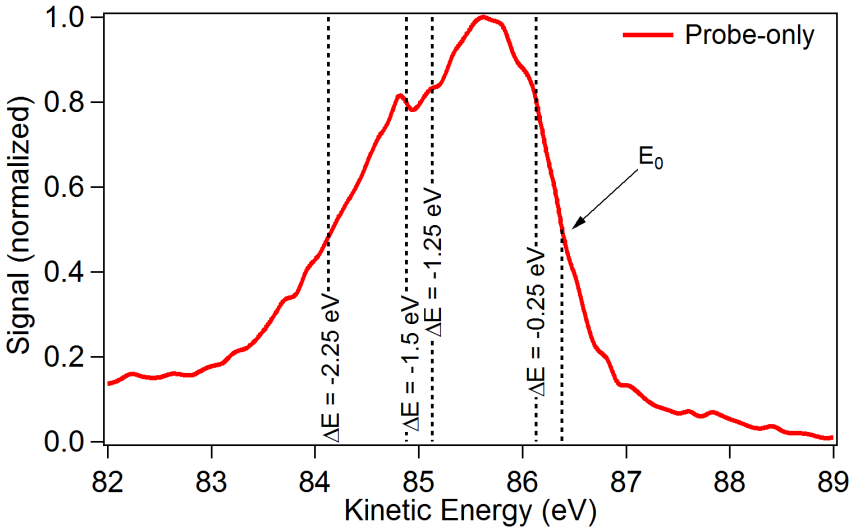

Fig. IV.7 *Probe-only spectrum showing the ΔE locations where the spectral shape changes $\Delta I = I\text{-}I_{ref}/I_{ref}$ were calculated.*

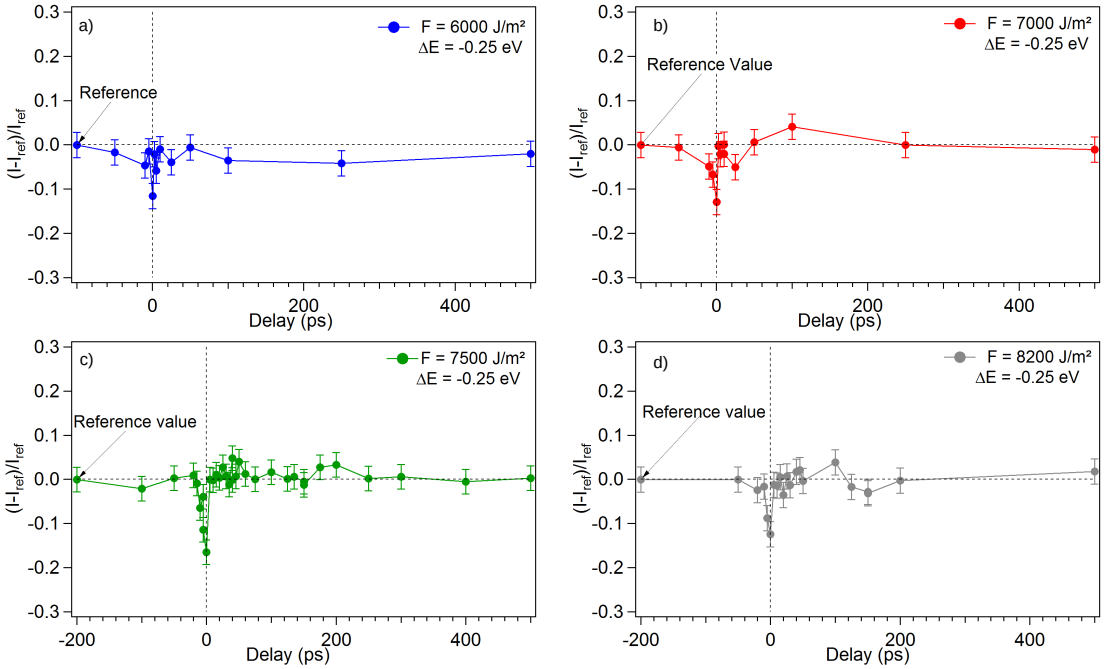

Fig. IV.8 *$\Delta I = I\text{-}I_{ref}/I_{ref}$ spectral modifications at ΔE = -0.25 eV for a) F = 6000 J/m², b) F = 7000 J/m², c) F = 7500 J/m² and d) F = 8200 J/m².*

the 0 ps delay (between -10 ps and +5 ps), where $\Delta I < 0$. This means that there is a spectral shape change in a certain direction (the signal is decreasing at that location). The maximum change happens at exactly 0 ps for all fluences. The variation of ΔI with the fluence is small, having a maximum at 7500 J/m^2.

Space-charge effect is believed to be at the origin of the spectral shape change ($\Delta I \neq 0$) at negative delays, since no laser-induced heating changes can happen in the sample before the pump excites it. Furthermore, the space-charge effect is known to have certain symmetry around the pump/probe zero time delay (according to the observed shift). Thus, the spectral shape changes ($\Delta I < 0$) happening around 0 ps on both positive and negative sides are probably related to the space-charge effect. Evidently, other contributions to the spectral change modifications, like laser-induced heating might also be present at positive delays (superimposed with the space-charge modifications).

A different behavior is observed for the following position ΔE = -1.25 eV, as seen in Fig. IV.9. ΔI is again, reaching an extremum at 0 ps, but now $\Delta I > 0$ in the vicinity of 0 ps. This means a spectral signal change in the opposite direction. The maximum ΔI value increases as a function of the fluence.

Away from the 0 ps delay, $\Delta I \sim 0$ for fluences 6000, 7000 and 8200 J/m^2. For the case at F = 7500 J/m^2, there is an inversion of the ΔI sign happening at $\sim$+10 ps that lasts up to the end of the delay range, which is +500 ps.

As mentioned before, the spectral shape modifications $\Delta I \neq 0$, happening at negative delays are associated with the space-charge effect. Thus, again, the spike visible around 0 ps for all fluences is associated to space-charge effect. On the contrary, for the case at

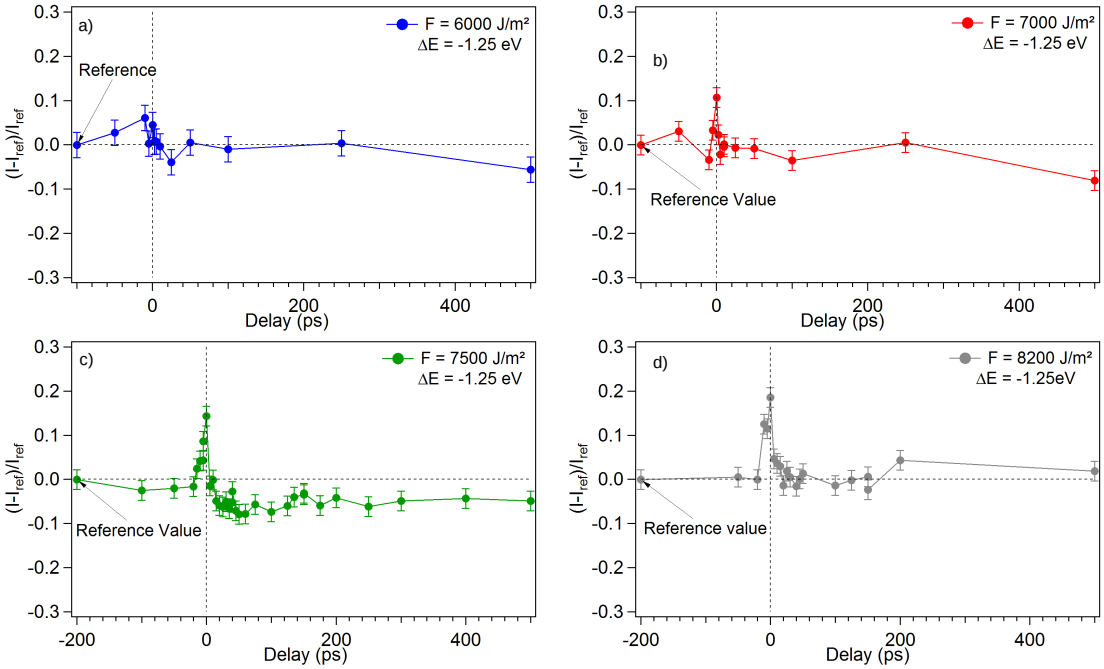

Fig. IV.9 $\Delta I = I\text{-}I_{ref}/I_{ref}$ *spectral modifications at* ΔE = *-1.25 eV for a)* F = *6000 J/m², b)* F = *7000 J/m², c)* F = *7500 J/m² and d)* F = *8200 J/m².*

7500 J/m^2, the spectral change ΔI < 0 on the positive delay side cannot, a priori, be associated with space-charge effect.

For spectral modifications at ΔE = -1.5 eV presented in Fig. IV.10, the same tendency is observed. The ΔI > 0 (which is slightly larger than the one at ΔE = -1.25 eV) around 0 ps is, again, associated with space-charge effect. They increase in magnitude with the fluence. The extremum is exactly at 0 ps, and for the 7500 and 8200 J/m^2 cases, it seems to grow much faster than for the lower fluences.

The ΔI changes sign and becomes negative at +10 ps for the case F = 7500 J/m^2, situation that is not associated with space-charge effect.

Finally, the spectral changes at ΔE = -2.25 eV are presented in Figure IV.11. Once more, for all fluences ΔI grows as it gets closer to the 0 ps delay. As the fluence increases from 6000 to 8200 J/m^2, the maximum value of this spike at 0 ps increases in magnitude. This is associated to the space-charge effect.

For the case F = 7500 J/m^2, at ΔE = -2.25 eV, there is not a flagrant sign inversion for the ΔI at positive delays away from 0 ps (taking into account the error bars) as observed for ΔE = -1.25 and -1.5 eV.

In summary, for all the four pump fluence series, the intensity changes ΔI = I-I$_{ref}$/I$_{ref}$ having a spike shape around the 0 ps delay are associated with space-charge effect. They extend in general from around -10 ps to +10 ps, which is much narrower than the shift(present from around -100 ps to 100 ps). The shift is also associated to

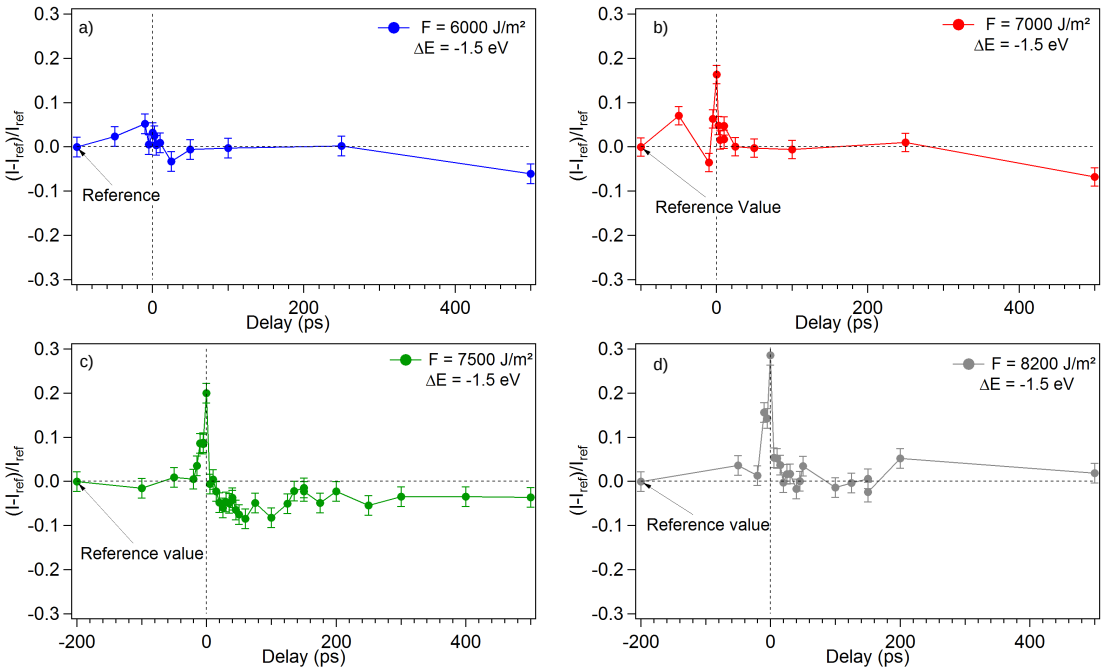

Fig. IV.10 $\Delta I = I\text{-}I_{ref}/I_{ref}$ *spectral modifications at* ΔE = *-1.5 eV for a)* F = *6000 J/m², b)* F = *7000 J/m², c)* F = *7500 J/m² and d)* F = *8200 J/m².*

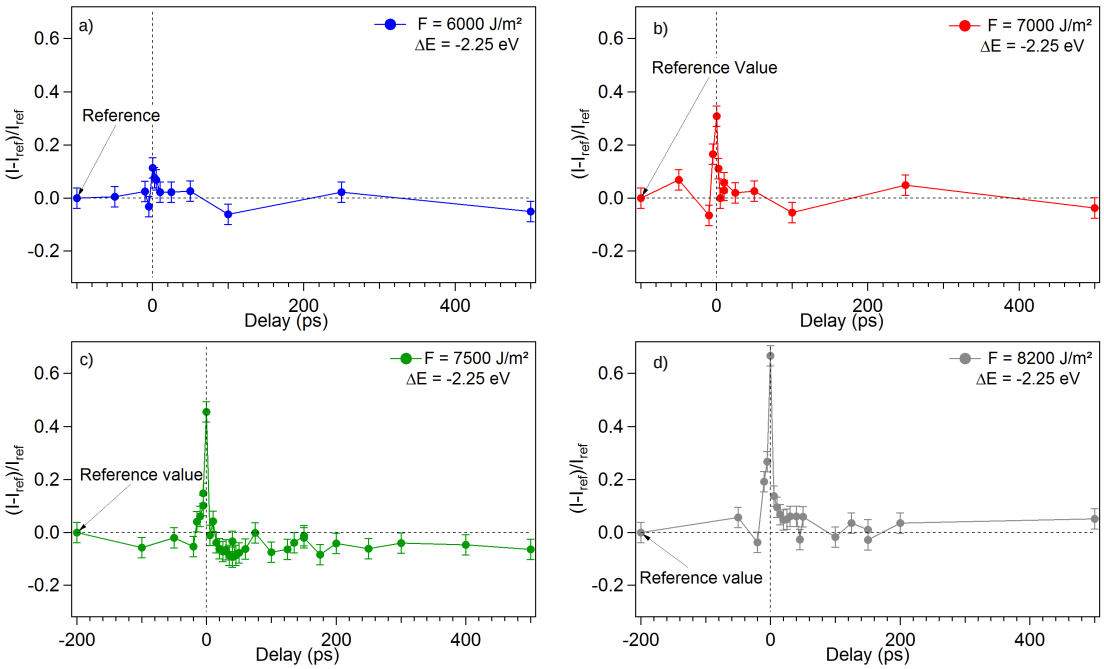

Fig. IV.11 $\Delta I = I\text{-}I_{ref}/I_{ref}$ *spectral modifications at* ΔE = *-2.25 eV for a)* F = *6000 J/m², b)* F = *7000 J/m², c)* F = *7500 J/m² and d)* F = *8200 J/m².*

space-charge effect. This means that the deformation due to space-charge effect extends less than the space-charge effect-induced shift.

If a laser-heating density of states (DOS) modification is happening at early times (0-20 ps), it is superimposed with the space-charge effect induced shape modifications. The disentanglement of the two effects can be, at best quite cumbersome, making it very difficult to exploit the data for this delay range.

The spectral modifications $\Delta I < 0$ happening at ΔE = -1.25 and -1.5 eV for the F = 7500 J/m^2 are probably not associated to the space-charge effect because they are not present at negative time delays. Given their spectral positions, and the fact that $\Delta I < 0$ (meaning a lowering of the signal, in agreement with the calculations in [14]) the origin of these spectral modifications could be a heating-induced density of occupied states (DOS) modification.

Supposing that the spectral modifications are due to a laser-induced heating DOS modification, why are these modifications not present for the highest fluence (8200 J/m^2)? A provisional interpretation is that a competition of effects is taking place: on one side, the space-charge effect induces positive changes ($\Delta I > 0$), and on the other side, the DOS modification induces negative changes ($\Delta I < 0$). The DOS modifications are too weak to be observed in the 6000 and 7000 J/m^2 cases, whereas in case 7500 J/m^2 the DOS modifications are stronger than the space-charge effect. Finally, this situation is inverted at 8200 J/m^2, and the space-charge effect dominates over the DOS modifications of the spectrum.

In order continue the precedent interpretation, the spectral changes need to be associated to a laser-induced heating modification of the density of occupied states (DOS). For this, different modelling tools are needed. In the next section, dedicated to the interpretation of the results, I will focus on the F = 7500 J/m^2 case.

IV.3 Interpretation

This section presents the interpretation of the different spectral shape modifications described previously for the case at F = 7500 J/m^2. As mentioned before, it is expected that some of these changes are associated with the space-charge effect. The modifications with $\Delta I < 0$ at ΔE = -1.25 and -1.5 eV are not expected to come from space-charge effect, but, to have as origin the DOS modifications upon pump laser excitation that we are looking for.

Evidently, the interpretation of the measurements is quite complex due to the presence of the space-charge effect (that motivated the in-depth study presented in chapter III). For this reason, I will first evaluate the space-charge effect in these measurements by performing a careful comparison with pump/probe space-charge effects simulations using the ASTRA code presented in chapter III (section III.3.3). This will allow to univoqually identify the space-charge modifications on the spectrum and to separate them from the modifications issued from the DOS change.

Once this comparison is done, two numerical tools will be used to present an interpretation of the experimental results: (1) the ABINIT code that calculates the DOS of ma-

terials using quantum molecular dynamics, proposed to link spectral shape modifications to a DOS modification by an effect of the sample temperature; and (2) the hydrodynamic ESTHER code that calculates the laser-matter interaction and thermodynamic evolution of matter under the two-temperature model description.

IV.3.1 Disentangling the space-charge effect

As discussed in chapter III dedicated to the space charge effect, the presence of pump induced photoelectrons generates modifications in the probe spectrum that are dependent on the number of pump electrons N_{pump} and the delay between pump and probe electron bunches. These pump electrons were present in our measurements even if the experimental conditions (small sample surface roughness, pump s-polarization and stretched pulse duration) allowed to reduce them drastically. Consequently, pump/probe space charge effect simulations with the ASTRA code, were carried out to assess the effect of these modifications.

The ASTRA space-charge simulations were set using two electron bunches: one of active particles for the pump, and another of passive particles for the probe. As in chapter III, only pump-induced space-charge effect is taken into account. The initial pump energy spectrum was assumed to follow the jellium-Volkov (J-V) approximation, meaning kinetic energies up to a few eV.

We used an s-polarized pump for the experiments, for which no photoemission is expected. The pump photoelectrons might come from residual p-polarized light, whose fluence would be low enough to justify using the J-V calculated spectrum in our simulations. Indeed, in these conditions, no laser acceleration is expected, given the reduced surface roughness of the sample and the pump pulse duration of 1 ps.

The input probe energy spectrum used was the probe-only measured spectrum. The number of probe particles was kept the same for all the simulations and was chosen such that after analysis it was possible to retrieve, with sufficient accuracy the experimental spectrum.

Both electron bunches were emitted from a sample (cathode emission option in ASTRA) and their spatial distributions corresponded to the sizes measured for the pump and probe residual IR laser spots (see Table IV.1). The emission times were assumed to happen within the pulse durations (1 ps and 25 fs for pump and probe respectively) and to have a Gaussian temporal profile. The emission was assumed to be perpendicular to the surface of the sample with an angular Gaussian distribution of 45° around the normal in both x and y directions.

The simulations were performed with mirror charges (MC) turned on and off. The number of pump electrons, N_{pump}, was varied for two reasons: (1) because we didn't have information on the number of pump emitted electrons in the experiment, so N_{pump} was the fitting parameter, and (2) to observe possible trends depending on the N_{pump} (associated to the fluence).

For each value of N_{pump}, simulations at different time delays between pump and probe were carried out. For the MC ON case, 10 repetitions of the simulations were done for each N_{pump}. This allowed us to reduce the statistical uncertainty and calculate error bars for the simulation results. The statistical fluctuations in the simulation are due to the random assignment of position and momentum to the particles. In contrast, for the MC

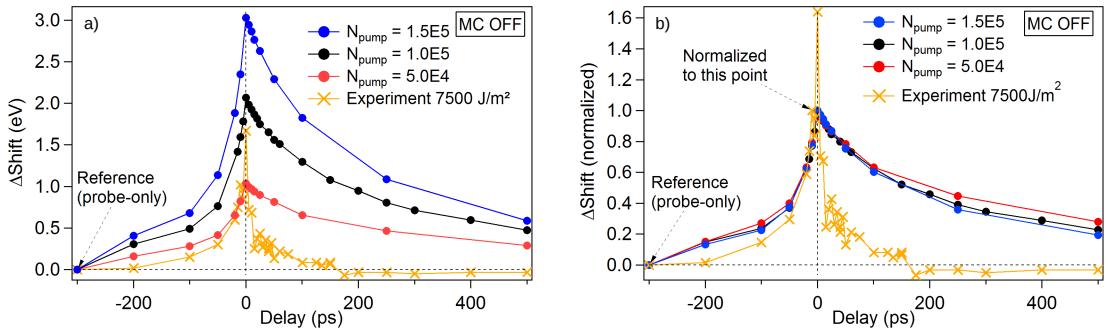

Fig. IV.12 *Comparison between experiment and ASTRA simulations with MC OFF for different N_{pump}. a) shift versus delay and b) normalized shift versus delay.*

OFF case, only one series of simulations were performed for every value of N_{pump}, so no evaluation of the uncertainty was performed.

In the following, I will discuss first the MC OFF case, then the MC ON case.

In Figure IV.12 a comparison of the shift between the MC OFF simulations and the experimental measurements at F = 7500 J/m^2 is presented. The simulated induced shift in the spectra is always positive, reaching a maximum at 0 ps delay, just as the experimental shift. An evident asymmetry in the simulated shift is observed between positive and negative delays: the positive delay side decay is much slower than the negative one. This asymmetry is not present in the experimental shift. Varying N_{pump} has a high impact in the magnitude of the shift. The decay of the shift is less sensitive to N_{pump} as seen in Figure IV.12 b) where the normalized shift is presented: the shift trend is almost identical on the negative delay side and varies very slightly on the positive one.

The overall agreement between the MC OFF simulated shift and experimental one is poor (Fig. IV.12).

However, even if the simulated spectral shift didn't agree with the experimental one, a comparison of the spectral shape modifications is possible. For this purpose, the same analysis procedure presented in section IV.2.2 was applied to the ASTRA pump/probe simulations. The spectral shape modifications were evaluated at the same ΔE positions using the same δE averaging range.

Figure IV.13 presents the spectral shape modifications ΔI for the MC OFF case compared to the experimental findings. The simulated modifications at ΔE = -0.25 eV (Fig. IV.13 a)) are negative ($\Delta I < 0$) around 0 ps delay. This is comparable to the experimental observations for which $\Delta I < 0$ was also observed. On the contrary, the simulated ΔI are much wider in duration than the experimental ΔI, with a clear assymetry: the positive delay side decay is much slower than the negative one. Nonetheless, the trend confirms the interpretation that the origin of the spectral shape modifications at this precise ΔE is due to space-charge effect only.

The spectral shape modifications at ΔE = -1.25, -1.5 and -2.25 eV are presented in Figure IV.13 b), c) and d) respectively. They present modifications that are positive

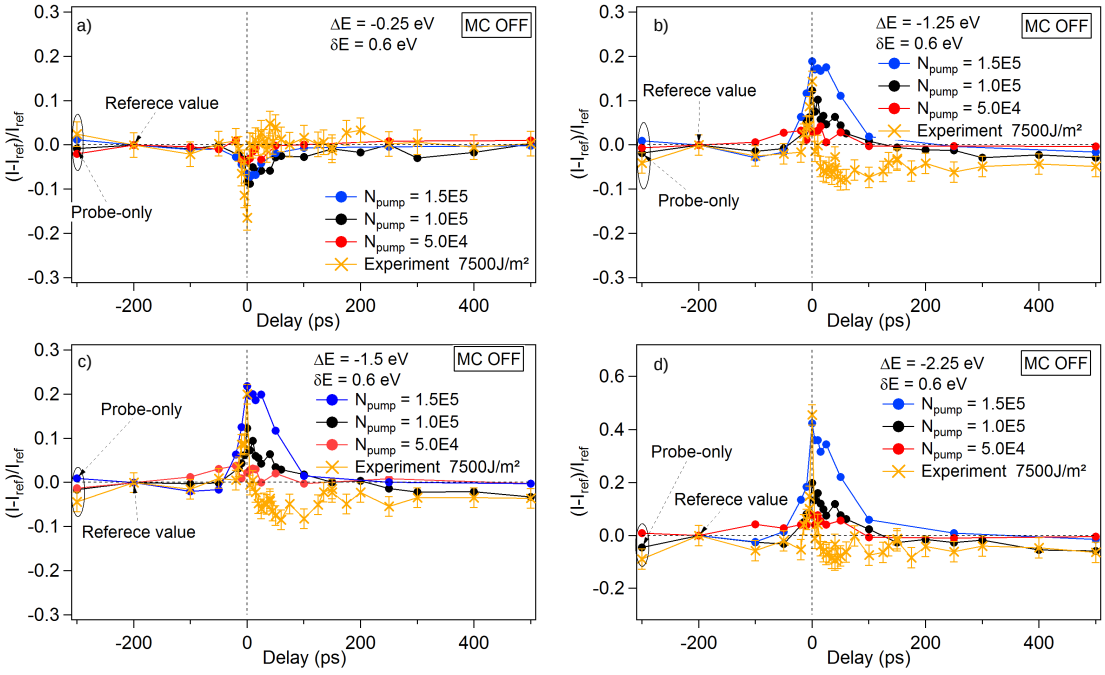

Fig. IV.13 *Comparison between experiment and ASTRA simulations with MC OFF for different N_{pump}. Spectral shape modifications $\Delta I = I\text{-}I_{ref}/I_{ref}$ at a) ΔE = -0.25 eV, b) ΔE = -1.0 eV, c) ΔE = -1.25 eV, d) ΔE = -1.5 eV.*

in sign ($\Delta I > 0$) around 0 ps delay and asymmetric, with the positive delay side decay being slower than the negative one. The simulated ΔI are, again, much broader than the experimental ones. Also, the simulations fail to reproduce the sign inversion ($\Delta I < 0$) at positive delays at ΔE = -1.25 and -1.5 eV observed experimentally, whereas for ΔE = -2.25 eV, where this inversion of ΔI is not present, they agree qualitatively.

As N_{pump} increases so does the magnitude of the spectral shape modification ΔI. For the simulations with the smallest N_{pump} (red line on Fig. IV.13) the changes seem to be different than for the two other used values of N_{pump}. The spike is not so clear at 0 ps and from -50 ps to 50 ps it appears to be oscillating. This is probably due to statistical errors from the simulation. As previously mentioned, no error bars were calculated for the MC OFF simulations.

Given the disagreement between simulated and observed shifts, simulations were also carried out using MC ON. The same analysis procedure was applied to the simulated pump/probe spectra. The shifts are presented in Figure IV.14. The error bars on the simulated shift are quite small (~0.03 eV) and hard to distinguish in the figure. Due to the attractive mirror charges, the simulations require a much larger N_{pump} to shift the spectra to the experimental values.

The first striking result is that the shift versus delay plot is much more symmetric than the MC OFF case and the decay is less sensitive to N_{pump} as evidenced in FigureIV.14 b). Moreover, the simulated shift is qualitatively and quantitatively much closer to the experimental data, being the case with $N_{pump} = 3.0 \times 10^5$ (red) the closest one. This

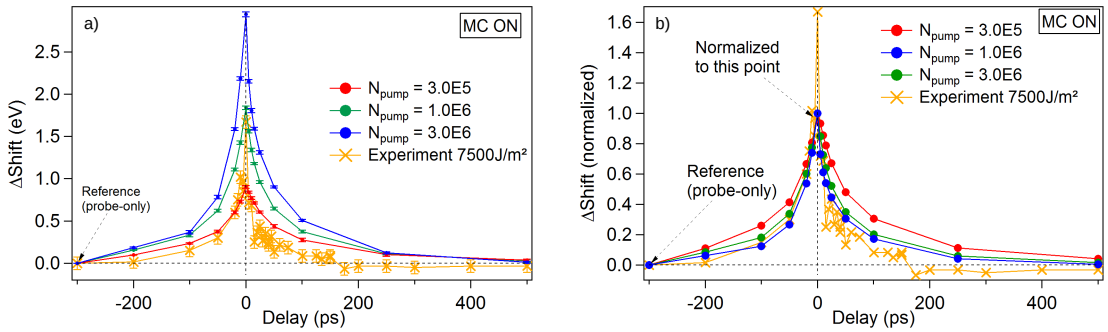

Fig. IV.14 *Comparison between experiment and ASTRA simulations with MC ON for different N_{pump}. a) shift versus delay and b) normalized shift versus delay.*

demonstrates the presence of mirror charges in the experiment and allows to take the calculations into account.

The spectral shape modifications for the MC ON simulations are presented in Figure IV.15. The error bars are in the order of ∼0.02 eV. At ΔE = -0.25 eV (a), the ΔI < 0 is again observed. The ΔI is much narrower around 0 ps delay than for the MC OFF case and thus, it resembles more to the experimental measurements. On the contrary, the maximum value of the simulated spike (located at exactly 0 ps) is smaller than that of the experimental values, especially for $N_{pump} = 3.0 \times 10^5$ (red), whose shift corresponds well to the experimental one. At 0 ps, both pump and probe pulses are present at the same time on the sample surface and this could lead to non-linear effects enhancing the photoemission or accelerating the photoelectrons, situation not modelled with ASTRA. This is discussed below.

The spectral shape modifications at ΔE = -1.25, -1.5 and -2.25 eV are presented in Figure IV.15 b) c) and d) respectively. They show an analogous trend as for the case MC OFF: they present modifications that are positive in sign (ΔI > 0) with an increase in magnitude as a function of N_{pump}. They are much narrower and symmetric around 0 ps delay than the MC OFF case, which is closer to the experimental ΔI. Moreover, as the experimental ΔI, the simulated ones have a light assymetry: the positive delay side decay is slightly faster than the negative one. The assymetry can be seen on the inset in Fig. IV.15 c), corresponding to ΔE = -1.5 eV. Nonetheless, the case that is closer to reproduce in magnitude the maximum at 0 ps is $N_{pump} = 3.0 \times 10^6$ (blue), whose simulated shift overestimates the experimental one.

As in the MC OFF case, the MC ON simulations do not reproduce the experimental sign inversion (ΔI < 0) at positive delays at ΔE = -1.25 and -1.5 eV but agrees qualitatively with the experimental ΔI at ΔE = -2.25 eV, where the sign inversion is not present.

In general, the results from the MC ON case are qualitatively and quantitatively much closer to the experimental measurements than the MC OFF case. Especially the simulated shift is very close to the experimental one. This is the unambiguous proof that mirror charges are present in our experimental conditions.

For both MC ON and OFF, the spectral shape modifications ΔI around the 0 ps delay

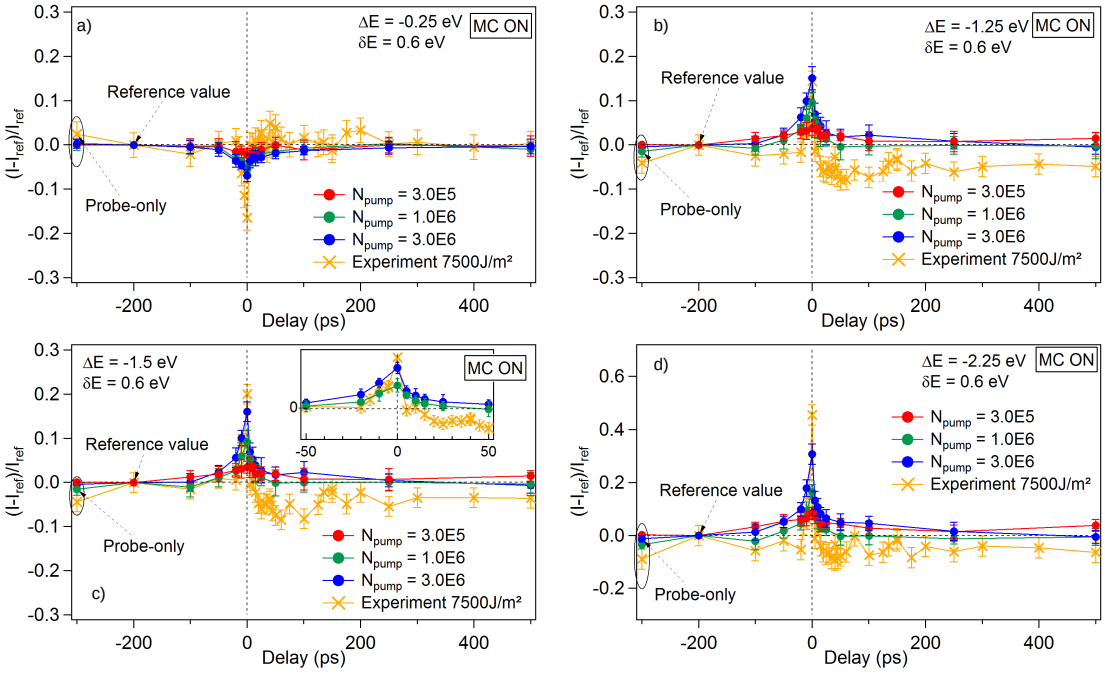

Fig. IV.15 *Comparison between experiment and ASTRA simulations with MC ON for different N_{pump}. Spectral shape modifications $\Delta I = I\text{-}I_{ref}/I_{ref}$ at a) ΔE = -0.25 eV, b) ΔE = -1.0 eV, c) ΔE = -1.25 eV, d) ΔE = -1.5 eV.*

are always qualitatively reproduced in sign and shape (including the slight assymetry of the MC ON case). For MC ON, we found simulated ΔI that were quantitatively compatible with the experiment. We thus conclude that assuming that the space-charge effect is the main origin of the ΔI modifications around 0 ps is correct.

A perfect simulation-experiment match in shift and ΔI was not found even for MC ON. The case $N_{pump} = 3 \times 10^6$ (blue) describes well ΔI but its shift is too large with respect to the experiment.

It is possible that, the J-V initial pump spectrum used in the simulations do not corresponds perfectly to the experimental one. As seen in chapter III, section III.4.4, the probe shift is more sensitive than the spectral shape modifications (probe broadening in that case) to the initial pump spectrum. For example, in Fig. III.22, as the initial pump spectrum changes, the probe shift goes from 8 eV to ∼14 eV, whereas the probe broadening goes from ∼0.6 eV to ∼2.1 eV. So, it might be possible to find a pump initial spectrum that allows to simulate a smaller shift while keeping the ΔI, thus yielding a better agreement between simulation and experiment.

As long as there is still disagreement between simulations and experiments, it is not possible to subtract the space-charge effect from the experimental measurements. As said before, the spectral shape modifications ΔI happening at early delay times are not exploitable.

Another important difference between simulation and experiment is especially notorious at 0 ps, where the measurement values makes a jump off the trend. As if at 0 ps the

shift and spectral shape modifications were augmented. This could mean that some effect happening at exactly 0 ps is enhancing the spectral shifts and modifications. For example a non-linear effect due to the superposition of pump and probe. Studies report that the simultaneous presence of both infrared and XUV pulses can greatly modify the photoelectron spectrum by a process known as laser-assisted photoemission [118]. Nonetheless, this effect can only be present at exactly 0 ps, hence, not disturbing the measurements at other delays.

Finally, the most important finding in this comparison is that the negative spectral shape modifications (ΔI $<$ 0) at ΔE = -1.25, and -1.5 eV at delays $>$ 20 ps, seen in the experimental data was not explained by the simulations. We conclude that these spectral modifications have a different origin. One possibility can be laser induced heating changes in the sample.

IV.3.2 Interpretation of the photoelectron spectrum

The preceding space-charge effect simulation and experiment comparison has evidenced that there is a component in the spectral shape modifications of the valence band that is not originated by the space-charge effect. We expect, then, that the modifications are related to laser heating.

To confirm this hypothesis, we need to compare the experimental measurements to the calculated valence band DOS at different lattice temperatures (T_i) to see if modifications of this magnitude are expected. Furthermore, if it is confirmed, such a comparison should allow us to quantitatively relate the spectral shape modifications ΔI to a temperature T_i. Thus, the technique would then be a time-resolved "lattice thermometer".

The set of results presented in this chapter, corresponding to F = 7500 J/m^2 are only exploitable in the long delay times ($\sim$20-500 ps) because of the presence of space-charge at earlier times (0-20 ps). The early times correspond to the heating of the ionic system. Thus, with this "lattice thermometer", the accessible dynamics would correspond to the cooling stage of the sample.

Figure IV.16 presents a schematic of the strategy proposed for interpreting the experimental data. (a) The DOS calculations will yield a theoretical spectral shape modification dependent on T_i ($\Delta I_{theo}(T_i)$), which would allow to get from the experimental data $T_i(\Delta I_{exp})$. Then, to obtain a thermodynamic interpretation of the experimental results, we need a description of the temporal evolution of the thermodynamic state of the sample. The temporal evolution of T_i can be simulated with the two-temperature model (TTM) (b). In this fashion, a calculated time-dependent lattice temperature T_i(t) could be directly compared to the experimental results (c).

DOS calculations were performed with quantum molecular dynamics within the treatment of density functional theory (DFT) using the ABINIT code. These are heavy calculations usually performed with supercomputers and take long times to be completed. As our principal objective was to demonstrate experimentally the validity of the study, the calculation of Cu DOS were started at the end of this thesis project. There was not enough time to obtain a complete set of data before the writing of this manuscript and the interpretation is still half-way. Nontheless, important details arise from the available

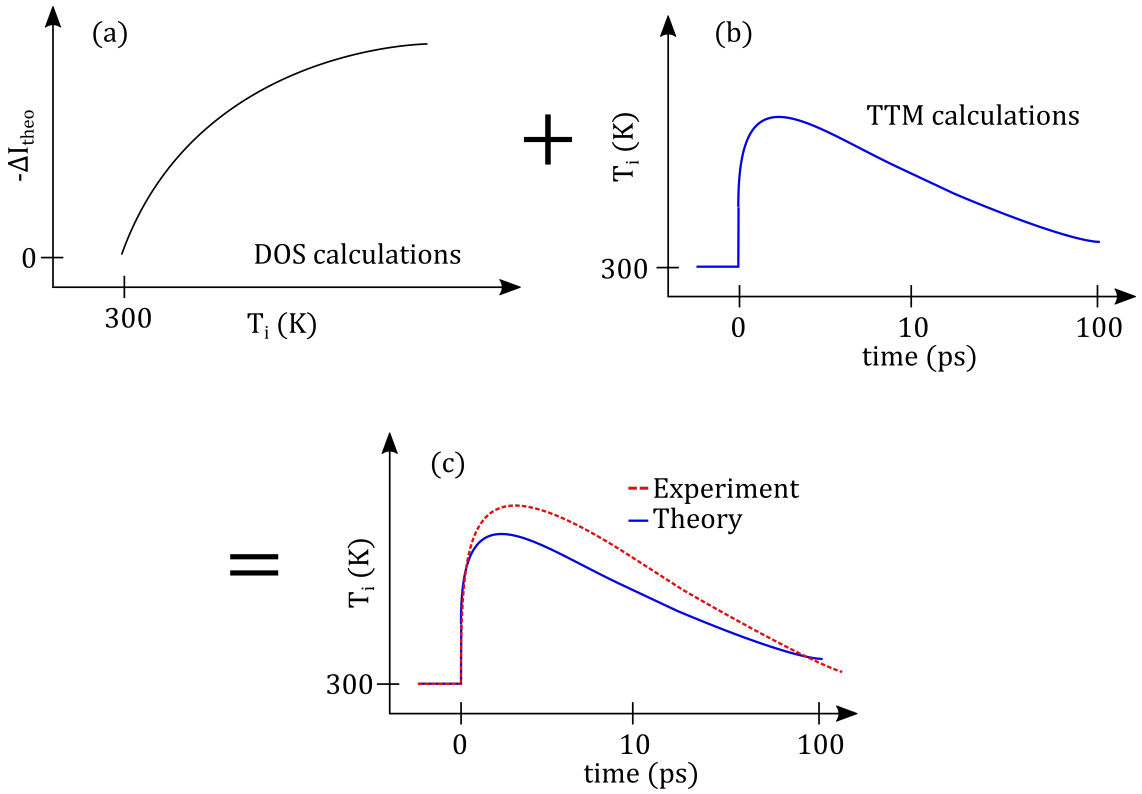

Fig. IV.16 *Schematic of the interpretation strategy. (a) Calculation of the DOS as a function of T_i. (b) Calculation of the T_i as a function of time. (c) Experiment and model comparison*

data and the future possibilities of this project will be presented.

a) ABINIT density functional theory calculations of the density of occupied states

The density of occupied states is modelled with quantum molecular dynamics. This type of calculations is described in chapter I, section e).

To solve the electronic system, the calculations are performed with the code ABINIT in the framework of the projected augmented wave (PAW) method. This code uses a base of plane waves and parameters called PAW data set [10].

The PAW data set considers only a certain number of valence electrons while core electrons are considered to be ”frozen”. This is justified by the fact that electrons close to the nucleus do not play an important role in the chemical or physical properties of the materials that mediate, for example, laser-matter interaction.

ABINIT quantum calculations solve the electronic system. The ionic part of the system is incorporated using classical molecular dynamics (MD). As previously described in chapter I, it is possible to assign different temperatures to both electronic and ionic populations. Usually, the electronic temperature is fixed and the ionic temperature is controlled by a thermostat [119]. The simulation evolves through a certain number of

timesteps until a stable ion temperature is reached. After convergence, the thermodynamical parameters as well as DOS can be obtained.

ABINIT calculation results

As it was mentioned in chapter I, by using an XUV probe in the order of 100 eV we obtain a photoelectron spectrum issued within the first 0.5 nm inside of the Cu sample (corresponding to its inelastic mean free path). The interatomic distance of Cu is 0.359 nm, thus, the experimental measurements are mainly sensitive to the very first atomic layer. This blocked the possibility of comparing our experimental measurements to the the calculated DOS found in literature, which usually include surface and "bulk" atoms. For example, in [14] they use a simulation cell filled with 32 atoms and calculate the DOS over all of them. Furthermore, the DOS "bulk" simulations found in literature include periodic boundary conditions in all 6 sides of the cell (i.e. not including the neighbouring vacuum of the topmost layer).

Thus, we needed to perform DOS calculations adapted to our experimental condition. For this purpose, and to validate this approach we decided to begin with simulations for a system at room temperature in equilibrium conditions ($T_e = T_i = 300$ K) to compare to our probe-only measurements.

The simulations were performed assuming a (100) crystallographic orientation, whereas the experiments were performed on a (111) orientated Cu sample. The (100) choice was made because the XRD measurements of our sample yielding a (111) surface orientation were obtained after the simulations had already started. Nonetheless, this discrepancy is not expected to change drastically the DOS form and will be corrected in the future.

A total of 256 Cu atoms were placed in a (100) configuration forming 8 layers inside a simulation box (i.e. 32 atoms per layer). A schematic of the simulation box is presented in Fig. IV.17. The used dimensions are $14.11 \times 14.11 \times 42.34$ $\mathring{A}^3$ with a 30 $\mathring{A}$ empty space on top of the first layer, simulating the neighbouring vacuum on top of the first atomic layer of our Cu sample.

The DOS was calculated for all the 256 atoms in the box (called "total DOS"), and then, separately, for the 32 atoms of the first, second and third atomic layers.

The results of the calculated total DOS as well as the DOS of the different layers are presented in Figure IV.18 (left).

The DOS of the layers show fast statistical oscillations due to the energy resolution used to compute the DOS. On the other hand, the total DOS was averaged over all the atoms, thus reducing the statistical fluctuations.

The DOS of the first layer (red) is the narrowest one. The second and third layer (blue and green) are broader and resemble more to the total DOS (dark gray). The difference between them might arise first, from the fact that the coordination number is different: there are missing bonds in the surface with respect to the bulk. Secondly, because the interatomic distance between planes changes with the layer position. The atomic planes are more relaxed close to the surface, whereas inside the bulk the interatomic distances are smaller and constant.

Figure IV.18 (right) compares the calculated DOS of the first atomic layer (red line) to the experimental probe-only PES spectrum (black solid line). The Fermi level was dif-

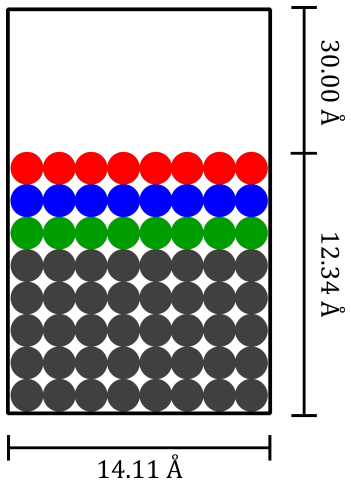

Fig. IV.17 *Schematic of the ABINIT simulation box with 8 layers of Cu atoms with a thick layer of vacuum on top (not in scale).*

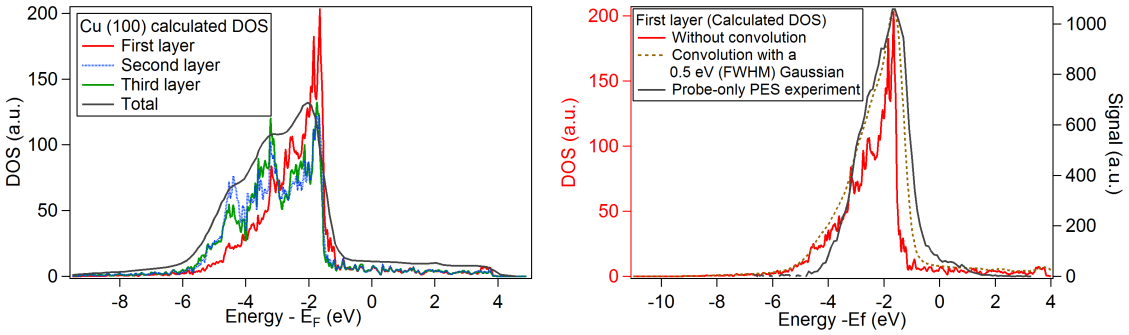

Fig. IV.18 *Calculated DOS of the Cu (100) crystal using ABINIT. Left: comparison of the DOS of the first, second and third layer and the total DOS. Right: calculated DOS of the first layer compared to the probe-only PES experimental measurement shifted in energy (see text).*

ficult to identify in the experimental curve because the measurement did no have enough resolution, so, in order to compare it to the calculated curve, an arbitrary shift was applied. The experimental curve is wider than the calculated one. The calculated curve was convoluted with a Gaussian function to account for the experimental resolution. Using a FWHM = 0.5 eV, the resulting curve (brown dashed line) has a similar width to the experimental one. This confirms that the experimental spectrum mainly corresponds to the first atomic layer of the Cu sample. Nonetheless, the agreement is not perfect. The discrepancies could be explained by the difference between measured and simulated orientations.

Regarding the interpretation of the spectral shape modifications in the pump/probe measurements at F = 7500 J/m^2, more DOS calculations are needed for different values of T_i. In this fashion, the functionality of the measured spectral shape modifications, with the lattice temperature T_i could be found.

In the following, I will present an example of the kind of interpretation and insight that could be obtained once the DOS simulations at different T_i are available. For this purpose, we make use of calculations of the temporal evolution of laser heated materials within the two temperature model (TTM).

b) Hydrodynamic calculations and the two temperature model: The ESTHER Code

To exemplify the interpretation procedure presented before (Fig. IV.16) a modelling of the thermodynamical properties of the sample upon laser excitation is needed.

Calculations can be performed using the ESTHER code (EffetS Thermo-mecaniques et Hydrodynamiques Engendrés par un Rayonnement) that has been developed by the Commisariat à l'énergie atomique (CEA-DAM) [47]. This 1D Lagrangian code solves the Helmholtz wave equation to describe the energy deposited by the laser electromagnetic field into the material. To simulate the system response to the energy deposition, the code incorporates the two temperature model (TTM) equations and a hydrodynamic model (both presented in chapter I). This relies on a multiphase equation of state (EOS) which is a self-consistent description of matter dynamics upon energy deposition. Moreover, the different models for the thermo-physical parameters (electron and phonon heat capacity $C_{e,i}$, electron heat conductivity K_e and electron-phonon coupling G) can also be incorporated. For example, the model proposed by Lin et al. [9] discussed in chapter I can be used. Finally, using ESTHER, thermal expansion and/or phase transitions can be evaluated.

Using such modelling, ESTHER gives access to the temporal evolution of the thermodynamic state of the sample during the energy deposition and relaxation. In other words, we can obtain information about T_e and T_i as well as the volume, density and pressure of the system, among others.

ESTHER calculation results

We performed two-temperature model (TTM) hydrodynamical simulations following our experimental conditions. The laser was modelled for the $F = 7500\ J/m^2$ case, for which the space-charge effect was low enough that the spectral shape modifications attributed to laser heating could be seen.

The Cu (48 nm)/V (2.5 nm)/Al_2O_3 (1 mm) structure of our sample was also taken into account and modelled.

As an illustrative example, the effect of varying the Cu layer thickness was evaluated by performing simulations with 48, 90, 180 nm and 50 μm. It is expected that reducing the thickness increases the confinement of the energy inside the sample as there is less volume for the heat to diffuse.

The heat diffusion is mediated by the electron and ion heat conductivities, K_e and K_i, respectively. In metals such as Cu, $K_i \ll K_e$ so K_i is neglected. In other words, the importance of the electron heat conductivity K_e will be varied with the thickness. Hence, changing the thickness would yield different thermodynamic evolutions.

The idea is to show the expected differences if the experiment is performed on samples

with different thicknesses. The 50 μm thickness is large enough to approximate a "bulk" sample, considering the penetration depth of the laser field ($\sim$ 4 nm).

Specifically, the pump laser pulse was assumed to follow a temporal Gaussian distribution, with a pulse duration $\tau = 1$ ps, arriving with a 45° incidence angle and at a fluence of F = 7500 J/m^2. The sample was set to an initial temperature T_e=T_i= 300 K. The models followed to describe the thermophysical quantities are specified in Table IV.5.

Parameter	Model
Ion heat capacity C_i	Equation of state from [120]
Electron heat capacity C_e	Model by Lin et al. [9]
Electron-phonon coupling G	Model by Lin et al. [9]
Ion heat conductivity K_i	neglected
Electron heat conductivity K_e	Model by Lin et al. [9]

Table IV.5: Two-temperature model thermophysical parameters used in ESTHER.

The sample was modelled using a thin layer of Cu (48, 90 or 180 nm) on top of a 10 μm Al layer as substrate. The vanadium layer is neglected because it is not expected to play a role in the dynamics, as discussed in section IV.1.1. The Al heat conductivity was set to the Al_2O_3 one (30 W/m·K). This choice was made because the input data (equations of state) for the Al_2O_3 (used as substrate in the real sample) was not available in ESTHER. Nonetheless, since the Cu thickness is larger than the skin depth of the pump laser, no laser absorption is expected to take place in the substrate. The main role of the substrate is to diffuse the heat. In consequence, the substitution of the Al_2O_3 substrate by Al should not lead to important differences.

A calculation consisting of 50 μm of Cu without a substrate was also carried out.

The effects on both the electronic and ionic temperatures (T_e and T_i) were computed for the first cell of the ESTHER simulation grid, located at $\sim$0.35 nm from the surface. This corresponds to the first atomic layer, which is the probing depth of our Tr-PES experiment.

The evolution of the temperatures is shown in Figure IV.19. It is noted that, for all the used thicknesses, ESTHER predicts a T_i smaller than the melting temperature $T_m = 1358$ K. T_e and T_i evolve very similarly in all four cases. The time = 0 ps corresponds to the arrival of the pump laser pulse. The energy is absorbed by the electrons and, within the first 2 ps a maximum value of T_e is reached. As expected, T_i remains almost constant for $\sim$1 ps and then it starts to rise due to electron-phonon interactions. The maximum T_i is reached at $\sim$5 ps. Nonetheless, as time continues, T_e decays fastly to a value that is lower than T_i. This happens because the heat diffusion of the electrons into the volume of the lattice happens much faster than the electron-phonon coupling. At later times ($\sim$ 500 ps), the $T_i = T_e$ equilibrium is completed.

The main difference between the four thicknesses is observed in the insets of the plots. This difference between T_e and T_i in the 10-20 ps range, is larger as a function of the thickness. This can be qualitatively explained by an effect of energy confinement. For a thick sample, with a larger Cu volume, the heat can diffuse more easily through the electron heat diffusion, mediated by the electron heat conductivity K_e. Whereas for a

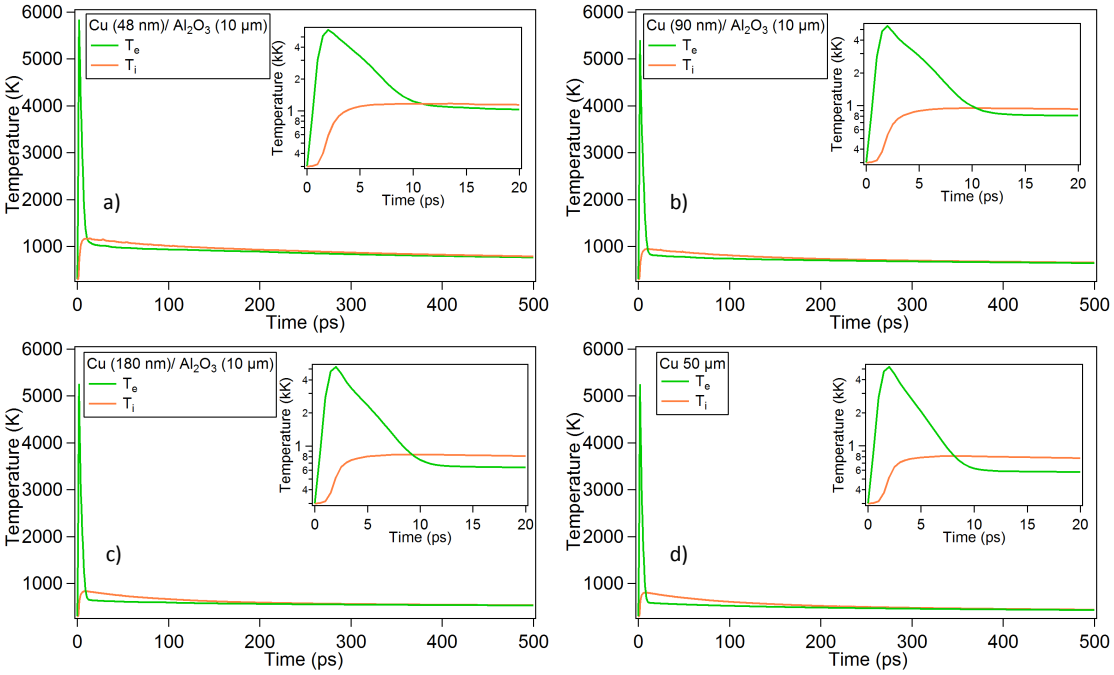

Fig. IV.19 *ESTHER calculations of the T_e and T_i evolutions in Cu samples irradiated with a 1 ps laser pulse and $F = 7500$ J/m^2. The sample thicknesses are a) 48 nm, b) 90 nm, c) 180 nm and d) 50 µm. The insets are on ylog scale.*

thin sample, the diffusion is less efficient allowing the electron-phonon energy transfer to bring T_e and T_i closer to each other. This confirms that the importance of the K_e is being varied with the thickness.

The effect of the thickness on the maximum values of T_e and T_i are presented in Fig. IV.20 and in Table IV.6. As the thickness increases, both T_e and T_i maximal values decrease. The simulated sample of 180 nm resembles closely to the simulation with 50 µm: the difference in T_i is less than 30 K. This means that beyond 180 nm, the sample starts to have a bulk-like dynamics.

Experimentally, if the function of the spectral shape modifications ΔI can be related to the T_i, then a direct comparison of the T_i modelled with ESTHER could be made. This would first allow to assess if the predicted T_i for our experiment is correct. An analysis of the T_i variation as a function of the thickness could be at hand.

The experimental measurements are representative of dynamics happening within hundreds of picoseconds. As already mentioned, the space-charge effect is present in the first ~20 ps, thus, impeding us to extract that information. The dynamics on a longer timescale are free of space-charge and are exploitable. They correspond to the expected relaxation stage in the irradiated sample.

The decay plots of T_i for different thicknesses, corresponding to the relaxation stage, are compared in Figure IV.21 (left). A bi-exponential fit ($A_1 \exp(-t/\tau_1) + A_2 \exp(-t/\tau_2)$) was performed on the T_i from 20 ps to 1500 ps. The results are summarized in Table IV.6. They present two decay times, one fast (τ_1 ~100 ps) and the second one slow (τ_1 >500

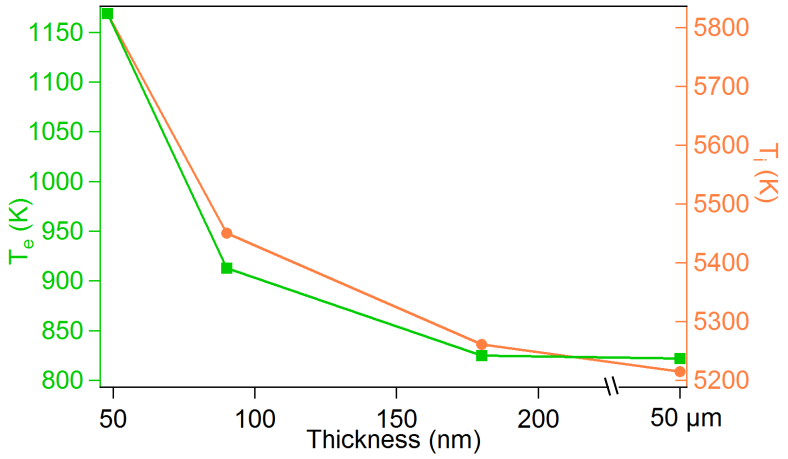

Fig. IV.20 *ESTHER calculations: maximum values of T_e T_i as a function of Cu thickness.*

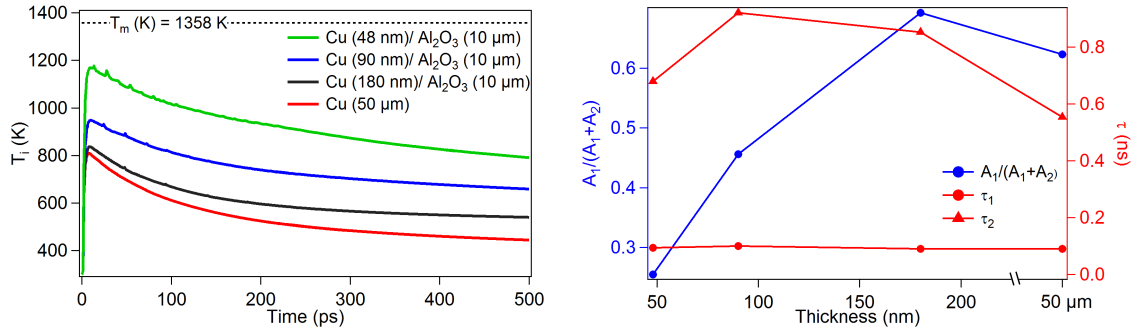

Fig. IV.21 *ESTHER calculations of the T_i evolution as a function of Cu thickness. Left: T_i versus time. Right: parameters of the bi-exponential fit $(A_1 \exp(-t/\tau_1) + A_2 \exp(-t/\tau_2))$ as a function of the Cu thickness.*

ps). In Fig.IV.21 (right) it is observed that as the thickness increases from 48 to 180 nm, the fast dissipation time, corresponding to the coefficient A_1, starts to dominate over the slow one A_2 ($A_1 > 0.5$ at thickness > 100 nm). This is a clear indication that as thickness increases, the dissipation dynamics are changing.

These simulated dynamics at different thicknesses could be compared to the experimental measurements following the strategy presented before in Fig. IV.16. Experimental values of T_i are obtained from ΔI as proposed. By comparing the experimental and theoretical trends as a function of thickness, it would be possible to assess the validity of the models used to describe the thermophysical properties of the system. Specifically, the description of the electron thermal conductivity K_e, whose importance was varied with the sample thickness, could be evaluated.

Cu thickness	T_e^{max} (K)	T_i^{max} (K)	Fit to two exponentials $\tau_{1,2}$ (ps)
48 nm	5824	1169	τ_1=93.3 ± 1, τ_2=679 ± 5
90 nm	5391	948	τ_1=100.2 ± 0.3, τ_2=920 ± 6
180 nm	5242	836	τ_1=90.1 ± 0.1, τ_2=852 ± 7
50 μm	5237	809	τ_1=90.7 ± 0.1, τ_2=553 ± 2

Table IV.6: Time decays of T_i for the ESTHER simulations at different Cu thicknesses. The bi-exponential fit range was 20-1500 ps.

IV.4 Summary and conclusion

This chapter presents the experimental results of the pump/probe Tr-PES measurements aiming to observe laser-induced lattice dynamics. We performed these measurements in controlled experimental conditions and on a sample carefully designed and fabricated in order to increase the possibilites of observing such dynamics as changes in the photoelectron spectrum.

The sample was made of Cu, a material that has a sufficiently large photoionization cross section and for which experimental and theoretical studies predict DOS changes upon heating. The fabrication technique (MBE) allowed to produce a sample surface with a reduced roughness. The surface quality and the pump laser set to 1 ps pulse duration and s-polarization allowed to minimize the space-charge effect issued from the pump photoemission. Also, the structure (a thin Cu layer on an substrate) allowed to increase the energy confinement to reach higher temperatures in the sample.

With all this in our favor, we performed experiments and obtained data at four different pump laser fluences (F = 6000, 7000, 7500 and 8200 J/m^2). We proceeded to establish a data treatment capable to extract the spectral shape modifications. We could attribute some of the modifications to the reminiscent space-charge effect. To further investigate this, we performed space-charge simulations.

Upon the simulation-experiment comparison we found unambiguous proof that mirror charges are present in our experiment. Also, spectral modifications happening at early times (0-20 ps) were mainly linked to the space-charge effect. On the other hand, for the F = 7500 J/m^2 we found that spectral shape modifications happening at later times (>20 ps) were not issued from the space-charge effect and concluded that these changes were laser-heating induced DOS modifications.

We concluded that a competition between the DOS spectral shape modifications and the space-charge effect might explain the fact that only the 7500 J/m^2 case showed laser-heating induced DOS modifications. For the first two fluences (F = 6000 and 7000 J/m^2) the DOS modifications are still not large enough to be detected, whereas at the highest fluence (F = 8200 J/m^2) the space-charge effect takes over them.

A strategy for interpreting the spectral shape modifications was presented. The implementation of this strategy is still an ongoing work and is expected to be fruitful. Nonetheless, intermediate milestones have already been reached.

The first step of the interpretation consisted in quantum calculations adapted to our

experimental conditions to compute the Cu DOS. The DOS at room temperature was compared to a probe-only measurement, showing very similar features, thus validating the assumption that the DOS is sensitive to the surface and that the DOS calculations must be performed for the first atomic layer.

Additionally, future calculations of the DOS at different lattice temperatures (T_i) are still needed.

An example of the kind of interpretation that could be done was presented. For this purpose, simulations of the thermodynamic evolution of the samples were performed. The specific features that could be compared to the experimental data were shown along with the kind of insight that could be gained. Specifically, we showed the simulated changes in T_i as a function of the sample thickness for the 7500 J/m^2 fluence and how, by comparing to experiments, we could assess the validity of the model used to describe the electron heat conductivity K_e.

To conclude, the Tr-PES technique used to investigate laser-induced structural dynamics has been validated. This study is the proof-of-principle. A data treatment and an interpretation strategy has been established and expected to succeed. In the future, experiments with different samples could be performed, for example with varying thickness or using different materials.

Finally, by further decreasing the space-charge effect, information on the early stages of heating could become accessible allowing to have a complete picture of the heating-cooling dynamics. Additionally, the further reduction of the space-charge could lead to experiments with shorter pump pulses giving access to Tr-PES with femtosecond resolution. Besides, reducing the space-charge could lead to better spectral resolutions, which would allow, for example, to measure the Fermi edge and obtain and T_e. If this were the case, a full picture of both T_i and T_e would become accessible through Tr-PES.

Conclusions

The study of ultrafast laser-matter interaction is quite pertinent given the extended use of femtosecond lasers. Their utility ranges from technological and industrial applications as well as to access extreme states of matter where the thermodynamic properties are still subject of debate.

Indeed, ultrafast excitation of materials gives rise to an out of equilibrium state that is complex to model theoretically. Especially because the thermal non-equilibrium between the electrons and the lattice atoms modifies thermophysical properties such as the electron-phonon coupling, the electron heat capacity and the electron thermal conductivity. For this reason, the input from experimental studies is fundamental. The work of this thesis aimed to be a contribution for the experimental study of the dynamics in these thermodynamic regimes.

To experimentally observe the evolution of the sample, we tracked the dynamics of the electronic structure upon excitation using time-resolved photoelectron spectroscopy.

With an infrared-pump/XUV-probe setup, we measured the photoelectron spectrum. This quantity gives access to the electronic structure of the sample, which in turn can undergo changes depending on the temperature or state (i.e. crystalline structure) of the sample. Hence, the evolution of the electronic structure, studied with picosecond-to-femtosecond time resolutions, can be linked to the atomic lattice dynamics.

In particular, our study allowed us to investigate the electronic structure modifications of the valence band density of occupied states (DOS) after intense laser excitation. We aimed to lay close to the melting threshold, to witness laser-induced phase-transitions through the tracking of spectral shape modifications.

During the course of this project, we were able to adress the main challenge inherent to this type of experimental technique: the pump-induced photoemission, which has two main consequences:

- It can form a photoelectron background that can superimpose with the probe spectrum.
- The pump photoelectrons produce space-charge effect, which, via Coulomb law, deforms the probe spectrum resulting in a loss of information.

To overcome these issues, I carried out various actions. First, an especially dedicated XUV beamline at 100 eV has been designed and built in order to prevent the overlapping between the pump background and probe spectrum. Then, the pump/probe

space-charge effect was thoroughly studied. Dedicated experimental measurements of the space-charge effect were performed, and numerical calculations were executed based on theoretical models describing all the stages of the phenomenon: multiphoton photoemission, laser-electron acceleration, and Coulomb interaction between pump and probe electrons travelling in vacuum. We highlighted that a combination of the three effects is present in our experimental data.

The beamline was designed to work in the desired energy range. The generation of harmonics was done in an all-vacuum setup with a specially made gas cell with variable length and position that, along with fine tuning of the laser pulses, allowed for a precise optimization of the photon output. The monochromator multilayer mirrors were designed to select a single harmonic and to maximize the output photon flux. The beamline performances were adapted to the experimental needs. Especially, the XUV photon flux was enough to record spectra in a few minutes with a sufficient resolution ($\sim$1 eV), and the focal spot had the required size (i.e. smaller than the pump spot size) to probe the excited region of the sample when performing pump/probe experiments.

The space-charge study led us to gain a deep understanding of our data. A set of experimental measurements and theoretical tools were used to investigate it. The different mechanisms at the origin of the pump photoelectron emission, such as multiphoton ionization, calculated with the jellium-Volkov approximation, and the laser-induced acceleration of electrons, calculated with the SMILEI PIC code, were assessed. On the other hand, the ASTRA PIC code allowed us to identify the most sensitive parameters in the space-charge interactions: notably, the number of emitted pump photoelectrons, the presence of mirror charges in the sample, and finally, the initial kinetic energies of the pump and probe photoelectrons. Additionally, the experimental findings led us to conclude that at high laser fluences, the possibility of space-charge happening inside the photoelectron detector must be considered.

The reduction of the pump-induced space-charge effect was experimentally explored. It was determined that using a s-polarized pump beam, and stretched pulses, along with a minimized sample surface roughness, greatly diminish the pump photoemission, which is at the origin of the space-charge effect. Using a single crystal Cu sample with a roughness of < 10 nm and 5 ps pump pulses, we tested the reduction of the space-charge effect in pump/probe experiments at very high laser fluences (up to 16000 J/m^2).

Finally, measurements of the dynamics on a nm-thick Cu sample were performed. The experimental conditions were chosen to further reduce the space-charge effect. A sample roughness of 1.4 nm allowed us to set the laser pulse duration to 1 ps. The sample was chosen to be 48 nm thick on top of a sapphire substrate, with lower thermal conductivity than Cu, to confine the excitation and reach high temperatures for long times (hundreds of picoseconds). By doing so, we expected to boost the spectral shape modifications triggered by the ultrafast laser pulses, and thus, increase the probabilities of success of this proof-of-principle experiment. The experiments were performed at four laser fluences (6000, 7000, 7500 and 8200 J/m^2). By carefully analyzing the data we were able to extract the spectral shape modifications. Then, upon comparison with space-charge effect calculations, the spectral shape modifications originated by the space-charge effect were disentangled from the data. The laser-heating induced changes were observed only with a laser fluence of 7500 J/m^2. We concluded that a competition between the two

mechanisms (space-charge effect and laser-heating of the lattice) explained the absence of laser-heating induced spectral shape modifications at the three other fluences.

The importance of having a deep undestanding of the space-charge effect has been highlighted. Choosing the correct experimental conditions is imperative to reduce it and avoid the loss of information. Additionally, a correct modelling is also needed to disentangle it from the measurements.

We also showed that the space charge is a very complex phenomenon involving different mechanisms. The pump-induced photoemission is a topic by itself and important theoretical developments are still needed to fully understand it. For example, a complete solution of the time-dependent Schrödinger equation with no approximation could be implemented to obtain the complete set of pump photoemission information (energy spectrum, angle of emission, and initial position of the electrons).

The study also evidenced that supressing the possibility of space-charge effects inside the electron energy analyzer would be helpful to have a better model-experiment agreement.

The work that I present here constitutes the proof-of-principle for the investigation of ultrafast laser induced dynamics using photoelectron spectroscopy. The upstream experimental and theoretical developments lead us to demonstrate that ultrafast laser heating can modify the photoelectron spectrum and that these modifications can be used to track the dynamics.

The interpretation of the results is still halfway but a strategy has been proposed. We rely on the comparison with complex density-functional theory (DFT) quantum calculations to obtain the DOS. The calculations need to take into account the particularity of the experimental conditions, which are extremely surface sensitive given the probe pulse energy of 100 eV. The first DFT calculations at room temperature for the three outermost atomic layers of the Cu sample were available. By comparing them to the steady state (probe-only) measurements, we concluded that the DOS is sensitive to the coordination number of the atoms and the first stage of the strategy was validated: reproduce the experimental measurement with the DOS calculation at 300 K. Next, calculations at different temperatures should lead us to complete the interpretation of the results. Additionally, this will allow us to compare our results with hydrodynamic simulations unveiling the information about the cooling process happening after the out-of-equilibrium heating.

Beyond the interpretation of the last experiment, many perspectives open up from my project. In particular, the possibilty to study material dynamics as a function of the sample thickness. The example of interpretation at the end of chapter IV could be at hand: by changing the thickness, the contribution from the electronic heat conductivity could be evaluated experimentally and compared to the models.

Moreover, different materials could be studied. For example, the Au dynamics could be investigated. This material is expected to present different behaviours depending on the excitation regime, such as bond-hardening, that increases the melting temperature and delays the phase transition. Or semiconducting materials that present the opposite behavior, non-thermal melting, which reduces their melting threshold and accelerates the phase transition. By comparing the corresponding measurements to the hydrodynamic

simulations, the contributions of electronic excitation could be assessed.

Finally, by pushing towards better quality samples and reducing even more the space-charge effect, Tr-PES could give access to the heating stage of the dynamics, which at this moment, is still not exploitable. Besides, the space-charge effect reduction could allow to further compress the pump pulse, leading to femtosecond-resolved studies of the dynamics that are particularly interesting during the heating stage at early moments after excitation, where the largest electron-phonon non-equilibrium takes place.

Context and contributions

A collaborative project

This PhD thesis is the contribution to a project that was started in 2013 in the Agrégats et surfaces sous excitations intenses (ASUR) group. The principal investigator of this project is Anna Lévy, who is also the co-supervisor of this thesis. It involves a large collaboration with researchers from different laboratories for both theoretical and experimental aspects.

The beamline design, installation, characterization and all the experiments were performed at the CELIA laboratory (Bordeaux, France) in collaboration with Jérôme Gaudin, Nikita Fedorov and Patrick Martin. Stéphane Macé (ASUR group) contributed specially with the design and fabrication of the variable gas cell for HHG and of the monochromator for harmonic selection.

We also received support from other researchers and the ensemble of the CELIA staff. Notably, Valérie Blanchet and Yann Mairesse gave us assistance with the HHG and Dominique Descamps, Robert Bouillaud and Stéphane Petit ensured the operation of the Aurore laser.

The experiments were performed with the help of members of the ASUR group: Anna Lévy, Martino Trassinelli, Emily Lamour and Dominique Vernhet. We also had the contributions of Robert Grisenti, from Goethe University Frankfurt and GSI (Frankfurt and Darmstadt, Germany), Ryszard Sobierajsky from the Polish Academy of Sciences (Warsaw, Poland) and Kiyoshi Ueda from Tohoku University (Sendai, Japan). All the people involved contributed to the development of the experimental setup and participated in performing the experiments. They also contributed with technical and scientific advises during discussions.

The numerical modelling part of the project also involved different collaborations. The first part of the space-charge effect study was done collaborating with Hervé Jouin from the CELIA laboratory, who implemented and used a Fortran routine to calculate the pump initial spectra using the jellium-Volkov approximation.
Samuel Marini and Caterina Ricconda from the LULI laboratory (Paris), collaborated on the second part of the space-charge effect study. They were involved in the exploration of the contributions from laser-induced electron acceleration to the pump photoelectron spectra. They used the SMILEI code for their calculations.

On the other hand, Boris Dorado from the CEA-DAM (France) collaborated in the interpretation of the Cu dynamics measurements. He calculated the density of occupied

states using the ABINIT code.

All of them were highly involved in very fruitful scientific discussions. They provided their expertise in ultrafast photoemission, laser-plasma interactions and density functional theory for the electronic structure computation of materials.

Personal contribution

The collaborative nature of the project has been presented, and evidently every step of it involved discussions and exchanges of ideas. The interpretation of the results was issued from this exchange. Now, I will highlight my personal contributions.

I prepared and led numerous upstream experiments from the beginning of the PhD: 6 weeks of experimental preparation plus 14 weeks of total beamtime over 6 experimental campaigns. Given the complexity of the time-resolved photoelectron spectroscopy setup, I always had the support from at least 3 or 4 researchers to perform the experiments.

These experimental campaigns included the investigation of space-charge effect and the study of the evolution of lattice induced spectral modifications. But also, the beamline implementation, optimization and characterization.

The latter consisted in an important development since the beamline and the pump/probe setup were built from the ground up. I was deeply involved in this technical conception. Due to the high requirements of this study, the beamline performances had to be precisely optimized. For that purpose, I had the help from Nikita Fedorov. Together we performed the necessary modifications to increase the efficiency and stability of the HHG allowing a two orders of magnitude increase in the photoelectron signal intensity, and an optimization of the vacuum, reaching 10^{-9} mbar. Both actions were crucial to perform the experiments.

I installed the characterization chamber and performed all the characterization measurements, again, with the help of Nikita Fedorov. I analyzed all the obtained data. To calibrate the HHG spectrum I used CELIA's home-made LabVIEW software, whereas for the spectral analysis I used the software Igor Pro.

I was in charge of all data analysis and interpretation. For the space-charge effect study I used the AAnalyzer (RDATAA 2015) software to fit the pump/probe spectra. For the ultrafast lattice dynamics study, I programmed a routine in Igor Pro to extract the spectral shape modifications from the data and applied it to the different sets of data.

Regarding the space-charge simulations, I was particularly involved in the study of infrared photoemission that used the jellium-Volkov calculations. I worked closely with Hervé Jouin so that the calculations were adapted to our case. I developed two Matlab routines: one to generate the pump and probe particle distributions following the desired parameters, and a second one to analyze the output ones. I used those routines along with the ASTRA code to perform all the space-charge effect calculations and subsequent analysis.

I also performed two-temperature model simulations using the ESTHER code to propose an interpretation of our experimental data.

Finally, during my PhD I had the opportunity to participate in other experiments (not discussed in this thesis). Two of them were carried out at the PLEIADES beamline of the synchrotron SOLEIL where we performed photoelectron spectroscopy on free-standing beams of nanoparticles (NP). The first experiment, led by Anna Lévy, was performed on Au NP to assess their oxidation state. The second one, led by Jérôme Gaudin, was performed on carbon dots to evaluate their chemical composition. Finally, I also participated in the frequency domain interferometry (FDI) experiments, led by Jérôme Gaudin, to investigate the ultrafast laser-matter interaction in nanometric Cu samples.

Bibliography

[1] D. Strickland and G. Mourou, "Compression of amplified chirped optical pulses," *Optics Communications*, vol. 56, pp. 219–221, Dec. 1985. xi, 32

[2] W. Watanabe, T. Tamaki, and K. Itoh, "Ultrashort Laser Welding and Joining," in *Femtosecond Laser Micromachining: Photonic and Microfluidic Devices in Transparent Materials* (R. Osellame, G. Cerullo, and R. Ramponi, eds.), Topics in Applied Physics, pp. 467–477, Berlin, Heidelberg: Springer Berlin Heidelberg, 2012. xi

[3] R. M. Vázquez, G. Cerullo, R. Ramponi, and R. Osellame, "Optofluidic Biochips," in *Femtosecond Laser Micromachining: Photonic and Microfluidic Devices in Transparent Materials* (R. Osellame, G. Cerullo, and R. Ramponi, eds.), Topics in Applied Physics, pp. 389–419, Berlin, Heidelberg: Springer Berlin Heidelberg, 2012. xi

[4] A. Vogel, J. Noack, G. Hüttman, and G. Paltauf, "Mechanisms of femtosecond laser nanosurgery of cells and tissues," *Applied Physics B*, vol. 81, pp. 1015–1047, Dec. 2005. xi

[5] C.-L. Chen, L.-R. Kuo, S.-Y. Lee, Y.-K. Hwu, S.-W. Chou, C.-C. Chen, F.-H. Chang, K.-H. Lin, D.-H. Tsai, and Y.-Y. Chen, "Photothermal cancer therapy via femtosecond-laser-excited FePt nanoparticles," *Biomaterials*, vol. 34, pp. 1128–1134, Jan. 2013. xi

[6] D. Lapotko, "Plasmonic Nanobubbles as Tunable Cellular Probes for Cancer Theranostics," *Cancers*, vol. 3, pp. 802–840, Mar. 2011. xi

[7] A. Rousse, C. Rischel, S. Fourmaux, I. Uschmann, S. Sebban, G. Grillon, P. Balcou, E. Förster, J. P. Geindre, P. Audebert, J. C. Gauthier, and D. Hulin, "Non-thermal melting in semiconductors measured at femtosecond resolution," *Nature*, vol. 410, pp. 65–68, Mar. 2001. xi, 3

[8] V. Recoules, J. Clérouin, G. Zérah, P. M. Anglade, and S. Mazevet, "Effect of Intense Laser Irradiation on the Lattice Stability of Semiconductors and Metals," *Physical Review Letters*, vol. 96, p. 055503, Feb. 2006. xi, 3, 5

[9] Z. Lin, L. V. Zhigilei, and V. Celli, "Electron-phonon coupling and electron heat capacity of metals under conditions of strong electron-phonon nonequilibrium," *Physical Review B*, vol. 77, p. 075133, Feb. 2008. xi, 1, 4, 5, 6, 7, 8, 9, 16, 94, 115, 116

[10] F. Dorchies and V. Recoules, "Non-equilibrium solid-to-plasma transition dynamics using XANES diagnostic," *Physics Reports*, vol. 657, pp. 1–26, Oct. 2016. xi, 14, 15, 112

[11] R. Li, K. Sundqvist, J. Chen, H. E. Elsayed-Ali, J. Zhang, and P. M. Rentzepis, "Transient lattice deformations of crystals studied by means of ultrafast time-resolved x-ray and electron diffraction," *Structural Dynamics*, vol. 5, p. 044501, June 2018. xi, 17, 18

[12] F. Deneuville, B. Chimier, D. Descamps, F. Dorchies, S. Hulin, S. Petit, O. Peyrusse, J. J. Santos, and C. Fourment, "Sub-picosecond and nanometer scale dynamics of aluminum target surface heated by ultrashort laser pulse," *Applied Physics Letters*, vol. 102, p. 194104, May 2013. xi, 16, 17

[13] J. Winter, S. Rapp, M. Schmidt, and H. P. Huber, "Ultrafast laser processing of copper: A comparative study of experimental and simulated transient optical properties," *Applied Surface Science*, vol. 417, pp. 2–15, Sept. 2017. xi, 2, 8, 9, 16, 17, 94

[14] B. I. Cho, K. Engelhorn, A. A. Correa, T. Ogitsu, C. P. Weber, H. J. Lee, J. Feng, P. A. Ni, Y. Ping, A. J. Nelson, D. Prendergast, R. W. Lee, R. W. Falcone, and P. A. Heimann, "Electronic Structure of Warm Dense Copper Studied by Ultrafast X-Ray Absorption Spectroscopy," *Physical Review Letters*, vol. 106, p. 167601, Apr. 2011. xii, xiii, 6, 16, 24, 25, 94, 98, 105, 113

[15] M. Dell'Angela, T. Anniyev, M. Beye, R. Coffee, A. Föhlisch, J. Gladh, S. Kaya, T. Katayama, O. Krupin, A. Nilsson, D. Nordlund, W. F. Schlotter, J. A. Sellberg, F. Sorgenfrei, J. J. Turner, H. Öström, H. Ogasawara, M. Wolf, and W. Wurth, "Vacuum space charge effects in sub-picosecond soft X-ray photoemission on a molecular adsorbate layer," *Structural Dynamics*, vol. 2, p. 025101, Mar. 2015. xii, 54, 55

[16] A. Pietzsch, A. Föhlisch, M. Beye, M. Deppe, F. Hennies, M. Nagasono, E. Suljoti, W. Wurth, C. Gahl, K. Döbrich, and A Melnikov, "Towards time resolved core level photoelectron spectroscopy with femtosecond x-ray free-electron lasers," *New Journal of Physics*, vol. 10, no. 3, p. 033004, 2008. xiii

[17] L.-P. Oloff, K. Hanff, A. Stange, G. Rohde, F. Diekmann, M. Bauer, and K. Rossnagel, "Pump laser-induced space-charge effects in HHG-driven time- and angle-resolved photoelectron spectroscopy," *Journal of Applied Physics*, vol. 119, p. 225106, June 2016. xiii, 54

[18] X. J. Zhou, B. Wannberg, W. L. Yang, V. Brouet, Z. Sun, J. F. Douglas, D. Dessau, Z. Hussain, and Z. X. Shen, "Space charge effect and mirror charge effect in photoemission spectroscopy," *Journal of Electron Spectroscopy and Related Phenomena*, vol. 142, pp. 27–38, Jan. 2005. xiii, 54, 62

[19] A. Fognini, G. Salvatella, T. U. Michlmayr, C. Wetli, U. Ramsperger, T. Bähler, F. Sorgenfrei, M. Beye, A Eschenlohr, N. Pontius, C. Stamm, F. Hieke,

M. Dell'Angela, S. d. Jong, R. Kukreja, N. Gerasimova, V. Rybnikov, H Redlin, J. Raabe, A. Föhlisch, H. A. Dürr, W. Wurth, D. Pescia, A. Vaterlaus, and Y. Acremann, "The role of space charge in spin-resolved photoemission experiments," *New Journal of Physics*, vol. 16, no. 4, p. 043031, 2014. xiii, 54

[20] B. Mahieu, N. Jourdain, K. T. Phuoc, F. Dorchies, J.-P. Goddet, A. Lifschitz, P. Renaudin, and L. Lecherbourg, "Probing warm dense matter using femtosecond X-ray absorption spectroscopy with a laser-produced betatron source," *Nature Communications*, vol. 9, pp. 1–6, Aug. 2018. 1, 15, 16

[21] B. Rethfeld, A. Kaiser, M. Vicanek, and G. Simon, "Ultrafast dynamics of nonequilibrium electrons in metals under femtosecond laser irradiation," *Physical Review B*, vol. 65, p. 214303, May 2002. 2, 4

[22] M. Kandyla, T. Shih, and E. Mazur, "Femtosecond dynamics of the laser-induced solid-to-liquid phase transition in aluminum," *Physical Review B*, vol. 75, p. 214107, June 2007. 3

[23] J. Chen, W.-K. Chen, J. Tang, and P. M. Rentzepis, "Time-resolved structural dynamics of thin metal films heated with femtosecond optical pulses," *Proceedings of the National Academy of Sciences*, vol. 108, pp. 18887–18892, Nov. 2011. 3, 9

[24] R. Li, O. A. Ashour, J. Chen, H. E. Elsayed-Ali, and P. M. Rentzepis, "Femtosecond laser induced structural dynamics and melting of Cu (111) single crystal. An ultrafast time-resolved x-ray diffraction study," *Journal of Applied Physics*, vol. 121, p. 055102, Feb. 2017. 3

[25] J. Bang, Y. Sun, X.-Q. Liu, F. Gao, and S. Zhang, "Carrier-Multiplication-Induced Structural Change during Ultrafast Carrier Relaxation and Nonthermal Phase Transition in Semiconductors," *Physical Review Letters*, vol. 117, p. 126402, Sept. 2016. 3

[26] P. Saeta, J.-K. Wang, Y. Siegal, N. Bloembergen, and E. Mazur, "Ultrafast electronic disordering during femtosecond laser melting of GaAs," *Physical Review Letters*, vol. 67, pp. 1023–1026, Aug. 1991. 3

[27] K. J. Gaffney, A. M. Lindenberg, J. Larsson, K. Sokolowski-Tinten, C. Blome, O. Synnergren, J. Sheppard, C. Caleman, A. G. MacPhee, D. Weinstein, D. P. Lowney, T. Allison, T. Matthews, R. W. Falcone, A. L. Cavalieri, D. M. Fritz, S. H. Lee, P. H. Bucksbaum, D. A. Reis, J. Rudati, A. T. Macrander, P. H. Fuoss, C. C. Kao, D. P. Siddons, R. Pahl, K. Moffat, J. Als-Nielsen, S. Duesterer, R. Ischebeck, H. Schlarb, H. Schulte-Schrepping, J. Schneider, D. von der Linde, O. Hignette, F. Sette, H. N. Chapman, R. W. Lee, T. N. Hansen, J. S. Wark, M. Bergh, G. Huldt, D. van der Spoel, N. Timneanu, J. Hajdu, R. A. Akre, E. Bong, P. Krejcik, J. Arthur, S. Brennan, K. Luening, and J. B. Hastings, "Observation of Structural Anisotropy and the Onset of Liquidlike Motion During the Nonthermal Melting of InSb," *Physical Review Letters*, vol. 95, p. 125701, Sept. 2005. 3

[28] E. S. Zijlstra, J. Walkenhorst, and M. E. Garcia, "Anharmonic Noninertial Lattice Dynamics during Ultrafast Nonthermal Melting of InSb," *Physical Review Letters*, vol. 101, p. 135701, Sept. 2008. 3

[29] C. V. Shank, R. Yen, and C. Hirlimann, "Time-Resolved Reflectivity Measurements of Femtosecond-Optical-Pulse-Induced Phase Transitions in Silicon," *Physical Review Letters*, vol. 50, pp. 454–457, Feb. 1983. 3

[30] B. Bauerhenne, E. S. Zijlstra, and M. E. Garcia, "Molecular dynamics simulations of a femtosecond-laser-induced solid-to-solid transition in antimony," *Applied Physics A*, vol. 123, p. 608, Sept. 2017. 3

[31] P. Baum, D.-S. Yang, and A. H. Zewail, "4d Visualization of Transitional Structures in Phase Transformations by Electron Diffraction," *Science*, vol. 318, pp. 788–792, Nov. 2007. 3

[32] S. Mazevet, J. Clérouin, V. Recoules, P. M. Anglade, and G. Zerah, "Ab-Initio Simulations of the Optical Properties of Warm Dense Gold," *Physical Review Letters*, vol. 95, p. 085002, Aug. 2005. 3

[33] A. Ng, P. Celliers, A. Forsman, R. M. More, Y. T. Lee, F. Perrot, M. W. C. Dharmawardana, and G. A. Rinker, "Reflectivity of intense femtosecond laser pulses from a simple metal," *Physical Review Letters*, vol. 72, pp. 3351–3354, May 1994. 3

[34] R. Ernstorfer, M. Harb, C. T. Hebeisen, G. Sciaini, T. Dartigalongue, and R. J. D. Miller, "The Formation of Warm Dense Matter: Experimental Evidence for Electronic Bond Hardening in Gold," *Science*, vol. 323, pp. 1033–1037, Feb. 2009. 3

[35] M. I. Kaganov, I. M. Lifshitz, and L. V. Tanatarov, "Relaxation between Electrons and the Crystalline Lattice," *Journal of Experimental and Theoretical Physics*, vol. 4, no. 2, p. 232, 1957. 4

[36] S. I. Anisimov, B. L. Kapeliovich, and T. L. Perel'man, "Electron emission from metal surfaces exposed to ultrashort laser pulses," *Journal of Experimental and Theoretical Physics*, vol. 39, no. 2, p. 375, 1974. 4

[37] L. Waldecker, R. Bertoni, R. Ernstorfer, and J. Vorberger, "Electron-Phonon Coupling and Energy Flow in a Simple Metal beyond the Two-Temperature Approximation," *Physical Review X*, vol. 6, p. 021003, Apr. 2016. 5

[38] E. Bévillon, J. P. Colombier, V. Recoules, and R. Stoian, "Free-electron properties of metals under ultrafast laser-induced electron-phonon nonequilibrium: A first-principles study," *Physical Review B*, vol. 89, p. 115117, Mar. 2014. 5, 24, 26

[39] P.-M. Leguay, *Dynamique structurelle ultra-rapide lors de la transition solide-plasma dense et tiède produite par laser*. PhD thesis, L'Université de Bordeaux, 2013. 6, 15

[40] S. Micheau, F. A. Gutierrez, B. Pons, and H. Jouin, "Screening models for laser–cluster interactions," *Journal of Physics B: Atomic, Molecular and Optical Physics*, vol. 38, pp. 3405–3422, Sept. 2005. 6

[41] J. Hohlfeld, S. S. Wellershoff, J. Güdde, U. Conrad, V. Jähnke, and E. Matthias, "Electron and lattice dynamics following optical excitation of metals," *Chemical Physics*, vol. 251, pp. 237–258, Jan. 2000. 7, 8

[42] M. Z. Mo, Z. Chen, R. K. Li, M. Dunning, B. B. L. Witte, J. K. Baldwin, L. B. Fletcher, J. B. Kim, A. Ng, R. Redmer, A. H. Reid, P. Shekhar, X. Z. Shen, M. Shen, K. Sokolowski-Tinten, Y. Y. Tsui, Y. Q. Wang, Q. Zheng, X. J. Wang, and S. H. Glenzer, "Heterogeneous to homogeneous melting transition visualized with ultrafast electron diffraction," *Science*, vol. 360, pp. 1451–1455, June 2018. 8, 18

[43] Z. Lin and L. V. Zhigilei, "Temperature dependences of the electron–phonon coupling, electron heat capacity and thermal conductivity in Ni under femtosecond laser irradiation," *Applied Surface Science*, vol. 253, pp. 6295–6300, May 2007. 8

[44] C. Wu, D. A. Thomas, Z. Lin, and L. V. Zhigilei, "Runaway lattice-mismatched interface in an atomistic simulation of femtosecond laser irradiation of Ag film–Cu substrate system," *Applied Physics A*, vol. 104, pp. 781–792, Sept. 2011. 9

[45] S. I. Anisimov and B. Rethfeld, "Theory of ultrashort laser pulse interaction with a metal," in *Nonresonant Laser-Matter Interaction (NLMI-9)*, vol. 3093, pp. 192–204, International Society for Optics and Photonics, Apr. 1997. 9

[46] B. Rethfeld, D. S. Ivanov, M. E. Garcia, and S. I. Anisimov, "Modelling ultrafast laser ablation," *Journal of Physics D: Applied Physics*, vol. 50, p. 193001, Apr. 2017. 9, 10

[47] J. P. Colombier, P. Combis, F. Bonneau, R. Le Harzic, and E. Audouard, "Hydrodynamic simulations of metal ablation by femtosecond laser irradiation," *Physical Review B*, vol. 71, p. 165406, Apr. 2005. 9, 115

[48] N. Jourdain, *Etude des propriétés du cuivre sous conditions extrêmes et hors de l'équilibre thermique*. PhD thesis, Université de Bordeaux, 2019. 11, 14

[49] N. D. Mermin, "Thermal Properties of the Inhomogeneous Electron Gas," *Physical Review*, vol. 137, pp. A1441–A1443, Mar. 1965. 11

[50] A. Döpp, B. Mahieu, A. Lifschitz, C. Thaury, A. Doche, E. Guillaume, G. Grittani, O. Lundh, M. Hansson, J. Gautier, M. Kozlova, J. P. Goddet, P. Rousseau, A. Tafzi, V. Malka, A. Rousse, S. Corde, and K. T. Phuoc, "Stable femtosecond X-rays with tunable polarization from a laser-driven accelerator," *Light: Science & Applications*, vol. 6, pp. e17086–e17086, Nov. 2017. 16

[51] J. P. Geindre, P. Audebert, A. Rousse, F. Falliès, J. C. Gauthier, A. Mysyrowicz, A. D. Santos, G. Hamoniaux, and A. Antonetti, "Frequency-domain interferometer for measuring the phase and amplitude of a femtosecond pulse probing a laser-produced plasma," *Optics Letters*, vol. 19, pp. 1997–1999, Dec. 1994. 16

[52] S. P. Weathersby, G. Brown, M. Centurion, T. F. Chase, R. Coffee, J. Corbett, J. P. Eichner, J. C. Frisch, A. R. Fry, M. Gühr, N. Hartmann, C. Hast, R. Hettel, R. K. Jobe, E. N. Jongewaard, J. R. Lewandowski, R. K. Li, A. M. Lindenberg,

I. Makasyuk, J. E. May, D. McCormick, M. N. Nguyen, A. H. Reid, X. Shen, K. Sokolowski-Tinten, T. Vecchione, S. L. Vetter, J. Wu, J. Yang, H. A. Dürr, and X. J. Wang, "Mega-electron-volt ultrafast electron diffraction at SLAC National Accelerator Laboratory," *Review of Scientific Instruments*, vol. 86, p. 073702, July 2015. 17

[53] O. Lundh, J. Lim, C. Rechatin, L. Ammoura, A. Ben-Ismaïl, X. Davoine, G. Gallot, J.-P. Goddet, E. Lefebvre, V. Malka, and J. Faure, "Few femtosecond, few kiloampere electron bunch produced by a laser–plasma accelerator," *Nature Physics*, vol. 7, pp. 219–222, Mar. 2011. 17

[54] J. Li, X. Wang, Z. Chen, J. Zhou, S. S. Mao, and J. Cao, "Real-time probing of ultrafast residual charge dynamics," *Applied Physics Letters*, vol. 98, p. 011501, Jan. 2011. 18

[55] P. Lenard, "Ueber die lichtelektrische Wirkung," *Annalen der Physik*, vol. 313, no. 5, pp. 149–198, 1902. 19

[56] A. Einstein, "Über einen die Erzeugung und Verwandlung des Lichtes betreffenden heuristischen Gesichtspunkt," *Annalen der Physik*, vol. 322, no. 6, pp. 132–148, 1905. 19

[57] S. Hofmann, *Auger- and X-Ray Photoelectron Spectroscopy in Materials Science*, vol. 49. springer-verlag berlin heidelberg ed., 2013. 19, 20, 23, 46, 47

[58] F. Prof H. R. Robinson and B. C. L. Young, "V. The influence of chemical state on critical X-ray absorption frequencies," *The London, Edinburgh, and Dublin Philosophical Magazine and Journal of Science*, vol. 10, pp. 71–75, July 1930. 19

[59] K. Siegbahn and K. Edvarson, "-ray spectroscopy in the precision range of 1 : 105," *Nuclear Physics*, vol. 1, pp. 137–159, Feb. 1956. 19

[60] B. Frietsch, R. Carley, K. Döbrich, C. Gahl, M. Teichmann, O. Schwarzkopf, P. Wernet, and M. Weinelt, "A high-order harmonic generation apparatus for time- and angle-resolved photoelectron spectroscopy," *Review of Scientific Instruments*, vol. 84, p. 075106, July 2013. 19

[61] C. Grazioli, C. Callegari, A. Ciavardini, M. Coreno, and F. Frassetto, "CITIUS: An infrared-extreme ultraviolet light source for fundamental and applied ultrafast science," *Review of Scientific Instruments*, vol. 85, p. 023104, Feb. 2014. 19

[62] J. Ojeda, C. Arrell, J. Grilj, F. Frassetto, L. Mewes, H. Zhang, F. van Mourik, L. Poletto, and L. Chergui, "Harmonium: A pulse preserving source of monochromatic extreme ultraviolet (30–110eV) radiation for ultrafast photoelectron spectroscopy of liquids," *Structural Dynamics*, vol. 3, p. 023602, Oct. 2015. 19

[63] T. Yamamoto, Y. Ishida, R. Yoshida, M. Okawa, K. Okazaki, T. Kanai, A. Kikkawa, Y. Taguchi, T. Kiss, K. Ishizaka, N. Ishii, J. Itatani, S. Watanabe, Y. Tokura, T. Saitoh, and S. Shin, "Nonequilibrium electronic and phonon dynamics of $Cu_{0.17}Bi_2Se_3$ investigated by core-level and valence-band time-resolved photoemission spectroscopy," *Physical Review B*, vol. 92, p. 121106, Sept. 2015. 19, 23

[64] G. Schönhense, K. Medjanik, and H.-J. Elmers, "Space-, time- and spin-resolved photoemission," *Journal of Electron Spectroscopy and Related Phenomena*, vol. 200, pp. 94–118, Apr. 2015. 19

[65] J. Freeouf, M. Erbudak, and D. E. Eastman, "Photoemission spectra for gold for 15hv90 eV and the X-ray limit," *Solid State Communications*, vol. 13, pp. 771–773, Oct. 1973. 21

[66] J. Stöhr, F. R. McFeely, G. Apai, P. S. Wehner, and D. A. Shirley, "Photoemission from Cu valence bands using 50-175-eV synchrotron radiation," *Physical Review B*, vol. 14, pp. 4431–4438, Nov. 1976. 21

[67] K. S. Robinson and P. M. A. Sherwood, "X-Ray photoelectron spectroscopic studies of the surface of sputter ion plated films," *Surface and Interface Analysis*, vol. 6, pp. 261–266, Dec. 1984. 21

[68] S. Tougaard, "Practical algorithm for background subtraction," *Surface Science*, vol. 216, pp. 343–360, June 1989. 21

[69] A. Herrera-Gomez, M. Bravo-Sanchez, F. S. Aguirre-Tostado, and M. O. Vazquez-Lepe, "The slope-background for the near-peak regimen of photoemission spectra," *Journal of Electron Spectroscopy and Related Phenomena*, vol. 189, pp. 76–80, Aug. 2013. 21

[70] B. L. Henke, E. M. Gullikson, and J. C. Davis, "X-Ray Interactions: Photoabsorption, Scattering, Transmission, and Reflection at E = 50-30,000 eV, Z = 1-92," *Atomic Data and Nuclear Data Tables*, vol. 54, pp. 181–342, July 1993. 22

[71] "CXRO X-Ray Interactions With Matter http://henke.lbl.gov/optical_constants/." 22, 23

[72] C. J. Powell and A. Jablonski, *NIST Electron Inelastic-Mean-Free-Path Database*. Gaithersburg, MD: National Institute of Standards and Technology, version 1.2 srd 71 ed., 2010. 22

[73] S. G. Johnson, "NIST Standard Reference Database 71," Aug. 2010. 22, 23

[74] J. J. Yeh and I. Lindau, "Atomic subshell photoionization cross sections and asymmetry parameters: 1 Z 103," *Atomic Data and Nuclear Data Tables*, vol. 32, pp. 1–155, Jan. 1985. 22

[75] "Atomic Calculation of Photoionization Cross-Sections and Asymmetry Parameters https://vuo.elettra.eu/services/elements/webelements.html." 22

[76] L. Perfetti, P. A. Loukakos, M. Lisowski, U. Bovensiepen, H. Eisaki, and M. Wolf, "Ultrafast Electron Relaxation in Superconducting $Bi_2Sr_2CaCu_2O_{8+\delta}$ by Time-Resolved Photoelectron Spectroscopy," *Physical Review Letters*, vol. 99, p. 197001, Nov. 2007. 23

[77] S. Hellmann, C. Sohrt, M. Beye, T. Rohwer, F. Sorgenfrei, M. Marczynski-Bühlow, M. Kalläne, H. Redlin, F. Hennies, M. Bauer, A. Föhlisch, L. Kipp, W. Wurth, and K. Rossnagel, "Time-resolved x-ray photoelectron spectroscopy at FLASH," *New Journal of Physics*, vol. 14, p. 013062, Jan. 2012. 23

[78] I. N. Shabanova, A. V. Kholzakov, and V. S. Kraposhin, "XPS study of transition metal electronic structure in crystalline and liquid states," *Journal of Electron Spectroscopy and Related Phenomena*, vol. 88-91, pp. 453–455, Mar. 1998. 24, 25, 94

[79] F. Kirchhoff, M. J. Mehl, N. I. Papanicolaou, D. A. Papaconstantopoulos, and F. S. Khan, "Dynamical properties of Au from tight-binding molecular-dynamics simulations," *Physical Review B*, vol. 63, p. 195101, Apr. 2001. 24, 25

[80] P. Oelhafen, R. Wahrenberg, and H. Stupp, "Electronic structure of liquid transition metals studied by time resolved photoelectron spectroscopy," *Journal of Physics: Condensed Matter*, vol. 12, pp. A9–A18, Feb. 2000. 25, 27

[81] A. J. Nelson, J. Dunn, J. Hunter, and K. Widmann, "Time-resolved x-ray laser induced photoelectron spectroscopy of isochoric heated copper," *Applied Physics Letters*, vol. 87, p. 154102, Oct. 2005. 26

[82] A. McPherson, G. Gibson, H. Jara, U. Johann, T. S. Luk, I. A. McIntyre, K. Boyer, and C. K. Rhodes, "Studies of multiphoton production of vacuum-ultraviolet radiation in the rare gases," *JOSA B*, vol. 4, pp. 595–601, Apr. 1987. 27

[83] A. L'Huillier and P. Balcou, "High-order harmonic generation in rare gases with a 1-ps 1053-nm laser," *Physical Review Letters*, vol. 70, pp. 774–777, Feb. 1993. 27

[84] M. Aeschlimann, C. A. Schmuttenmaer, H. E. Elsayed-Ali, R. J. D. Miller, J. Cao, Y. Gao, and D. A. Mantell, "Observation of surface enhanced multiphoton photoemission from metal surfaces in the short pulse limit," *The Journal of Chemical Physics*, vol. 102, pp. 8606–8613, June 1995. 28, 55

[85] J. Kupersztych and M. Raynaud, "Anomalous Multiphoton Photoelectric Effect in Ultrashort Time Scales," *Physical Review Letters*, vol. 95, p. 147401, Sept. 2005. 28, 55

[86] R. Al-Obaidi, M. Wilke, M. Borgwardt, J. Metje, A. Moguilevski, N. Engel, D. Tolksdorf, A. Raheem, T. Kampen, S. Mähl, I. Y. Kiyan, and E. F. Aziz, "Ultrafast photoelectron spectroscopy of solutions: space-charge effect," *New Journal of Physics*, vol. 17, no. 9, p. 093016, 2015. 28, 54, 55

[87] S. Hellmann, K. Rossnagel, M. Marczynski-Bühlow, and L. Kipp, "Vacuum space-charge effects in solid-state photoemission," *Physical Review B*, vol. 79, p. 035402, Jan. 2009. 28

[88] N. Fedorov, S. Beaulieu, A. Belsky, V. Blanchet, R. Bouillaud, M. de Anda Villa, J. C. Delagnes, A. Filippov, C. Fourment, J. Gaudin, R. E. Grisenti, E. Lamour, A. Lévy, S. Macé, Y. Mairesse, P. Martin, P. Martinez, P. Noé, I. Papagionnouli,

S. Petit, D. Vernhet, and D. Descamps, "Aurore : A platform for ultrafast science," *Under preparation*, 2019. 32

[89] P. B. Corkum, "Plasma perspective on strong field multiphoton ionization," *Physical Review Letters*, vol. 71, pp. 1994–1997, Sept. 1993. 32

[90] J. L. Krause, K. J. Schafer, and K. C. Kulander, "High-order harmonic generation from atoms and ions in the high intensity regime," *Physical Review Letters*, vol. 68, pp. 3535–3538, June 1992. 32

[91] S. Augst, D. Strickland, D. D. Meyerhofer, S. L. Chin, and J. H. Eberly, "Tunneling ionization of noble gases in a high-intensity laser field," *Physical Review Letters*, vol. 63, pp. 2212–2215, Nov. 1989. 33

[92] S. Daboussi, *Accord de phase et quasi-accord de phase en génération d'harmoniques d'ordres élevés : effet de la pression et du guidage laser*. PhD thesis, Université Paris Sud, Paris, France, Feb. 2013. 34, 36

[93] A. L'Huillier, "High-Order harmonic generation. Coherence and phase matching. Photoionization time delays," Apr. 2017. 34

[94] K. L. Ishikawa, "High-Harmonic Generation." 35

[95] M. Lewenstein, P. Balcou, M. Y. Ivanov, A. L'Huillier, and P. B. Corkum, "Theory of high-harmonic generation by low-frequency laser fields," *Physical Review A*, vol. 49, pp. 2117–2132, Mar. 1994. 35

[96] A. Taylor, "Practical surface analysis, 2nd edn., vol I, auger and X-ray photoelectron spectroscopy. Edited by D. Briggs & M. P. Seah, John Wiley, New York, 1990, 657 pp., price: $86.50. ISBN 0471 92081 9," *Journal of Chemical Technology & Biotechnology*, vol. 53, no. 2, pp. 215–215, 1992. 48

[97] C. Corder, P. Zhao, J. Bakalis, X. Li, M. D. Kershis, A. R. Muraca, M. G. White, and T. K. Allison, "Ultrafast extreme ultraviolet photoemission without space charge," *Structural Dynamics*, vol. 5, p. 054301, Sept. 2018. 54

[98] M. Dell'Angela, F. Hieke, F. Sorgenfrei, N. Gerken, M. Beye, N. Gerasimova, H. Redlin, and W. Wurth, "Ultrafast surface dynamics probed with time resolved photoemission," *Surface Science*, vol. 643, pp. 197–202, Jan. 2016. 54

[99] L.-P. Oloff, M. Oura, K. Rossnagel, A. Chainani, M. Matsunami, R. Eguchi, T. Kiss, Y. Nakatani, T. Yamaguchi, J Miyawaki, M. Taguchi, K. Yamagami, T. Togashi, T. Katayama, K. Ogawa, M. Yabashi, and T. Ishikawa, "Time-resolved HAXPES at SACLA: probe and pump pulse-induced space-charge effects," *New Journal of Physics*, vol. 16, no. 12, p. 123045, 2014. 54

[100] L.-P. Oloff, A. Chainani, M. Matsunami, K. Takahashi, T. Togashi, H. Osawa, K. Hanff, A. Quer, R. Matsushita, R. Shiraishi, M. Nagashima, A. Kimura, K. Matsuishi, M. Yabashi, Y. Tanaka, G. Rossi, T. Ishikawa, K. Rossnagel, and M. Oura,

"Time-resolved HAXPES using a microfocused XFEL beam: From vacuum space-charge effects to intrinsic charge-carrier recombination dynamics," *Scientific Reports*, vol. 6, p. 35087, Oct. 2016. 54, 55

[101] G. Geoffroy, G. Duchateau, N. Fedorov, P. Martin, and S. Guizard, "Influence of electron Coulomb explosion on photoelectron spectra of dielectrics irradiated by femtosecond laser pulses," *Laser Physics*, vol. 24, p. 086101, July 2014. 55

[102] F. Banfi, C. Giannetti, G. Ferrini, G. Galimberti, S. Pagliara, D. Fausti, and F. Parmigiani, "Experimental Evidence of Above-Threshold Photoemission in Solids," *Physical Review Letters*, vol. 94, p. 037601, Jan. 2005. 55

[103] H. Jouin, M. Raynaud, G. Duchateau, G. Geoffroy, A. Sadou, and P. Martin, "Quantum-classical model for the surface plasmon enhanced photoemission process at metal surfaces," *Physical Review B*, vol. 89, p. 195136, May 2014. 55, 58

[104] J. Derouillat, A. Beck, F. Pérez, T. Vinci, M. Chiaramello, A. Grassi, M. Flé, G. Bouchard, I. Plotnikov, N. Aunai, J. Dargent, C. Riconda, and M. Grech, "Smilei : A collaborative, open-source, multi-purpose particle-in-cell code for plasma simulation," *Computer Physics Communications*, vol. 222, pp. 351–373, Jan. 2018. 55, 60

[105] K. Floettmann, "ASTRA User Manual," 2017. 56, 62

[106] A. Herrera-Gomez, M. Bravo-Sanchez, O. Ceballos-Sanchez, and M. O. Vazquez-Lepe, "Practical methods for background subtraction in photoemission spectra," *Surface and Interface Analysis*, vol. 46, pp. 897–905, Oct. 2014. 57

[107] M. N. Faraggi, M. S. Gravielle, and D. M. Mitnik, "Interaction of ultrashort laser pulses with metal surfaces: Impulsive jellium-Volkov approximation versus the solution of the time-dependent Schrödinger equation," *Physical Review A*, vol. 76, p. 012903, July 2007. 58, 59

[108] N. Fedorov, G. Geoffroy, G. Duchateau, L. Štolcová, J. Proška, F. Novotný, M. Domonkos, H. Jouin, P. Martin, and M. Raynaud, "Enhanced photoemission from laser-excited plasmonic nano-objects in periodic arrays," *Journal of Physics: Condensed Matter*, vol. 28, p. 315301, June 2016. 58

[109] H. Jouin and G. Duchateau, "Spectral broadening effects on metal photoemission by femtosecond laser pulses," *Physical Review A*, vol. 99, p. 013433, Jan. 2019. 59

[110] C. Mitchell, "Introduction to PIC Codes and Astra," 2016. 61

[111] H. Popescu, *Génération et transport des électrons rapides dans l'interaction laser-plasma à haut flux.* thesis, Palaiseau, Ecole polytechnique, Jan. 2005. 60

[112] W. Kruer, "Ponderomotive and thermal filamentation of laser light.," *Comments on Plasma Physics and Controlled Fusion*, vol. 9, no. 2, pp. 63–72, 1985. 60

[113] J. P. Freidberg, R. W. Mitchell, R. L. Morse, and L. I. Rudsinski, "Resonant Absorption of Laser Light by Plasma Targets," *Physical Review Letters*, vol. 28, pp. 795–799, Mar. 1972. 61

[114] F. Brunel, "Not-so-resonant, resonant absorption," *Physical Review Letters*, vol. 59, pp. 52–55, July 1987. 61

[115] E. Colomés, Z. Zhan, and X. Oriols, "Comparing Wigner, Husimi and Bohmian distributions: which one is a true probability distribution in phase space?," *Journal of Computational Electronics*, vol. 14, pp. 894–906, Dec. 2015. 90

[116] M. Rettenmayr and H. E. Exner, "Directional Solidification," in *Encyclopedia of Materials: Science and Technology* (K. H. J. Buschow, R. W. Cahn, M. C. Flemings, B. Ilschner, E. J. Kramer, S. Mahajan, and P. Veyssière, eds.), pp. 2183–2189, Oxford: Elsevier, Jan. 2001. 94

[117] K. Alavi, "Molecular Beam Epitaxy," in *Encyclopedia of Materials: Science and Technology* (K. H. J. Buschow, R. W. Cahn, M. C. Flemings, B. Ilschner, E. J. Kramer, S. Mahajan, and P. Veyssière, eds.), pp. 5765–5780, Oxford: Elsevier, Jan. 2001. 94

[118] G. Saathoff, L. Miaja-Avila, M. Aeschlimann, M. M. Murnane, and H. C. Kapteyn, "Laser-assisted photoemission from surfaces," *Physical Review A*, vol. 77, p. 022903, Feb. 2008. 111

[119] B. Holst, V. Recoules, S. Mazevet, M. Torrent, A. Ng, Z. Chen, S. E. Kirkwood, V. Sametoglu, M. Reid, and Y. Y. Tsui, "Ab initio model of optical properties of two-temperature warm dense matter," *Physical Review B*, vol. 90, p. 035121, July 2014. 112

[120] I. V. Lomonosov, A. V. Bushman, and V. E. Fortov, "Equations of state for metals at high energy densities," *AIP Conference Proceedings*, vol. 309, p. 117, 1994. 116

Subject : Ultrafast laser induced structural dynamics probed by time-resolved photoelectron spectroscopy

Abstract: This work aims to study the lattice structural dynamics of metals under laser femtosecond excitation using time-resolved photoelectron spectroscopy (Tr-PES). When irradiated by short infrared laser pulses, the thermal out-of-equilibrium state established between hot electrons and a cold lattice rises specific dynamics where the thermodynamic properties of matter are still subject to debate. The theoretical description of highly excited materials is difficult and appeals new experimental results to improve the understanding of these physical processes and material properties. Nonetheless, important challenges arise from the use of Tr-PES. When metals are irradiated with strong femtosecond infrared laser pulses, non-linear effects, like multi-photon ionization, can take place and produce photoelectrons with tenths of eV of kinetic energy. This pump photoelectron background can conceal the probe-induced photoelectron spectrum, and perturb the probe spectrum via Coulomb interactions (called space-charge effect). To overcome these challenges three actions were carried out. We designed and built a 100 eV beamline to avoid the superposition between the pump background and the probe photoelectron spectrum. The pump/probe space-charge effect was extensively studied theoretically and experimentally. Finally, the pump photoemission was greatly reduced in our experiments by carefully tuning the experimental parameters. This led us to perform Tr-PES measurements on copper samples of the lattice structural dynamics following the evolution of the photoelectron spectrum. The experiment constituted a proof-of-principle of the Tr-PES technique to study materials under strong excitation.

Keywords : Ultrafast heating, out-of-equilibrium, structural dynamics, metals, time-resolved photoemission, space-charge effect

Manuel DE ANDA VILLA **17 décembre 2019**

Sujet : Dynamique structurelle induite par laser ultrabref sondée par spectroscopie des photoélectrons résolue en temps

Résumé : Ce travail est dédié à l'étude de la dynamique structurelle des métaux sous excitation laser femtoseconde en utilisant la technique de spectroscopie de photoémission résolue en temps (Tr-PES). Quand un matériau est irradié avec un pulse infrarouge bref, un régime hors-équilibre est établi entre les électrons chauds et le réseau atomique froid et sa description théorique reste controversée. La complexité de ce régime d'interaction appelle des études expérimentales permettant d'améliorer notre connaissance des propriétés thermodynamiques des matériaux sous excitation intense. Néanmoins, l'utilisation du diagnostic Tr-PES s'accompagne d'importants défis tant du point de vue purement expérimental que conceptuellement. Quand un métal est irradié avec un pulse laser très intense, des effets non-linéaires, comme l'ionisation multi-photonique, peuvent donner lieu à une émission de photoélectrons à des énergies cinétiques de dizaines d'eV. Le spectre, issu de l'impulsion pompe, peut masquer et déformer le spectre de photoélectrons de la sonde par interactions Coulombiennes, appelées effet de charge-espace. Pour surmonter cet effet, trois actions ont étés menées. Une ligne de lumière à 100 eV a été concue et construite pour éviter la superposition des spectres pompe et sonde. L'effet de charge-espace a été étudié en profondeur de facon théorique et expérimentale. Enfin, l'émission issue de la pompe a été drastiquement réduite en ajustant judicieusement les paramètres expérimentaux. Cela nous a amené à réaliser des mesures Tr-PES de la dynamique structurelle sur des échantillons en cuivre en suivant l'évolution du spectre sonde de photoélectrons. Cette expérience démontre que la spectroscopie de photoémission résolue en temps peut être un diagnostic amenant des informations importantes concernant l'étude des matériaux sous excitation intense.

Mots clés : Chauffage ultrarapide, régime hors-équilibre, dynamique structurelle, métaux, photoémission résolue en temps, effet de charge-espace